



Graduate School of
Systemic Neurosciences
LMU Munich

Robust Visual Feedforward and Feedback Signal Processing in the Mouse Thalamus

YANNIK T. BAUER



DOCTORAL
DISSERTATION

Graduate School of Systemic Neurosciences
Ludwig-Maximilians-Universität München

February 2022

Robust Visual Feedforward and Feedback Signal Processing in the Mouse Thalamus

Doctoral dissertation
by Yannik T. Bauer
Graduate School of Systemic Neurosciences
Ludwig-Maximilians-Universität München
February 2022



Except where otherwise noted, this work is licensed under a Creative Commons Attribution 4.0 International License (CC BY 4.0).

SUPERVISORS:

Prof. Dr. Laura Busse
Division of Neurobiology
Faculty of Biology
Ludwig-Maximilians-Universität München
Germany

Prof. Dr. Philipp Berens
Werner Reichardt Centre for Integrative Neuroscience (CIN)
Institute for Ophthalmic Research
Eberhard Karls University of Tübingen
Germany

FIRST REVIEWER: Prof. Dr. Laura Busse
SECOND REVIEWER: Prof. Dr. Philipp Berens
EXTERNAL REVIEWER: Prof. Dr. Stefan Treue

DATE OF SUBMISSION: 28.02.2022
DATE OF DEFENSE: 24.06.2022

To my mother.

ACKNOWLEDGEMENTS

It is always good to be reminded of those I am grateful to, especially when the going gets tough. My thanks go to Laura Busse and Philipp Berens, for giving me the opportunity to pursue this project and for their continued support throughout. Also to Thomas Euler, with whom it all started, to Katrin Franke, Timm Schubert, Tom Baden, Gordon Eske and Valeska Botzenhardt, who helped me with the practical aspects of visual research, and to Miroslav Román Rosón, from whom I inherited this project. Lisa Schmors: Without you, this work would be nowhere near where it is now and I will miss our regular meetings. I am also thankful for the company of the other past and present members of the Euler and Berens labs that I spent time with, especially Theresa Stadler, David Klindt, Camille Chapot, Yanli Ran, Zhijian Zho, Yongrong Qiu, Luke Rogerson, Michael Power, Inmaculada Soldado, Klaudia Szatko, Marili Korympidou, André Chagas, Sophie Laternus, Jan Lause, Ziwei Huang, Cornelius Schröder, Marie Bellet, Christian Behrens, Lara Hoefling, Dmitry Kobak, Murat Seckin Ayan, Sacha Sokoloski and Yves Bernaerts. There are many people that I met during my time at the Graduate Training Center Tübingen that fully deserve my gratitude for providing the context in which all this was possible and who should consider themselves tacitly included here.

In the Busse lab, I would also like to address thanks to the following alumni, who helped me get started: Matilde Fiorini, Agne Klein, Sinem Erisken, Ovidio Jurjut, and Alexandra Wal. Thanks also to the present members, including Martin Spacek, for being a reassuring helping constant. Ann Kotkat: I count myself lucky that you were my first Master's student to supervise and I know the project is in good hands with you. Felix Schneider: thanks for the lively debates about everything and anything – this will continue. And all the other Busse Lab members, namely Lukas Meyerrollersleben, Gregory Born, Simon Renner, Davide Crombie, Magdalena Kautzky, Shreya Khanal, Steffen Katzner, and Melanie Stogia. I would also like to thank the people in the Neurobiology Division and the people of the GSN, for adopting us into their circles, especially Benedikt Grothe, Michael Pecka, and Hilde Wohlfrom. Then I am fondly reminded of the people of the Python summer school, especially Tiziano Zito, who gave me food for the soul.

Thanks to my friends and family, who have kept me grounded throughout these years.

Johanna, words cannot express my gratitude for you, so I hope that my actions in everyday life speak louder than words. Here, I will keep it simple: thank you for being there.

And lastly, I would like to recognize all the mice, whose lives have been created and sacrificed to make this work possible.

ABSTRACT

Robust vision starts in the retina and is finally accomplished in the cortex – but what role does the dorsolateral geniculate nucleus of the thalamus (dLGN) play at the intermediate stage of the early visual processing pathway?

In this thesis, I investigated how the dLGN in the awake mouse computes visual representations and how dLGN activity is shaped by retinal feedforward signals, cortico-thalamic feedback and behavioural state. A guiding hypothesis was that the dLGN is not a passive relay of retinal inputs, but an active signal transformer that may improve the reliability, efficiency, and robustness of the neural population code.

In the first study included in this work, we investigated which functional retinal ganglion cell (RGC) types project to the dLGN and how multiple RGC types converge onto single dLGN relay cells. The second study explored the impact of global suppression of V1 cortico-thalamic feedback on dLGN responses to naturalistic stimuli, and compared the effects of feedback versus locomotion and natural versus artificial stimuli. Lastly, in the third study, we modelled dLGN activity to more complex movie stimuli and used a more selective optogenetic feedback suppression method and assessed if and how the model benefits from additional information about feedback, as well as locomotion and pupil size.

To summarize our results, we first found that the majority of functional RGCs project to the dLGN, which displays a large response diversity, and that an average of five types converge onto a given relay cell, two of which exert the strongest functional impact. Secondly, global feedback suppression reduced dLGN firing rates and increased bursting, with stronger effects observed for naturalistic stimuli than artificial ones, and similar but independent effects of feedback versus locomotion. Lastly, the third study confirmed that dLGN mean firing rates are decreased by direct feedback suppression, and increased during periods of running and large pupil sizes. These observations are reflected in the model, whose predictions benefit mostly from additional feedback but not behavioural state information, but which nevertheless manages to extract dLGN spatio-temporal receptive fields (STRFs) for complex movies as well as artificial stimuli.

In conclusion, *in vivo* mouse dLGN activity is shaped mostly by the influences of sparse functional retino-thalamic convergence, and is modulated to a lesser degree by cortico-thalamic feedback and behavioural state. This suggests that the dLGN is not a passive relay but instead actively transforms visual signals by combining its visual and extra-visual inputs, in agreement with the consensus view on the subject.

CONTENTS

<i>Abstract</i>	v
<i>Contents</i>	vii
<i>List of Figures</i>	viii
<i>Acronyms</i>	ix
1 INTRODUCTION	1
1.1 Overview	3
1.2 Thalamic feedforward inputs – from retina to dLGN . . .	3
1.2.1 Retinal outputs	3
1.2.2 Retino-geniculate convergence & the functional diversity of dLGN cells	4
1.3 Thalamic feedback inputs – the cortico-thalamic loop . . .	7
1.3.1 Anatomy of the cortico-thalamic feedback circuit .	7
1.3.2 The functional role(s) of cortico-thalamic feedback	9
1.4 Modelling dLGN activity to movies, feedback & behaviour	10
1.4.1 Behavioural state influences on dLGN activity . .	10
1.4.2 Feedback suppression via inhibitory optogenetics	11
1.4.3 Naturalistic stimuli	13
1.4.4 Modelling dLGN cell activity	14
2 RETINO-GENICULATE FUNCTIONAL CONVERGENCE IS DIVERSE BUT SPARSE	17
2.1 Román Rosón & Bauer et al. (2019)	17
3 CORTICOTHALAMIC FEEDBACK ELICITS ROBUST EFFECTS IN DLGN RESPONSES TO MOVIES	59
3.1 Spacek et al. (2022)	59
4 MODELLING DLGN ACTIVITY TO MOVIES, FEEDBACK & BEHAVIOUR	93
4.1 Bauer & Schmors et al. (2022) [<i>in preparation</i>]	93
5 DISCUSSION	117
5.1 Feedforward signals to the dLGN	117
5.2 Feedback and behavioural state signals to the dLGN . . .	119
5.3 Future directions	122
5.4 Conclusion	124
<i>Bibliography</i>	125
<i>CV</i>	143
<i>Publications</i>	149
<i>Affidavit</i>	151
<i>Author Contributions</i>	153

LIST OF FIGURES

Figure 1 The cortico-thalamic feedback circuit 16

ACRONYMS

2P	two-photon
Arch	archaerhodopsin
ChR	channelrhodopsin
CT	cortico-thalamic
dLGN	dorsolateral geniculate nucleus of the thalamus
DNN	deep neural network
DOG	difference of Gaussians
DS	direction selectivity
FB	feedback
FF	feedforward
GLM	generalized linear model
Halo/NpHR	halorhodopsin
L6	cortical layer 6
LIF	leaky integrate-and-fire
LNP	linear-nonlinear-Poisson
MEA	multi-electrode array
MLR	mesencephalic locomotor region
Ntsr1	neurotensin receptor 1
OS	orientation selectivity
PBR	parabrachial region (midbrain)
PGN	perigeniculate nucleus (of the thalamus)
PV	parvalbumin
RF	receptive field
RGC	retinal ganglion cell
SbC	suppressed-by-contrast
SC	superior colliculus (midbrain)
stGtACR2	soma-targeting <i>Guillardia Theta</i> anion channelrhodopsin 2
STRF	spatio-temporal receptive field
TRN	thalamic reticular nucleus
V1	primary visual cortex

INTRODUCTION

Vision allows us to see and navigate the world around us, and the fact that it works so reliably is at the same time one of its most remarkable and least noticeable features. Most remarkable, because it works in visual environments that are highly complex, diverse and variable, with noisy and limited visual information. Least noticeable, because most of its workings happen effortlessly and subconsciously.

Visual perception is more than mere sensation of light, more than a simple, passive and direct translation of the retinal image (Gibson, 1972) — it is an active process of transformation and interpretation of visual information (Ullman, 1980), necessary to create a meaningful representation in the mind's eye. While the term *interpretation* may evoke conscious control, perception is largely the product of, as Hermann von Helmholtz put it, *unconscious inference* (von Helmholtz, 1867).

Visual processing is physically implemented in the visual system (Marr & Poggio, 1976), a complex neuro-computational machinery that extracts information at every single stage. All biological vision begins in the eye, the sensory organ that transduces light energy in the visible spectrum of electromagnetic radiation into the neural code. When patterns of photons stimulate the retina, they trigger a cascade of signals through a massively interconnected hierarchical neural network of converging and diverging feedforward pathways (Felleman & Van Essen, 1991; Siegle et al., 2021) and recurrent feedback connections (Riesenhuber & Poggio, 1999). Whereas the visual feedforward hierarchy is generally thought to underlie the increase of neural receptive field (RF) size and feature complexity at successive levels (Hubel & Wiesel, 1962; Lamme & Roelfsema, 2000; Riesenhuber & Poggio, 1999), feedback is hypothesized to serve diverse concepts involving top-down, contextual and predictive processing (Gilbert & Sigman, 2007; Rao & Ballard, 1999), as well as attention, working memory and prior experience (Gazzaley & Nobre, 2012). Insofar as feedforward and feedback processes provide pattern recognition, they can be regarded as active inference and interpretation mechanisms for perception in the above sense.

Yet, our understanding of the computations in the visual system is incomplete (Carandini et al., 2005), as evidenced, for instance, by recent efforts in computer vision to algorithmically emulate the visual object recognition abilities of biological systems (Yamins et al., 2014). Despite the recent breakthroughs the field experienced owing to the development of deep neural network (DNN) (LeCun et al., 2015), the robustness and efficiency of those networks still falls short of human performance levels by a large margin (Dodge & Karam, 2016; Szegedy et al., 2013).

Already at the early precortical stages of the image-forming visual pathway connecting the retina, the thalamic dLGN, and the primary visual cortex (V₁) (Seabrook et al., 2017), little is known about if and how visual representations change between the retina and the dLGN (Usrey & Alitto, 2015). The dLGN occupies the first station after the retina

receptive field:
region of sensory space in which the presence of a stimulus can alter the neuron's response.

robustness:
ability of a system to tolerate perturbations without changing its properties, e.g. neural response reliability or invariance despite changing conditions.

and provides the most direct route for visual information to V1 (Berson, 2008). Since all sensory info (except olfaction) is first processed in the respective first-order nuclei of the thalamus, including the dLGN, before reaching the cortex, the thalamus has also been dubbed the gateway to cortex (Usrey & Alitto, 2015). However, this gateway has classically been viewed as a simple passive relay (Sherman, 2007; Usrey & Alitto, 2015), implying that it essentially passes on or blocks signals from the sensory periphery unchanged, and also implying that no information would be lost if this relay station were skipped (Ghodrati et al., 2017). This stands in contrast to the view of the dLGN as an active signal transformer that changes incoming information before passing it on.

In this thesis, I investigated how the mouse dLGN processes the combined signals from its various visual and extra-visual input sources (Sherman & Guillery, 2002). A central hypothesis that we will revisit throughout this work is that the dLGN is not a mere passive relay but an active signal transformer that improves the efficiency and robustness of the visual population code (e.g. Andolina et al., 2013; Barlow, 1961; Briggs & Usrey, 2011; Dong & Atick, 1995; Ghodrati et al., 2017; Sillito et al., 2006; Usrey & Alitto, 2015). By now, this view reflects the established consensus of the recent literature on the mouse model system, to the point that it may come off as a cliché to say that the dLGN acts as more than a mere passive relay (Babadi et al., 2010). Making this contrast nevertheless provides a useful research framework that continues to be supported by an emerging body of evidence uncovering a hitherto unexpected diversity of mouse dLGN feature selectivity (Cruz-Martín et al., 2014; Marshel et al., 2012; Piscopo et al., 2013). This diversity may be based on, firstly, massive retino-thalamic feedforward (FF) convergence (Ellis et al., 2016; Hammer et al., 2015; Morgan et al., 2016) of the many different retinal ganglion cell (RGC) types (Baden et al., 2016), allowing the dLGN to recombine incoming information into diverse novel features. Secondly, signal transformations may be further aided by ubiquitous cortico-thalamic (CT) feedback (FB) connections (Sillito et al., 2006), adjusting response gain and the spatio-temporal structure of retinal activity patterns (Cudeiro & Sillito, 1996; Usrey & Alitto, 2015).

However, the functional roles of feedforward convergence and feedback are poorly understood, with conflicting evidence arguing either for (Alitto & Usrey, 2008) or against (Sillito et al., 2006) a significant influence. Furthermore, the difficulty of interpreting results in either direction is exacerbated by methodological differences including choice of species, behavioural state of the animal, data type, CT FB manipulation technique, stimuli, and analysis focus, to name but a few. In particular, the interpretation of most of the studies is hampered by the fact that they have probed CT FB effects by manipulating CT FB non-specifically while showing artificial stimuli to anaesthetized cats, which could lead to a substantial underestimation of feedback effects (Durand et al., 2016).

In this regard, the primary contribution of this work is to provide *in vivo* studies of dLGN diversity in the awake, behaving mouse in response to various stimuli, including modelling of responses to naturalistic stimuli and behaviour with or without direct L6 CT FB suppression.

1.1 OVERVIEW

In the following introductory sections, I shall first examine the literature on the topics of the retino-geniculate feedforward pathway (Section 1.2) and the cortico-geniculate feedback pathway (Section 1.3), and then move on to discussing the use of behavioural state information, inhibitory optogenetics, naturalistic movie stimuli and modelling in the service of neural systems identification of the dLGN (Section 1.4).

The subsequent three chapters contain the studies conducted to address these topics in more depth. Chapter 2 includes the first study, Román Rosón et al., 2019, in which we focussed on the question of retino-geniculate convergence as the basis of the functional diversity of the dLGN. Chapters 3 and 4 contain the study published as Spacek et al., 2022 and the manuscript Bauer et al., 2022 (*in preparation*), in which we investigated the functional impact of CT FB via different optogenetic CT FB inhibition techniques and further assessed the influence of different naturalistic movie stimuli and behavioural state. Lastly, in the discussion chapter (Chapter 5), I will summarize our findings, discuss their interpretation and provide an outlook for future directions for this work.

1.2 THALAMIC FEEDFORWARD INPUTS – FROM RETINA TO DLGN

1.2.1 Retinal outputs

The dorsolateral geniculate nucleus of the thalamus (dLGN) receives its main feedforward (FF) input drive from the retina, a thin sheet of light-sensitive tissue at the back of the eye that converts light into the neural code at the basis of vision (Dhande et al., 2015). Every aspect of visual processing is built on the spiking activity of RGCs, the output layer of the retina (Dhande & Huberman, 2014). Retinal inputs to the dLGN are of a *feedforward* nature insofar as the retina precedes the dLGN in the image-forming visual path linking retina→dLGN→V1 (the retino-geniculo-cortical path). Retino-thalamic RGCs also provide the only *driver* synapses input onto dLGN cells, all other inputs synapses to the dLGN being *modulatory* (Sherman & Guillery, 2002).

It may be tempting to liken the retina to the light-detection functions of a camera sensor, but that analogy grossly ignores the enormous signal processing capabilities of the retinal machinery (Gollisch & Meister, 2010). These include single-photon detection (Baylor et al., 1979; Trenholm & Krishnaswamy, 2020), edge detection and decorrelation (Franke et al., 2017) via center-surround RFs (Barlow, 1953), adaptation / gain control (Fairhall et al., 2001; Wark et al., 2007), image compression, extraction of parallel feature channels (Baden et al., 2016; Lettvin et al., 1959; Roska & Meister, 2014), to name but some general processes. In vertebrates, retinal processing is a signal cascade through multiple successive neuronal layers. Visual information flows through the vertical pathway starting with photoreceptor cells, via bipolar cells, and ending with RGCs. On this route, the signals are extensively shaped by the activity of interneurons, namely horizontal cells and amacrine cells (Masland, 2012). The RGC layer is thus the final output layer of the retina.

The RGC layer comprises many different RGC types (based on function, morphology, genetics, intra-retinal connectivity, retinal mosaic and immunohistochemical profile (Baden et al., 2016)). In the mouse retina, information gets distributed across 40+ functional RGC types (Baden et al., 2016; Laboissonniere et al., 2019; Peng et al., 2019; Sanes & Masland, 2015; Sümbül et al., 2014) extracting distinct features from the visual input in parallel and evenly tiling the retina. A few fundamental response features include ON-, OFF-, and ON-OFF responses, transient vs. sustained responses, (opponent) colour-coding, orientation selectivity (OS), direction selectivity (DS), suppressed-by-contrast (SbC) responses, looming responses, and more (Baden et al., 2016; Dhande et al., 2013), which may also get combined with each other to give rise to a continuum of feature filters. For approximately half of the RGC types the precise function has yet to be determined (Sanes & Masland, 2015), but there are results promising to continue towards a consensus on a unified classification catalogue of RGC types (Goetz et al., 2021).

It is yet unclear precisely what retinal information is sent to the dLGN and how it is processed there. The mouse retina projects RGC output axons to approximately 50+ retino-recipient areas (Martersteck et al., 2017), including the SC and dLGN as the main targets, as well the ventral LGN (vLGN), the hypothalamus, the suprachiasmatic nucleus, and pretectal nuclei of the midbrain, to name but a few. In fact, in the mouse, ca. 90 % of all RGCs project to the SC (Ellis et al., 2016; Seabrook et al., 2017), compared to ca. 30-40 % projecting to dLGN (Martin, 1986). Of the dLGN-projecting RGCs, 80 % also innervate the SC (Ellis et al., 2016; Huberman et al., 2008).¹ Nevertheless, to determine the functional consequences of retinal projection patterns on dLGN visual processing, we also need to assess both the types of features sent to dLGN, as well as the patterns of retino-geniculate convergence.

1.2.2 *Retino-geniculate convergence & the functional diversity of dLGN cells*

The issue of retino-geniculate convergence is relevant to the questions of thalamic functional diversity and signal transformation insofar as convergence can enable recombination of visual feature channels to generate new features - a result that would run counter to the notion of the dLGN as a passive relay. It is a matter of current debate which functional RGC types project to the dLGN, what their convergence patterns are, and how much this contributes to thalamic signal transformations, if at all (Usrey & Alitto, 2015). The answer mainly seems to depend on the species and on whether we are considering functional or anatomical evidence.

On the one hand, classical research in cats and primates has suggested little convergence (reviewed in Sherman & Guillery, 2002). Evidence of parallel retinogeniculate feature channels has typically been confined to few channels, the X-, Y-, and W-pathways for cats, or the anal-

¹ This contrasts with the distribution in primates, where the pattern reverses with ca. 10 % of RGCs projecting to the SC vs. 90 % to dLGN (Kremkow & Alonso, 2018; Perry & Cowey, 1984), indicating a potential species-specific difference in the relative importance of the pathways.

ogous parvo-, magno-, and konio-cellular pathways in monkeys. Since the dLGN exhibits the textbook layered structure in those species, which map on to the termination patterns of these three feature channels, this might lead to the assumption that the dLGN was just passively relaying this information en route to V_1 , without much recombination (reviewed in Sherman & Guillery, 2002; Usrey & Alitto, 2015).

However, given the recent discoveries of RGC feature diversity in the mouse (e.g. Baden et al., 2016), it seems implausible that RGC types in cats and primates, who rely on vision as their primary sense and who have better vision than mice (Huberman & Niell, 2011), should be limited to only three types. Indeed, a retrograde tracing study in macaques has revealed at least 13 different retino-geniculate RGC types (Dacey et al., 2003), which conversely also suggests that the dLGN is receiving more diverse information than previously assumed.

As regards thalamic signal transformations, earlier evidence also has largely argued against a substantial dLGN contribution. This view is based on observations that feature selectivity in the cat and macaque dLGN closely resembles that of retinal afferents (Hubel & Wiesel, 1961; Kaplan et al., 1987; Sincich et al., 2007), based on so called S-potentials, extracellular post-synaptic potential (EPSP) signatures of incoming RGC spike input into dLGN cells.

On the other hand, dLGN cells have also been shown to have a stronger inhibitory surround RF, lower firing rates and transmitting only a small fraction of incoming RGC spikes to cortex (Hubel & Wiesel, 1961), pointing towards a role of a signal transformer sharpening RFs, and increasing the sparseness and efficiency of the visual code (Usrey & Alitto, 2015). Overall then, cat and primate studies are not unequivocal but seem to point more towards a view of the dLGN as a passive relay.

For the mouse dLGN, there is a parallel debate about the degree of functional diversity, signal transformations and convergence, yet with a clear time trend towards more diversity and transformations (Chen et al., 2016). First quantitative characterizations of dLGN feature diversity in mice (Grubb & Thompson, 2003) have concluded that, barring ON- vs. OFF-center differences, there was overall little evidence for parallel processing. However, the authors also pointed out that not all recorded cells could be mapped quantitatively using their stimulus set, which opens up the distinct possibility that other stimuli, e.g. naturalistic ones, might elicit different type responses. Furthermore, while the authors did find a potential distinction of transient vs. sustained responses, they did not call this a type distinction because it did not hold up in other spatial and temporal domains. This requirement may arguably be overly strict, which points to a deeper issue about the criteria for cell type classification. The idea of little dLGN signal transformations sits well with anatomical evidence of little retino-thalamic convergence. Chen and Regehr, 2000 found convergence of as few as 1-3 RGC types onto dLGN cells, favouring the idea of a passive inheritance of dLGN RF properties such as spatial configuration and size from input RGCs.

On the other hand, we now do have evidence in favour of mouse dLGN feature diversity, signal transformation and convergence. Clearly starting to go beyond the classical three dLGN types, like in the retina

(Baden et al., 2016), more recent studies have revealed more complex and diverse representations in dLGN cells displaying OS, DS and SbC properties, varying transient vs. sustained response latencies, and ON- and OFF- sign-preferences (Cruz-Martín et al., 2014; Marshel et al., 2012; Piscopo et al., 2013; Zhao et al., 2013). This shows that dLGN receives input from a rich diversity of RGC types. Different RGC types also seem to terminate in different regions of the mouse dLGN, which does not have a layered structure but is still subdivided into a medial core and a lateral shell region (Sherman, 2001). Whereas ON-OFF DS RGCs and ON DS RGCs terminate preferentially in the dLGN shell (Dhande et al., 2013; Osterhout et al., 2015), transient-OFF alpha RGCs (Huberman et al., 2008; Huberman et al., 2009) and ON alpha RGCs (Ecker et al., 2010; Osterhout et al., 2014) selectively terminate in the dLGN core.

Still, this diversity could simply be inherited from the retina, with little need for thalamic signal transformations. Here however, recent anatomical evidence of massive retino-geniculate convergence favours the idea of novel dLGN feature generation. Mono-transsynaptic rabies virus tracing revealed that 40-50 % of single dLGN neurons could receive input from > 90 RGCs, sometimes from both eyes, and composed of up to 9 different types (Rompani et al., 2017). This finding corroborates connectomics, tracing and chronic imaging studies that uncovered a surprisingly large degree of *anatomical* retino-geniculate convergence and divergence patterns (Ellis et al., 2016; Hammer et al., 2015; Liang et al., 2018; Martersteck et al., 2017; Morgan et al., 2016), which also seem to hold for dLGN inhibitory interneurons (Morgan & Lichtman, 2020).

Nevertheless, this anatomical evidence needs to be brought in line with evidence about the *functional* impact of those synapses on dLGN responses. Indeed, functional studies have usually promoted a much lower number of functionally relevant RGCs, with recent optogenetic studies estimating that, while dLGN relay cells may receive inputs from multiple RGCs, their activity is dominated by the minority (Bauer et al., 2021; Litvina & Chen, 2017). If functional diversity and novel feature generation match the anatomical data, then this would speak in favour of a role of the dLGN as an active signal transformer. If, on the other hand, it turns out that the impact of massive convergence on functional diversity and signal transformation is insignificant, this would again speak in favour of a role of the dLGN as a passive relay, but would also raise questions about the purpose of such massive convergence. Perhaps then, we will be able to reconcile the two types of evidence by considering the synaptic connection strength, consistent with idea that dLGN cells may receive massively converging retinal inputs, with just a few dominant ones determining the dLGN cell response and the other weak ones fine-tuning the response and allowing adult synaptic plasticity. Whatever the debate on retino-geniculate convergence may settle on, there is still another candidate mechanism that may shape dLGN signals: cortico-thalamic feedback.

1.3 THALAMIC FEEDBACK INPUTS – THE CORTICO-THALAMIC LOOP

In general, feedback (FB) occurs when systems or their parts have recurrent connections, i.e. they are connected to themselves or each other in such a way as to form a loop, such that outputs also become inputs in a cyclic cause-and-effect chain of processes. The mammalian visual system includes numerous brain areas that are profusely interconnected. Since most of the lateral and top-down connections eventually result in recurrent feedback connections that far outnumber feedforward (FF) connections, this has fuelled speculations that feedback plays a critical role in visual processing (Macknik & Martinez-Conde, 2009).

Hypotheses about the functional role of feedback circuits abound, including top-down attention, working memory, expectation, prediction, (Bayesian) priors, context, and consciousness (Angelucci & Sainsbury, 2006; Bar, 2004; Bastos et al., 2012; Gazzaley & Nobre, 2012; Knill & Pouget, 2004; Kok et al., 2012; Kreiman & Serre, 2020; Lamme & Roelfsema, 2000; Rao & Ballard, 1999; Roelfsema & de Lange, 2016; Summerfield & Egnér, 2009; van Bergen & Kriegeskorte, 2020). Compared to theories of FF processing, however, there is little consensus on the specific function of FB connections (Gilbert & Li, 2013; Heeger, 2017). In other words, there is unequivocal evidence for recurrent computation in the brain, but it is less obvious *why* and *how* the brain uses recurrent algorithms (van Bergen & Kriegeskorte, 2020).

1.3.1 Anatomy of the cortico-thalamic feedback circuit

In the mammalian visual pathway linking retina→dLGN→V1 (the retinogeniculo-cortical path), direct feedback from cortex to dLGN arises exclusively from primary visual cortex (V1) cortical layer 6 (L6) cortico-thalamic (CT) pyramidal cells (Briggs, 2010; Sherman & Guillery, 2002; Sillito & Jones, 2002). These close the cortico-thalamo-cortical (CTC) loop (Shepherd & Yamawaki, 2021) (henceforth referred to as *CT FB loop/circuit*) in multiple ways, including direct excitatory synapses onto dLGN relay cells, as well as onto dLGN inhibitory interneurons and TRN inhibitory neurons, both of which thus provide disynaptic inhibition to dLGN relay cells, as illustrated in Figure 1.² In mice, L6 CT cells selectively express the neurotensin receptor 1 (*Ntsr1*) promoter (Bortone et al., 2014; Gong et al., 2007) and can be targeted genetically via the Cre-Lox system (Josh Huang et al., 2013; Madisen et al., 2010; Nagy, 2000) in order to investigate their structure and function (Olsen et al., 2012; Velez-Fort et al., 2014). Using *Ntsr1*-Cre mouse lines, it has been shown that *Ntsr1*-positive L6 CT pyramidal cells constitute approximately 65 % of the L6 pyramidal cell population, and are distinct from L6 cortico-cortical (CC) pyramidal neurons (35 %) whose axons remain within cortex to communicate intra-cortical information transfer (Olsen et al., 2012; Velez-Fort et al., 2014). As can be seen in the circuit diagram, L6 CT cells are in a good anatomical position to exert strong control over what infor-

² This is not the first instance of feedback on the visual pathway, which already occurs as early as the first visual synapse of the outer retina, between photoreceptor cells and horizontal cells (Drinnenberg et al., 2018).

mation reaches the cortex (Sillito et al., 2006): Not only do they provide extensive feedback connections both to dLGN relay cells and dLGN inhibitory cells (Briggs, 2010), as well as GABAergic neurons in the TRN (in cats known as the perigeniculate nucleus (of the thalamus) (PGN), the visual part of the TRN) (Murphy & Sillito, 1996). But also within cortex, L6 CT cells (in contrast to L6 CC cells) extend their dendrites to the layers L5a (Kim et al., 2014), L4, and beyond (Augustinaite & Kuhn, 2020; Niell, 2015; Velez-Fort et al., 2014).

Nevertheless, it should be pointed out that L6 CT typification may not be as clear-cut due to the possible heterogeneity of L6 CT cells (Briggs, 2010). Thus, morphological, transcriptomic and electrophysiological data suggests a possible subdivision into 2-4 subtypes (Frandolig et al., 2019; Gouwens et al., 2019; Tasic et al., 2016). While it is currently unknown whether L6 CT subtypes mediate separate functional aspects of FB, it may be possible to disentangle their role through genetic targeting in the future (Graybuck et al., 2020).

Feedback synapses far outnumber feedforward synapses, and this seems true for most brains of across most mammal species (Macknik & Martinez-Conde, 2009). In the cat dLGN, L6 CT FB synapses constitute 30 % vs. 5-10 % retinal afferents (Erişir et al., 1997)³. The general agreement is that the cortical-to-retinal input ratio is between 1:2 and 1:6 in both cats and primates (Erişir et al., 1997; Macknik & Martinez-Conde, 2009; Sherman & Guillery, 2002). Interestingly, this preponderance of FB over FF connections also extends to cortex. Peters et al., 1994 showed that only 1–8 % of the synaptic inputs into primate V1 layer 4C neurons originate in the LGN, while Ahmed et al., 1994 puts the estimate of cat dLGN afferents to V1 L4 to only 6-9 %, in contrast to 45 % from L6 CT cells. Lastly, Dana Ballard, 2015 made a cross-species estimate of a cortico-cortical FB:FF ratio of 1:10.

At the same time, it would be a potential mistake to assume that a numerically larger number of inputs means that those inputs are functionally most important (Macknik & Martinez-Conde, 2009; Sherman & Guillery, 2002). Indeed, the functional impact of a synapse depends more on its position on the dendrite, as well as its receptor types and density. Since CT FB inputs contact the distal dendrites of dLGN cells (Erişir et al., 1997) via synapses containing mGluR1 metabotropic receptors (Godwin et al., 1996) and lacking NMDA-receptors (Thompson et al., 2016), this implies rather small, slow and long-lasting effects on dLGN processing (Sherman & Guillery, 2002). By contrast, RGC inputs contact proximal dLGN cell dendrites and exert a strong and fast influence via ionotropic receptors (Sherman & Guillery, 2002). Thus, the general consensus is that the effects of L6 CT FB synapses are rather *modulatory*, compared to RGCs, which provide the only *driving* input to the dLGN (Sherman & Guillery, 2002). Moreover, as shown in the circuit diagram, L6 CT FB contacts onto dLGN relay cells are both directly excitatory, as well as indirectly inhibitory, both via dLGN inhibitory in-

³ The remaining proportions of input synapses are divided between 30 % inputs from GABAergic inhibitory interneurons and TRN, and 30 % inputs from the brainstem (SC and PBR).

terneurons (Sillito & Jones, 2002; Usrey & Sherman, 2019), and via the TRN, so the effects of CT FB are expected to be complex.

Nevertheless, the emerging picture of the visual system seems to include a general pattern of massive and ubiquitous FB connections that modulate ascending inputs at every stage of visual processing (Sillito et al., 2006).

1.3.2 *The functional role(s) of cortico-thalamic feedback*

In contrast to the anatomy of cortico-thalamic (CT) feedback (FB), there is much less consensus on its potential functional role(s) as most research has uncovered diverse and sometimes inconsistent findings (Briggs & Usrey, 2011). This is in no small part because of the aforementioned fact that the modulatory CT FB effects are rather subtle, compared to the retinal drive, whereby a small percentage of driving RGC inputs seems to be sufficient to largely determine the STRF properties of dLGN cells (Weyand, 2016).

A second factor is that L6 CT cells themselves, despite having been identified as the source of CT FB, still play an elusive role in V1 and dLGN processing. On the one hand, their aforementioned anatomical position, taken together with physiological evidence, has been interpreted to point to a special role of L6 CT cells as ‘gain controllers’ (Bortone et al., 2014; Olsen et al., 2012) or ‘gatekeepers’ (Sillito et al., 2006). On the other, the potential heterogeneity of the L6 CT population (see Section 1.3.1), together with their deep location in cortex and their extremely sparse firing rates (Velez-Fort et al., 2014), have made it difficult to target them via imaging (Andermann et al., 2013; Augustinaite & Kuhn, 2020), electrophysiology (Briggs, 2010), or optogenetics (Denman & Contreras, 2015).

Thirdly, the diversity of findings may partly be explained by the diversity of methods employed. This diversity arises from the unique combination of methods in each study, including *species* (e.g. cat, macaque, marmoset, ferret, mouse); *behavioural state* (e.g. anaesthetized, awake, head-fixed, freely moving); *feedback manipulation technique* differing in spatial and temporal scale, specificity, reversibility, (in-)directness, sign (e.g. V1 aspiration, V1 ablation, V1 cooling, V1 muscimol, TMS, GABA or CGP iontophoresis, optogenetic enhancement (ChR2) of PV-neurons, or suppression (archaerhodopsin (Arch), halorhodopsin (Halo/NpHR)) of L6 CT cells); *recording type* (e.g. patch-clamp or multi-electrode array electrophysiology, functional imaging); *stimulus type* (e.g. static vs. dynamic, artificial vs. naturalistic); and *functional readout* (e.g. mean firing rates, spatial and temporal processing, RF surround suppression, cross-correlation, precision, reliability, orientation and direction selectivity, firing mode etc.). Understandably, this makes it hard to infer general functional properties of CT FB.

In general, studies on cats, primates and ferrets using pharmacological or cooling techniques for cortex-wide FB suppression, have found that CT FB modulates both dLGN spatial integration (Andolina et al., 2013; Cudeiro & Sillito, 1996; Hasse & Briggs, 2017; Jones et al., 2012; Murphy & Sillito, 1987; Nolt et al., 2007; Rivadulla et al., 2002; Sillito & Jones,

2002; Wang et al., 2018; Webb et al., 2002), temporal processing (Andolina et al., 2007; Hasse & Briggs, 2017; Sillito & Jones, 2002), response gain (Przybylski et al., 2000; Rivadulla et al., 2002; Wörgötter et al., 2002) and transitions between thalamic tonic and burst firing modes (De Labra et al., 2007; Sherman, 2001; Wang et al., 2006). In these studies, CT FB removal has been associated with decreased STRF precision, less extra-classical RF surround-suppression, and increased bursting.

In mice, comparatively fewer studies exist, though arguably with higher CT FB manipulation specificity and precision. While Olsen et al., 2012 reported increased dLGN firing rates during optogenetic CT FB silencing, Denman and Contreras, 2015, using optogenetic suppression of L6 CT cells via the light-driven proton pump Archaeorhodopsin-3 (Arch) (Chow et al., 2010) in *Ntsr1-Cre* mice, found a mix of inhibitory and excitatory effects without any clear net effect. Other researchers also failed to find any effects of CT FB on the above dLGN properties (Hasse & Briggs, 2017; King et al., 2016; Li et al., 2013; Lien & Scanziani, 2013), or argued that some reported effects were implausible (Alitto & Usrey, 2008).

But the difficulty of getting a unified framework of CT FB function is not simply a matter of correctly generalizing from the diversity of methods. The interpretation of most of the studies is hampered by the fact that they have probed CT FB effects by manipulating CT FB non-specifically while showing artificial stimuli to anaesthetized animals, which could lead to a substantial underestimation of feedback effects (Durand et al., 2016). Firstly, anaesthesia may significantly affect the responsiveness of L6 CT FB neurons (Briggs & Usrey, 2011; Keller et al., 2020). And secondly, CT FB might be most relevant not for processing simple stimuli, but instead for processing complex (Gulyás et al., 1990), dynamic (Sillito & Jones, 2002), naturalistic stimuli seen during wakefulness, consistent with the notion of FB providing context based on an internal model built from the statistics of the natural visual world (Cudeiro & Sillito, 1996; Rao & Ballard, 1999). Therefore, a paradigm that probes dLGN activity in the awake, behaving mouse in response to naturalistic movie stimuli during direct L6 CT cell suppression, would appear well-suited to address these points.

A last note of caution: given the heterogeneity of previously discovered effects, it might not make sense to expect to find a single functional role of CT FB, but instead acknowledge the potential existence of a corresponding multitude of roles.

1.4 MODELLING DLGN ACTIVITY TO MOVIES, FEEDBACK & BEHAVIOUR

1.4.1 *Behavioural state influences on dLGN activity*

While the brain is classified into sensory areas and motor areas, it has long been evident that the activity of sensory brain areas is also influenced by behavioural state (Busse, 2018; McCormick, 1992; Sherman & Guillery, 1996; Swadlow & Weyand, 1987). The term ‘behavioural states’ can refer to a range of phenomena, including sleeping, waking, anaesthesia, attention etc., and here, the focus will be on locomotion and pupil size during wakefulness, which are often also used as proxies to binarize

behavioural states into periods of arousal vs. quiescence⁴. Their effects on neural activity have been reported across sensory domains, including visual (Niell & Stryker, 2010), auditory (Pluta et al., 2015) and somatosensory (Schneider et al., 2014) cortices.

In the mouse visual system, behavioural state effects extend throughout, apparent not only in V1 (Niell & Stryker, 2010), but also further upstream in dLGN (Aydın et al., 2018; Erisken et al., 2014), and even as early as in the retina (Schröder et al., 2020). Interestingly, these behavioural state effects in the visual system are not limited to stimulus periods but also extend into periods of spontaneous behaviour in the absence of visual stimulation (Stringer et al., 2019). In V1, locomotion increases the neural response gain of orientation contrast and size tuning (Erisken et al., 2014; Niell & Stryker, 2010) and shifts spatial (Mineault et al., 2016) and temporal (Andermann et al., 2011) frequency tuning towards higher resolutions. In the dLGN, locomotion enhances neural firing rates, shifts thalamic firing mode from burst to tonic mode and also increases spatial integration (Erisken et al., 2014).

Similar to locomotion, pupil size has also been studied as a proxy of arousal. Indeed, a common observation is that periods of increased locomotion are accompanied by increases in pupil size, and periods of sitting with decreased pupil size (Erisken et al., 2014). However, it has been shown that, even in the absence of locomotion, increased pupil size coincides with sharpened sensory coding (under constant illumination to rule out the pupil light reflex) (Reimer et al., 2014; Vinck et al., 2015) in V1, and are correlated with dLGN relay cell activity (Molnár et al., 2021).

The underlying neural circuits mediating locomotion-related activity effects in dLGN seem to be located in the brain stem McCormick, 1992; Nestvogel and McCormick, 2021; Sherman and Guillery, 1996, specifically cholinergic pathways originating in the mesencephalic locomotor region (MLR), a brain stem structure encompassed by the parabrachial region (midbrain) (PBR) (Lee et al., 2014). The MLR projects cholinergic axons both directly to dLGN, and indirectly to V1, via the basal forebrain (Lee et al., 2014). Stimulation of MLR axons in the basal forebrain or direct stimulation of the basal forebrain have both been shown to induce effects in V1 similar to those of locomotion (Lee et al., 2014; Pinto et al., 2013), and activity of cholinergic axons in V1 is correlated with locomotion (Reimer et al., 2016).

In conclusion, thalamic activity is influenced not only by retinal feed-forward and cortico-thalamic feedback signals, but also by behavioural state. What is less clear is what the individual contributions of these factors to dLGN activity are when they all act in concert.

1.4.2 *Feedback suppression via inhibitory optogenetics*

Optogenetics refers to the integration of optics and genetics in order to excite or inhibit specific neurons with light via the genetic introduction of microbial opsins (light-sensitive membrane proteins) into the neural

⁴ Although these motor readouts can also be independent from the more abstract state of arousal or alertness (Vinck et al., 2015).

system (Boyden et al., 2005; Deisseroth, 2011; Dugué et al., 2012; Fenno et al., 2011; Yizhar et al., 2011)⁵. This selective and reversible control of targeted neurons enables researchers to investigate their causal role within the complex, dynamic neural system with unprecedented spatio-temporal resolution. Thus, optogenetics offers clear advantages to alternative manipulation techniques mentioned in the previous section (e.g. cooling, ablation) that are neither as spatio-temporally precise nor reversible.

Since excitatory optogenetics alone only establish the causal sufficiency of the manipulated neural population for a given neural readout measure, inhibitory optogenetics are required to supplement their causal necessity (Yizhar et al., 2011). Yet, in contrast to opto-excitation (typically done via cation-conducting channelrhodopsins (ChRs) (Nagel et al., 2002)), optogenetic suppression has long been more challenging in a number of ways (Wiegert et al., 2017).

One technique has been to inhibit the target neurons *indirectly* by activating inhibitory neurons via the channelrhodopsin ChR2, which benefits from the sensitivity and efficiency of ion channels (e.g. Atallah et al., 2012; Vaiceliunaite et al., 2013). However, the indirect nature of this manipulation may result in diffuse circuit effects, so care must be taken to compare the observed effects to more direct manipulation methods.

Alternatively, direct inhibition may be achieved via hyperpolarizing ion pumps such as the outward-proton pump archaerhodopsin (Arch) (Mattis et al., 2011) or the inward-Chloride pump halorhodopsin (Halo/NpHR) (Matsuno-Yagi & Mukohata, 1980). However, issues arise from limited light-sensitivity and efficiency (Wiegert & Oertner, 2016), which are particularly severe for deep targets such as L6 CT cells, because light intensities are highly variable in light-scattering brain tissue (Berndt et al., 2014). The need for continuous, high-intensity light may pose problems by denaturing brain tissue, creating non-physiological tissue temperatures, or creating photo-electric artefacts. Moreover, since ion pumps can work against the electrochemical gradient, they are at risk of producing physiologically abnormal ion concentrations. This may result in ‘paradoxical’ depolarizing currents caused by NpHR-induced reversed chloride (Cl⁻) resting potentials that trigger Cl⁻ efflux upon GABA_A receptor opening. Similarly, archaerhodopsin-induced alkalization of presynaptic boutons might trigger opening of pH-sensitive Ca²⁺-channels, leading to undesired vesicle fusion into the synaptic cleft and thus unintentional synaptic signalling (Mahn et al., 2016; Wiegert & Oertner, 2016).

Recent developments and discoveries of anion-conducting channelrhodopsins promise to address these issues, enabling direct photosuppression with higher sensitivity and efficiency (Berndt et al., 2014; Berndt et al., 2015; Govorunova et al., 2015; Wietek et al., 2017). The high efficiency arises from the channel-opening acting like a shunting inhibition, which additionally avoids creating abnormal concentration gradients seen in ion pumps (Berndt et al., 2014). In particular, the soma-targeting

⁵ I will refer synonymously to the terms of excitation, depolarization, activation, and gain-of-function on the one hand, and inhibition, hyperpolarization, inactivation, loss-of-function, and suppression, on the other, although it should be pointed out that optogenetic manipulation may not completely activate or inactivate a neuron so that gain-of-function and loss-of-function would most accurately describe the effects.

Guillardia Theta anion channelrhodopsin 2 (stGtACR2) (Mahn et al., 2018) exhibits high light sensitivity and improved photocurrents. Importantly, stGtACR2 also offers the additional benefit of being expression-restricted to the region around the soma and the axon-initial segment (AIS), which is achieved via the insertion of a soma-targeting motif of the somalocalized voltage-gated potassium channel Kv2.1 (Baker et al., 2016). This is especially relevant to photosuppression in the light of reports of reversed chloride membrane potentials in the axons of some neurons under normal, physiological conditions, where axonal Cl⁻ currents may inadvertently trigger action potentials (Mahn et al., 2018).

Taken together, stGtACR2 thus seems to be a good candidate for direct silencing of L6 CT cells. Yet, it is not perfect, and remaining issues regarding this optogenetic suppression tool will be considered in the Discussion (Chapter 5).

1.4.3 *Naturalistic stimuli*

The purpose of a biological organism's visual system is to process visual information about its natural environment, and so it has been shaped by natural visual statistics through the forces of evolution and experience-dependent development (Felsen & Dan, 2005).

Yet historically, the fundamental insights of visual neuroscience into the computations of the visual system (such as basic STRF structure and feature selectivity) have mostly been informed by artificial stimuli (Felsen & Dan, 2005). This is in large part because artificial stimuli offer the advantage of experimental control: being simple and easily parameterized into the component of interest (Felsen & Dan, 2005; Mante et al., 2008; Rust & Movshon, 2005).

Over the recent years, the debate over the ecological validity of visual neuroscience experiments (Sonkusare et al., 2019) has also taken hold in the emerging view that artificial stimuli may not be sufficient for visual systems identification and that naturalistic stimuli may be needed as a complement (Felsen & Dan, 2005). Indeed, with regards to feedback processing, naturalistic stimuli may shed light into the previously discussed inconsistent findings about the functions of feedback in the cortico-thalamic feedback circuit. Specifically, if the role of feedback was to provide context based on an internal model built from the statistics of the world (Lee & Mumford, 2003; Rao & Ballard, 1999), natural stimuli would be expected to best comply with this model, and likely drive these feedback mechanisms in a more robust way.

However, naturalistic stimuli present their own challenges, so much so that they have stirred a controversy over their usefulness (Rust & Movshon, 2005). Conceptually, natural or naturalistic stimuli are not yet well-defined and often imbued with an anthropocentric perspective, ranging from static images to movies of man-made objects and environments and nature scenes. Commercial movies may have rather unnatural characteristics such as multiple camera angles, zooms, pans, scene-cuts, the inclusion of music and exaggerated sound effects, the ability to skip time, etc. (Vanderwal et al., 2019).

1/f-like power spectrum:

*"'1/f-like noise' refers to a stochastic phenomenon whose spectral energy S decreases in proportion to frequency, f . That is, the spectral density has the form $S(f) \sim 1/f^a$, for some positive constant a . In the case where $a=1$, the energy scales inversely with frequency and is called 'pink noise'. 1/f-like fluctuations are widely found in nature, such as the power spectrum of natural scene intensities."
(Felsen & Dan, 2005).*

Nevertheless, they may be united by the key elements of being complex, dynamic and rich (Hasson et al., 2009), and individual movie frames share certain statistical properties with natural still images, most notably a distinctly (non-Gaussian) 1/f-like spatio-temporal power spectrum (adapted from Felsen & Dan, 2005).

A key challenge of naturalistic movies lies in the analysis of their effects on neural responses, as naturalistic stimuli do not offer the same experimental control as artificial stimuli. Here, various modelling approaches may prove increasingly necessary (Ghodrati et al., 2017). These modelling approaches will also help us in evaluating various empirical questions regarding naturalistic stimuli themselves, such as what key features naturalistic movies must have to mimic the natural world and evoke naturalistic patterns of neural activity, and what differences, if any, exist between naturalistic movies and artificial stimuli that matter to the visual system. On the one hand, non-linear coding mechanisms in the visual system, such as adaptation, contrast gain control, and burst mode may operate differently for different classes of stimuli at different processing stages on the visual path (Felsen & Dan, 2005; Lesica et al., 2007; Lesica & Stanley, 2004; Olshausen & Field, 2005). On the other, comparisons of model responses to artificial and naturalistic movies of different types have indicated that stimulus class may not be so important in predicting neural activity in dLGN accurately (Mante et al., 2008), but have cautioned that this might not be true for fast adaptation, bursting and stimulus coding downstream in V1 (Mante et al., 2008; Olshausen & Field, 2005). Further studies in this direction will allow us to standardize naturalistic movie stimuli and understand their key properties from the perspective of the different processing stages of the visual system.

1.4.4 Modelling dLGN cell activity

The dLGN has been extensively modelled at a variety of levels, from the biophysical properties of its neurons to feedback network models dealing with issues in high-level vision (reviewed in Ghodrati et al., 2017). Modelling approaches abound in various model types (descriptive, mechanistic, prescriptive) and architectures (broadly, spiking or firing rate models), in order to explore various dLGN activity phenomena such as its basic STRF structure (e.g. using a difference of Gaussians (DOG) model to describe the centre-surround RF (Irvin et al., 1993)), temporal dynamics (Keat et al., 2001), non-linear phenomena like bursting (Lesica et al., 2007; Lesica & Stanley, 2004), contrast gain control (Bonin et al., 2006) and adaptation (Mante et al., 2005); or general visual system phenomena such as decorrelation and coding efficiency (Dong & Atick, 1995), synchronous oscillations (Robinson, 2006), reliability (Wang et al., 2010) and predictive coding (Jehee & Ballard, 2009).

Focusing on descriptive models of dLGN activity in anaesthetized cats viewing naturalistic stimuli, a surprising fact is that pure feedforward (FF) models perform quite well even without the inclusion of feedback (FB) mechanisms (Ghodrati et al., 2017). Estimating dLGN STRFs by training linear convolution models (Wang et al., 2007), leaky integrate-and-fire (LIF) models (Lesica et al., 2007; Lesica & Stanley, 2004), or RC

(resistor-capacitor) circuit models (Mante et al., 2008) on different stimuli, it was possible to explain a large fraction of variance of dLGN activity based on retinal inputs or the stimulus input itself, and elucidate the contribution of adaptation and contrast gain (Mante et al., 2008) or bursting (Lesica et al., 2007; Lesica & Stanley, 2004). In addition, these studies have also been informative with regards to the debate about the usefulness of natural stimuli in dLGN systems identification (see previous subsection). But the good performance of purely FF models raises questions about the importance of FB mechanisms in dLGN processing.

Despite the apparent irrelevance of FB, we should bear in mind that FB mechanisms might still have been incorporated tacitly into the models (Ghodrati et al., 2017), in a similar manner that retinal computations may sometimes be approximated in a single step of dLGN STRF construction (e.g. Mante et al., 2008), rather than being used as explicit input into dLGN (e.g. Wang et al., 2007). On the other hand, there are models that do integrate FB, albeit implicitly via modified FF transfer characteristics (e.g. Einevoll & Plesser, 2012), and accurately predict its effects on dLGN spatial integration in line with experimental findings (Cudeiro & Sillito, 1996; Sillito & Jones, 2002), but this model type does not include an explicit FB loop and is solely based on responses to artificial stimuli.

Another major caveat is that most of the studies mentioned are based on recordings in anaesthetized cats, and since FB is strongly affected by anaesthesia (Briggs & Usrey, 2011; Keller et al., 2020), there might not be any FB effect to account for in the first place.

Furthermore, dLGN activity has also been shown to be modulated by locomotion (Erisken et al., 2014) and arousal (as indicated by pupil diameter) (Molnár et al., 2021), raising questions about the potential contribution of behavioural state variables in model performance.

Therefore, in order to disentangle the combined influences of retinal inputs, cortico-thalamic feedback and behavioural state on dLGN response properties to arbitrary visual stimuli, what is required is an approach that combines the following elements: recordings of dLGN activity, locomotion and pupil size in awake, behaving animals; direct and reversible L6 CT FB suppression; modelling of each of these elements to yield quantitative, interpretable results on their respective influence. Here, generalized linear models (GLMs) provide a powerful descriptive framework that has already been used to great effect in numerous studies to predict responses in the early visual system (Pillow et al., 2008; Schwartz et al., 2006), including the dLGN (Babadi et al., 2010). While GLMs have been employed to show the independent influences of retinal and extra-retinal inputs as well as and spike-history (Babadi et al., 2010; Butts et al., 2011), to our knowledge, they have not yet been used to show their combined influence in the way proposed above, and so this approach holds much promise in disentangling the combined influences of retinal inputs, cortico-thalamic feedback and behavioural state on *in vivo* mouse dLGN response properties to naturalistic stimuli.

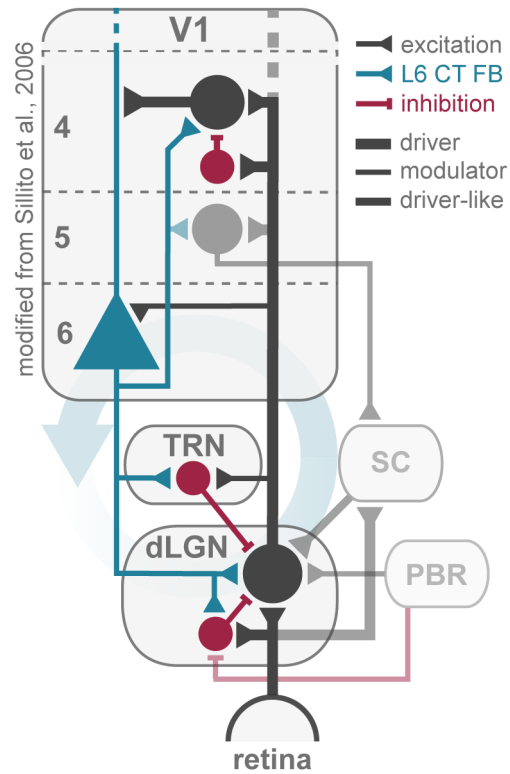


Figure 1 | The cortico-thalamic feedback circuit. Visual signals are transduced in the retina, from whence RGC project output to the thalamic dLGN relay cells (black) via strong driver synapses (Sherman & Guillery, 2002). These relay cells project driver synapses to V1 L4 excitatory cells (black), the main subcortico-cortical input layer, which contact the dendrites of V1 cortical layer 6 (L6) CT pyramidal cells (blue). L6 CT cells in turn send direct excitatory modulatory synapses to dLGN relay cells, thus closing the feedback loop (Sillito et al., 2006). In addition, at every stage, there are numerous axon collaterals to other areas, making the feedback circuit effect on dLGN cells more complex. To begin with, RGC axons also project dLGN inhibitory neurons (red), as well as superior colliculus (mid-brain) (SC) (greyed out) (Ellis et al., 2016), the main retino-recipient area in the mouse (other 50+ targets (Martersteck et al., 2017) not shown here), which feeds back onto dLGN shell relay cells (Bickford et al., 2015). DLGN core relay cells (core-shell distinction (Seabrook et al., 2017) not shown here) also contact GABAergic thalamic reticular nucleus (TRN) cells (red), in turn inhibiting dLGN relay cells. They also project to V1 L6, to V1 L5 (grey), which feeds back onto the dLGN shell region, and to V1 L4 inhibitory interneurons (red) contacting L4 excitatory cells. DLGN shell relay cells further project (grey dotted line) to V1 layers 1, 2, and 3 (not shown). L6 CT cells also project subcortically to dLGN inhibitory interneurons, as well as TRN inhibitory neurons (Montero, 1991), thus also providing indirect, disynaptic, inhibitory feedback to dLGN relay cells; intracortically to V1 L5 (Kim et al., 2014) and L4 excitatory neurons (Sillito et al., 2006); and to L6 translaminal inhibitory neurons projecting to layers 6 - 2/3 (Bortone et al., 2014). Lastly, dLGN inhibitory cells receive modulatory inhibitory inputs from the parabrachial region (midbrain) (PBR) (grey), which encompasses the mesencephalic locomotor region (MLR) (Sherman & Guillery, 2002).

RETINO-GENICULATE FUNCTIONAL CONVERGENCE IS DIVERSE BUT SPARSE

2.1 ROMÁN ROSÓN & BAUER ET AL. (2019)

SUMMARY: In the mouse, the parallel output of more than 30 functional types of retinal ganglion cells (RGCs) serves as the basis for all further visual processing. Little is known about how the representation of visual information changes between the retina and the dorso-lateral geniculate nucleus (dLGN) of the thalamus, the main relay station between the retina and cortex. Here, we functionally characterized responses of retrogradely labeled dLGN-projecting RGCs and dLGN neurons to the same set of visual stimuli. We found that many of the previously identified functional RGC types innervate the dLGN, which maintained a high degree of functional diversity. Using a linear model to assess functional connectivity between RGC types and dLGN neurons, we found that the responses of dLGN neurons could be predicted as a linear combination of inputs from on average five RGC types, but only two of those had the strongest functional impact. Thus, mouse dLGN receives input from a diverse population of RGCs with limited functional convergence.

THE MANUSCRIPT WAS PUBLISHED AS:

Román Rosón, M., Bauer, Y., Kotkat, A., Berens, P., Euler, T., & Busse, L. (2019). Mouse dLGN Receives Functional Input from a Diverse Population of Retinal Ganglion Cells with Limited Convergence. *Neuron*, 102(2), 462–476. <https://doi.org/10.2139/ssrn.3205414>*

*shared first authorship between M.R.R. and Y.B.

CONTRIBUTION SUMMARY: Conceptualization, T.E., L.B., P.B.; Methodology, T.E., L.B., P.B., M.R.R., Y.B.; Software, Y.B., P.B., L.B., T.E., A.H.K., M.R.R.; Formal Analysis, Y.B., A.H.K., M.R.R.; Investigation, Y.B., M.R.R.; Writing – Initial Draft, P.B., L.B., T.E.; Writing – Reviewing and Editing, Y.B., P.B., L.B., T.E., M.R.R.; Funding Acquisition, Y.B., P.B., L.B., T.E.; Supervision, P.B., L.B., T.E.

PERSONAL CONTRIBUTIONS: Y.B. provided analyses for the functional characterization of dLGN-p RGCs, signal deconvolution and creation of a match index (Mi) to assign dLGN-p RGC to functional RGC types, and calculated cluster proportions in dLGN-p and RGC-all cells (Fig2). Y.B. also provided the analyses of the cross-validated non-negative matrix factorization (CV-NNMF) (Fig4), as well as the linear feedforward model (Fig5). For supplemental materials, Y.B. created the injection histology overview (FigS1), deconvolution of retinal 2P traces (FigS3), match index population histogram (FigS4), cluster assignments (FigS5), assesment of model limitations (FigS9), and comparison of distributions (FigS10). Y.B. also ran additional injection experiments for retrograde labelling of dLGN-p RGCs, and functional two-photon imaging of ex vivo retina visual responses (data not used in publication). Y.B. maintained the code repository. Lastly, Y.B. secured project funding via the Volkswagen-Stiftung-funded *SmartStart* programme for Computational Neuroscience by the *Bernstein Network Computational Neuroscience*.

Mouse dLGN Receives Functional Input from a Diverse Population of Retinal Ganglion Cells with Limited Convergence

Highlights

- The majority of functionally identified RGCs types projects to dLGN
- Factorization of the dLGN population response reveals diverse components
- Responses of dLGN cells can be modeled as combination of, on average, 5 RGC types
- Among those, 2 RGC types have the most dominant functional impact

Authors

Miroslav Román Rosón, Yannik Bauer, Ann H. Kotkat, Philipp Berens, Thomas Euler, Laura Busse

Correspondence

philipp.berens@uni-tuebingen.de (P.B.), thomas.euler@cin.uni-tuebingen.de (T.E.), busse@bio.lmu.de (L.B.)

In Brief

Román Rosón, Bauer, et al. show that most functionally identified retinal ganglion cell (RGC) types project to the dLGN of thalamus. A linear feedforward model accounts for dLGN responses using input from ~ 5 RGC types, of which 2 are dominant.



Mouse dLGN Receives Functional Input from a Diverse Population of Retinal Ganglion Cells with Limited Convergence

Miroslav Román Rosón,^{1,2,3,4,9} Yannik Bauer,^{1,3,5,9} Ann H. Kotkat,^{3,6} Philipp Berens,^{1,2,7,10,*} Thomas Euler,^{1,2,7,10,*} and Laura Busse^{1,3,7,8,10,11,*}

¹Centre for Integrative Neuroscience, University of Tübingen, 72076 Tübingen, Germany

²Institute for Ophthalmic Research, University Hospital Tübingen, 72076 Tübingen, Germany

³Division of Neurobiology, Department Biology II, LMU Munich, 82151 Munich, Germany

⁴Graduate School of Neural & Behavioural Sciences, International Max Planck Research School, University of Tübingen, 72074 Tübingen, Germany

⁵Graduate School of Systemic Neuroscience (GSN), LMU Munich, 82151 Munich, Germany

⁶ENB Elite Master of Science Program in Neuroengineering, Technical University of Munich, 80333 Munich, Germany

⁷Bernstein Centre for Computational Neuroscience, 72076 Tübingen, Germany

⁸Bernstein Centre for Computational Neuroscience, 82151 Munich, Germany

⁹These authors contributed equally

¹⁰Senior author

¹¹Lead Contact

*Correspondence: philipp.berens@uni-tuebingen.de (P.B.), thomas.euler@cin.uni-tuebingen.de (T.E.), busse@bio.lmu.de (L.B.)
<https://doi.org/10.1016/j.neuron.2019.01.040>

SUMMARY

Mouse vision is based on the parallel output of more than 30 functional types of retinal ganglion cells (RGCs). Little is known about how representations of visual information change between retina and dorsolateral geniculate nucleus (dLGN) of the thalamus, the main relay between retina and cortex. Here, we functionally characterized responses of retrogradely labeled dLGN-projecting RGCs and dLGN neurons to the same set of visual stimuli. We found that many of the previously identified functional RGC types innervate dLGN, which maintained a high degree of functional diversity. Using a linear model to assess functional connectivity between RGC types and dLGN neurons, we found that responses of dLGN neurons could be predicted as linear combination of inputs from on average five RGC types, but only two of those had the strongest functional impact. Thus, mouse dLGN receives functional input from a diverse population of RGC types with limited convergence.

INTRODUCTION

In the mammalian retina, the photoreceptor signal is decomposed into multiple parallel channels (Euler et al., 2014; Masland, 2012), carried to the brain by more than 30 types of retinal ganglion cells (RGCs) (Baden et al., 2016; Sanes and Masland, 2015). Each type of RGC extracts specific features of the visual environment, which are projected via the optic nerve to more

than 50 retino-recipient areas in the brain (Martersteck et al., 2017; Morin and Studholme, 2014). Among those, a key center transmitting information to the primary visual cortex (V1) is the dorsolateral geniculate nucleus (dLGN) of the thalamus.

Retino-geniculate information transmission has been studied extensively in cats and monkeys, where the majority of dLGN neurons seems to be driven by only few (1–3) dominant RGCs (Cleland et al., 1971; Usrey et al., 1999). This dominant input can evoke such strong excitatory postsynaptic potentials (EPSPs)—so-called “S-potentials”—that they can be picked up by extracellular recordings. Consistent with a low degree of convergence, the S-potentials of a dLGN neuron and its spiking output have closely matching receptive fields (RFs) in terms of location, center-surround organization, and size (Hubel and Wiesel, 1961; Kaplan et al., 1987; Sincich et al., 2007). Besides these dominant inputs, individual cat dLGN cells receive additional weaker inputs, as shown by *in vivo* electrophysiology (Cleland et al., 1971; Mastrorarde, 1987, 1992; Usrey et al., 1999) and inferred from ultrastructural assessment of synaptic bouton placement and number (Hamos et al., 1987). Given the strict spatial layering of the dLGN, in particular in primates, it has generally been assumed that, in these species, the inputs into individual dLGN neurons arise from RGCs of similar functional type, although at least 13 anatomical types of dLGN-projecting RGCs have been identified in monkeys (Dacey et al., 2003).

In the mouse, recent anatomical studies have started to explore retino-geniculate connectivity and revealed a more complex picture. Mono-transsynaptic rabies virus tracing of inputs to individual dLGN neurons demonstrated that mouse dLGN neurons can be divided into two groups based on the pattern of their retinal inputs (Rompani et al., 2017): although some dLGN neurons received inputs from mostly a single RGC type (“relay mode”), others showed a high degree of convergence, with inputs being composed of up to several dozen RGCs of different



types (“combination mode”). A high degree of retino-geniculate convergence is further supported by recent ultrastructural studies of retinal afferents and their thalamic relay cell targets (Hammer et al., 2015; Morgan et al., 2016).

Given the functional diversity of mouse RGCs (Baden et al., 2016; Farrow and Masland, 2011; Sanes and Masland, 2015), whose properties might vary with retinal region (Bleckert et al., 2014; Joesch and Meister, 2016; Nath and Schwartz, 2016; Warwick et al., 2018), and complex input of RGCs to dLGN neurons (Ellis et al., 2016; Hammer et al., 2015; Liang et al., 2018; Morgan et al., 2016; Rompani et al., 2017), one would expect an at least similarly rich functional representation in mouse dLGN. In contrast, the majority of mouse dLGN neurons has been reported to have circularly symmetric RFs (Piscopo et al., 2013) and is believed to perform linear spatial summation (Denman and Contreras, 2016; Grubb and Thompson, 2003), similar to primates (Grubb and Thompson, 2003). However, mouse dLGN also contains neurons with more complex and diverse response properties: orientation-selective (OS) and direction-selective (DS) cells (Cruz-Martín et al., 2014; Marshel et al., 2012; Piscopo et al., 2013; Zhao et al., 2013), “suppressed-by-contrast” neurons, potentially signaling uniformity of the visual field (Piscopo et al., 2013), as well as a heterogeneous population of cells with long latencies and responses to both light on- and offset (Piscopo et al., 2013). It is currently unknown to which degree these response properties are inherited from the innervating retinal afferents (Cruz-Martín et al., 2014; Liang et al., 2018) or emerge *de novo* in dLGN by a combination of converging retinal inputs and dLGN-intrinsic computations (Liang et al., 2018; Marshel et al., 2012).

Here, we sought to determine how the visual representation in mouse dLGN arises from retinal inputs. We show that many previously identified functional RGC types (Baden et al., 2016) innervate the dLGN, where, in accordance with this richness of input, the population response consists of diverse fundamental components. The dLGN responses in response to our simple, full-field stimuli, and at the temporal resolution of calcium signals, can be modeled by a linear combination of on average five RGC types, among which two have the strongest functional impact. We conclude that mouse dLGN neurons receive functional input from multiple RGC types and relay these diverse retinal representations to the cortex with limited convergence.

RESULTS

Retrograde Viral Tracing to Functionally Characterize dLGN-Projecting RGCs

To identify dLGN-projecting (dLGN-p) RGCs, we injected a Cre-encoding retrograde herpes simplex virus 1 (LT HSV-hEF1 α -cre; Neve, 2012) into the dLGN of a transgenic reporter mouse line with a floxed genetically encoded Ca²⁺ indicator (GCaMP6f; Chen et al., 2013; Madisen et al., 2015). After transducing the axon terminals (Antinone and Smith, 2010; McGovern and Kang, 2011) in the dLGN, the virus was retrogradely transported to the soma, where it triggered the expression of Cre-recombinase and, subsequently, the Cre-dependent expression of GCaMP6f. Because the virus does not spread *trans-synapti-*

cally, it only labeled cells with afferents in the dLGN. This enabled us to identify only the subset of dLGN-p RGCs in the retina (Figure 1A).

We histologically confirmed the target location of the virus injection, as well as its limited diffusion (Figures 1B, top, and S1). Given our dorsal approach, the HSV virus was injected into both shell and core regions of dLGN, but due to the sheer volume difference between these regions, it is likely that more terminals were transduced in the dLGN core. In line with earlier studies, we found retrogradely labeled neurons in additional dLGN-projecting structures, including the superior colliculus (Figure 1B, center), the thalamic reticular nucleus, and the deep layers of primary visual cortex (Figure 1B, bottom; Guillery and Sherman, 2002; Harting et al., 1991).

We then used two-photon Ca²⁺ imaging to measure the light-evoked responses of the dLGN-p RGCs (Figures 1C–1F). We probed their response properties across the whole retina with a stimulus set used in a previous RGC classification study (Baden et al., 2016). As the labeled RGCs were sparse (Figure 1C, top), we analyzed their Ca²⁺ responses using manually drawn regions of interest (ROIs) (Figure 1C, bottom). In total, we identified 581 virus-labeled RGCs from 4 mice (contralateral eye only) as ROIs, with a range of 1–25 ROIs per field (median = 6). As expected from earlier work, we found ON- and OFF-RGCs (without any direction or orientation preference; Huberman et al., 2008) as well as direction-selective RGCs (Cruz-Martín et al., 2014; Ellis et al., 2016; Rivlin-Etzion et al., 2011). In addition, we found dLGN-p RGCs that, for example, responded differently to local and full-field stimuli, showed preference to higher or lower frequency stimulation, or were suppressed by frequency and contrast (Figures 1D–1F).

The Majority of Functional RGC Types Project to dLGN

We next asked which of the previously characterized functional mouse RGC types (Baden et al., 2016) project to the dLGN. We used the functional RGC clusters obtained previously (henceforth “RGC-all clusters”) and identified, for each retrogradely labeled dLGN-p RGC, the RGC-all cluster with the best matching response properties (Figure S2). To account for the differences in Ca²⁺ indicators between the two studies, we first de-convolved the Ca²⁺ signals of the GCaMP6f dataset and the published OGB-1 dataset (Baden et al., 2016), using each indicator’s Ca²⁺ kernels, calculated as average thresholded Ca²⁺ peak events to the white noise stimulus of multiple ROIs (Figure S3; see STAR Methods). For both the “chirp” stimulus and the moving bar stimulus, we correlated the trial-averaged responses of each dLGN-p RGC to the mean response of each RGC-all cluster. The correlation coefficients were then weighted by a quality index (Q), which is a measure of signal-to-noise ratio and reproducibility of the responses, and averaged. This weighted mean correlation (“match index” [Mi]) was then used to assign each dLGN-p RGC to the best-matching RGC-all cluster, i.e., the cluster with the highest Mi (for statistics of Mi , see Figure S4). For both individual example cells (Figure 2A), and across the population of dLGN-p RGCs, the assignment worked well (median Mi = 0.62). Accordingly, population mean responses of dLGN-p RGCs assigned to the same

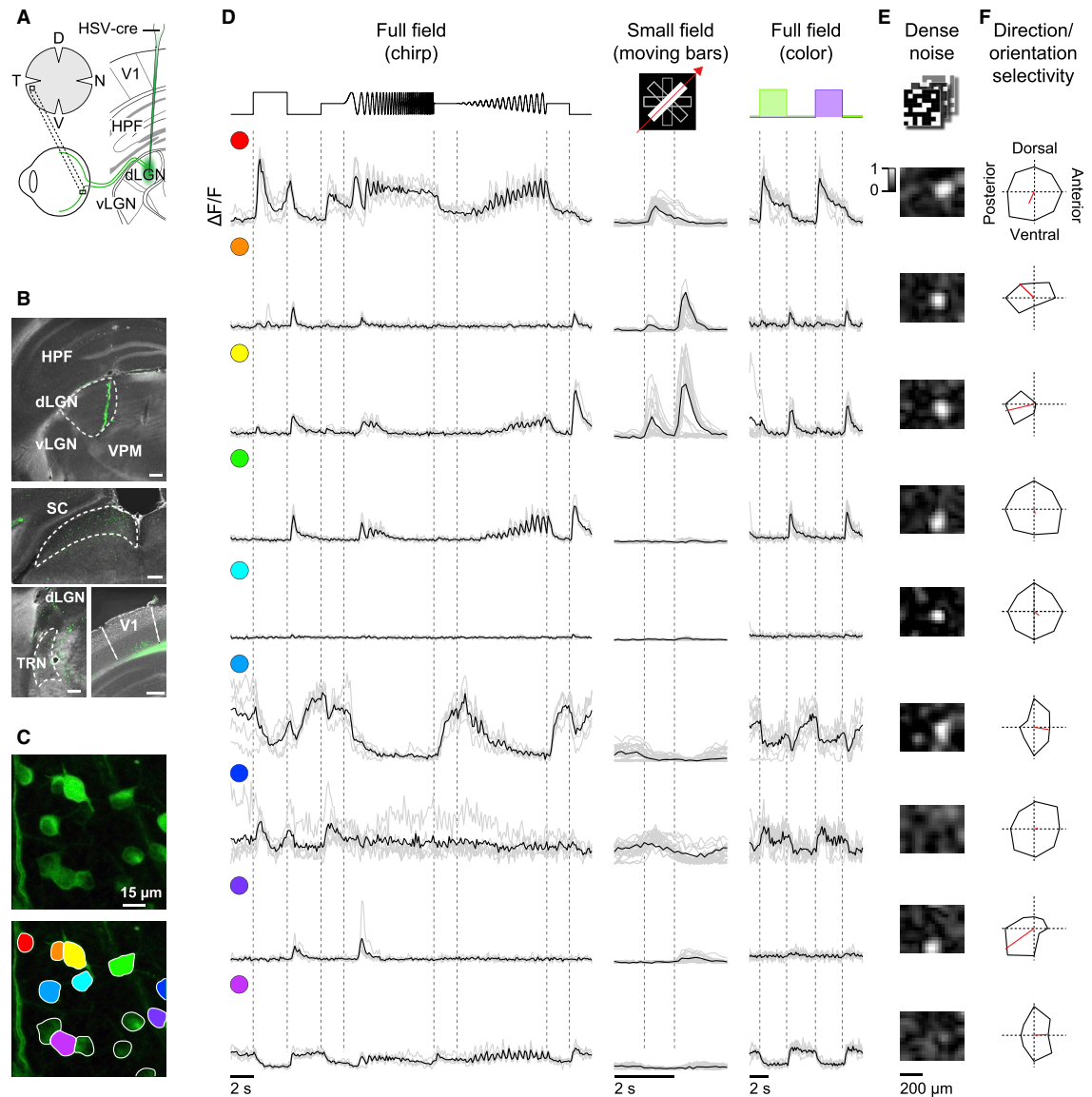


Figure 1. Functional Characterization of dLGN-Projecting RGCs

(A) Schematic of the experimental approach.

(B) Injection of a Cre-encoding retrograde herpes simplex virus 1 (LT HSV-hEF1α-cre; Neve, 2012) into dLGN (green, GCaMP6f; gray, DAPI). Injection site (top) and areas with retrogradely labeled cell bodies (below) and outlines of the dorsolateral geniculate complex (dLGN), superior colliculus (SC), reticular nucleus of the thalamus (TRN), and primary visual cortex (V1) are shown. Scale bars, 200 μm.

(C) Whole-mounted mouse retina of a floxed GCaMP6f mouse transduced with LT HSV-hEF1α-cre and recorded with a two-photon microscope in the ganglion cell layer. (Top) Scan field (110 × 110 μm) is shown. (Bottom) Regions of interest (ROIs) on GCaMP6f-expressing RGCs are shown.

(D) Ca²⁺ responses (ΔF/F) from 9 exemplary ROIs color coded in (C) to full-field chirp, bright bars moving in eight directions, and full-field alternating green-UV stimuli. Single trials are in gray and averages of n = 5 (chirp), 7 (green-UV), or 24 (moving bars) trials are in black. Traces are scaled to the maximal ΔF/F for each stimulus separately over all ROIs.

(E and F) Spatial RFs (E) and polar plots indicating direction and orientation selectivity (F; vector sum in red) for the same 9 cells as in (D).

HPF, hippocampus; vLGN, ventral lateral geniculate complex; VPM, ventral posteromedial nucleus of the thalamus. See also Figure S1.

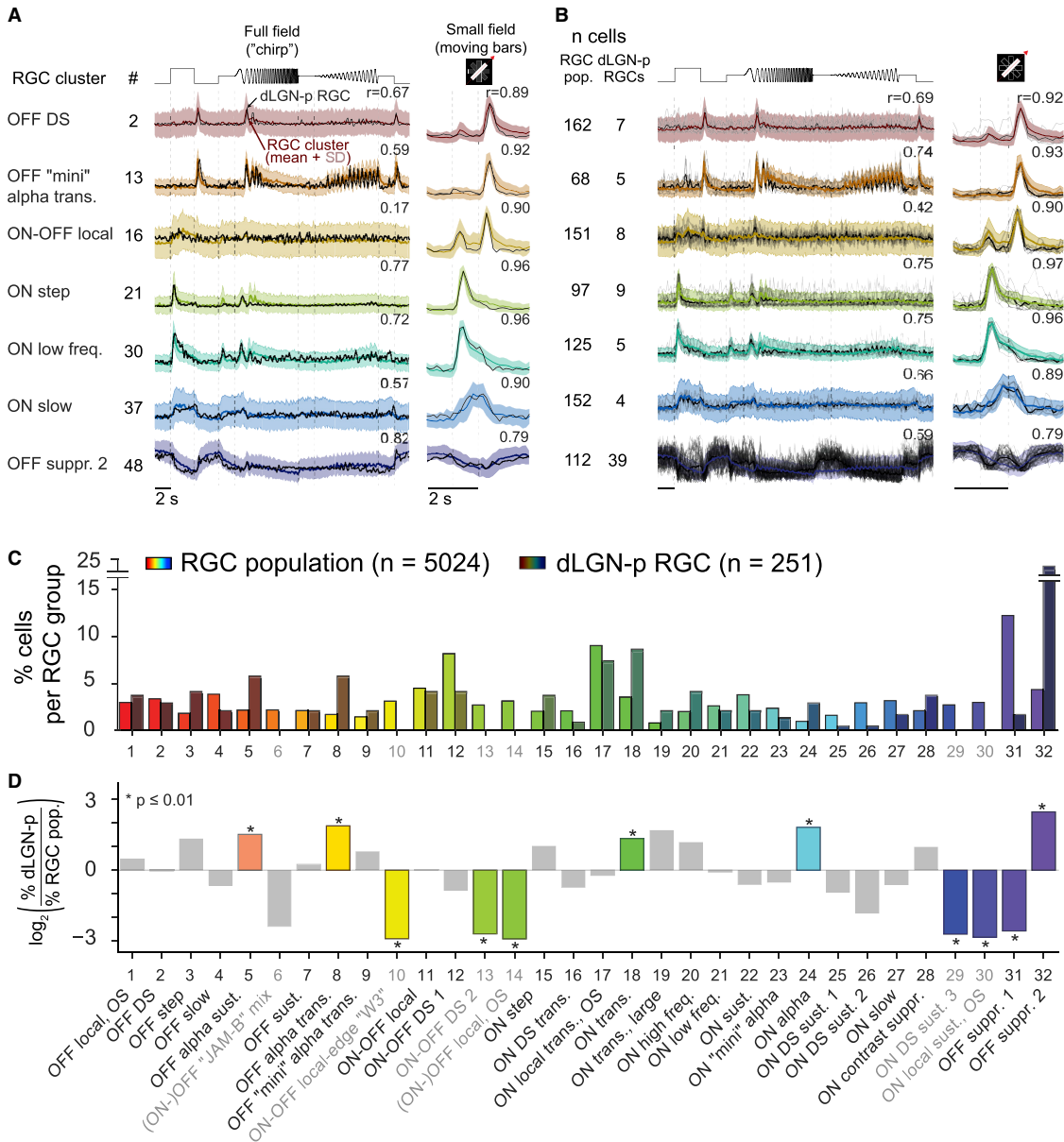


Figure 2. Cluster Assignments

(A) Responses of selected RGC-all clusters (colored line, mean; shaded area, ± 1 SD) with mean responses of assigned example dLGN-p RGCs (black) to chirp (left) and bar stimulus (right). Numbers indicate correlation coefficients.

(B) Same, for all assigned dLGN-p RGCs in the corresponding clusters (gray, responses of single dLGN-p RGCs; black, mean).

(C) Distribution of cells per RGC-all group from [Baden et al. \(2016\)](#) versus cells per dLGN-p group.

(D) Comparison of cell-per-group percentages as \log_2 ratio (%dLGN-p RGCs/%RGC-all). Significant differences in cell proportions ($p < 0.01$; binomial test) are marked as colored bars and with asterisks.

See also [Figures S3](#), [S4](#), and [S5](#).

cluster agreed well with the population mean responses of their RGC-all cluster (Figure 2B).

We then determined which RGC types were over- or underrepresented in the dLGN-p RGC population compared to the complete RGC population. Following Baden et al. (2016), we grouped the 49 RGC-all clusters into 32 groups, where each group represents an RGC type based on domain knowledge not only about functional features but also about soma size, RF size, and direction and orientation selectivity (Figure 2C; see STAR Methods; see Figure S5 for same analysis without grouping). This analysis revealed that 75% of RGC-all groups were assigned dLGN-p RGCs (24/32 groups with at least two cells), suggesting that the majority of functional RGC types projects to the dLGN.

Several RGC types were systematically over- or underrepresented in the dLGN-p population (Figures 2C and 2D; binomial test, $p < 0.01$): overrepresented were “OFF-suppressed 2” cells (Figures 2C and 2D: group [G] 32) and all classical alpha cells (Figures 2C and 2D), including OFF alpha sustained (G_6), OFF alpha transient (G_8), and ON alpha (G_{24}), as well as an ON transient RGC (G_{19}). Underrepresented, in turn, were the ON-OFF local-edge “W3” (G_{10}) and several orientation- and direction-selective RGCs (i.e., ON-OFF DS 2 [G_{13}], [ON-]OFF local OS [G_{14}], ON DS sust. 3 [G_{20}], and ON local sustained OS [G_{30}]). Other groups contributed roughly the same percentage to the dLGN-p cells as to the total RGC population (see Discussion). These results indicate that dLGN receives diverse, parallel input from many functional RGC groups, with a striking overrepresentation of alpha and of one group of suppressed-by-contrast (SbC) RGCs.

The dLGN Population Response Can Be Factorized into Many Components

Having established that many functional RGC types provide input to mouse dLGN, we next asked how this diversity is reflected in the dLGN population. We performed extracellular single-unit recordings with linear silicon probes of geniculate neurons in head-fixed mice, using the same dorsal approach as for the virus injections (Figures 3A and 3B). We verified the recording sites by histological reconstruction of the electrode tract (Figure 3B) and the characteristic progression of retinotopy along the electrode channels (Figures 3C and S6; see also Piscopo et al., 2013). Given our dorsal approach to dLGN, the recorded neurons likely come from both the core and shell region of dLGN, although volume differences likely bias our results toward properties of the dLGN core. RF centers of the recorded neurons were approximately between -20° and $+50^\circ$ elevation and -10° and $+100^\circ$ azimuth (Figure S6). We presented the same full-field chirp stimulus as in the retinal experiments. To assess the stability of the dLGN recordings and the consistency of our spike sorting, we flanked the chirp by presentations of drifting gratings with varying orientation and temporal and spatial frequency (Figure S7).

Chirp responses of dLGN neurons were surprisingly diverse: the cells not only displayed the “standard” transient and sustained ON-OFF responses or were suppressed by contrast but also differed in their temporal frequency or contrast preferences as well as their response kinetics (Figure 3D). Some of the cells even displayed slow ramping responses (Figures 3D4 and 3D5). To ensure that this response diversity did not result from poor unit isolation during spike sorting, we considered only units

with firing rates >1 spike/s, which were stable across time, had a clean refractory period, and a distinct extracellular spike waveform (Figures 3E and 3F). This diversity is likely not related to influences of locomotion (Figure S8).

To quantitatively assess the degree of diversity present in the dLGN neuron population, we decomposed the single-unit responses to the chirp stimulus into “response components” using non-negative matrix factorization (NNMF) (Lee and Seung, 1999). Individual neuron responses can then be reconstructed as a weighted sum of these elementary response components (Figures 4A and S2). Interestingly, these components can be well correlated to the responses of our dLGN-p RGCs, supporting the NNMF approach for analyzing the diversity of geniculate representations. For example, decomposing our dLGN population response into only two fundamental components (ranks) revealed components resembling responses with ON and OFF features; increasing the rank number to four added temporal diversity with transient and sustained features, and increasing rank number further led to additional contrast-suppressed features (Figure 4B). To determine the mathematically optimal number of components, we used cross-validation (Williams et al., 2018; Figure 4C), where we repeatedly performed the factorization on different training sets for an increasing number of ranks (Figure 4C) and evaluated the mean squared errors (MSEs) of the NNMF model on validation sets not used for factorization (STAR Methods). For a conservative estimate, we chose the model with 5% more error than the minimal error, resulting in 29 components (Figures 4D and 4E). This is indicative of a large diversity in the dLGN population response.

Besides this rich representation of luminance steps, temporal frequencies, and changes in contrast in the overall dLGN population, 82/443 (18.5%) dLGN neurons only displayed weakly modulated responses to the chirp stimulus, despite having robust and consistent responses to the drifting gratings presented before and afterward (Figure S7). This response behavior is consistent with these dLGN neurons preferring local variations in luminance instead of uniform full-field stimuli, as is the case for $\sim 30\%$ of RGCs (Baden et al., 2016; their Figure 2b and extended data Figure 10), suggesting that the overall diversity of dLGN responses may be larger than reported here. Together, we conclude that the response diversity observed at the level of dLGN-p RGCs is also present in dLGN.

Modeling dLGN Responses as Linear Combinations of RGC Inputs

Next, we combined the dLGN-p RGC dataset (Figure 2) and the dLGN dataset (Figure 3) to study how the dLGN responses are computed from the retinal output. We first accounted for the differences in recording methods by convolving the dLGN spiking responses with the OGB-1 Ca^{2+} indicator kernel (Figures S3 and S9). We then used a parsimonious, linear model, constrained to have non-negative weights, to predict dLGN responses—on the temporal scale of Ca^{2+} signals—as a sum of weighted RGC inputs (Figures 5A and S2). For prediction, we used the RGC-all cluster means (Baden et al., 2016) that were assigned to at least two dLGN-p cells. Each dLGN recording consisted of multiple trials (stimulus repetitions; $n = 10$ – 30), which were divided into training and test sets (50%/50%). The model was evaluated

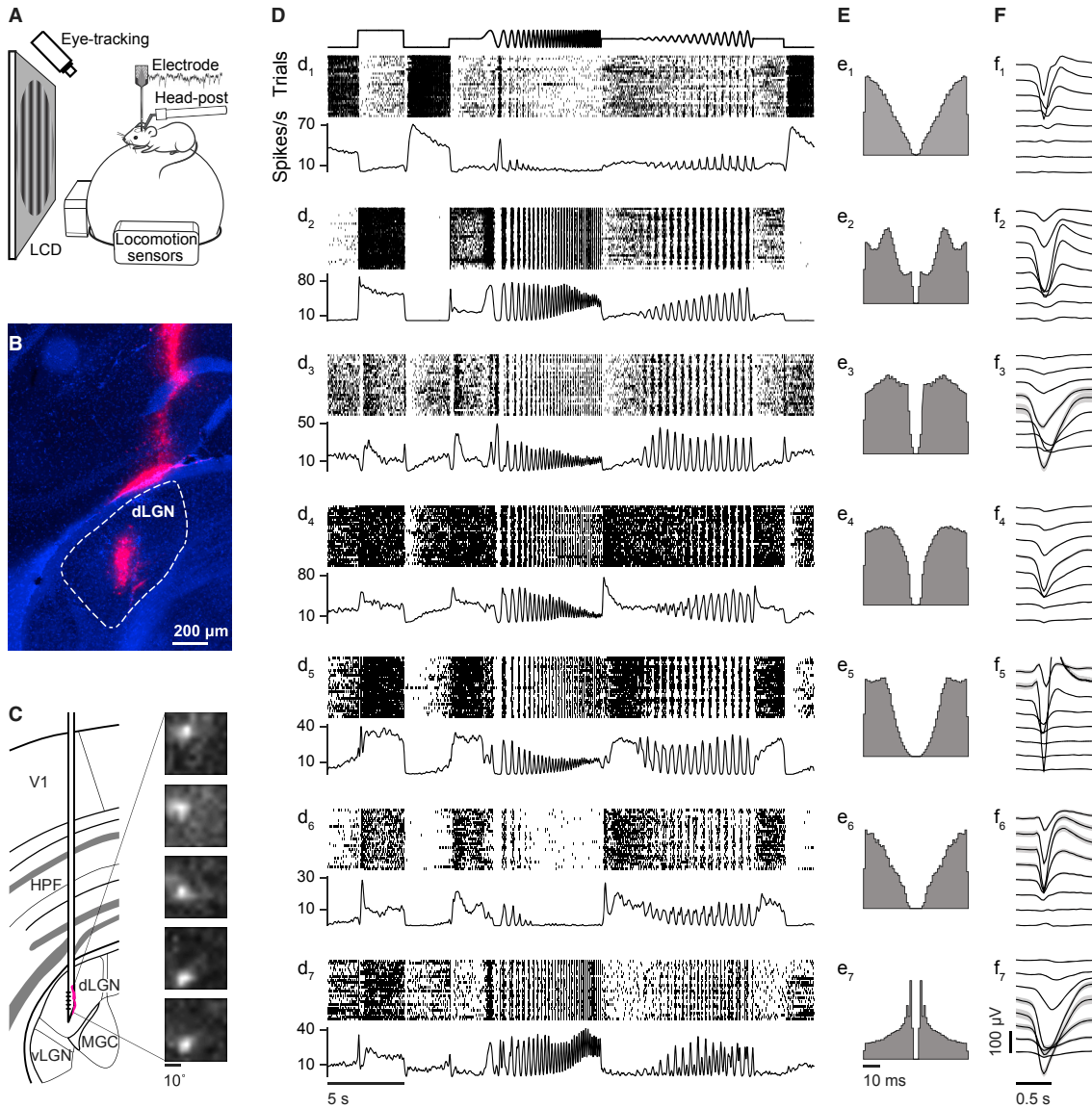


Figure 3. Functional Characterization of dLGN Neurons

(A) Schematic of experimental setup for extracellular dLGN recordings.

(B) Reconstruction of the electrode track in dLGN (coronal section; dLGN outlined in white; blue: DAPI; red: DiD coating the electrode).

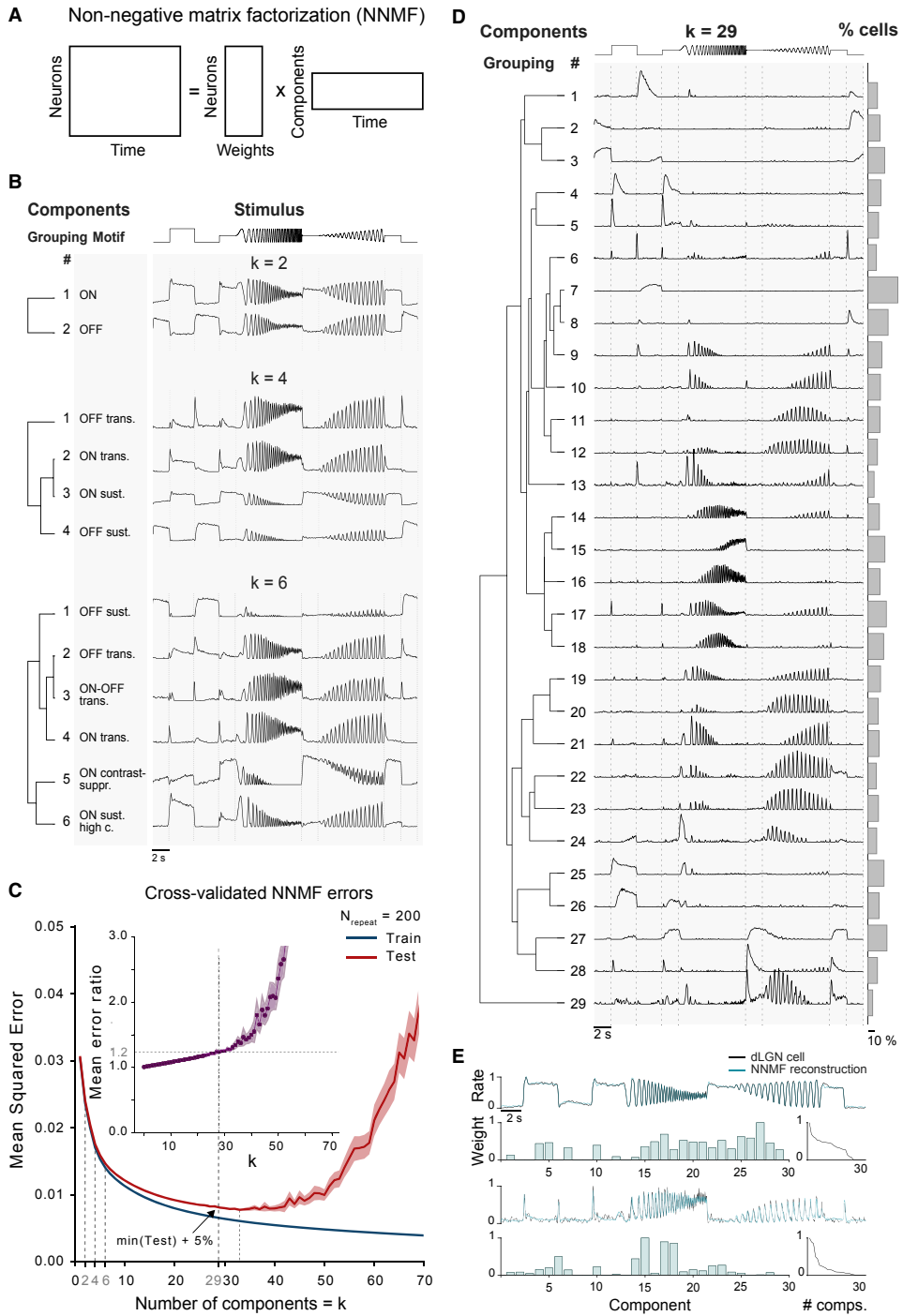
(C) Schematic of recording site with RFs mapped for several electrode channels (dorsal to ventral), showing the retinotopic progression in elevation typical of mouse dLGN.

(D-F) Spike raster plots (top) and spike density function (bottom) of 7 exemplary dLGN neurons in response to the chirp stimulus (D), their autocorrelograms (E), and spike waveforms in 5 selected channels of the 32-channel probe (F).

MGC, medial geniculate complex. See also [Figures S6](#), [S7](#), and [S8](#).

using repeated random sub-sampling cross-validation with 1,000 repetitions ([STAR Methods](#)). The reported weights represent mean values across the repeats.

With notable exception of the transient response changes ([Figure S9](#)), this simple excitation-only linear feedforward model successfully reconstructed responses of most dLGN neurons,



(legend on next page)

including transient ON, sustained ON and OFF, and SbC cells (Figure 5B). Typically, the responses of dLGN neurons could be predicted using only a few non-zero weights (weight > 0.001; Figure 5B1–3); some cells were predicted by a combination of one dominant and few weaker RGC inputs (Figure 5B2), and even others were best modeled with responses from many RGC clusters (Figure 5B4). Across dLGN neurons, prediction quality was high (average correlation: 0.64; average RMSE: 0.17; Figure 5C).

Using this model, we next asked how many RGC types provided input to mouse dLGN neurons and found that the answer directly depends on the threshold used for considering inputs as functionally relevant (Figure 5D). Choosing a low weight threshold, the responses of dLGN neurons ($n = 814$) could be predicted by the combined input of on average 5 RGC groups (Figure 5D, left inset; mean = 5.33; median = 5.19; range = 2–11; middle 90% range = 3–8). Choosing a more conservative threshold for functionally relevant inputs, in turn, identified on average 2 most dominant RGC groups (Figure 5D, right inset; mean = 2.01). Together, these results indicate that the responses of many dLGN neurons, at least on the temporal scale of Ca^{2+} transients and for the presented set of visual stimuli, can be explained to a large extent by excitatory feedforward processing with limited convergence.

We also tested other, more flexible models, allowing also negative weights and an exponential non-linearity. Although these yielded small improvements in terms of prediction quality (~15%), they predicted convergence of dozens of RGC types, all with very low relative weights. Equalized input from many types without a dominant one is incompatible with results from *in vivo* recordings correlating spiking activity of RGC-dLGN neuron pairs (Carandini et al., 2007; Cleland et al., 1971; Hubel and Wiesel, 1961; Mastronarde, 1992; Rathbun et al., 2016; Usrey et al., 1999) and *in vitro* slice recordings (Chen and Regehr, 2000; Litvina and Chen, 2017), according to which some RGC inputs are clearly more dominant than others (reviewed in Alonso et al., 2006).

Finally, we explored which of the previously identified dLGN-p RGC groups were used for prediction in the model (Figure 5E). For the liberal weight threshold of 0.001, we found that the majority (24/32) of these groups were used by the model (Figure 5E, top), with some of them contributing more frequently than others. Interestingly, some of the groups contributing most strongly belonged to those RGC groups that were significantly overrepresented among the dLGN-p RGCs (Figure S10), although informa-

tion about the relative frequency of the projections was not used for inference. As expected, imposing a more conservative weight threshold resulted in an even more pronounced pattern of often-used RGC groups (Figure 5E, bottom), although their relative weights tended to equalize. Together, our modeling approach suggests that these RGC types have a significant functional role in the processing of visual information along the retinogeniculate pathway.

DISCUSSION

We functionally characterized the population of dLGN-projecting RGCs as well as dLGN neurons and provide a quantitative account of the functional connectivity between RGC types and dLGN neurons, for simple, full-field stimuli, and at the temporal resolution of Ca^{2+} signals. We present three main findings. First, combining a retrograde viral transduction approach and two-photon Ca^{2+} imaging of RGC responses, we show that the majority of previously functionally identified RGC types project to dLGN. Second, decomposing dLGN responses into their elementary response components revealed a rich diversity of geniculate visual representations, similar to that of RGCs. Third, we demonstrate that the responses of individual dLGN cells can be modeled as a linear combination of responses of on average 5 RGC types, among them 2 with the most dominant functional impact.

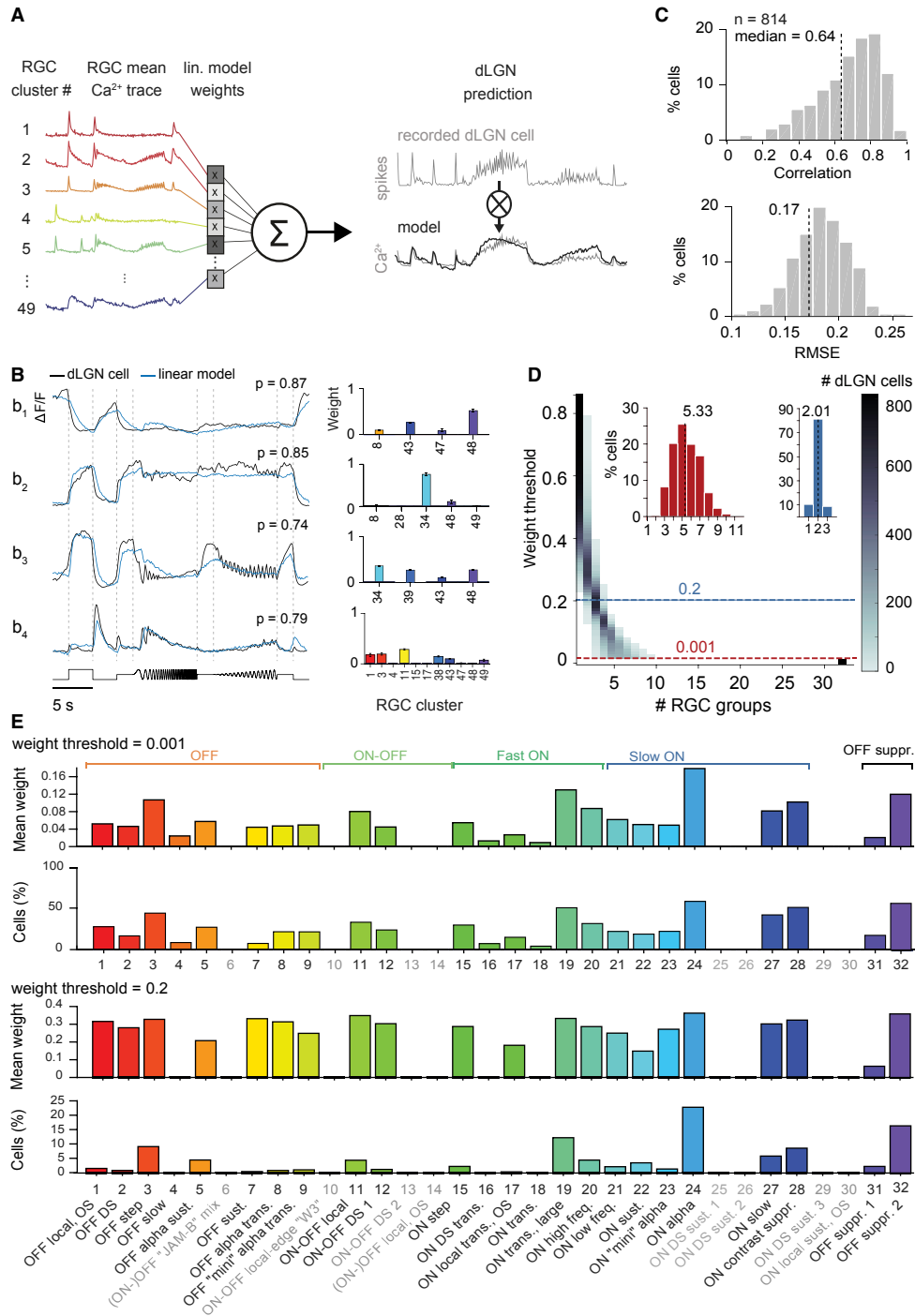
Retrograde Labeling of dLGN-Projecting RGCs

Retrograde viral tracing with HSV-cre combined with two-photon Ca^{2+} imaging of RGCs proved to be a suitable tool to determine functional properties of the dLGN-p RGCs. HSV is known to have a strictly synaptic uptake mechanism (Antonone and Smith, 2010; McGavern and Kang, 2011), which prevents infection of axons passing nearby and not synapsing within the dLGN. This is an issue with commonly used retrograde tracers, such as DiO/Dil, horseradish peroxidase, fluorophore-conjugated latex microspheres, or cholera toxin (Ellis et al., 2016). In addition, our observation that GCaMP6f expression in the retina was limited to spatially confined regions is consistent with the interpretation that HSV-infected neurons were restricted to the retinotopically corresponding region in dLGN instead of labeling passing RGC axons, which would likely have resulted in a larger spread of RGC locations.

To date, there are no data available supporting or arguing against an RGC type bias in HSV uptake. We think, however,

Figure 4. Decomposition of the dLGN Population Response

- (A) Schematic of the non-negative matrix factorization (NNMF), used to extract a set of time-varying response components, from which neuronal responses can be reconstructed as a weighted sum.
- (B) Example NNMF models with $k = 2, 4,$ and 6 components. Top: a model with two components clearly factorizes the data into an ON and OFF component. Middle: allowing four components introduces ON-transient and OFF-transient features in addition to sustained ON and OFF features. Bottom: with six components, components reflect ON-OFF transient as well as contrast suppressed features.
- (C) Mean squared errors (MSEs) as a function of model components k both for training (blue) and test (red) sets in NNMF model cross-validation ($n_{\text{repeats}} = 200$; lines, mean; shaded areas, CI_{95}). NNMF cross-validation was used to determine a conservative estimate of the optimal number of components as the location of the minimum mean $\text{MSE}_{\text{test}} + 5\%$ ($k = 29$). Inset: MSE ratio ($\text{MSE}_{\text{test}}/\text{MSE}_{\text{train}}$) per rank is shown (line: mean; shaded area: CI_{95}).
- (D) dLGN response components as computed by NNMF (middle), organized according to a hierarchical cluster tree with an optimized leaf order (left), and percentage of neurons with weight of respective component > 0 (right).
- (E) Top: examples of dLGN cell responses (black) and their NNMF reconstruction (blue). Bottom: weights used for reconstruction for each component (left), sorted in descending order (right).



(legend on next page)

that viral tropism is likely not a major confound. First, we could retrogradely transfect the majority of functional RGC types, which is inconsistent with strong viral tropism. Second, even if there were biases, the amplification step of utilizing Cre to unlock transgene expression likely reduces potential differences, because only few viral particles retrogradely transported to the RGC soma suffice for robust cre-mediated GCaMP6f expression. Third, where direct comparisons with anatomical or genetic cell types are possible (see below and Table S1), our retrograde tracing experiments provide congruent results. Fourth, our results are overall in agreement with a previous retrograde labeling study (Ellis et al., 2016) using G-deleted rabies virus, indicating that the particular retrograde virus employed in our study does not grossly influence results about over- and underrepresentation of certain RGC types.

Functional Classification of dLGN-Projecting RGCs

The functional classification of dLGN-projecting RGCs, which was based on the functional classification obtained for the entire RGC population (Baden et al., 2016), revealed that around 75% of all functional RGC types innervate the dLGN. This high number of types is in line with a previous retrograde labeling study, which reported that, of the 88% of all RGCs projecting to the superior colliculus (SC), ~80% also send an axon collateral to dLGN (Ellis et al., 2016). Moreover, ON alpha RGCs and OFF transient alpha RGCs (Krieger et al., 2017; van Wyk et al., 2009) could be found more frequently among the dLGN-p cells than in the general RGC population. In agreement with this, ON-sustained alpha RGCs were shown to target the core region of the dLGN (Brown et al., 2010; Ecker et al., 2010; Hattar et al., 2006) and also OFF transient alpha RGCs project to dLGN (for a comparison to the literature, see Table S1). Sbc RGCs were also overrepresented in our dLGN-p dataset. They typically exhibit a high baseline firing rate that is suppressed by light stimulation (Jacoby and Schwartz, 2018)—a type of response that has been recorded all along the mouse retino-geniculate-cortical pathway (Niell and Stryker, 2010; Piscopo et al., 2013; Tien et al., 2015), suggesting a dedicated early visual pathway signaling uniformity of the visual field (Levick, 1967; Masland and Martin, 2007; Sivyer et al., 2010) and/or controlling contrast gain (Troy et al., 1989).

Certain RGC types, like W3 RGCs or sustained ON DS RGCs, were underrepresented among dLGN-p cells, in agreement with the literature (Dhande et al., 2013; Kim et al., 2010; Yonehara et al., 2008, 2009; Zhang et al., 2012). In particular, the absence of dLGN-p cells among the W3 RGCs resonates well with find-

ings by Ellis et al. (2016) that ON RGCs with transient responses to small-diameter stimuli were more frequent among SC- than dLGN-projecting RGCs. In two cases, our data seem at odds with the previous literature: none of the dLGN-p RGCs in our study were classified as JAM-B cells (Kim et al., 2008), which are known to project to dLGN. This is likely because JAM-B cells barely respond to our stimuli set, and is consistent with Baden et al. (2016), where some RGC types, including JAM-Bs, did neither respond strongly to full-field chirps nor moving bars, and therefore, our clustering method had assigned these to a “mixed” RGC group. Also, OFF-sustained alpha RGCs were overrepresented among dLGN-p cells, although RGCs marked in the transgenic W7-line thought to correspond to OFF-sustained alpha RGCs have been shown not to project to dLGN (Kim et al., 2010). Interestingly, there was a cluster in the OFF-sustained group that was not assigned any dLGN-p cells, possibly indicating that this subgroup corresponds to W7A. Alternatively, W7A RGCs are a different RGC type—in this case, according to our data, all four alpha RGC types (ON-sustained, OFF-sustained, ON-transient, OFF-transient; Krieger et al., 2017) would project to dLGN, splitting the visual signal on the way to dLGN into four channels arranged symmetrically with respect to polarity and kinetics (Krieger et al., 2017; Pang et al., 2003; van Wyk et al., 2009).

Components of the dLGN Population Response

Consistent with our result of most functional RGC types projecting to dLGN and previous studies demonstrating rich retinal input to dLGN (Ellis et al., 2016; Liang et al., 2018), we found that the dLGN population responses can be factored into ~29 components. The specific number certainly depends on exactly which method is used for determining the optimal rank of the NNMf. We tested several of these methods (Akaike information criterion [AIC], Bayesian information criterion [BIC], randomization, and cross-validation) and found none of them to suggest numbers as low as the classical notion of 3 parallel pathways (reviewed in Kerschensteiner and Guido, 2017). Instead, the high number of NNMf components is—at least in mice—consistent with a larger diversity of dLGN inputs than commonly appreciated. These diverse inputs, in turn, will likely mediate or contribute to diverse visual features being represented in dLGN. This interpretation is supported by recent studies reporting “non-classical” responses in rodent dLGN (Cruz-Martín et al., 2014; Howarth et al., 2014; Marshel et al., 2012; Piscopo et al., 2013; Scholl et al., 2013; Zhao et al., 2013), rabbit dLGN

Figure 5. Functional Modeling of Retinogeniculate Convergence

(A) Illustration of the linear model, predicting responses of a dLGN neuron, convolved with a Ca^{2+} indicator kernel, as a linear combination of weighted dLGN-p RGC cluster inputs.
 (B) Example responses of dLGN neurons (black) and predictions by the linear model (blue), along with the relative weights > 0.001 of RGC clusters used for modeling of dLGN responses.
 (C) Prediction quality. Top: correlation between actual response and predicted response for all dLGN neurons is shown ($n = 814$). Bottom: distribution of root mean squared errors is shown.
 (D) Distribution of the number of RGC groups used for reconstruction of dLGN neuron responses, shown as a function of weight threshold to consider when an input is functionally relevant. (Insets) Histograms of the percentage of dLGN cells as a function of number of RGC groups used for modeling are shown, considering only weights >0.001 (left) or >0.2 (right) as functionally relevant.
 (E) Distribution of RGC groups from Baden et al. (2016) used for reconstructing the population of dLGN cell responses, shown as mean weight and percentage of dLGN cells (top: weight threshold = 0.001; bottom: weight threshold = 0.2). RGC types not projecting to dLGN are greyed out.
 See also Figures S9 and S10.

(Hei et al., 2014), and the koniocellular layers of primate dLGN (Cheong et al., 2013; White et al., 2001; Zeater et al., 2015), such as direction and orientation selectivity and binocularity.

Recombination of RGC Channels in dLGN

In previous work, the question of retinogeniculate connectivity has been addressed from two different angles. Most studies focused on the absolute number and strength of RGC inputs to single dLGN neurons, whereas fewer studies also assessed convergence of retinogeniculate inputs in terms of RGC types.

Estimates of the absolute number of individual RGCs providing input to a single dLGN relay cell differ widely between studies (1 to ~90), with the discrepancy likely arising from differences in species, age, and method. Both *in vitro* and *in vivo* physiology studies concluded that dLGN neurons typically receive input from 1–3 dominant RGCs, with the possibility of additional, weaker inputs in cats and rodents (Chen and Regehr, 2000; Cleland et al., 1971; Jaubert-Miazza et al., 2005; Litvina and Chen, 2017; Mastronarde, 1992; Reid and Usrey, 2004; Usrey et al., 1999; Weyand, 2016; Ziburkus and Guido, 2006). For example, in parasagittal dLGN slices of adult mice, Litvina and Chen (2017) reported three dominantly driving inputs, with an average total number of 10 RGC inputs per dLGN relay cell. Recent anatomical studies using electron microscopy (EM) reconstructions (Hammer et al., 2015; Morgan et al., 2016) and mono-transsynaptic rabies virus tracing (Rompani et al., 2017) in mice indicated that a rather large number (≤ 91) of RGCs can converge onto single dLGN neurons. These numbers appear high compared to previous estimates but are not necessarily in conflict with functional findings, in particular if many of the structurally identified synapses had low weights (Chen et al., 2016), or were subject to later functional refinement, including synapse elimination and axon retraction, which occurs in mice between the ages of P9 and P60 (Chen and Regehr, 2000; Hong et al., 2014; Litvina and Chen, 2017). Convergence and divergence in dLGN has been hypothesized to underlie several functions, such as promotion of synchrony (Alonso et al., 1996; Usrey et al., 1998), enhancement of resolution (Alonso et al., 2006; Martinez et al., 2014), and robustness of feature detectors (Liang et al., 2018). These roles of convergence in retino-geniculate circuits seem different compared to those of convergence in thalamocortical circuits, where in mice, ~80 dLGN relay cells have been estimated to converge on V1 L4 simple cells with highly precise spatiotemporal offset to provide an origin for cortical direction selectivity (Lien and Scanziani, 2013, 2018).

Similarly, the estimated number of RGC types projecting to a single dLGN relay cell varies across studies and will likely differ depending on species (reviewed in Chen et al., 2016). In cats, where dLGN is organized into layers, paired recordings of RGCs (Usrey et al., 1999) or S potentials (Cleland et al., 1971) and dLGN relay cells have generally found an increase in connection probability with increasing similarity of RF properties. In particular, monosynaptic connections between RGCs and dLGN relay cells of opposite polarity seem rare (Cleland et al., 1971; Mastronarde, 1987, 1992; Usrey et al., 1999), indicating that, at least in cats, convergence of RGC types is low. The most direct estimates of convergence among RGC types to date has been obtained in mice, where single dLGN relay cell-

initiated mono-transsynaptic rabies virus tracing combined with morphological analysis of labeled RGCs revealed that some dLGN relay cells received input from RGCs of mostly one anatomical RGC type (relay mode), and others received input from up to nine different anatomical types (combination mode; Rompani et al., 2017). The presence of both relay- and combination-type retinogeniculate convergence in mouse thalamus seems consistent with recent ultrastructural (Morgan et al., 2016) and functional analyses (Liang et al., 2018) of thalamic RGC boutons, demonstrating both specificity and mixing: EM reconstructions of several thalamocortical dLGN cells and their retinal afferents revealed that two morphologically distinct RGC axon types made connections to different sets of target geniculate relay cells, as expected if these represented separate information channels. At the same time, these RGC types also converged onto an additional set of mixed-input thalamocortical neurons, consistent with convergence of types (Morgan et al., 2016). Similarly, a recent two-photon Ca^{2+} imaging study of RGC boutons in the shell region of dLGN has found that, at the scale of 2–6 μm , boutons from different RGCs often exhibited similar response preferences for one or several stimulus features, such as orientation, spatial frequency, and ON-OFF polarity (Liang et al., 2018). Critically, on this scale, RGC boutons have up to 50% probability of converging onto the same dLGN neuron (Liang et al., 2018). Hence, functional similarity of bouton clusters for multiple stimulus features might indicate convergence from single RGC types, and similarity in only one feature in the presence of mismatches in other feature preferences might indicate convergence from multiple RGC types (Liang et al., 2018). In line with these previous studies, our model of functional retinogeniculate convergence provides evidence for both specificity and mixing of RGC input types. At least for those dLGN neurons responding well to our stimulus set, it predicts that synaptic strength would be high for 1 or 2 types of functional RGC inputs and moderate for the remaining ones.

Our modeling results thus agree with the presence of both relay- and combination-mode functional convergence but critically extend the recent results to spatial scales larger than dendritic domains and to dLGN core. In addition, our results highlight the importance of considering connection weight in determining how many and which inputs are functionally relevant: with a liberal weight threshold, response prototypes from 3–8 RGC types are required to account for single-cell dLGN responses, compatible with the recent anatomical estimates from EM reconstructions and mono-transsynaptic rabies virus tracing (Morgan et al., 2016; Rompani et al., 2017). Raising the threshold to weights that likely have functionally relevant impact reduces the estimated number of RGC types providing inputs to mouse dLGN neurons to two, consistent with the large body of literature on functional convergence in the retino-geniculate pathway. It would be interesting to test these predictions on the identified connections in the published EM dataset from the Lichtman lab (Morgan et al., 2016), where ultrastructural features of the active zones, such as the volume of the postsynaptic densities and size of vesicle pools, may be assessed as indicators of synaptic strength.

Geniculate shell and core regions (Grubb and Thompson, 2004) differ in type and diversity of retinal projections (Huberman et al.,

2009; Kay et al., 2011; Kim et al., 2010; Rivlin-Etzion et al., 2011), as well as functional responses (Cruz-Martín et al., 2014; Piscopo et al., 2013). Although our dorsal approach for virus injection and electrophysiology traverses both shell and core, the volume difference between the regions suggests that our results are dominated by the dLGN core. Among our recorded population of dLGN neurons, we see a trend for higher DS in neurons recorded more dorsally (putative shell) versus ventrally (putative core region) within dLGN (Figure S6). We also observe a relative absence of DS for dLGN neurons with RFs covering the frontal space, further pointing to regional functional differences in dLGN representations. Interestingly, clusters of RGC terminals seem larger and more widespread in dLGN shell than core (Hammer et al., 2015), consistent with the possibility of more functional convergence in the shell. At the same time, retrograde transsynaptic tracing suggests a labeled-line communication for retinal direction selectivity running via the dLGN shell region to the upper layers of V1 (Cruz-Martín et al., 2014). Future studies will be required to explicitly compare and contrast the rules of retino-geniculate convergence between dLGN shell and core regions.

Considering its simplicity, our feedforward model of dLGN responses performed well. This is surprising, because the model does not consider known components of geniculate circuits, such as local inhibitory interneurons (Martinez et al., 2014), cortico-geniculate feedback (Sillito et al., 2006), and neuromodulatory influences (Antal et al., 2010; Fitzpatrick et al., 1989), and ignores transformations arising at the retino-geniculate synapse, such as postsynaptic summation (Carandini et al., 2007; Casti et al., 2008; Rathbun et al., 2010) and increases in contrast gain control (Alitto et al., 2018; Kaplan et al., 1987; Rathbun et al., 2016; Scholl et al., 2013). Potential explanations for the model's success—despite disregarding these essential circuits—include the spatial simplicity of our stimuli and the low-pass nature of our retinal signals. Indeed, local inhibition is known to increase push-pull mechanisms in dLGN, thereby enhancing temporal and spatial contrast (Hirsch et al., 2015; Martinez et al., 2014). These mechanisms will likely play a larger role in the processing of local or more complex stimuli, such as natural scenes (Lesica et al., 2006), than in the full-field stimulus used here. Similarly, performing the model predictions at the temporal resolution of Ca^{2+} signals smoothens over fine-grained differences in geniculate firing patterns, such as precise responses to high-frequency stimulation or bursting (Hirsch et al., 2015). In the future, it will be essential to extend our model by incorporating more of the geniculate circuit elements and to challenge the model predictions with more complex visual stimulation and signals of higher temporal resolution.

STAR★METHODS

Detailed methods are provided in the online version of this paper and include the following:

- **KEY RESOURCES TABLE**
- **CONTACT FOR REAGENT AND RESOURCE SHARING**
- **EXPERIMENTAL MODEL AND SUBJECT DETAILS**
 - Functional characterization of dLGN-p RGCs
 - Functional characterization of dLGN responses

● METHOD DETAILS

- Functional characterization of dLGN-p RGCs
- Functional characterization of dLGN responses

● QUANTIFICATION AND STATISTICAL ANALYSIS

- Functional characterization of dLGN-p RGCs
- Pre-processing
- Direction and orientation selectivity
- Signal deconvolution
- Response quality index (Qi)
- Match index (Mi) for dLGN-p RGC type assignment
- Cluster proportions in dLGN-p RGCs and RGC-all
- Linear feedforward model
- Functional characterization of dLGN responses
- Unit extraction and spike sorting
- Chirp quality index
- STFO correlation value
- Receptive field mapping
- Contrast response function
- Tuning
- Non-negative matrix factorization (NNMF)
- Analysis of visual field coverage

● DATA AND SOFTWARE AVAILABILITY

SUPPLEMENTAL INFORMATION

Supplemental Information includes ten figures and one table and can be found with this article online at <https://doi.org/10.1016/j.neuron.2019.01.040>.

ACKNOWLEDGMENTS

We thank G. Eske and M. Sotgia for excellent technical support and Alex H. Williams for discussion regarding NNMF cross-validation. This research was funded by the German Research Foundation (DFG; project number 276693517 – SFB 1233 [TP13]; EXC 307, CIN; BE5601/4), the German Ministry for Science and Education (BMBF; FKZ 01GQ1002 and 01GQ1601), the LMU Munich's Institutional Strategy LMUexcellent within the framework of the German Excellence Initiative (MRR), and the SmartStart-program of the Bernstein Network for Computational Neuroscience funded by the Volkswagen Foundation (Y.B.).

AUTHOR CONTRIBUTIONS

Conceptualization, T.E., L.B., and P.B.; Methodology, T.E., L.B., P.B., M.R.R., and Y.B.; Software, Y.B., P.B., L.B., T.E., A.H.K., and M.R.R.; Formal Analysis, Y.B., A.H.K., and M.R.R.; Investigation, Y.B. and M.R.R.; Writing – Initial Draft, P.B., L.B., and T.E.; Writing – Reviewing and Editing, Y.B., P.B., L.B., T.E., and M.R.R.; Funding Acquisition, Y.B., P.B., L.B., and T.E.; Supervision, P.B., L.B., and T.E.

DECLARATION OF INTERESTS

The authors declare no competing interests.

Received: June 14, 2018

Revised: November 8, 2018

Accepted: January 17, 2019

Published: February 21, 2019

SUPPORTING CITATIONS

The following references appear in the Supplemental Information: Estevez et al. (2012); Ivanova et al. (2013); Rousso et al. (2016); Zhu et al. (2014).

REFERENCES

- Alitto, H.J., Rathbun, D.L., Fisher, T.G., Alexander, P.C., and Usrey, W.M. (2018). Contrast gain control and retinogeniculate communication. *Eur. J. Neurosci.* Published online March 8, 2018. <https://doi.org/10.1111/ejn.13904>.
- Alonso, J.M., Usrey, W.M., and Reid, R.C. (1996). Precisely correlated firing in cells of the lateral geniculate nucleus. *Nature* 383, 815–819.
- Alonso, J.M., Yeh, C.I., Weng, C., and Stoelzel, C. (2006). Retinogeniculate connections: a balancing act between connection specificity and receptive field diversity. *Prog. Brain Res.* 154, 3–13.
- Antal, M., Acuna-Goycolea, C., Pressler, R.T., Blitz, D.M., and Regehr, W.G. (2010). Cholinergic activation of M2 receptors leads to context-dependent modulation of feedforward inhibition in the visual thalamus. *PLoS Biol.* 8, e1000348.
- Antinone, S.E., and Smith, G.A. (2010). Retrograde axon transport of herpes simplex virus and pseudorabies virus: a live-cell comparative analysis. *J. Virol.* 84, 1504–1512.
- Baden, T., Schubert, T., Chang, L., Wei, T., Zaichuk, M., Wissinger, B., and Euler, T. (2013). A tale of two retinal domains: near-optimal sampling of achromatic contrasts in natural scenes through asymmetric photoreceptor distribution. *Neuron* 80, 1206–1217.
- Baden, T., Berens, P., Franke, K., Román Rosón, M., Bethge, M., and Euler, T. (2016). The functional diversity of retinal ganglion cells in the mouse. *Nature* 529, 345–350.
- Bleckert, A., Schwartz, G.W., Turner, M.H., Rieke, F., and Wong, R.O.L. (2014). Visual space is represented by nonmatching topographies of distinct mouse retinal ganglion cell types. *Curr. Biol.* 24, 310–315.
- Brown, T.M., Gias, C., Hatori, M., Keding, S.R., Semo, M., Coffey, P.J., Gigg, J., Piggins, H.D., Panda, S., and Lucas, R.J. (2010). Melanopsin contributions to irradiance coding in the thalamo-cortical visual system. *PLoS Biol.* 8, e1000558.
- Carandini, M., Horton, J.C., and Sincich, L.C. (2007). Thalamic filtering of retinal spike trains by postsynaptic summation. *J. Vis.* 7, 1–11.
- Casti, A., Hayot, F., Xiao, Y., and Kaplan, E. (2008). A simple model of retina-LGN transmission. *J. Comput. Neurosci.* 24, 235–252.
- Chen, C., and Regehr, W.G. (2000). Developmental remodeling of the retinogeniculate synapse. *Neuron* 28, 955–966.
- Chen, T.-W., Wardill, T.J., Sun, Y., Pulver, S.R., Renninger, S.L., Baohan, A., Schreiter, E.R., Kerr, R.A., Orger, M.B., Jayaraman, V., et al. (2013). Ultrasensitive fluorescent proteins for imaging neuronal activity. *Nature* 499, 295–300.
- Chen, C., Bickford, M.E., and Hirsch, J.A. (2016). Untangling the web between eye and brain. *Cell* 165, 20–21.
- Cheong, S.K., Tailby, C., Solomon, S.G., and Martin, P.R. (2013). Cortical-like receptive fields in the lateral geniculate nucleus of marmoset monkeys. *J. Neurosci.* 33, 6864–6876.
- Cleland, B.G., Dubin, M.W., and Levick, W.R. (1971). Simultaneous recording of input and output of lateral geniculate neurones. *Nat. New Biol.* 231, 191–192.
- Cruz-Martín, A., El-Danaf, R.N., Osakada, F., Sriram, B., Dhande, O.S., Nguyen, P.L., Callaway, E.M., Ghosh, A., and Huberman, A.D. (2014). A dedicated circuit links direction-selective retinal ganglion cells to the primary visual cortex. *Nature* 507, 358–361.
- Dacey, D.M., Peterson, B.B., Robinson, F.R., and Gamlin, P.D. (2003). Fireworks in the primate retina: in vitro photodynamics reveals diverse LGN-projecting ganglion cell types. *Neuron* 37, 15–27.
- Denman, D.J., and Contreras, D. (2016). On parallel streams through the mouse dorsal lateral geniculate nucleus. *Front. Neural Circuits* 10, 20.
- Dhande, O.S., Estevez, M.E., Quattrochi, L.E., El-Danaf, R.N., Nguyen, P.L., Berson, D.M., and Huberman, A.D. (2013). Genetic dissection of retinal inputs to brainstem nuclei controlling image stabilization. *J. Neurosci.* 33, 17797–17813.
- Dorostkar, M.M., Dreosti, E., Odermatt, B., and Lagnado, L. (2010). Computational processing of optical measurements of neuronal and synaptic activity in networks. *J. Neurosci. Methods* 188, 141–150.
- Ecker, J.L., Dumitrescu, O.N., Wong, K.Y., Alam, N.M., Chen, S.K., LeGates, T., Renna, J.M., Prusky, G.T., Berson, D.M., and Hattar, S. (2010). Melanopsin-expressing retinal ganglion-cell photoreceptors: cellular diversity and role in pattern vision. *Neuron* 67, 49–60.
- Ecker, A.S., Berens, P., Cotton, R.J., Subramanian, M., Denfield, G.H., Cadwell, C.R., Smirnakis, S.M., Bethge, M., and Tolias, A.S. (2014). State dependence of noise correlations in macaque primary visual cortex. *Neuron* 82, 235–248.
- Ellis, E.M., Gauvain, G., Sivyer, B., and Murphy, G.J. (2016). Shared and distinct retinal input to the mouse superior colliculus and dorsal lateral geniculate nucleus. *J. Neurophysiol.* 116, 602–610.
- Erisken, S., Vaiceliunaite, A., Jurjut, O., Fiorini, M., Katzner, S., and Busse, L. (2014). Effects of locomotion extend throughout the mouse early visual system. *Curr. Biol.* 24, 2899–2907.
- Estevez, M.E., Fogerson, P.M., Ilardi, M.C., Borghuis, B.G., Chan, E., Weng, S., Auferkorte, O.N., Demb, J.B., and Berson, D.M. (2012). Form and function of the M4 cell, an intrinsically photosensitive retinal ganglion cell type contributing to geniculocortical vision. *J. Neurosci.* 32, 13608–13620.
- Euler, T., Hausselt, S.E., Margolis, D.J., Breuninger, T., Castell, X., Detwiler, P.B., and Denk, W. (2009). Eyecup scope—optical recordings of light stimulus-evoked fluorescence signals in the retina. *Pflugers Arch.* 457, 1393–1414.
- Euler, T., Haverkamp, S., Schubert, T., and Baden, T. (2014). Retinal bipolar cells: elementary building blocks of vision. *Nat. Rev. Neurosci.* 15, 507–519.
- Farrow, K., and Masland, R.H. (2011). Physiological clustering of visual channels in the mouse retina. *J. Neurophysiol.* 105, 1516–1530.
- Fitzpatrick, D., Diamond, I.T., and Raczkowski, D. (1989). Cholinergic and monoaminergic innervation of the cat's thalamus: comparison of the lateral geniculate nucleus with other principal sensory nuclei. *J. Comp. Neurol.* 288, 647–675.
- Grubb, M.S., and Thompson, I.D. (2003). Quantitative characterization of visual response properties in the mouse dorsal lateral geniculate nucleus. *J. Neurophysiol.* 90, 3594–3607.
- Grubb, M.S., and Thompson, I.D. (2004). Biochemical and anatomical subdivision of the dorsal lateral geniculate nucleus in normal mice and in mice lacking the $\beta 2$ subunit of the nicotinic acetylcholine receptor. *Vision Res.* 44, 3365–3376.
- Guillery, R.W., and Sherman, S.M. (2002). Thalamic relay functions and their role in corticocortical communication: generalizations from the visual system. *Neuron* 33, 163–175.
- Hammer, S., Monavarfeshani, A., Lemon, T., Su, J., and Fox, M.A. (2015). Multiple retinal axons converge onto relay cells in the adult mouse thalamus. *Cell Rep.* 12, 1575–1583.
- Hamos, J.E., Van Horn, S.C., Raczkowski, D., and Sherman, S.M. (1987). Synaptic circuits involving an individual retinogeniculate axon in the cat. *J. Comp. Neurol.* 259, 165–192.
- Harting, J.K., Huerta, M.F., Hashikawa, T., and van Lieshout, D.P. (1991). Projection of the mammalian superior colliculus upon the dorsal lateral geniculate nucleus: organization of tectogeniculate pathways in nineteen species. *J. Comp. Neurol.* 304, 275–306.
- Hattar, S., Kumar, M., Park, A., Tong, P., Tung, J., Yau, K.-W., and Berson, D.M. (2006). Central projections of melanopsin-expressing retinal ganglion cells in the mouse. *J. Comp. Neurol.* 497, 326–349.
- Hazan, L., Zugaro, M., and Buzsáki, G. (2006). Klusters, NeuroScope, NDManager: a free software suite for neurophysiological data processing and visualization. *J. Neurosci. Methods* 155, 207–216.
- Hei, X., Stoelzel, C.R., Zhuang, J., Bereshpolova, Y., Huff, J.M., Alonso, J.M., and Swadlow, H.A. (2014). Directional selective neurons in the awake LGN: response properties and modulation by brain state. *J. Neurophysiol.* 112, 362–373.

- Hirsch, J.A., Wang, X., Sommer, F.T., and Martinez, L.M. (2015). How inhibitory circuits in the thalamus serve vision. *Annu. Rev. Neurosci.* **38**, 309–329.
- Hong, Y.K., Park, S., Litvina, E.Y., Morales, J., Sanes, J.R., and Chen, C. (2014). Refinement of the retinogeniculate synapse by bouton clustering. *Neuron* **84**, 332–339.
- Howarth, M., Walmsley, L., and Brown, T.M. (2014). Binocular integration in the mouse lateral geniculate nuclei. *Curr. Biol.* **24**, 1241–1247.
- Hubel, D.H., and Wiesel, T.N. (1961). Integrative action in the cat's lateral geniculate body. *J. Physiol.* **155**, 385–398.
- Huberman, A.D., Manu, M., Koch, S.M., Susman, M.W., Lutz, A.B., Ullian, E.M., Baccus, S.A., and Barres, B.A. (2008). Architecture and activity-mediated refinement of axonal projections from a mosaic of genetically identified retinal ganglion cells. *Neuron* **59**, 425–438.
- Huberman, A.D., Wei, W., Elstrott, J., Stafford, B.K., Feller, M.B., and Barres, B.A. (2009). Genetic identification of an On-Off direction-selective retinal ganglion cell subtype reveals a layer-specific subcortical map of posterior motion. *Neuron* **62**, 327–334.
- Ivanova, E., Lee, P., and Pan, Z.H. (2013). Characterization of multiple bistratified retinal ganglion cells in a purkinje cell protein 2-Cre transgenic mouse line. *J. Comp. Neurol.* **521**, 2165–2180.
- Jacoby, J., and Schwartz, G.W. (2018). Typology and circuitry of suppressed-by-contrast retinal ganglion cells. *Front. Cell. Neurosci.* **12**, 269.
- Jaubert-Miazza, L., Green, E., Lo, F.-S., Bui, K., Mills, J., and Guido, W. (2005). Structural and functional composition of the developing retinogeniculate pathway in the mouse. *Vis. Neurosci.* **22**, 661–676.
- Joesch, M., and Meister, M. (2016). A neuronal circuit for colour vision based on rod-cone opponency. *Nature* **532**, 236–239.
- Kaplan, E., Purpura, K., and Shapley, R.M. (1987). Contrast affects the transmission of visual information through the mammalian lateral geniculate nucleus. *J. Physiol.* **391**, 267–288.
- Kay, J.N., De la Huerta, I., Kim, I.-J., Zhang, Y., Yamagata, M., Chu, M.W., Meister, M., and Sanes, J.R. (2011). Retinal ganglion cells with distinct directional preferences differ in molecular identity, structure, and central projections. *J. Neurosci.* **31**, 7753–7762.
- Kerschensteiner, D., and Guido, W. (2017). Organization of the dorsal lateral geniculate nucleus in the mouse. *Vis. Neurosci.* **34**, E008.
- Kim, I.-J., Zhang, Y., Yamagata, M., Meister, M., and Sanes, J.R. (2008). Molecular identification of a retinal cell type that responds to upward motion. *Nature* **452**, 478–482.
- Kim, I.-J., Zhang, Y., Meister, M., and Sanes, J.R. (2010). Laminar restriction of retinal ganglion cell dendrites and axons: subtype-specific developmental patterns revealed with transgenic markers. *J. Neurosci.* **30**, 1452–1462.
- Krieger, B., Qiao, M., Rousso, D.L., Sanes, J.R., and Meister, M. (2017). Four alpha ganglion cell types in mouse retina: Function, structure, and molecular signatures. *PLoS ONE* **12**, e0180091.
- Lee, D.D., and Seung, H.S. (1999). Learning the parts of objects by non-negative matrix factorization. *Nature* **401**, 788–791.
- Lesica, N.A., Weng, C., Jin, J., Yeh, C.I., Alonso, J.M., and Stanley, G.B. (2006). Dynamic encoding of natural luminance sequences by LGN bursts. *PLoS Biol.* **4**, e209.
- Levick, W.R. (1967). Receptive fields and trigger features of ganglion cells in the visual streak of the rabbits retina. *J. Physiol.* **188**, 285–307.
- Liang, L., Fratzl, A., Goldey, G., Ramesh, R.N., Sugden, A.U., Morgan, J.L., Chen, C., and Andermann, M.L. (2018). A fine-scale functional logic to convergence from retina to thalamus. *Cell* **173**, 1343–1355.e24.
- Lien, A.D., and Scanziani, M. (2013). Tuned thalamic excitation is amplified by visual cortical circuits. *Nat. Neurosci.* **16**, 1315–1323.
- Lien, A.D., and Scanziani, M. (2018). Cortical direction selectivity emerges at convergence of thalamic synapses. *Nature* **558**, 80–86.
- Litvina, E.Y., and Chen, C. (2017). Functional convergence at the retinogeniculate synapse. *Neuron* **96**, 330–338.e5.
- Madisen, L., Garner, A.R., Shimaoka, D., Chuong, A.S., Klapoetke, N.C., Li, L., van der Bourg, A., Niino, Y., Ego, L., Monetti, C., et al. (2015). Transgenic mice for intersectional targeting of neural sensors and effectors with high specificity and performance. *Neuron* **85**, 942–958.
- Marshall, J.H., Kaye, A.P., Nauhaus, I., and Callaway, E.M. (2012). Anterior-posterior direction opponency in the superficial mouse lateral geniculate nucleus. *Neuron* **76**, 713–720.
- Martersteck, E.M., Hirokawa, K.E., Evarts, M., Bernard, A., Duan, X., Li, Y., Ng, L., Oh, S.W., Ouellette, B., Royall, J.J., et al. (2017). Diverse central projection patterns of retinal ganglion cells. *Cell Rep.* **18**, 2058–2072.
- Martinez, L.M., Molano-Mazón, M., Wang, X., Sommer, F.T., and Hirsch, J.A. (2014). Statistical wiring of thalamic receptive fields optimizes spatial sampling of the retinal image. *Neuron* **81**, 943–956.
- Masland, R.H. (2012). The neuronal organization of the retina. *Neuron* **76**, 266–280.
- Masland, R.H., and Martin, P.R. (2007). The unsolved mystery of vision. *Curr. Biol.* **17**, R577–R582.
- Mastrorade, D.N. (1987). Two classes of single-input X-cells in cat lateral geniculate nucleus. II. Retinal inputs and the generation of receptive-field properties. *J. Neurophysiol.* **57**, 381–413.
- Mastrorade, D.N. (1992). Nonlagged relay cells and interneurons in the cat lateral geniculate nucleus: receptive-field properties and retinal inputs. *Vis. Neurosci.* **8**, 407–441.
- McGavern, D.B., and Kang, S.S. (2011). Illuminating viral infections in the nervous system. *Nat. Rev. Immunol.* **11**, 318–329.
- Morgan, J.L., Berger, D.R., Wetzel, A.W., and Lichtman, J.W. (2016). The fuzzy logic of network connectivity in mouse visual thalamus. *Cell* **165**, 192–206.
- Morin, L.P., and Studholme, K.M. (2014). Retinofugal projections in the mouse. *J. Comp. Neurol.* **522**, 3733–3753.
- Nath, A., and Schwartz, G.W. (2016). Cardinal orientation selectivity is represented by two distinct ganglion cell types in mouse retina. *J. Neurosci.* **36**, 3208–3221.
- Neve, R.L. (2012). Overview of gene delivery into cells using HSV-1-based vectors. *Curr. Protoc. Neurosci. Chapter 4*. Unit 4.12.
- Niell, C.M., and Stryker, M.P. (2010). Modulation of visual responses by behavioral state in mouse visual cortex. *Neuron* **65**, 472–479.
- Pang, J.-J., Gao, F., and Wu, S.M. (2003). Light-evoked excitatory and inhibitory synaptic inputs to ON and OFF alpha ganglion cells in the mouse retina. *J. Neurosci.* **23**, 6063–6073.
- Paxinos, G., and Franklin, K.B.J. (2008). *The Mouse Brain in Stereotaxic Coordinates* (Elsevier Science).
- Piscopo, D.M., El-Danaf, R.N., Huberman, A.D., and Niell, C.M. (2013). Diverse visual features encoded in mouse lateral geniculate nucleus. *J. Neurosci.* **33**, 4642–4656.
- Rathbun, D.L., Warland, D.K., and Usrey, W.M. (2010). Spike timing and information transmission at retinogeniculate synapses. *J. Neurosci.* **30**, 13558–13566.
- Rathbun, D.L., Alitto, H.J., Warland, D.K., and Usrey, W.M. (2016). Stimulus contrast and retinogeniculate signal processing. *Front. Neural Circuits* **10**, 8.
- Reid, R.C., and Usrey, W.M. (2004). Functional connectivity in the pathway from retina to striate cortex. In *The Visual Neurosciences*, L.M. Chalupa and J.S. Werner, eds. (MIT), pp. 673–679.
- Rivlin-Etzion, M., Zhou, K., Wei, W., Elstrott, J., Nguyen, P.L., Barres, B.A., Huberman, A.D., and Feller, M.B. (2011). Transgenic mice reveal unexpected diversity of on-off direction-selective retinal ganglion cell subtypes and brain structures involved in motion processing. *J. Neurosci.* **31**, 8760–8769.
- Rompani, S.B., Müllner, F.E., Wanner, A., Zhang, C., Roth, C.N., Yonehara, K., and Roska, B. (2017). Different modes of visual integration in the lateral geniculate nucleus revealed by single-cell-initiated transsynaptic tracing. *Neuron* **93**, 767–776.e6.

- Rouso, D.L., Qiao, M., Kagan, R.D., Yamagata, M., Palmiter, R.D., and Sanes, J.R. (2016). Two pairs of ON and OFF retinal ganglion cells are defined by intersectional patterns of transcription factor expression. *Cell Rep.* 15, 1930–1944.
- Sanes, J.R., and Masland, R.H. (2015). The types of retinal ganglion cells: current status and implications for neuronal classification. *Annu. Rev. Neurosci.* 38, 221–246.
- Scholl, B., Tan, A.Y.Y., Corey, J., and Priebe, N.J. (2013). Emergence of orientation selectivity in the Mammalian visual pathway. *J. Neurosci.* 33, 10616–10624.
- Sillito, A.M., Cudeiro, J., and Jones, H.E. (2006). Always returning: feedback and sensory processing in visual cortex and thalamus. *Trends Neurosci.* 29, 307–316.
- Sincich, L.C., Adams, D.L., Economides, J.R., and Horton, J.C. (2007). Transmission of spike trains at the retinogeniculate synapse. *J. Neurosci.* 27, 2683–2692.
- Sivyer, B., Taylor, W.R., and Vaney, D.I. (2010). Uniformity detector retinal ganglion cells fire complex spikes and receive only light-evoked inhibition. *Proc. Natl. Acad. Sci. USA* 107, 5628–5633.
- Supèr, H., and Roelfsema, P.R. (2005). Chronic multiunit recordings in behaving animals: advantages and limitations. *Prog. Brain Res.* 147, 263–282.
- Tien, N.-W., Pearson, J.T., Heller, C.R., Demas, J., and Kerschensteiner, D. (2015). Genetically identified suppressed-by-contrast retinal ganglion cells reliably signal self-generated visual stimuli. *J. Neurosci.* 35, 10815–10820.
- Troy, J.B., Einstein, G., Schuurmans, R.P., Robson, J.G., and Enroth-Cugell, C. (1989). Responses to sinusoidal gratings of two types of very nonlinear retinal ganglion cells of cat. *Vis. Neurosci.* 3, 213–223.
- Usrey, W.M., Reppas, J.B., and Reid, R.C. (1998). Paired-spike interactions and synaptic efficacy of retinal inputs to the thalamus. *Nature* 395, 384–387.
- Usrey, W.M., Reppas, J.B., and Reid, R.C. (1999). Specificity and strength of retinogeniculate connections. *J. Neurophysiol.* 82, 3527–3540.
- van Wyk, M., Wässle, H., and Taylor, W.R. (2009). Receptive field properties of ON- and OFF-ganglion cells in the mouse retina. *Vis. Neurosci.* 26, 297–308.
- Warwick, R.A., Kaushansky, N., Sarid, N., Golan, A., and Rivlin-Etzion, M. (2018). Inhomogeneous encoding of the visual field in the mouse retina. *Curr. Biol.* 28, 655–665.e3.
- Weyand, T.G. (2016). The multifunctional lateral geniculate nucleus. *Rev. Neurosci.* 27, 135–157.
- White, A.J., Solomon, S.G., and Martin, P.R. (2001). Spatial properties of koniocellular cells in the lateral geniculate nucleus of the marmoset *Callithrix jacchus*. *J. Physiol.* 533, 519–535.
- Williams, A.H., Kim, T.H., Wang, F., Vyas, S., Ryu, S.I., Shenoy, K.V., Schnitzer, M., Kolda, T.G., and Ganguli, S. (2018). Unsupervised discovery of demixed, low-dimensional neural dynamics across multiple timescales through tensor component analysis. *Neuron* 98, 1099–1115.e8.
- Yatsenko, D., Reimer, J., Ecker, A.S., Walker, E.Y., Sinz, F., Berens, P., Hoenselaar, A., Cotton, R.J., Siapas, A.S., and Tolias, A.S. (2015). DataJoint: managing big scientific data using MATLAB or Python. *bioRxiv*. <https://doi.org/10.1101/031658>.
- Yonehara, K., Shintani, T., Suzuki, R., Sakuta, H., Takeuchi, Y., Nakamura-Yonehara, K., and Noda, M. (2008). Expression of SPIG1 reveals development of a retinal ganglion cell subtype projecting to the medial terminal nucleus in the mouse. *PLoS ONE* 3, e1533.
- Yonehara, K., Ishikane, H., Sakuta, H., Shintani, T., Nakamura-Yonehara, K., Kamiji, N.L., Usui, S., and Noda, M. (2009). Identification of retinal ganglion cells and their projections involved in central transmission of information about upward and downward image motion. *PLoS ONE* 4, e4320.
- Zeater, N., Cheong, S.K., Solomon, S.G., Dreher, B., and Martin, P.R. (2015). Binocular visual responses in the primate lateral geniculate nucleus. *Curr. Biol.* 25, 3190–3195.
- Zhang, Y., Kim, I.-J., Sanes, J.R., and Meister, M. (2012). The most numerous ganglion cell type of the mouse retina is a selective feature detector. *Proc. Natl. Acad. Sci. USA* 109, E2391–E2398.
- Zhao, X., Chen, H., Liu, X., and Cang, J. (2013). Orientation-selective responses in the mouse lateral geniculate nucleus. *J. Neurosci.* 33, 12751–12763.
- Zhu, Y., Xu, J., Hauswirth, W.W., and DeVries, S.H. (2014). Genetically targeted binary labeling of retinal neurons. *J. Neurosci.* 34, 7845–7861.
- Ziburkus, J., and Guido, W. (2006). Loss of binocular responses and reduced retinal convergence during the period of retinogeniculate axon segregation. *J. Neurophysiol.* 96, 2775–2784.

STAR★METHODS

KEY RESOURCES TABLE

REAGENT or RESOURCE	SOURCE	IDENTIFIER
Bacterial and Virus Strains		
Cre-encoding Herpes-Simplex-Virus 1	MIT Vector Core, Cambridge, USA	hEFlz-cre - RN425
Experimental Models: Organisms/Strains		
Ai95(RCL-GCaMP6f)-D or Ai95D mice, B6;129S-Gt(ROSA)26Sor ^{tm95.1(CAG-GCaMP6f)Hze/J}	The Jackson Laboratory	IMSR Cat#JAX:024105; RRID: IMSR_JAX:024105
C57BL/6J mice	The Jackson Laboratory	RRID: IMSR_JAX:000664
Software and Algorithms		
QDSpy 0.77	developed and maintained by Thomas Euler	https://github.com/eulerlab/QDSpy
Python 3.4	https://www.python.org/	https://www.python.org/ ; RRID: SCR_008394
MATLAB R2017a	MathWorks	https://www.mathworks.com/products/matlab/ ; RRID: SCR_001622
IgorPro 6.3.7.2	Wavemetrics	https://www.wavemetrics.com/products/igorpro/igorpro.htm ; RRID: SCR_000325
SARFIA toolbox for IGOR Pro	Dorostkar et al., 2010	https://www.wavemetrics.com/project/SARFIA
Fiji/ImageJ	NIH	https://imagej.nih.gov/ij/ ; RRID: SCR_003070
Datajoint	Yatsenko et al., 2015	https://datajoint.github.io/ ; RRID: SCR_014543
EXPO visual display software	developed by Dr. Peter Lennie and maintained by Rob Dotson for the Center for Neural Science at New York University	https://sites.google.com/a/nyu.edu/expo/home
NDManager software suite	Hazan et al., 2006	http://neurosuite.sourceforge.net/
KlustaKwik	Kenneth D. Harris	http://klustakwik.sourceforge.net/
Klusters	Hazan et al., 2006	http://neurosuite.sourceforge.net/
NNMF cross-validation	Alex H. Williams; Williams et al., 2018	https://gist.github.com/ahwillia/65d8f87fcd4bded3676d67b55c1a3954
Other		
Aladdin syringe pump	WPI Germany, Berlin, DE	AL-1000
Hamilton syringe	Hamilton Robotics, Reno, USA	Gastight (10 µl); Model#1701;
Stereotactic frame	Neurostar, Tübingen, DE	Robot Stereotaxic
Closed loop temperature control system for small rodents	HD, Hugo Sachs Elektronik-Harvard Apparatus GmbH, March-Hugstetten, DE	Cat#50-7221-F
Dental drill motor	NSK	Volvere Vmax NE120 Model#VMAX35RV
Sharp micropipette	Science Products, Hofheim, DE	GB150F-8P
Ceramic filters	GE Healthcare, Buckinghamshire, UK	Anodisc #13, 0.2 µm pore size
Vibratome	Thermo Fisher Scientific, Waltham, Massachusetts, USA	Microm HM 650 V
DAPI-containing mounting medium	Vector Laboratories Ltd, Peterborough, UK	Vectashield DAPI
Epi-fluorescent microscope	Zeiss, Oberkochen, DE	Zeiss Imager.Z1m
MOM-type two-photon microscope	designed by W. Denk, MPI, Martinsried; purchased from Sutter Instruments / Science Products, Hofheim, Germany; Euler et al., 2009	N/A
Mode-locked Ti:Sapphire laser	Newport Spectra-Physics, Darmstadt, Germany	MaiTai-HP DeepSee

(Continued on next page)

Continued		
REAGENT or RESOURCE	SOURCE	IDENTIFIER
Fluorescence detection channel for GCaMP6f	AHF/Chroma Tübingen, Germany	HQ 510/84
Fluorescence detection channel for SR101	AHF/Chroma Tübingen, Germany	HQ 630/60, AHF
Water immersion objective	Zeiss, Oberkochen, Germany	W Plan-Apochromat 20x/1.0 DIC M27
DLP projector	Acer	K11
Band-pass-filtered light-emitting diodes 'green'	AHF/Chroma Tübingen, Germany	578 BP 10
Band-pass-filtered light-emitting diodes 'blue'	AHF/Chroma Tübingen, Germany	HC 405 BP 10
OptiBond FL primer and adhesive	Kerr dental, Rastatt, DE	Cat#35369
Dental cement	Ivoclar Vivadent, Ellwangen, DE	Tetric EvoFlow
Ground and reference screws	Bilaney	00-96 X 1/16 stainless steel screws
Kwik-Cast	WPI Germany, Berlin, DE	https://www.wpi-europe.com/products/laboratory-supplies/adhesives/kwik-cast.aspx
Gamma-corrected LCD screen	Samsung	Samsung SyncMaster 2233
32-channel edge silicon probes	Neuronexus, Ann Arbor, USA	A1x32Edge-5mm-20-177-A32
Arduino-type microcontroller	Arduino	http://www.arduino.cc/
Infrared light illumination	Allied Vision, Exton, USA	Guppy AVT camera
Red-shifted fluorescent lipophilic tracer	Thermo Fisher Scientific, Waltham, Massachusetts, USA	DiD
Blackrock microsystems amplifier	Blackrock Microsystems Europe GmbH, Hannover DE	128-Channel Neural signal processor

CONTACT FOR REAGENT AND RESOURCE SHARING

Further information and requests for resources and reagents should be directed to, and will be fulfilled by, the Lead Contact, Laura Busse (busse@bio.lmu.de).

EXPERIMENTAL MODEL AND SUBJECT DETAILS

All procedures complied with the European Communities Council Directive 2010/63/EC and the German Law for Protection of Animals, and were approved by local authorities, following appropriate ethics review.

Functional characterization of dLGN-p RGCs

We used five mice of either sex aged 8 to 12 weeks of the Ai95D reporter line (B6; 129S-Gt(ROSA)26Sor^{tm95.1(CAG-GCaMP6f)Hze/J}; JAX 024105; RRID:IMSR_JAX:024 105). Ai95D features a floxed-STOP cassette preventing transcription of the genetically-encoded Ca²⁺ indicator GCaMP6f (Chen et al., 2013). Stereotactic injection of a Cre-encoding Herpes-Simplex-Virus 1 (hEF1z-cre, MIT Vector Core, Cambridge, USA) into the dLGN resulted in retrograde Cre-recombinase expression in dLGN-projecting (dLGN-p) RGCs, where Cre-recombinase, in turn, removed the LoxP sites and activated GCaMP6f expression.

Functional characterization of dLGN responses

We used 8- to 12-week-old wild-type mice (C57BL/6J; RRID: IMSR_JAX:000 664) of either sex.

METHOD DETAILS

Functional characterization of dLGN-p RGCs

Virus injection

After induction of anesthesia using isoflurane (4% in oxygen), mice received isoflurane maintenance anesthesia (typically 1.2% in oxygen, adjusted to maintain a surgical plane of anesthesia as assessed by the absence of the pedal reflex), and were fixed in a stereotactic frame (Neurostar, Tübingen, DE). At the beginning of the surgical procedure, atropine (Atropine sulfate, 0.3 mg/kg, sc, Braun, Melsungen, DE) and analgesics (Buprenorphine, 0.1 mg/kg, sc, Bayer, Leverkusen, DE) were administered, and the eyes were protected with an eye ointment (Bepanthen, Bayer, Leverkusen, DE). The animal's temperature was kept constant at 37°C via a closed loop temperature control system for small rodents (HD, Hugo Sachs Elektronik-Harvard Apparatus GmbH, March-Hugstetten, DE).

After a midline scalp incision, a small hole was made with a dental drill (Sinco, Jengen, DE) over the dLGN located in the left hemisphere, 2.5 mm posterior to the bregma and 2.3 mm lateral from the midline. The virus was loaded in a sharp micropipette

(GB150F-8P, Science Products, inner tip diameter 20–25 μm , Hofheim, DE) connected through a 10 μl Hamilton syringe (Hamilton Robotics, Reno, USA) to an Aladdin syringe pump (AL-1000, WPI Germany, Berlin, DE). A volume of 20–40 nL of virus was injected at a depth of 2.7 mm. The pipette was left in place for an additional 5 min to allow for viral diffusion. Antibiotics (Baytril, 5 mg/kg, sc, Bayer, Leverkusen, DE) and a longer lasting analgesic (Carprofen, 5 mg/kg, sc, Rimadyl, Zoetis, Berlin, DE) were administered continuously for 3 days post-surgery. Two-photon Ca^{2+} imaging was carried out 3 weeks after viral injection.

Perfusion and retinal tissue preparation

Animals were housed under a standard 12 h day/night rhythm. Before perfusion and two-photon imaging, animals were dark-adapted for ≥ 1 h, and then deeply anaesthetized with a lethal dose of sodium pentobarbital (Narcoren, 400 mg/kg, injected intraperitoneally, Böhringer Ingelheim, Ingelheim, DE). When the animal reached the asphyxia stage and complete paralysis, the eyes were enucleated, and the mouse was transcardially perfused with 0.2 M sodium phosphate buffered saline (PBS), followed by 4% paraformaldehyde (PFA) solution in PBS. The brains were postfixed in PFA for 24 h at 4 $^{\circ}$ and then stored in PBS.

The eyes were dissected in carboxygenated (95% O_2 , 5% CO_2) extracellular solution containing (in mM): 125 NaCl, 2.5 KCl, 2 CaCl_2 , 1 MgCl_2 , 1.25 NaH_2PO_4 , 26 NaHCO_3 , 20 glucose, and 0.5 L-glutamine (pH 7.4). The retina was extracted from the eyecup and flat-mounted onto a ceramic filter (Anodisc #13, 0.2 μm pore size, GE Healthcare, Buckinghamshire, UK) with the ganglion cell layer (GCL) facing up and transferred to the recording chamber of the microscope, where it was continuously perfused with carboxygenated solution at $\sim 36^{\circ}\text{C}$. In all experiments, ~ 0.1 μM Sulforhodamine-101 (SR101, Sigma, Steinheim, DE) was added to the extracellular solution to reveal blood vessels and any damaged cells in the red fluorescence channel of the microscope (Euler et al., 2009). All procedures were carried out under dim red (> 650 nm) illumination.

Histological reconstruction of injection sites

To verify the injection site within the dLGN, we used histological reconstructions. Brains were sliced for coronal sections (50 μm) using a vibratome (Microm HM 650 V, Thermo Fisher Scientific, Waltham, Massachusetts, USA) and mounted on glass slides with DAPI-containing mounting medium (Vectashield DAPI, Vector Laboratories Ltd, Peterborough, UK), which labels the cell nuclei, and coverslipped. Brain slices were inspected using a Zeiss Imager.Z1m epi-fluorescent microscope (Zeiss, Oberkochen, DE) for the expression of the retrogradely transported HSV-1, visualized by the expression of the GCaMP6f protein containing the enhanced green fluorescent protein (eGFP). The stereotactic slice coordinates were estimated based on Paxinos and Franklin (2008). We excluded one mouse from analysis of functional Ca^{2+} data because viral expression was spread beyond dLGN boundaries.

Two-photon Ca^{2+} imaging and light stimulation

We used a MOM-type two-photon microscope (designed by W. Denk, MPI, Martinsried; purchased from Sutter Instruments/Science Products, Hofheim, Germany). Design and procedures were described previously (Baden et al., 2016; Euler et al., 2009). In brief, the system was equipped with a mode-locked Ti:Sapphire laser (MaiTai-HP DeepSee, Newport Spectra-Physics, Darmstadt, Germany) tuned to 927 nm, two fluorescence detection channels for GCaMP6f (HQ 510/84, AHF/Chroma Tübingen, Germany) and SR101 (HQ 630/60, AHF), and a water immersion objective (W Plan-Apochromat 20 \times /1.0 DIC M27, Zeiss, Oberkochen, Germany). For image acquisition, we used custom-made software (ScanM, by M. Müller, MPI, Martinsried, and T. Euler) running under IGOR Pro 6.37 for Windows (Wavemetrics, Lake Oswego, OR, USA; RRID: SCR_000325), taking 64 \times 64 pixel image sequences (7.8 frames/s) for activity scans or 512 \times 512 pixel images for high-resolution morphology scans.

For light stimulation, we focused a DLP projector (K11, Acer) through the objective, fitted with band-pass-filtered light-emitting diodes (LEDs) (“green”, 578 BP 10; and “UV”, HC 405 BP 10, AHF/Chroma) to match the spectral sensitivity of mouse M- and S-opsins. LEDs were synchronized with the microscope’s scan retrace. Stimulator intensity (as photoisomerization rate, 10^3 P*/s/cone) was calibrated as described previously (Euler et al., 2009) to range from 0.6 and 0.7 (black image) to 18.8 and 20.3 for M- and S-opsins, respectively. An additional, steady illumination component of $\sim 10^4$ P*/s/cone was present during the recordings because of two-photon excitation of photopigments (for detailed discussion, see Baden et al., 2013; Euler et al., 2009). For all experiments, the tissue was kept at a constant mean stimulator intensity level for at least 15 s after the laser scanning started and before light stimuli were presented.

Four types of light stimuli were used (Figure 1D, top; Baden et al., 2016): (i) Full-field (800 \times 600 μm) “chirp” stimuli consisting of a bright step and two sinusoidal intensity modulations, one with increasing frequency (0.5–8 Hz) and one with increasing contrast; (ii) 0.3 \times 1 mm bright bar moving at 1 mm s^{-1} in eight directions; (iii) alternating UV and green 3 s flashes; and (iv) binary dense noise (20 \times 15 matrix with 40 μm pixel-side length; each pixel displayed an independent, balanced random sequence at 5 Hz for 5 min) for space-time receptive field mapping. All stimuli, except (iii), were achromatic, with matched photo-isomerization rates for mouse M- and S-opsins. Visual stimuli were presented using custom software (QDSpy, <https://github.com/eulerlab/QDSpy>).

Functional characterization of dLGN responses

Surgical procedures

After induction of anesthesia using isoflurane (4% in oxygen), mice received isoflurane maintenance anesthesia (typically 1.2% in oxygen, adjusted to maintain a surgical plane of anesthesia as assessed by the absence of the pedal reflex). At the beginning of the surgical procedure, atropine (Atropine sulfate, 0.3 mg/kg, sc, Braun, Melsungen, DE) and analgesics (Buprenorphine, 0.1 mg/kg, sc, Bayer, Leverkusen, DE) were administered, and the eyes were protected with an eye ointment (Bepanthen, Bayer, Leverkusen, DE). The animal’s temperature was kept constant at 37 $^{\circ}\text{C}$ via a closed loop temperature control system for small rodents (HD, Hugo Sachs Elektronik-Harvard Apparatus GmbH, March-Hugstetten, DE).

After a midline scalp incision and skin removal, a drop of H₂O₂ (3%) was applied on the surface of the skull for the removal of tissue residues. A custom lightweight aluminum head post was placed on the posterior skull using OptiBond FL primer and adhesive (Kerr dental, Rastatt, DE) and Tetric EvoFlow dental cement (Ivoclar Vivadent, Ellwangen, DE). Miniature ground and reference screws (00-96 X 1/16 stainless steel screws, Bilaney) soldered to custom-made connector pins were placed bilaterally over the cerebellum. A well of dental cement was formed to hold the silicone elastomer sealant Kwik-Cast (WPI Germany, Berlin, DE) covering the skull. Antibiotics (Baytril, 5 mg/kg, sc, Bayer, Leverkusen, DE) and a longer lasting analgesic (Carprofen, 5 mg/kg, sc, Rimadyl, Zoetis, Berlin, DE) continued to be administered for 3 days post-surgery.

After recovery, animals were familiarized with a simulation of the experimental procedures in multiple training sessions until they were deemed comfortable with the conditions. Before experiments, a craniotomy (ca. 1 mm²) was performed over dLGN (2.3 mm lateral to the midline and 2.5 mm posterior to bregma), which was re-sealed with Kwik-Cast (WPI Germany, Berlin, DE). Experiments started one day after craniotomy and were continued on consecutive days as long as electrophysiological signals remained of high quality.

In-vivo multisite extracellular recordings

Our experimental configuration for in-vivo recordings is described in detail in [Erisken et al. \(2014\)](#). The mouse was head-fixed and could run freely on an air-suspended styrofoam ball while stimuli were presented on a gamma-corrected LCD screen (Samsung SyncMaster 2233). Extracellular neural signals were recorded 2.5 mm posterior from bregma and 2.3 mm lateral from midline through a small craniotomy window over dLGN with 32-channel edge silicon probes (Neuronexus, A1x32Edge-5mm-20-177- A32, Ann Arbor, USA). Neurons were verified as belonging to the dLGN based on the characteristic RF progression from top to bottom along the electrode shank ([Figure 3C](#)), the preference for high temporal frequencies, and a high prevalence of F1 responses to drifting gratings ([Grubb and Thompson, 2003](#); [Piscopo et al., 2013](#)). Ball movements were registered at 90 Hz by two optical mice connected to an Arduino-type microcontroller (<http://www.arduino.cc/>). Eye movements were monitored under infrared light illumination (Guppy AVT camera, frame rate 50 Hz, Allied Vision, Exton, USA).

Visual stimulation

We used custom software (EXPO, <https://sites.google.com/a/nyu.edu/expo/home>) to present visual stimuli on a gamma-calibrated liquid crystal display (LCD) monitor (Samsung SyncMaster 2233RZ; mean luminance 50 cd/m², 60 Hz) at 25 cm distance to the animal's right eye. Four types of light stimuli were presented: (i) a "contrast stimulus" to measure the contrast response function, consisting of drifting sinusoidal gratings at a single orientation and 12 different randomly interleaved contrasts for 2 s with 5 s pauses between trials. (ii) the full-field chirp stimulus (see RGC section). (iii) a spatial-temporal-frequency-orientation (STFO) stimulus to capture preferred tuning properties of a large number of neurons simultaneously; the stimulus consisted of drifting sinusoidal gratings with 8 orientations, 6 temporal (0.5, 1, 2, 4, 8, 16 cycles/sec) and 2 spatial frequencies (0.5, 0.15 cycles/°) (443 of 814 cells, [Figure S7](#)). Trials were randomly interleaved and presented for 1 s with 0.1 s pauses between trials. The stimulus was shown at 100% contrast with the background at mean luminance. (iv) a sparse noise stimulus for receptive field mapping, consisting of white or black squares (5° visual angle) presented on a background of mean luminance (50 cd/m²). Squares were flashed for 200 ms each at every position on a 12 × 12 square grid of 60 degrees.

Except for the sparse noise stimulus, all stimuli were presented in full-field mode. In experiments measuring tuning curves, a blank screen condition (mean luminance) was included to estimate the spontaneous firing rate.

Histological reconstruction of recording sites

To verify recording sites from dLGN, we used histological reconstructions. Before recording from the dLGN, electrodes were coated with a red-shifted fluorescent lipophilic tracer (DiD; Thermo Fisher Scientific, Waltham, Massachusetts, USA). After the last recording session, mice were transcardially perfused and the brain fixed in a 4% paraformaldehyde phosphate buffered saline (PBS) solution for 24 h and then stored in PBS. Brains were sliced for coronal sections (50 μm) using a vibratome (Microm HM 650 V, Thermo Fisher Scientific, Waltham, Massachusetts, USA) and mounted on glass slides with Vectashield DAPI (Vectashield DAPI, Vector Laboratories Ltd, Peterborough, UK), and coverslipped. Slices were inspected for DAPI and DiD presence using a Zeiss Imager.Z1m fluorescent microscope (Zeiss, Oberkochen, DE), and post-processed using Fiji/ImageJ (NIH; <https://imagej.nih.gov/ij/>; RRID: SCR_003070).

QUANTIFICATION AND STATISTICAL ANALYSIS

Functional characterization of dLGN-p RGCs

The data analysis was performed using IGOR Pro (Wavemetrics, Lake Oswego, OR, USA), MATLAB (The Mathworks, Natick, Massachusetts, USA) and Python (distribution by Anaconda Inc., Austin, TX; RRID:SCR_008394) using methods described previously ([Baden et al., 2016](#)).

Pre-processing

Regions of interest (ROIs) were manually drawn around the GCaMP6f-expressing somata in the recording fields. The Ca²⁺ traces for each ROI were extracted (as $\Delta F/F$) using the image analysis toolbox SARFIA for IGOR Pro ([Dorostkar et al., 2010](#)). A stimulus time marker embedded in the recorded data served to align the Ca²⁺ traces relative to the visual stimulus with a temporal precision of 2 ms. For this, Ca²⁺ traces were up-sampled to 512 Hz, and the timing for each ROI was corrected for sub-frame time-offsets related to the

scanning. The Ca^{2+} traces were then de-trended using a high-pass filtering above ~ 0.1 Hz and resampled to 7.8 Hz. For all stimuli except the dense noise (for RF mapping), the baseline was subtracted (median of first eight samples), median activity $r(t)$ across stimulus repetitions was computed (typically three to five repetitions) and normalized such that $\max_t(|r(t)|) = 1$.

Direction and orientation selectivity

To extract time course and directional tuning of the Ca^{2+} response to the moving bar stimulus, we performed a singular value decomposition (SVD) on the T by D normalized mean response matrix M (times samples by number of directions; $T = 32$; $D = 8$):

$$[U, S, V] = \text{svd}(M)$$

This procedure decomposes the response into a temporal component in the first column of U and a direction dependent component or tuning curve in the first column of V , such that the response matrix can be approximated as an outer product of the two:

$$M \approx S_{1,1} U_{:,1} V_{:,1}^T$$

An advantage of this procedure is that it does not require manual selection of time bins for computing direction tuning but extracts the direction-tuning curve given the varying temporal dynamics of different neurons.

To measure direction selectivity (DS) and its significance, we projected the tuning curve $V_{:,1}$ on a complex exponential $\phi_k = \exp(i\alpha_k)$, where α_k is the direction of the k_{th} condition:

$$K = \phi^T V_{:,1}$$

This is mathematically equivalent to computing the vector sum in the 2D plane or computing the power in the first Fourier component. We computed a DS index as the resulting vector length:

$$DS_i = |K|$$

correcting for the direction spacing. We additionally assessed the statistical significance of direction tuning using a permutation test (Ecker et al., 2014). To this end, we created surrogate trials (that is, stimulus repetitions) by shuffling the trial labels (that is, destroying any relationship between condition and response), computed the tuning curve for each surrogate trial and projected it on the complex exponential ϕ . Carrying out the procedure 1,000 times generated a null distribution for K , assuming no direction tuning. We used the percentile of the true K as the p value for direction tuning (Baden et al., 2016).

Orientation selectivity (OS) was assessed in an analogous way. However, we used the complex exponential $\phi_k = \exp(2i\alpha_k)$, corresponding to the second Fourier component.

Signal deconvolution

Comparing neural activity measured with different methods (i.e., spikes versus Ca^{2+} signals; different Ca^{2+} indicators) is a non-trivial task. To assign dLGN-p RGCs to previously characterized RGC types, we needed account for the fact that the different Ca^{2+} indicators used (OGB-1 versus GCaMP6f) have different kinetics (Chen et al., 2013). We decided to convert both signals to a “common currency,” by deconvolving both signal types using Ca^{2+} kernels calculated for each indicator separately, using Ca^{2+} recordings of multiple ROIs ($n_{\text{OGB-1}} = 327$; $n_{\text{GCaMP6f}} = 19$) to the white noise stimulus, and averaging thresholded Ca^{2+} peak events ($> 80\%$ of the maximum normalized activity). The kernel area under the curve was normalized to 1 (Figure S3). These kernels were then used to deconvolve the respective calcium signal types.

Response quality index (Qi)

To measure how well a cell responded to a stimulus (local and full-field chirp, flashes), we computed the Qi, a signal-to-noise ratio, as a selection criterion:

$$Q_i = \frac{\text{Var}[\langle \mathbf{C} \rangle_r]_t}{\langle \text{Var}[\mathbf{C}]_t \rangle_r}$$

where \mathbf{C} is the T by R response matrix (time samples by stimulus repetitions), while $\langle \rangle_x$ and $\text{Var}[\]_x$ denote the mean and variance across the indicated dimension, respectively (Baden et al., 2016). If all trials are identical, such that the mean response is a perfect representative of the response, Q_i is equal to 1. If all trials are completely random with fixed variance (so that the mean response is not informative about the individual trial responses at all), Q_i is proportional to $1/R$. For further analysis, we used only cells that responded well to the chirp and/or to the moving bar stimulus ($Q_{i_{\text{chirp}}} > 0.45$ or $Q_{i_{\text{DS}}} > 0.6$; Baden et al. 2016). Of the original $n = 581$ ROIs, $n = 251$ ROIs passed this criterion (Figure S2).

Match index (Mi) for dLGN-p RGC type assignment

The pre-processed ROI traces of dLGN-p RGCs ($n = 251$) were assigned to the functional RGC population clusters reported by Baden et al. (2016), by identifying for each dLGN-p cell the cluster with the best matching response properties. After deconvolution with the respective Ca^{2+} kernel (see above), we calculated the linear correlation coefficients r between a dLGN-p cell's mean trace (over trials)

and all cluster mean traces (over all cells in an RGC population cluster) for the chirp stimulus (r_{chirp}) and the moving bar stimulus (r_{bar}). To combine the information about stimulus-specific correlations (r_{chirp} and r_{bar}), weighted by stimulus-specific cell response quality ($Q_{i_{chirp}}$ and $Q_{i_{bar}}$), we generated an overall match index (M_i) of each dLGN-p cell to all RGC population clusters:

$$M_i = \frac{Q_{i_{chirp}}}{Q_{i_{chirp}} + Q_{i_{bar}}} * r_{chirp} + \frac{Q_{i_{bar}}}{Q_{i_{chirp}} + Q_{i_{bar}}} * r_{bar}$$

Finally, each dLGN-p cell was assigned to the cluster with the highest M_i .

Cluster proportions in dLGN-p RGCs and RGC-all

We used a binomial test to assess the statistical significance of deviations of cluster cell numbers in the dLGN-p RGCs subpopulation compared to the RGC-all population. Starting with a total dLGN-p RGC cell number $n_{dLGN-p\ RGC} = 251$, for each dLGN-p RGC cluster i , we computed the test parameters $k_i =$ “number of cells cluster i in dLGN-p RGC population,” and $p_i =$ “proportion of cells in cluster i in the RGC-all population” ($n_{RGC-all} = 5024$), where p_i would be the expected proportion, or probability, of cells in that cluster if it were the same as in the RGC-all cluster. We then performed a two-tailed binomial test of obtaining a cell number deviation that extreme given the null hypothesis of equal cluster cell numbers in the two populations. After p value correction for false discovery rate (FDR, Benjamini-Hochberg), p values were considered significant at the significance level $alpha = 0.01$.

For the \log_2 -ratio (% dLGN-p RGCs / % RGC population) plot, we used additive smoothing of the histogram, i.e., by adding one to each group’s cell count n per default and normalizing the group cell counts by $n+k$, where k is the number of clusters.

Linear feedforward model

For modeling dLGN responses as a linear combination of weighted RGC types, we used RGC-all cluster means (Baden et al., 2016) only of those clusters that were assigned at least two cells from our dLGN-p RGC data (Figure S2). The spike dataset recorded in dLGN was smoothed, down-sampled and convolved with an artificial OGB-1 kernel to allow for a direct comparison of the dLGN traces with the dLGN-p RGC Ca^{2+} responses. We then modeled dLGN responses as a linear combination of weighted RGC inputs (Figure S2). The weights were computed, using a linear-regression algorithm (*lsqlin*, MATLAB) with a non-negativity constraint, and then applied to their respective RGC population cluster responses, yielding the optimal prediction of the dLGN cell response. The non-negativity constraint is motivated by the non-negativity of feedforward excitatory connections between RGCs and dLGN. The model performance was cross-validated using repeated random sub-sampling with 1,000 repetitions. The trials were randomly shuffled and divided into a training set (50% trials) and a validation set (50% trials). Both sets thus contained unique trials with no duplicates. The training set was used to compute the weights and the performance of the model was evaluated on the validation set. In the end, a particular dLGN cell was modeled with the mean weights across all repeats, and the performance of the model represents the mean value across the repeats.

Functional characterization of dLGN responses

Data analysis was performed using MATLAB (The Mathworks, Natick, Massachusetts, USA; RRID:SCR_001622) and Python. Data were organized in a custom written schema using the relational database framework “DataJoint” (Yatsenko et al., 2015) (<https://datajoint.io>; RRID: SCR_014543).

Unit extraction and spike sorting

Wideband extracellular signals were digitized at 30 kHz (Blackrock microsystems, Blackrock Microsystems Europe GmbH, Hannover DE) and analyzed using the NManager software suite (Hazan et al., 2006), as described in detail in Erisken et al. (2014). The LFP was computed after downsampling to 1,250 Hz. To isolate single neurons from the linear arrays, we grouped neighboring channels into 5 equally sized “virtual octrodes” (8 channels per group with 2 channel overlap for 32 channel probes). Using a median-based automatic spike detection threshold multiplied by a factor of 1.5, spikes were extracted from the high-pass filtered continuous signal for each group separately. The first three principal components of each channel were used for semi-automatic isolation of single neurons with KlustaKwik. Clusters were manually refined with Klusters (Hazan et al., 2006). We assigned each unit to the contact with the largest waveform. Units were given a subjective quality score by the manual sorter, the firing rate, the cleanness of the refractory period, and the stability over time. To avoid duplication of neurons extracted from linear probe recordings, we computed cross-correlation histograms (CCHs, 1 ms bins) between neuron pairs from neighboring groups. Pairs for which the CCH’s zero-bin was three times larger than the mean of non-zero-bins were considered to be in conflict. For each conflicting pair, the cell with the best score was kept. Conflicts across pairs were resolved by collecting all possible sets of cells and by keeping the set with the best total score.

Chirp quality index

We used the chirp quality index as a selection criterion that determines whether a dLGN neuron was visually driven by the full-field chirp. We separated the stimulus into two segments (e.g., separated a 32 s stimulus into two 16 s segments), and computed the

average between-trial correlations (CCs) (responses binned at the stimulus frame rate) within segment and between segments. Only those cells that had significantly higher within-segment CCs ($Q_{i_{chirp}}$, $p < 0.01$, Wilcoxon rank sum test) and firing rate > 1 spike/s were considered to be visually responsive.

STFO correlation value

The STFO correlation value was a further unit selection criterion to assure neuronal response stability and to determine whether there were neurons that did not respond to the full-field chirp stimulus. We played the STFO stimulus directly before and after the chirp stimulus and performed linear regression analysis (Figure S7). To determine how well the model predicts the data, we computed a correlation value R :

$$R = \sqrt{1 - \frac{\sum_{i=1}^n (y_i - \hat{y}_i)^2}{\sum_{i=1}^n (y_i - \bar{y})^2}}$$

where \hat{y} represents the calculated values of y and \bar{y} is the mean of y .

For further analysis, we used only cells that responded well to the chirp stimulus ($Q_{i_{RF}} \geq 0.05$ and $Q_{i_{chirp}} \leq 0.001$) or had a high STFO correlation value ($R > 0.65$, Figure S2).

Receptive field mapping

Receptive fields were mapped by reverse correlating unit activity to the sparse noise stimulus and fitting the center of a two-dimensional ellipse / 2D-Gaussian for both ON- and OFF-fields:

$$f(x, y) = \frac{A}{2\pi ab} \exp\left(-\frac{x'^2}{2a^2} - \frac{y'^2}{2b^2}\right)$$

where A is the maximum amplitude, a and b are half-axes of the ellipse, and x' and y' are transformations of the stimulus coordinates x and y , considering the angle θ and the coordinates of the center (x_c, y_c) of the ellipse. For each contact, we computed a single RF center by averaging coordinates of the best-fit ON and OFF subfield (explained variance $> 70\%$).

Contrast response function

Contrast responses were fitted with a hyperbolic ratio function:

$$r_c = r_0 \frac{r_{max} * c^n}{(c_{50}^n + c^n)}$$

with baseline response r_0 , responsiveness r_{max} , semi-saturation contrast c_{50} , and exponent n .

Tuning

Orientation tuning curves were fitted with a sum of two Gaussians with peaks θ_{pref} and $\theta_{pref} - \pi$ of different amplitudes A_1 and A_2 but equal width σ , with a constant baseline r_0 . For each neuron, spatial and temporal frequency tuning curves were taken at its preferred direction; orientation and direction-tuning curves were taken at its optimal spatial and temporal frequencies.

Direction selectivity

Direction selectivity index (DSI) was calculated as the ratio of

$$DSI = \frac{r_{pref} - r_{opp}}{r_{pref} + r_{opp}}$$

where r_{pref} was the response at the preferred direction and r_{opp} was the response at the opposite direction. We additionally assessed the statistical significance of direction tuning using a permutation test (Ecker et al., 2014) as described above.

Orientation selectivity

Orientation selectivity index (OSI) was computed as:

$$OSI = \frac{r_{pref} - r_{ortho}}{r_{pref} + r_{ortho}}$$

where r_{pref} is the response to the preferred orientation and r_{ortho} is the response to the orthogonal orientation.

Non-negative matrix factorization (NNMF)

NNMF decomposes a matrix A into two low-rank non-negative matrices U and V^T , representing elementary components and their weights (Lee and Seung, 1999). In the case of our dLGN cell responses, this translates into finding a set of time-varying visual response components from which cell responses can be reconstructed as a weighted combination of those components. Given a

positive matrix A of size $N \times M$ (neuron \times time) and a desired number of features k , the NNMF algorithm iteratively computes an approximation $A \sim UV^T$, where U and V^T are non-negative matrices with respective sizes $N \times k$ (neuron \times weight) and $k \times M$ (component \times time).

To determine the optimal number of components k , we applied NNMF cross-validation (Williams et al., 2018), also described by Alex H. Williams on <http://alexhwilliams.info/itsneuronalblog/2018/02/26/crossval/> and implemented on <https://gist.github.com/ahwillia/65d8f87fcd4bded3676d67b55c1a3954>. Analogous to cross-validation in supervised learning settings, NNMF cross-validation splits the data into a training and a test set in order to compare model performance on both sets and uses decreasing test set performance as a function of k as an indicator of model overfitting. In contrast to supervised settings, data entries cannot simply be held out for entire rows or columns as this would not allow to fit all parameters. Here, this problem was overcome by randomly holding out individual data entries from the data matrix and using the remaining data entries as training set. Formally, we define a binary matrix M , which acts as a mask over our data. The results in the following optimization problem:

$$\underset{U, V}{\text{minimize}} \|M \circ (UV^T - A)\|_F^2$$

The optimization problem amounts to the low-rank matrix completion problem which was solved by alternating minimization of the above equation for U and V^T . The model error can then be evaluated on the held-out data points as follows:

$$\|(1 - M) \circ (UV^T - A)\|_F^2$$

We fitted NNMF models on the training data for ranks (= number of components k) 1 to 70, and compared the mean squared error (MSE) for the training versus the validation set. Due to the random model initialization for each run, this was done with $n_{\text{repeats}} = 200$. The optimal number of components was determined as the rank with the minimal average MSE over all runs $\pm 5\%$.

The resulting components were organized into a hierarchical cluster tree by a single linkage algorithm using Euclidean distances and the Ward's minimum variance method. The results were plotted using the dendrogram function and the leaf order was optimized using the MATLAB function *optimallleaforder*.

Analysis of visual field coverage

To compute visual field coverage for dLGN recordings, we used the envelope of multi-unit activity (MUAe) to the sparse noise stimulus. To do so, we full-wave rectified the median-subtracted, high pass filtered signals, before low-pass filtering (200 Hz) and down-sampling to 2000 Hz (Supèr and Roelfsema, 2005). To compute RF maps, we used average MUAe between 0 to 150 ms after stimulus onset (Figure S6A). To identify channels within the dLGN, we collapsed the MUAe RF map amplitudes for each channel across the x-dimension and range-normalized collapsed amplitudes. Channels with normalized amplitudes higher than an empirically set threshold (0.39) were included for further analysis. Non-detected channels located between detected channels were added. This procedure was evaluated against manually labeled ground truth data (using the Python Sloth GUI, <https://sloth.readthedocs.io/en/latest/>). We calculated RF centers as the location of the peaks of normalized amplitudes in x and y (Figures S6B and S6C). Since the distribution of DS cells has been suggested to vary between dLGN shell and core, we examined DS in a subpopulation of our recorded dLGN neurons with localized RFs and stable responses to the drifting gratings flanking the chirp stimulus ($n = 243$ cells). To test for the distribution of DSI as a function of RF location (Figure S6D), we extracted recorded units whose peak spike amplitude occurred at the identified RF-containing channels. To test for the distribution of DSIs as a function of dLGN depth, we compared DSIs of neurons in the top dLGN channel against the rest of the population (Figure S6E).

DATA AND SOFTWARE AVAILABILITY

The essential code and data to reproduce the analyses presented is available on <http://retinal-functomics.net/>.

Neuron, Volume 102

Supplemental Information

**Mouse dLGN Receives Functional Input
from a Diverse Population of Retinal Ganglion
Cells with Limited Convergence**

Miroslav Román Rosón, Yannik Bauer, Ann H. Kotkat, Philipp Berens, Thomas Euler, and Laura Busse

SUPPLEMENTAL FIGURES

1. Injection histology

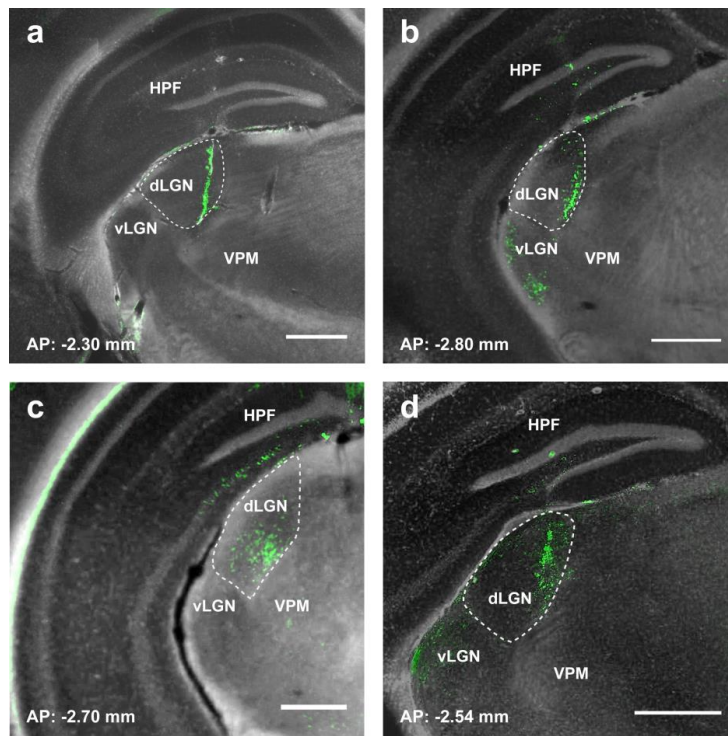


Figure S1. Related to Figure 1 | Histology of virus injections. Coronal sections at the injection site of a Cre-encoding retrograde Herpes Simplex Virus 1 (LT HSV-hEF1 α -cre) (Neve, 2012) for the four floxed GCaMP6f mice (a-d) that passed the criteria of injections being local and targeted to dLGN (green, GCaMP6f; grey DAPI). While the histological analysis provides evidence for retrograde viral labeling in both dLGN shell and core, more RGC terminals are expected to be transduced in the core than the shell due to the large volume difference between these two structures. Scale bars: 500 μ m; AP: anterior-posterior section coordinate (Paxinos et al., 2004); dLGN: dorsolateral geniculate nucleus; vLGN: ventrolateral geniculate nucleus; VPM: ventral posteromedial nucleus of the thalamus; HPF: hippocampal formation.

2. Overview of analysis steps

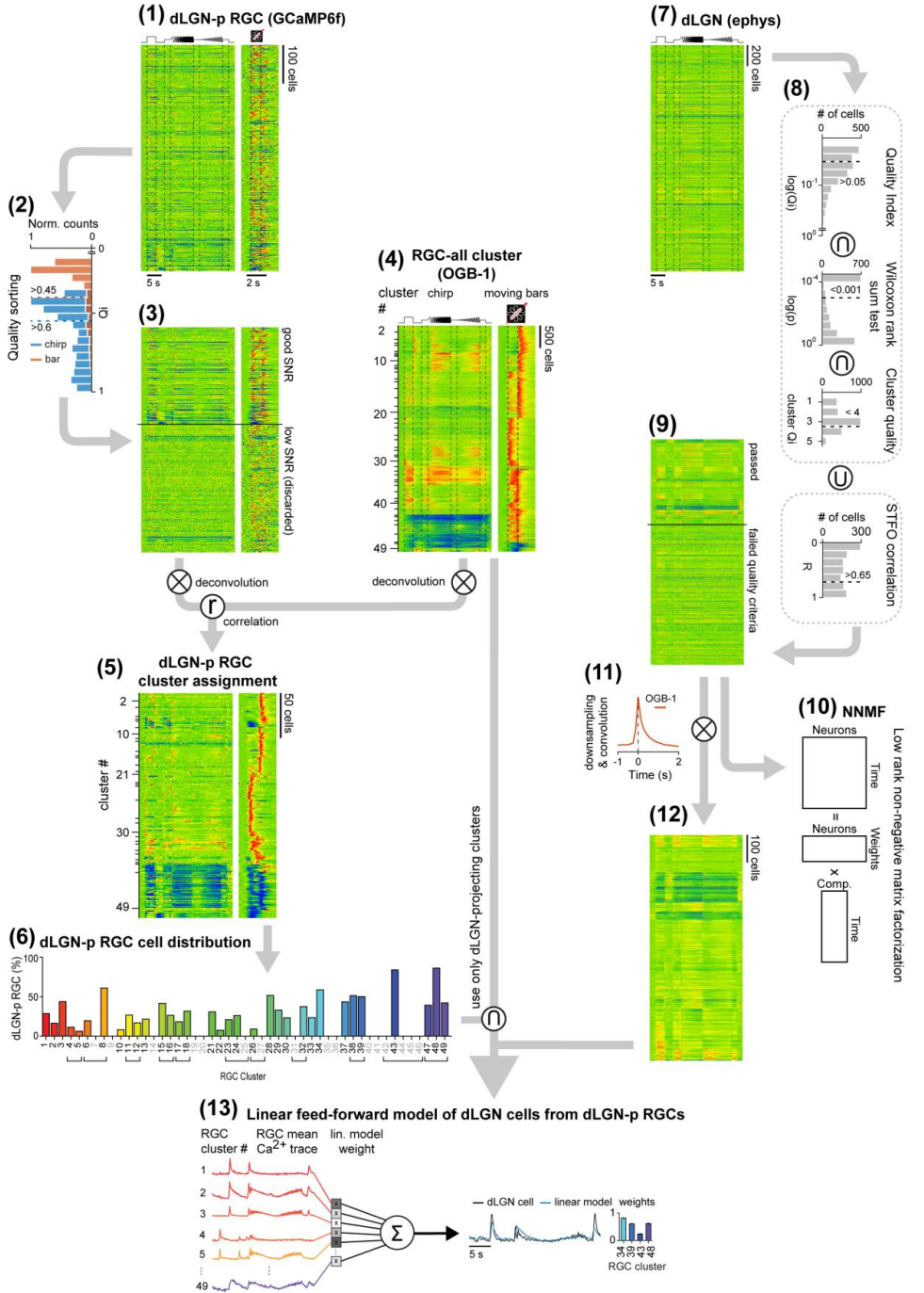


Figure S2. Related to STAR Methods | Processing pipeline. (1) Heat maps of dLGN-p RGC Ca²⁺

responses to the to the chirp and the moving bar stimulus (n = 581, recorded with genetically encoded Ca²⁺-indicator GCaMP6f, responses sorted by experimental day). Each line represents the responses of an individual cell (activity color-coded, with warmer colors representing increased activity). **(2)** Histogram of cell quality indices (Q_i) to chirp and bar stimulus. Only cells with Q_i > 0.45 for the chirp and with Q_i > 0.6 for the bar stimulus were considered for further processing. (Methods) **(3)** Heat maps of dLGN-p RGC responses passing (top, n = 251) or failing (bottom, n = 330) the Q_i-thresholds, sorted by Q_i. **(4)** Heat maps (like in **(1)**) of Ca²⁺ responses for all RGC clusters ("RGC-all" from (Baden et al., 2016), recorded with Ca²⁺-indicator OGB-1, n = 49 clusters). Responses are sorted by cluster index, with the height of a cluster 'block' representing the number of individual cells. **(5)** Heat maps of dLGN-p RGCs after the cluster assignment to RGC-all clusters, including trace deconvolution and trace correlation (Methods). The height of each cluster represents the number of included cells. **(6)** Distribution of dLGN-p RGCs per RGC-all cluster based on the cell cluster assignment. **(7)** Heat map of dLGN cell responses to chirp stimulus (responses sorted by experimental day). **(8)** Histograms of quality criteria, including, from top to bottom, quality index, Wilcoxon rank sum test for equal medians, cluster quality values, and STFO correlation values as computed by the linear regression analysis from two STFO stimuli played before and after the chirp. Cells had to be either above each of the top three quality criteria thresholds or the bottom one to pass into the analysis dataset. **(9)** Heat maps of dLGN cell responses that passed (top, n = 814) or failed (bottom, n = 1,376) the quality criteria, sorted by quality criteria values. **(10)** Schematic of the low-rank non-negative matrix factorization (NNMF), which was applied on the dLGN cell data from **(9)** Each neuron response is considered to be composed of particular temporal response components multiplied by neuron-specific weights. **(11)** OGB-1 Ca²⁺-kernel used for the convolution of dLGN spike traces into simulated OGB-1 Ca²⁺ traces (after down-sampling) with their characteristically slower Ca²⁺ response kinetics. This preprocessing step was applied so that the dLGN data better match the RGC data for the subsequent dLGN-model. **(12)** Heat map of dLGN responses after downsampling and convolution. **(13)** Illustration of the linear feedforward model of single dLGN cell responses from dLGN-p RGC cell types. The model is restricted to using only RGC clusters that received cell assignments in the dLGN-p RGC data set. It then predicts individual dLGN cell responses as a linear combination of weighted mean RGC-all cluster responses. Right of black arrow: Sample dLGN response (black) and its linear prediction (blue), and bar plot of contributing RGC-all cluster weights.

3. Deconvolution of retinal two-photon Ca^{2+} -traces

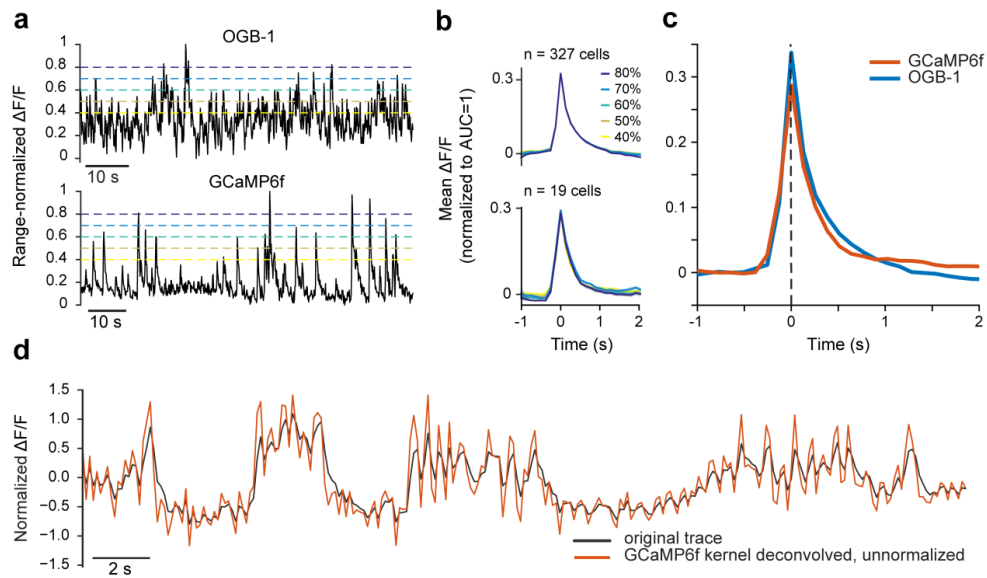


Figure S3. Related to Figure 2 | Deconvolution of retinal two-photon Ca^{2+} -traces. **a**, Raw traces to binary white noise stimulus with various calcium event thresholds (top: OGB-1; bottom: GCaMP6f). **b**, Extracted mean Ca^{2+} event kernels for OGB-1 (top) and GCaMP6f (bottom) for thresholds shown in (a). **c**, Superposition of OGB-1 and GCaMP6f kernels. **d**, Example GCaMP6f trace (in black), and deconvolution with the GCaMP6f kernel (orange).

4. Match index

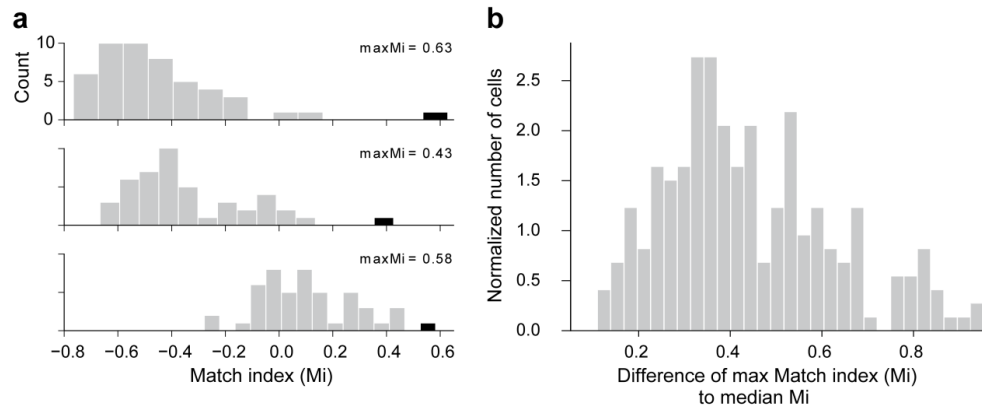


Figure S4. Related to Figure 2 | Statistics of match index (Mi). **a**, Some dLGNp-RGCs have a maximal MI, used for cluster assignment, which is considerably different from the match indices computed for the remaining clusters (top). Other dLGNp-RGCs, however, have a maximal match index closer to the match indices for some of the other clusters (middle and bottom). This is not surprising, as the responses of RGC clusters are not orthogonal to each other but can share general features, such as ON or OFF selectivity. **b**, Yet, assignments based on maximal MI are meaningful: the distribution of match indices for each individual dLGNp-RGC does have considerable variance, such that the median match index for each dLGNp-RGC is substantially different from that for the best-matching cluster.

5. Cluster assignment of dLGN-projecting RGCs

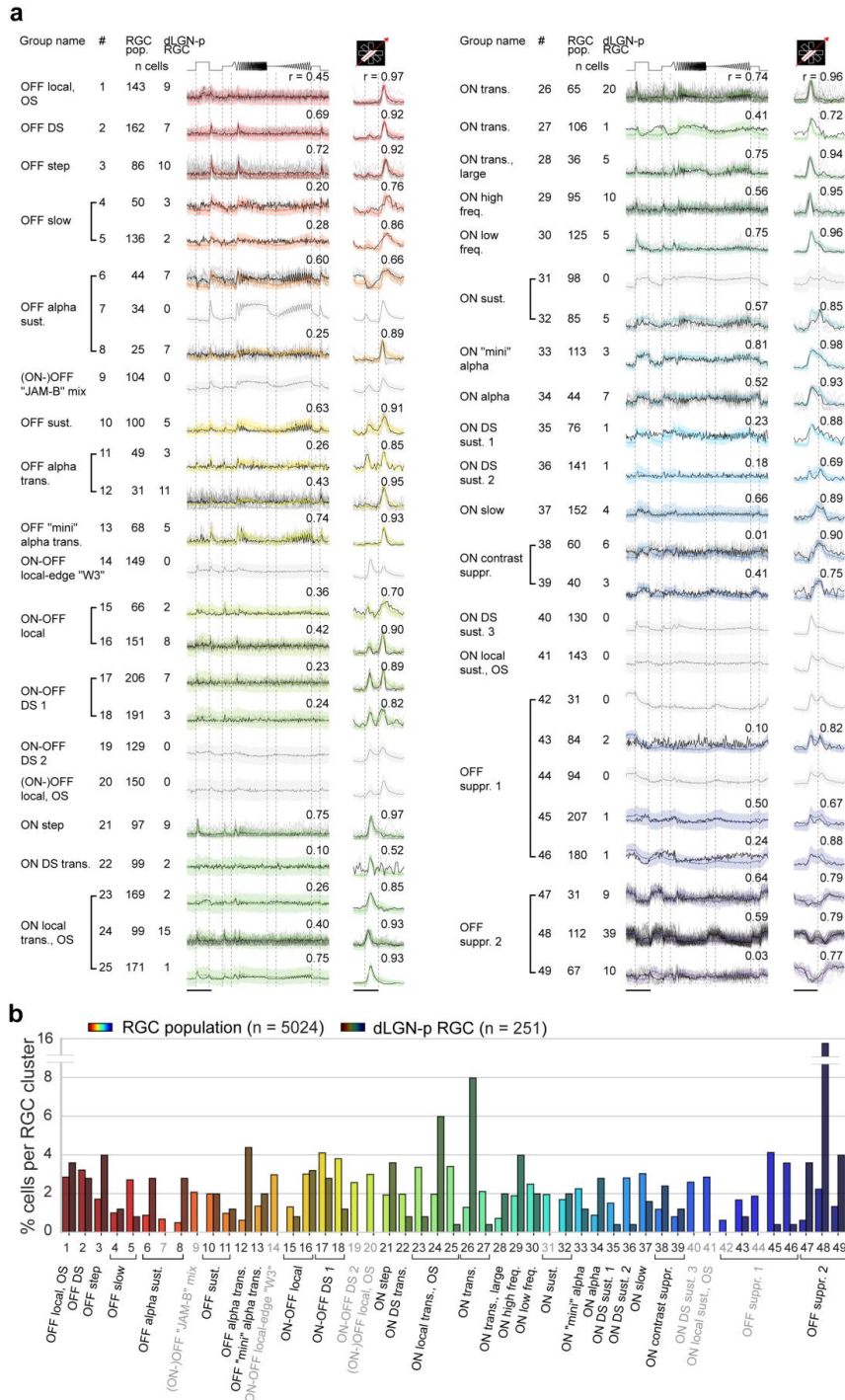


Figure S5. Related to Figure 2 | dLGN-p RGC cluster assignments. a, All dLGN-p RGC cluster

responses (grey: single RGCs; black: cluster mean), along with assigned RGC population cluster response mean (color) and SD (colored area). RGC population clusters that were not assigned any dLGN-p RGCs are greyed out. Scale bars: chirp stimulus: 5 s; moving bar stimulus: 2 s. **b**, Percentage of cells per RGC cluster for dLGN-p RGCs (dark colors) and all RGCs obtained from (Baden et al., 2016) (saturated colors).

6. Receptive field coverage of the recorded dLGN population

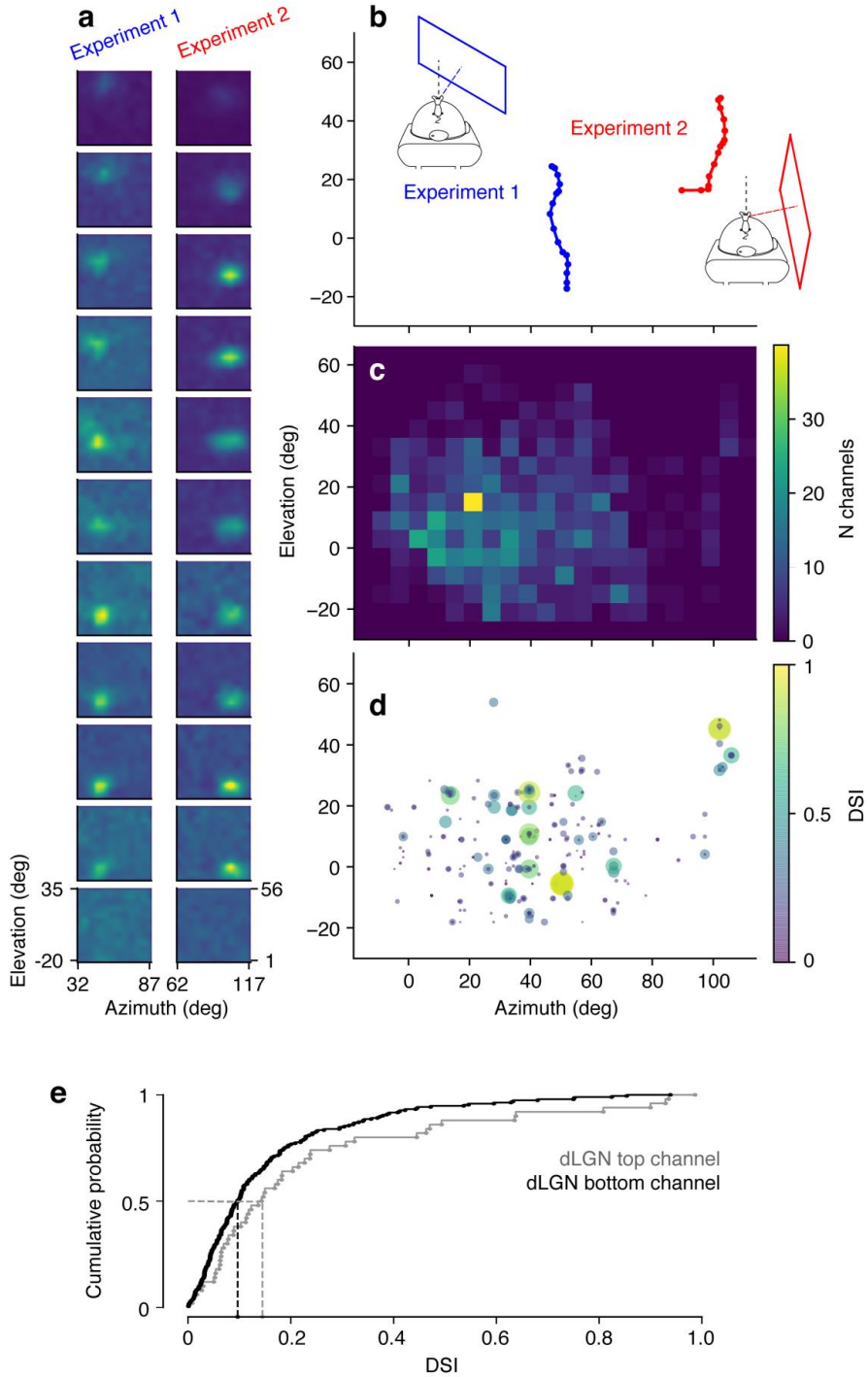


Figure S6. Related to Figure 3 | Receptive field coverage of the recorded dLGN population. a,

Multiunit RF maps for selected channels along the linear probe in two example experiments. Several top and bottom channels do not show clear RFs, indicating that the corresponding channels are likely outside of dLGN. **b**, RF center locations for the two example experiments. **c**, Coverage of RF centers across experiments. **d**, Distribution of DSI as a function of RF location. **e**, Comparison of DSI distributions of dLGN cell subpopulations located in the top or the bottom channels (Kolmogorov-Smirnov-Test, $p = 0.085$).

7. Responses of dLGN neurons to grating stimuli presented before and after the chirp stimulus

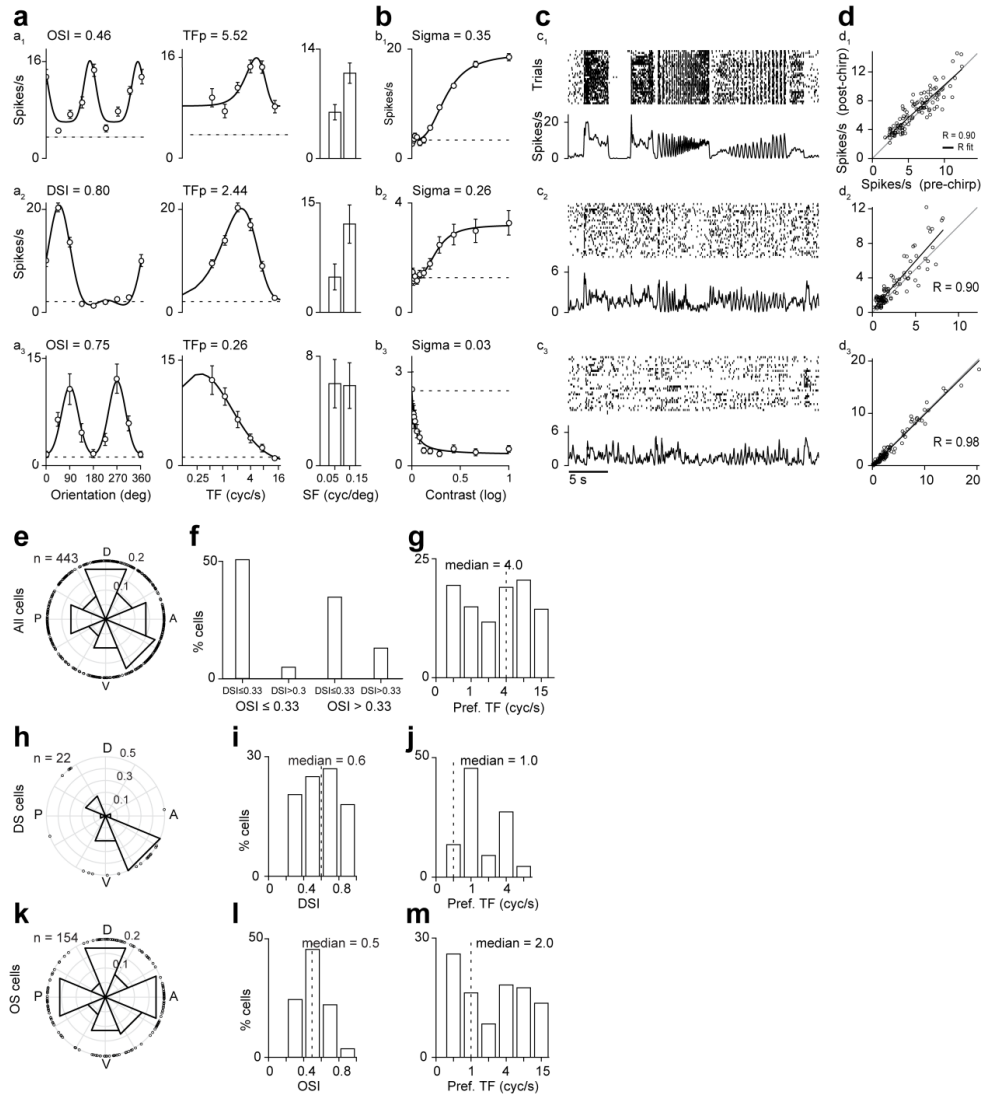


Figure S7. Related to Figure 3 | dLGN responses to drifting gratings. **a-d**, Responses of three example dLGN cells to the full stimulus set. **a**, Mean firing rates and fitted tuning curves (red) for orientation, spatial frequency, and temporal frequency. **b**, Same as **a**, for contrast response functions. **c**, Responses to the chirp stimulus. **d**, Scatter plot of average firing rates across all conditions of the drifting grating stimuli presented before and after the chirp stimulus, used to determine the stability of the recorded cells. We chose $R > 0.65$ as criterion to determine that a dLGN neuron was stable over time. **e-g**, Population data for direction and orientation selectivity: Distribution of preferred direction of motion for all responsive dLGN neurons ($n = 443$) (**e**); percentage of direction/orientation-selective cells, with a cut-off of 0.33 for DSI and OSI (**f**);

distribution of preferred temporal frequencies (g). **h-j**, Same as (e-g), for DS cells (n = 22). **k-m**, Same as (e-g), for OS cells (n = 154).

8. Locomotion

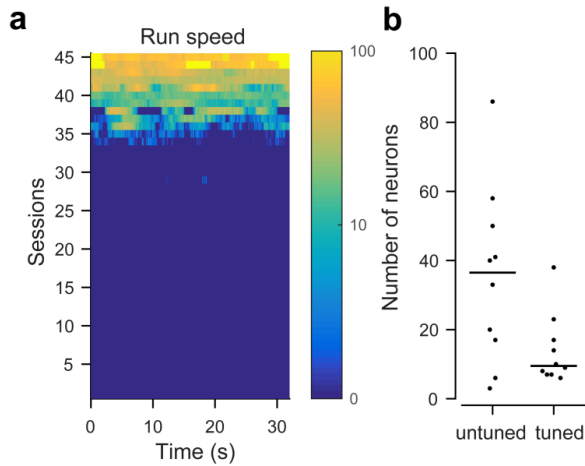


Figure S8. Related to Figure 3 | Locomotion and run speed tuning of dLGN neurons. **a**, Average run speed (cm/s) per recording session as a function of time during the chirp stimulus. Locomotion speed was computed as the Euclidean norm of three perpendicular components of ball velocity (Dombeck et al., 2007). **b**, Number of neurons untuned and tuned for running speed per animal ($n = 10$ mice). We determined speed tuning as previously described in (Saleem et al., 2013). In brief, speed traces were smoothed with a Gaussian filter ($\sigma = 150$ ms), re-sampled at 60 Hz, and binned such that each bin contained equal amounts of time (> 30 s). Unsmoothed neural responses were binned at 60 Hz. Neurons were considered speed modulated if the variance of mean responses across bins was greater than 99.9% of the variance of shuffled responses ($p < 0.001$).

9. Assessment of model limitations

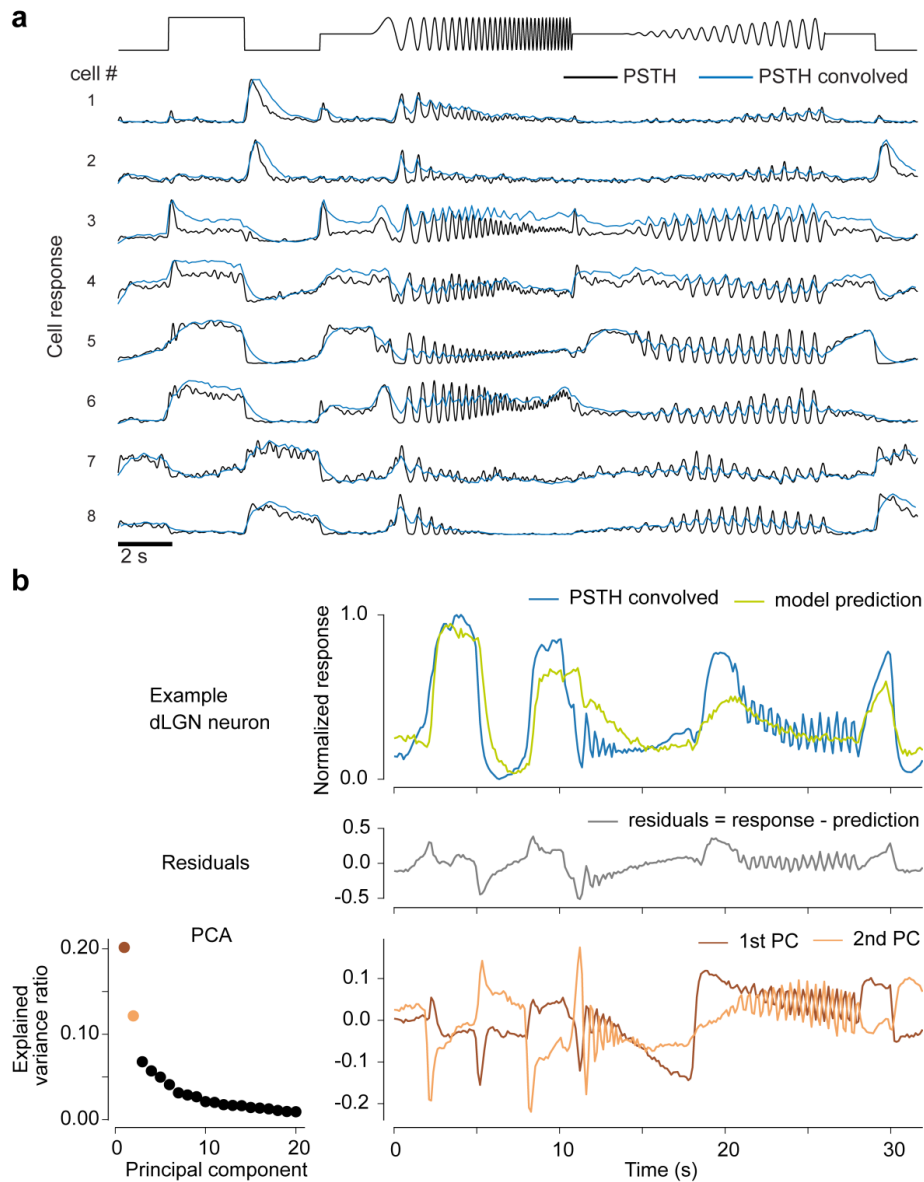


Figure S9, Related to Figure 5 | Filtering by convolution with Ca^{2+} -kernel and systematic model prediction errors. **a**, Mean responses of 8 example dLGN cells to the chirp stimulus before (SDF, black) and after convolution with the OGB-1 Ca^{2+} -kernel extracted from retinal two-photon imaging data (blue). Top: time course of luminance changes in the chirp stimulus. **b**, Top: Responses (blue) and model predictions (green; linear feedforward, positive weights) for an example dLGN neuron. Middle: Difference between data and model prediction. Bottom, left: Explained variance ratio for PCA components computed on the residuals for the entire population of recorded dLGN cells. Bottom, right: First and second principal components.

10. Comparing distributions of dLGN-p RGC and model RGC types

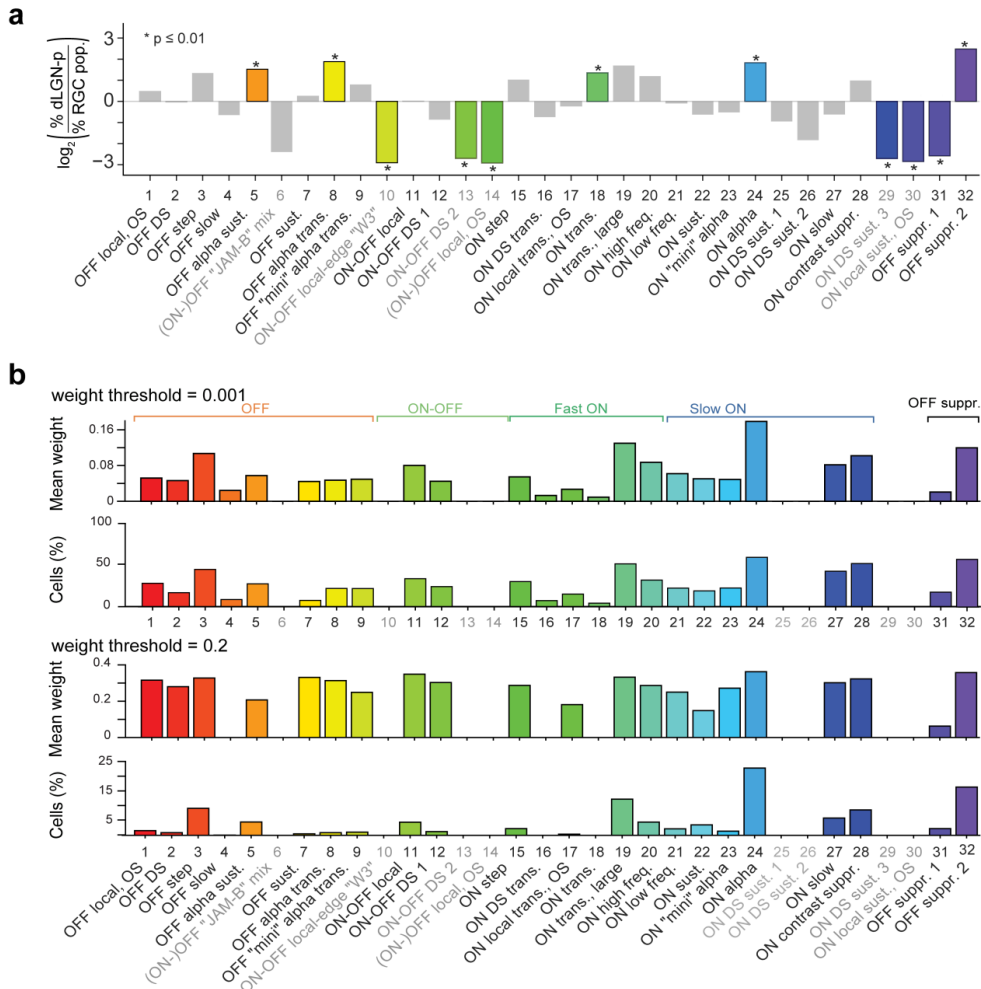


Figure S10. Related to Figure 5 | Comparing distributions of dLGN-p RGC types and model RGC types. For easier comparison, the figure panels from Figure 2d and Figure 5e are shown together. **a**, Copy of Figure 2d. Comparison of cell-per-group percentages as log₂-ratio (%dLGN-p RGCs / %RGC-all). Significant differences in cell proportions ($p < 0.01$; binomial test) are marked as colored bars and with asterisks. **b**, Copy of Figure 5e. Distribution of RGC groups from Baden et al. (2016) used for reconstructing the population of dLGN cell responses, shown as mean weight and percentage of dLGN cells (top: weight threshold = 0.001, bottom: weight threshold = 0.2). RGC types not projecting to dLGN are greyed-out.

SUPPLEMENTAL TABLE

T1. Comparison of current data with the literature

transgenic line or marker	dLGN projections	reference	RGC name	group	cluster	dLGN-p in current dataset
JAM-B-CreER	yes	(Kim et al., 2008, 2010)	JAM-B	6?	9?	no?
FSTL4-CreER	yes	(Kay et al., 2011; Kim et al., 2010)	ON-OFF DS 1	12	17, 18	yes
Drd4-GFP	yes	(Huberman et al., 2009; Kay et al., 2011)	ON-OFF DS 1	12	17, 18	yes
TRHR-GFP	yes	(Rivlin-Etzion et al., 2011)	ON-OFF DS 1	12	17, 18	yes
CB2-GFP	yes	(Huberman et al., 2008)	OFF alpha transient	8	11, 12	yes
Opn4-Cre	yes	(Ecker et al., 2010; Estevez et al., 2012; Schmidt et al., 2014)	ON alpha	24	34	yes
Foxp2	yes	(Rouso et al., 2016)	?	?	?	?
TYW3	no	(Kim et al., 2010; Zhang et al., 2012)	W3	10	14	no
TYW7	no	(Kim et al., 2010)	OFF alpha sust.	5	7?	no?
Hoxd10-GFP	no	(Dhande et al., 2013)	ON DS sust. 1	25	35	no
Hoxd10-GFP, Spig1-GFP	no	(Dhande et al., 2013; Yonehara et al., 2008, 2009)	ON DS sust. 2/3	26, 29	36, 40	no
Hoxd10-GFP	no	(Dhande et al., 2013)	ON-OFF DS 2	12, 13	19	no
CCK-Cre, PCP2-Cre	(yes)	(Ivanova et al., 2013; Zhu et al., 2014)	SbC (CCK-1 / s-BGC) +others	32	47-49	yes

Table S1. Comparison of current data with the literature, related to Figure 5. Table showing putative correspondences between previously studied transgenic lines/markers for subgroups of RGCs following (Dhande et al., 2015) and our functional RGC groups/clusters demonstrates an overall good match of our assignments of dLGN-p RGC groups with the literature. In case of JAM-B RGCs, there is a group labeled “ON-OFF JAM-B mix” in Baden et al. (2016), which is assigned no dLGN-p cells. However, it is uncertain whether this group really corresponds to JAM-B cells, which seem to be poorly responding to the stimulus set. For FSTL4, Drd4 and TRHR-cells, we chose ON-OFF DS1 as corresponding group in Baden et al. (2016), since the RGC types marked in these three lines are all ON-OFF DS and project to dLGN, as do cells in group 12. Correspondences in case of the CB2- and Opn4-lines to OFF alpha transient and ON alpha RGCs were based on the literature and the projection patterns matched well. We could not identify a match for Foxp2-RGCs. TYW3 cells were clearly identified in Baden et al. (2016) and were not among dLGN projecting RGCs. A subpopulation

labeled W7A of TYW7 cells seems to correspond to OFF alpha sustained RGCs and does not project to dLGN. Interestingly, there was a cluster in the group labeled “OFF alpha sustained” in Baden et al. (2016) which was not assigned any dLGN-p cells. It is possible that the “OFF alpha sustained” group consists of heterogeneous RGC types. Alternatively, W7A cells are not “OFF alpha sustained” RGCs and all alpha RGCs project to dLGN. The three types of ON DS sustained in the Hoxd10 line do not project to the dLGN, and neither do the “ON DS sustained 1-3” groups in our data (although not for all of them the reduction in the representation is significant). Finally, the ON-OFF DS RGCs in the Hoxd10 line do not project to dLGN. Therefore, they most likely correspond to the ON-OFF DS 2 group of Baden et al. (2016), which is also not assigned any dLGN-p cells. While so far no SbC-exclusive lines is known, evidence from two transgenic mouse lines with multiple labeled RGCs suggest that at least one type of SbC project to the dLGN core (Ivanova et al., 2013; Zhu et al., 2014).

CORTICOTHALAMIC FEEDBACK ELICITS ROBUST EFFECTS IN DLGN RESPONSES TO MOVIES

3.1 SPACEK ET AL. (2022)

SUMMARY: Neurons in the dorsolateral geniculate nucleus (dLGN) of the thalamus are contacted by a large number of feedback synapses from cortex, whose role in visual processing is poorly understood. Past studies investigating this role have mostly used simple visual stimuli and anesthetized animals, but corticothalamic (CT) feedback might be particularly relevant during processing of complex visual stimuli, and its effects might depend on behavioral state. Suppressing CT feedback via global V1 parvalbumin (PV) interneuron photoactivation, we find that CT feedback robustly modulates responses to naturalistic movie clips by increasing response gain and promoting tonic firing mode. Compared to these robust effects for naturalistic movies, CT feedback effects on firing rates were less consistent for grating stimuli. Finally, while CT feedback and locomotion affected dLGN responses in similar ways, we found their effects to be largely independent. We propose that CT feedback and behavioral state use separate circuits to modulate visual information on its way to cortex in a stimulus-dependent manner.

THE MANUSCRIPT WAS PUBLISHED AS:

Spacek, M. A., Crombie, D., Bauer, Y., Born, G., Liu, X., Katzner, S., & Busse, L. (2022). Robust effects of corticothalamic feedback and behavioral state on movie responses in mouse dLGN. *eLife*, 11, e70469. <https://doi.org/10.7554/eLife.70469>

CONTRIBUTION SUMMARY: Conceptualization, L.B. and M.A.S.; Methodology, M.A.S., D.C.; Software, M.A.S., S.K., D.C., G.B., Y.B., X.L.; Formal Analysis, S.K.; Investigation, M.A.S., Y.B., X.L.; Data Curation, M.A.S., G.B., D.C., S.K., L.B.; Writing – Original Draft, L.B., G.B.; Writing – Review & Editing, L.B., S.K., M.A.S., G.B., D.C.; Visualization, M.A.S., G.B., Y.B., S.K.; Supervision, L.B.; Project Administration, L.B.; Funding Acquisition, L.B.

PERSONAL CONTRIBUTIONS: Y.B. adapted the experimental method for direct L6 CT photosuppression with stGtACR2 in Ntsr1-Cre-mice to the Busse Lab (Fig1S4), and conducted a control experiment on an Ntsr1-Cre-negative mouse (Fig1S5). Y.B. also created Fig1b to illustrate the histological expression volume of Chr2 in V1 of PV-Cre mice.

Robust effects of corticothalamic feedback and behavioral state on movie responses in mouse dLGN

Martin A Spacek^{1*}, Davide Crombie^{1,2†}, Yannik Bauer^{1,2†}, Gregory Born^{1,2†}, Xinyu Liu^{1,2}, Steffen Katzner¹, Laura Busse^{1,3*}

¹Division of Neurobiology, Faculty of Biology, LMU Munich, Planegg-Martinsried, Germany; ²Graduate School of Systemic Neurosciences, LMU Munich, Munich, Germany; ³Bernstein Centre for Computational Neuroscience, Munich, Germany

Abstract Neurons in the dorsolateral geniculate nucleus (dLGN) of the thalamus receive a substantial proportion of modulatory inputs from corticothalamic (CT) feedback and brain stem nuclei. Hypothesizing that these modulatory influences might be differentially engaged depending on the visual stimulus and behavioral state, we performed in vivo extracellular recordings from mouse dLGN while optogenetically suppressing CT feedback and monitoring behavioral state by locomotion and pupil dilation. For naturalistic movie clips, we found CT feedback to consistently increase dLGN response gain and promote tonic firing. In contrast, for gratings, CT feedback effects on firing rates were mixed. For both stimulus types, the neural signatures of CT feedback closely resembled those of behavioral state, yet effects of behavioral state on responses to movies persisted even when CT feedback was suppressed. We conclude that CT feedback modulates visual information on its way to cortex in a stimulus-dependent manner, but largely independently of behavioral state.

*For correspondence: m.spacek@lmu.de (MAS); busse@bio.lmu.de (LB)

†These authors contributed equally to this work

Competing interest: The authors declare that no competing interests exist.

Funding: See page 26

Preprinted: 19 September 2019

Received: 18 May 2021

Accepted: 13 March 2022

Published: 22 March 2022

Reviewing Editor: Tatyana O Sharpee, Salk Institute for Biological Studies, United States

© Copyright Spacek et al. This article is distributed under the terms of the [Creative Commons Attribution License](https://creativecommons.org/licenses/by/4.0/), which permits unrestricted use and redistribution provided that the original author and source are credited.

Editor's evaluation

This paper will be of interest to neuroscientists interested in understanding the role of corticothalamic feedback in coding of sensory inputs. The authors show that feedback is stronger for natural stimuli compared to artificial stimuli. Surprisingly, the feedback from the cortex works in parallel with other modulatory influences reflecting changes in the arousal (measured here with pupil size) or changes in locomotion.

Introduction

Mammalian vision is based on a hierarchy of processing stages that are connected by feedforward circuits projecting from lower to higher levels, and by feedback circuits projecting from higher to lower levels. Feedforward processing is thought to create feature selectivity (*Lien and Scanziani, 2018; Hubel and Wiesel, 1962*) and invariance to low-level stimulus features (*Hubel and Wiesel, 1962; Chance et al., 1999; Riesenhuber and Poggio, 1999; Riesenhuber and Poggio, 2000*), to ultimately enable object recognition (*DiCarlo et al., 2012*). Hypotheses about the functional role of feedback circuits include top-down attention, working memory, prediction, and awareness (*Squire et al., 2013; Roelfsema and de Lange, 2016; Bastos et al., 2012; Lamme and Roelfsema, 2000; Takahashi et al., 2016; Larkum, 2013*). Compared to theories of feedforward processing, however, there is little consensus on the specific function of feedback connections (*Heeger, 2017; Gilbert and Li, 2013*).

Feedback in the mammalian visual system targets brain areas as early as the dorsolateral geniculate nucleus (dLGN) of the thalamus, where up to 30% of synaptic connections onto relay cells are established by corticothalamic (CT) feedback (Sherman and Guillery, 2002). Direct CT feedback is thought to arise from V1 layer 6 (L6) CT pyramidal cells (Briggs, 2010; Sillito and Jones, 2002), which are known for their notoriously low firing rates (Vélez-Fort et al., 2014; Stoelzel et al., 2017; Crandall et al., 2017; Oberlaender et al., 2012; Swadlow, 1989; Pausin and Krieger, 2018), their sharp tuning for orientation (Vélez-Fort et al., 2014; Liang et al., 2021), and their diverse signaling of behavioral state (Augustinaite and Kuhn, 2020; Liang et al., 2021). The action of CT feedback on dLGN activity is generally considered modulatory rather than driving (Sherman and Guillery, 1998), as CT feedback inputs contact the distal dendrites of relay cells via NMDA glutamate (Augustinaite et al., 2014) or mGluR1 metabotropic receptors (Godwin et al., 1996), implying rather slow and long-lasting effects on dLGN activity. Similar to other depolarizing inputs to dLGN, such as neuromodulatory brain stem inputs (McCormick, 1992), CT feedback has been linked to promoting switching from burst to tonic firing mode, and to facilitating transmission of retinal signals (Augustinaite et al., 2014; de Labra et al., 2007; Wang et al., 2006; Dossi et al., 1992). However, since L6 CT pyramidal cells provide both direct excitation and indirect inhibition of dLGN via the thalamic reticular nucleus (TRN) and dLGN inhibitory interneurons (Sillito and Jones, 2002; Usrey and Sherman, 2019), the effects of CT feedback are expected to be complex and dependent on temporal and spatial aspects of the stimulus (Crandall et al., 2015; Born et al., 2021; Murphy and Sillito, 1987; McClurkin and Marrocco, 1984; Jones et al., 2012; Hasse and Briggs, 2017).

Most of the previous in vivo studies have probed the functional role of CT feedback with artificial stimuli, and often in anesthetized animals; CT feedback, however, might be most relevant for processing of dynamic naturalistic information and during wakefulness. From a conceptual perspective, if the role of feedback was to provide context based on an internal model built from the statistics of the world (Berkes et al., 2011; Lee and Mumford, 2003; Rao and Ballard, 1999; Clark, 2013), natural stimuli would be expected to best comply with this model, and hence better drive these feedback mechanisms. Indeed, it has previously been suggested that CT feedback might be more strongly engaged for moving compared to stationary stimuli (Sillito and Jones, 2002), and for complex dynamic noise textures than simple moving bars (Gulyás et al., 1990), consistent with a potential role in figure-ground processing (Poltoratski et al., 2019; Sillito et al., 1993; Cudeiro and Sillito, 1996). Furthermore, since the responsiveness of feedback projections (Makino and Komiyama, 2015; Keller et al., 2020), including those originating from V1 CT neurons (Briggs and Usrey, 2011), seem to be strongly reduced by anesthesia, it is critical to examine CT feedback effects in awake animals. Indeed, L6CT neurons have recently been found to have diverse response modulations according to pupil-indexed behavioral state (Augustinaite and Kuhn, 2020).

Here, we recorded spiking activity in dLGN of awake mice and investigated how CT feedback affected dLGN responses to naturalistic movie clips. Suppressing CT feedback either via photostimulation of V1 parvalbumin-positive (PV+) inhibitory interneurons or via direct photosuppression of L6CT neurons, we found that CT feedback had consistent modulatory effects on dLGN responses to movie clips, which could largely be captured by an increase in gain. Effects of CT feedback on dLGN responses to grating stimuli were more diverse, highlighting the stimulus-dependency of CT feedback effects. Finally, while geniculate responses to movies during V1 suppression resembled those during quiescence, we found effects of CT feedback and behavioral state to be largely independent. Overall, our results demonstrate that neural responses to naturalistic movies en route to cortex can be robustly modulated by extra-retinal influences such as cortical feedback and behavioral state, which seem to be largely conveyed via different modulatory pathways.

Results

CT feedback robustly modulates dLGN responses to naturalistic movie clips

To investigate the impact of CT feedback on visual processing of naturalistic stimuli, we presented to head-fixed mice full-screen movie clips and compared responses of dLGN neurons during optogenetic suppression of V1 activity to a control condition with CT feedback left intact (Figure 1 and -Supplement 1). The responses of individual dLGN neurons to naturalistic movie clips were characterized by distinct

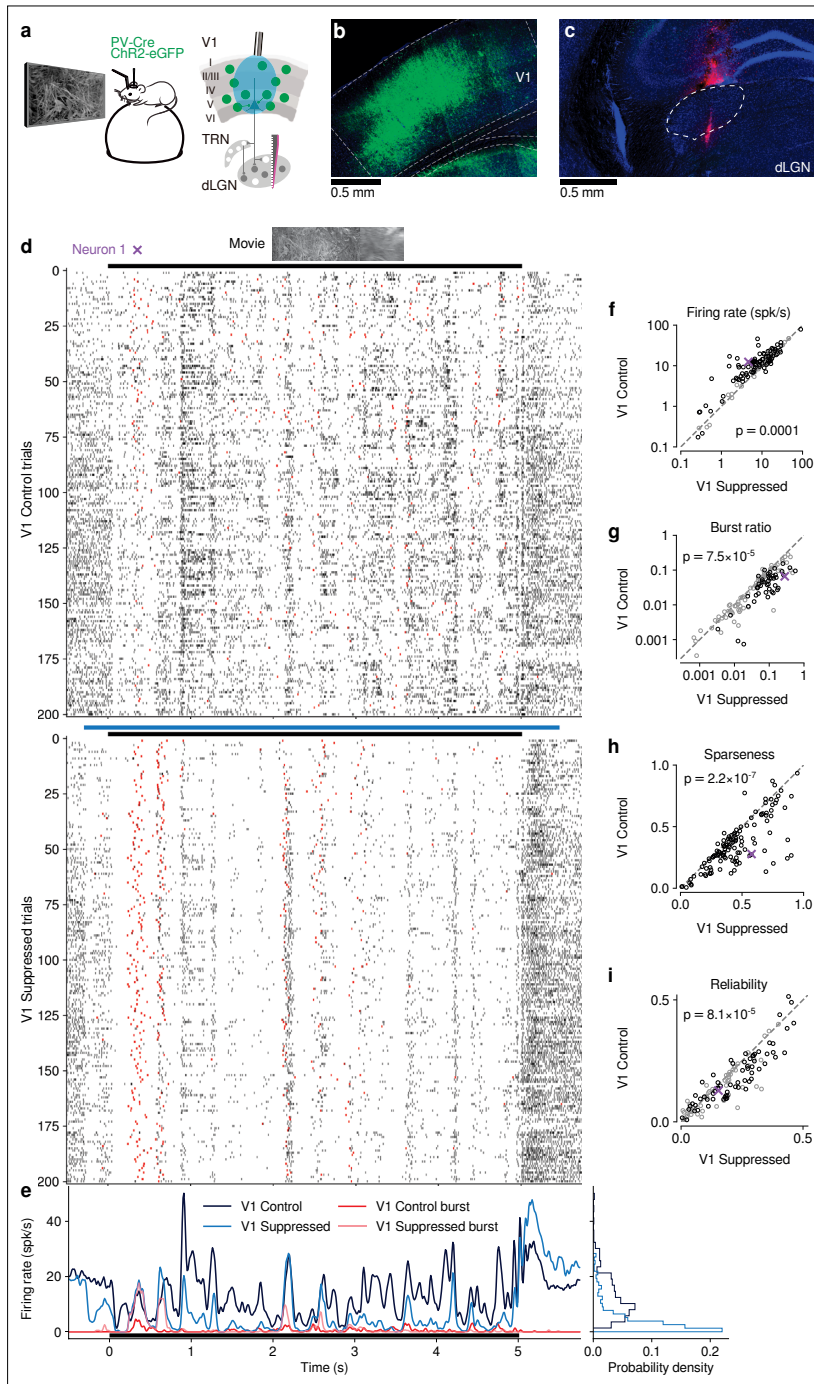


Figure 1. CT feedback modulates dLGN responses to full-screen naturalistic movie clips. (a) Left: Schematic of experimental setup. Head-fixed mice were placed on a floating Styrofoam ball and visual stimuli were presented on a screen located ~25 cm away from the animal. Right: Chr2 was conditionally expressed in PV + inhibitory interneurons (green) in all layers of V1 using a viral approach. Extracellular silicon electrode recordings were taken from dLGN. (b) Fluorescence image of V1 showing Chr2-eGFP expression. (c) Fluorescence image of dLGN showing Chr2-eGFP expression. (d) Raster plots for 'Neuron 1 x' comparing 'V1 Control trials' (0-200) and 'V1 Suppressed trials' (0-200) in response to a 'Movie'. (e) Firing rate (spk/s) vs Time (s) for V1 Control (black), V1 Control burst (red), V1 Suppressed (blue), and V1 Suppressed burst (orange), with a probability density histogram. (f-i) Scatter plots comparing V1 Control vs V1 Suppressed for firing rate ($p = 0.0001$), burst ratio ($p = 7.5 \times 10^{-5}$), sparseness ($p = 2.2 \times 10^{-7}$), and reliability ($p = 8.1 \times 10^{-5}$).

Figure 1 continued on next page

Figure 1 continued

performed in dLGN with and without optogenetic suppression of V1. **(b)** Coronal section close to the V1 injection site for an example PV-Cre mouse (blue: DAPI; green: eYFP; Bregma: -3.4 mm). **(c)** Coronal section at the dLGN (white outline) recording site, same animal as in **(b)**. For post-mortem confirmation of the electrode position, the back of the probe was stained with Dil (magenta) for one of the recording sessions (blue: DAPI; Bregma: -1.82 mm). **(d)** Raster plots of an example neuron for 200 presentations of a 5 s naturalistic movie clip, with CT feedback intact (control condition, top) and during V1 suppression (bottom). Red: burst spikes; black bar: movie clip presentation; light blue bar: V1 suppression. **(e)** Left: PSTHs for both the control (dark blue) and V1 suppression (light blue) conditions. Superimposed are PSTHs of burst spikes only, separately for control (red) and V1 suppression (pink) conditions. Right: Corresponding instantaneous firing rate distributions. **(f–i)** Comparison of control vs. V1 suppression conditions for mean firing rate **(f)**, burst ratio **(g)**, temporal sparseness **(h)**, and response reliability **(i)**, all calculated for the duration of the movie clip. Sparseness captures the activity fraction of a neuron, re-scaled between 0 and 1 (Vinje and Gallant, 2000). Response reliability is defined as the mean Pearson correlation of all single trial PSTH pairs (Goard and Dan, 2009). For sample sizes, see Table 1. Purple: example neuron. Black markers in **(f,g,i)** indicate neurons with individually significant effects (Welch's t-test). See also Figure 1—figure supplement 1 to Figure 1—figure supplement 6.

The online version of this article includes the following video and figure supplement(s) for figure 1:

Figure supplement 1. Confirmation of optogenetic suppression of V1 responses and targeting dLGN for recordings.

Figure supplement 2. Effects of CT feedback on additional parameters of responses to naturalistic movies and their relationship with firing rate.

Figure supplement 3. Feedback effects during movie presentation are largely independent of functional cell type classification.

Figure supplement 4. Selective optogenetic suppression of L6 CT feedback in Ntsr1-Cre yielded similar results as global V1 suppression via PV + activation.

Figure supplement 5. Photostimulation in an Ntsr1- control mouse injected with cre-dependent stGtACR2 had no effect on neural responses.

Figure supplement 6. Effects of photostimulation on pupil size were unrelated to CT feedback effects on dLGN neuronal activity.

Figure 1—video 1. First example 5 s movie clip used for visual stimulation.

<https://elifesciences.org/articles/70469/figures#fig1video1>

Figure 1—video 2. Second example 5 s movie clip used for visual stimulation.

<https://elifesciences.org/articles/70469/figures#fig1video2>

response events that were narrow in time and reliable across trials (Figure 1d, top, example neuron). Consistent with the notion that CT feedback has a modulatory rather than driving role (Sherman, 2016), even during V1 suppression this temporal response pattern remained somewhat preserved (Pearson correlation $r = 0.54$, $p < 10^{-6}$, Figure 1d and e). Yet, as illustrated in the example neuron, with CT feedback intact, firing rates were higher and burst spikes were less frequent (Figure 1e, left). Accordingly, the distributions of instantaneous firing rates in the two conditions were significantly different (KS test, $p < 10^{-6}$), and were more skewed during V1 suppression than with CT feedback intact ($\gamma = 2.02$ vs 1.22; Figure 1e, right).

We observed similar effects in the recorded population of dLGN neurons, where CT feedback enhanced overall responses and promoted tonic firing mode. Indeed, while mean firing rates varied almost 4 orders of magnitude across the population (~ 0.1 –100 spikes/s), they were higher in control conditions with CT feedback intact than during V1 suppression (13.7 vs 10.5 spikes/s; linear multilevel-model (LMM): $F_{1,63.2} = 17.1$, $p = 0.0001$; Figure 1f). In addition, CT feedback also influenced more fine-grained properties of geniculate responses. First, with CT feedback, the mean proportion of spikes occurring as part of a burst event was about half of what we observed during suppression (0.05 vs 0.09; LMM: $F_{1,64.0} = 17.9$, $p = 7.5 \times 10^{-5}$; Figure 1g). Second, consistent with the distributions of firing rate for the example neuron (Figure 1e, right), responses to the naturalistic movie clips with CT feedback intact were, on average, less sparse (0.35 vs 0.45; LMM: $F_{1,63.0} = 33.7$, $p = 2.2 \times 10^{-7}$; Figure 1h), indicating that neurons fired less selectively across the frames of the movie. Finally, we also examined the effect of CT feedback on response reliability. To quantify reliability, we computed the Pearson correlation coefficient of a neuron's responses between each pair of the 200 stimulus repeats

per condition, and averaged the correlation coefficients over all pair-wise combinations (Goard and Dan, 2009). With CT feedback intact, mean response reliability was lower than without feedback (0.15 vs 0.18; LMM: $F_{1,63.1} = 17.8, p = 8.1 \times 10^{-5}$; Figure 1i). Except for the effects on sparseness, the feedback effects on responses to naturalistic movies were unrelated to changes in firing rates (Figure 1—figure supplement 2c-g). The increased trial-to-trial reliability during V1 suppression could not be explained by higher stability in eye positions, because variability in eye position was slightly larger with CT feedback intact vs. suppressed (Figure 1—figure supplement 2h), and effects of CT feedback on neural reliability were unrelated to changes in variability of eye position (Figure 1—figure supplement 2i). Splitting the dLGN population into putative cell types according to several functional characteristics and location within dLGN revealed few differences in how global V1 suppression affected firing rates and bursting (Figure 1—figure supplement 3). As V1 suppression by PV + activation is robust, yet lacks selectivity (Wiegert et al., 2017), we repeated our experiments while directly photo-suppressing L6CT neurons. To this end, we expressed the inhibitory opsin stGtACR2 (Mahn et al., 2018) in V1 Ntsr1+ neurons, which correspond to $\geq 90\%$ to L6 CT neurons (Bortone et al., 2014; Kim et al., 2014, Figure 1—figure supplement 4). These experiments with specific suppression of L6 CT neurons during viewing of naturalistic movies yielded identical conclusions (Figure 1—figure supplement 4a-h).

Lastly, we performed two additional controls to rule out that photostimulation *per se* caused our findings. First, we repeated our experiments on an Ntsr1- control mouse, which was injected and underwent the same visual and photostimulation protocol. This negative control mouse did not show any effects of photostimulation on dLGN responses (Figure 1—figure supplement 5a-d). Second, we identified those experiments (14/31 for PV + activation, 0/10 for Ntsr1 + suppression experiments), where photostimulation decreased pupil size, indicative of light leakage into the retina. Even with these sessions removed, we found that our results remained qualitatively unchanged (Figure 1—figure supplement 6a-f). Finally, considering again all recordings, the effects of CT feedback on neuronal activity were unrelated to light-induced changes in pupil size (Figure 1—figure supplement 6g-j). Together, these results rule out that photostimulation *per se* led to the modulation of dLGN responses during naturalistic movie viewing.

Taken together, our results indicate that CT feedback can robustly modulate responses of dLGN neurons to naturalistic movie clips. The modulations are consistent with a net depolarizing effect, which supports higher firing rates and more linear, tonic firing mode with higher dynamic range, at the expense of sparseness, trial-to-trial reliability, and signal-to-noise.

V1 suppression decreases dLGN responses to naturalistic movies by reducing response gain

To better understand the effects of V1 suppression on dLGN firing rate, we next asked whether the observed reduction in responsiveness could be explained by a divisive and/or subtractive change (Figure 2). Using repeated random subsampling cross-validation, we fit a simple threshold linear model (Figure 2a, inset) to timepoint-by-timepoint responses in suppression vs. feedback conditions, and extracted the slope and threshold of the fit for each subsample (Figure 2b and d). In the two example neurons shown in Figure 2a-d, the fitted slope was significantly smaller than 1 (neuron 2: median slope of 0.66, 95% CI: 0.63–0.69, Figure 2b; neuron 1: median slope of 0.37, 95% CI: 0.32–0.41, Figure 2d), while the threshold (x -intercept) was either small or not significantly different from 0 (neuron 2: median of 1.58, 95% CI: 0.39–2.91; neuron 1: median of -0.14 , 95% CI: -1.49 – 0.89). We obtained similar results for the population of recorded neurons, where V1 suppression decreased the neurons' responses to naturalistic movie clips via a substantial change in response gain (slope of 0.75 ± 0.1 ; LMM) without a significant shift in baseline (threshold of -0.19 ± 1.15 ; LMM; Figure 2e). This demonstrates that V1 suppression influences responses in dLGN to naturalistic movie clips predominantly via a divisive effect.

We noticed that the threshold linear model could predict the effects of V1 suppression better for some neurons than for others. We therefore explored whether poor fits of the model might be related to our finding that V1 suppression can trigger non-linear, burst-mode firing. For instance, the threshold-linear model accurately captured the responses of example neuron 2 (median $R^2 = 0.90$, cross-validated; Figure 2a and b), which exhibited little bursting during V1 suppression (burst ratio: 0.007). Neuron 1, in contrast, had a higher burst ratio during suppression (0.28) and the prediction

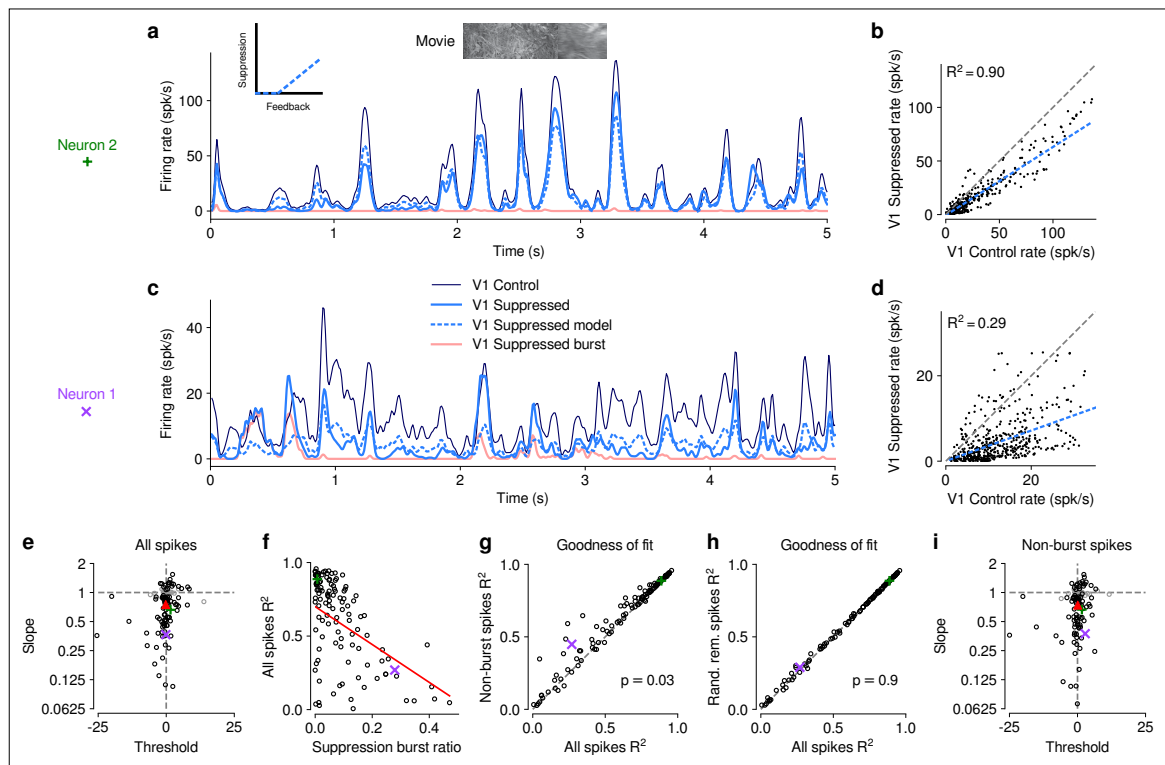


Figure 2. The effect of V1 suppression on dLGN responses to naturalistic movie clips is predominantly divisive. **(a)** PSTHs of an example neuron during control (dark blue) and V1 suppression (light blue) conditions, for a random subset of 50% of trials per condition not used for model fitting. Responses during the V1 suppression condition are approximated by the threshold linear model (dashed light blue) based on responses during the control condition. Pink: PSTH during V1 suppression for burst spikes only. Inset: cartoon of threshold linear model. **(b)** Timepoint-by-timepoint comparison of instantaneous firing rates of the PSTHs (derived from the 50% of trials not used for fitting) during the suppression vs. feedback conditions. PSTH data points are plotted at 0.01ms resolution. Dashed light blue line: threshold linear model fit. **(c,d)** Same as **(a,b)** for a second example neuron (same as in **Figure 1d and e**). **(a,b)** and **(c,d)** each contain data from 1 representative subsample. **(e)** Slope and threshold parameters for all neurons. Each point represents the median for each neuron across 1000 random subsamples of trials. Black points indicate neurons with slopes significantly different from 1 (95% CI). **(f)** Cross-validated model prediction quality (median R^2) vs. burst ratio during V1 suppression. Red line: LMM fit. **(g)** Model prediction quality R^2 with and without removal of burst spikes. **(h)** Model prediction quality with and without removal of an equivalent number of tonic spikes. **(i)** Same as **(e)** but with burst spikes removed. **(e–h)** Purple, green: example neurons; red triangle: LMM estimate of the mean.

sometimes overestimated or underestimated peaks in the actual response, such that the percentage of explained variability was rather low (median $R^2 = 0.29$, cross-validated, **Figure 2c and d**).

Indeed, across the population of recorded neurons, the model goodness of fit (median R^2 , cross-validated) during V1 suppression was inversely related to the burst ratio (slope of -1.29 ± 0.5 ; LMM; **Figure 2f**), consistent with the notion that the highly non-linear, all-or-none-like burst mode firing (**Sherman, 2001**) cannot be captured by the threshold-linear model (see also **Lesica and Stanley, 2004**). To further investigate the impact of bursting on response transformations by CT feedback, we re-computed the PSTHs for each neuron during V1 suppression after removing all burst spikes. Removal of burst spikes allowed our model to capture the effects of V1 suppression even better (all spikes: mean $R^2 = 0.58$; non-burst spikes: mean $R^2 = 0.61$; LMM: $F_{1,160.8} = 4.8$, $p = 0.03$; **Figure 2g**). Importantly, this increase in model performance was not simply a consequence of removing a certain proportion of spikes that originally needed to be predicted: discarding an equivalent number of randomly selected tonic spikes did not yield improved fit quality (random tonic spikes removed: mean $R^2 = 0.58$; LMM: $F_{1,162} = 0.005$, $p = 0.9$; **Figure 2h**). While burst spikes cannot be captured by the threshold-linear model, removing burst spikes, however, did not change our conclusion that the

effect of V1 suppression on movie responses was predominantly divisive (slope: 0.74 ± 0.09 ; threshold: 0.09 ± 1.3 ; LMM; **Figure 2i**), likely because burst events were much rarer than tonic spikes (see also **Figure 1g**). Indeed, firing mode (all spikes vs. non-burst spikes) had no effect on either slope (LMM: $F_{1,162.7} = 0.6$, $p = 0.4$) or threshold estimates (LMM: $F_{1,157.3} = 0.2$, $p = 0.7$) of the simple linear model. Together, these results show that V1 suppression decreases dLGN responses to naturalistic movies mostly by reducing response gain.

CT feedback modulates dLGN responses evoked by drifting gratings

Previous studies have investigated the effects of CT feedback using artificial stimuli, such as gratings and bars (**Olsen et al., 2012; Denman and Contreras, 2015; Wang et al., 2006; Murphy and Sillito, 1987**). To relate our findings to these studies, and to investigate the role of stimulus type, we next examined the effects of V1 suppression during the presentation of drifting gratings (**Figure 3**). To approximate the visual stimulus configuration used for naturalistic movie clips, we presented full-screen gratings drifting in one of 12 different orientations, and selected a pseudo-random subset of trials for V1 suppression. As expected, we found that many single dLGN neurons in the control condition with CT feedback responded at the temporal frequency (TF, 4 cyc/s) of the drifting grating (**Figure 3a and b**). Similar to previous studies in mouse dLGN (**Piscopo et al., 2013; Román Rosón et al., 2019; Marshel et al., 2012**), we also encountered some dLGN neurons with tuning for grating orientation or direction (**Figure 3, a2, b**).

Contrary to the robust effects of CT feedback on movie responses, V1 suppression had mixed effects on dLGN responses to drifting gratings. Example neuron 1, for instance, had lower firing rates with CT feedback intact, both in the orientation tuning (**Figure 3, a2**) and the cycle-averaged response to the preferred orientation (**Figure 3a3**). In addition, in control conditions with CT feedback intact, there were markedly fewer burst spikes. In contrast, example neuron 3 responded more strongly with CT feedback intact (**Figure 3, b2,3**). Such diverse effects of CT feedback, as reported before for anesthetized mice (**Denman and Contreras, 2015**), were representative of the recorded population (**Figure 3c**): V1 suppression during grating presentation significantly reduced responses for some neurons, but significantly increased responses for others, such that the average firing rates in the two conditions were almost identical (control: 14.5 spikes/s, V1 suppression: 15.0 spikes/s) and statistically indistinguishable (LMM: $F_{1,43.0} = 0.15$, $p = 0.70$). In contrast to these diverse effects on firing rate, but similar to our findings for naturalistic movie clips, intact CT feedback was consistently associated with less bursting (burst ratios of 0.043 vs 0.15; LMM: $F_{1,43.0} = 25.3$, $p = 9.2 \times 10^{-6}$; **Figure 3d**). Also similar to our findings for movies, there was no relationship between the strength of feedback effects on firing rate and on bursting (LMM: slope 0.029 ± 0.41 , **Figure 4—figure supplement 1a**).

Beyond studying overall changes in responsiveness and firing mode, we next asked how CT feedback affected the tuning for grating orientation of dLGN neurons. It is known from previous studies (**Piscopo et al., 2013; Cruz-Martín et al., 2014; Marshel et al., 2012; Zhao et al., 2013; Scholl et al., 2013**) that mouse dLGN neurons show various degrees of orientation tuning, ranging from few strongly tuned neurons, potentially relaying tuned input from the retina (**Cruz-Martín et al., 2014**), to a larger group with orientation bias (**Piscopo et al., 2013; Scholl et al., 2013**). We computed orientation tuning curves separately for control conditions with CT feedback and V1 suppression conditions. For neuron 1, intact CT feedback was associated not only with lower average firing rates, but also poorer selectivity (OSIs of 0.14 vs 0.25; **Figure 3, a2**). In contrast, for neuron 3, orientation selectivity was similar during control and V1 suppression conditions (OSIs of 0.1 vs 0.09; **Figure 3, b2**). These results were representative of the population, where CT feedback affected orientation selectivity in diverse ways, with virtually no difference in population means (control OSI: 0.13; V1 suppression: 0.12; LMM: $F_{1,88.7} = 0.31$, $p = 0.58$; **Figure 3e**; see also **Scholl et al., 2013; Li et al., 2013; Lien and Scanziani, 2013; Denman and Contreras, 2015**). For neurons with OSI > 0.02 and well-fit orientation tuning curves ($R^2 > 0.5$), preferred orientation during feedback and suppression conditions was largely similar, except for some cases where it shifted (**Figure 3f**). As was the case for movies, splitting the dLGN population into putative cell types according to several functional characteristics and their location within dLGN revealed few consistent differences in how global V1 suppression during gratings affected firing rates and bursting (**Figure 3—figure supplement 1**). Taken together, although effects of V1 suppression on firing rate were more diverse in magnitude and sign for grating stimuli, the similarity of orientation

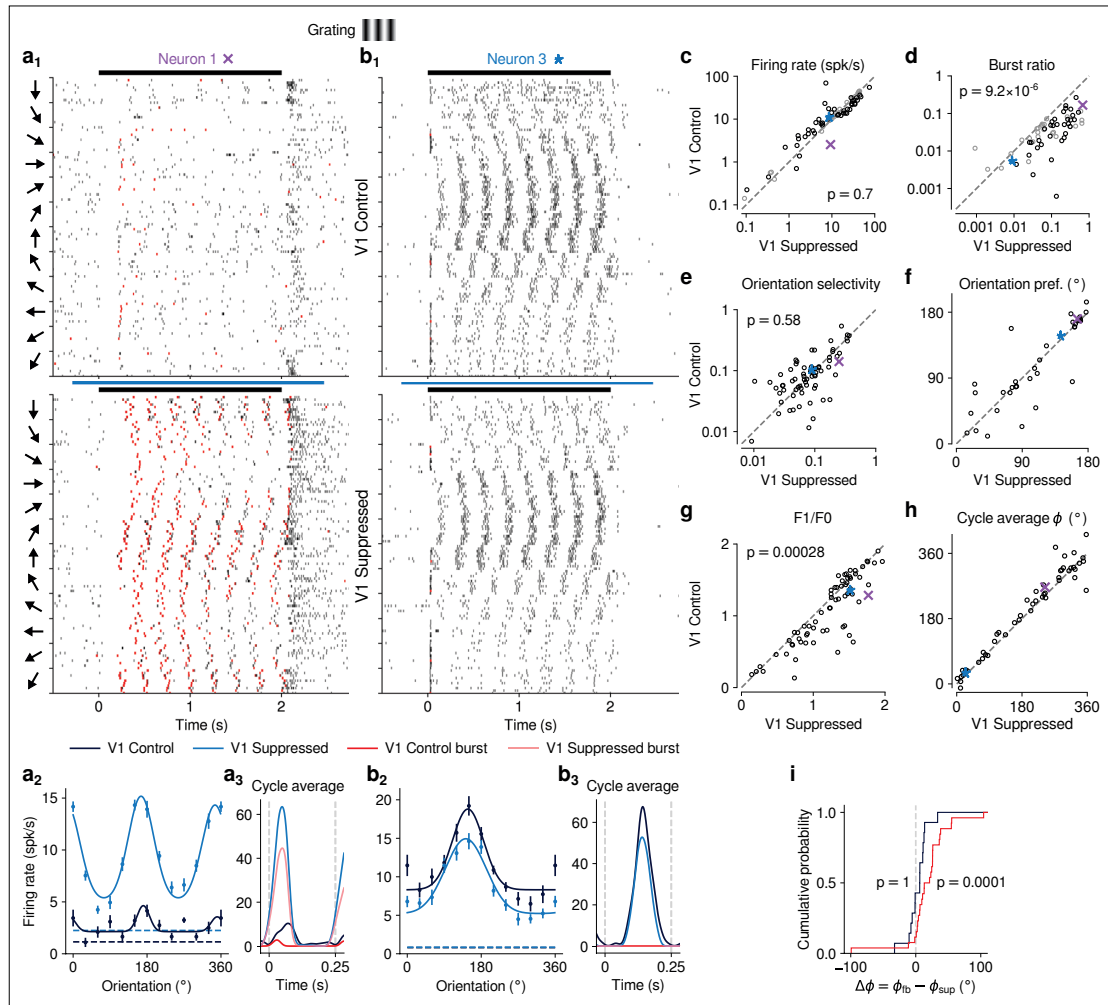


Figure 3. CT feedback modulates dLGN responses to drifting gratings. **(a)** Responses of example neuron 1 (same as in **Figures 1d, e, 2c and d**) to full-screen, drifting gratings. **(a1)** Raster plot in response to drifting gratings, with trials sorted by grating orientation (10 trials per orientation, 30° steps). Red: burst spikes; black bar: grating stimulation; light blue bar: V1 suppression. **(a2)** Corresponding orientation tuning curve. Dashed lines represent spontaneous firing rates in response to medium gray screen. Error bars: standard error of the mean. **(a3)** Cycle average response to preferred orientation. Dark blue, light blue: cycle average constructed from all spikes. Red, pink: cycle average constructed from burst spikes only. Dark blue, red: Control condition with CT feedback intact; light blue, pink: V1 suppression. **(b)** Same as **(a)**, for another example neuron (example neuron 3). **(c–h)** Comparison of the control condition with CT feedback intact vs. V1 suppression, for mean firing rate **(c)**, burst ratio **(d)**, orientation selectivity index (OSI) **(e)**, preferred orientation θ **(f)**, F_1/F_0 **(g)**, and cycle average phase ϕ **(h)**. Purple, blue: example neurons. Black markers in **(c,d)** indicate neurons with individually significant effects (Welch’s t-test). **(i)** Cumulative distribution of cycle average phase differences between control and V1 suppression conditions. Dark blue: neurons with little burst spiking (ratio of cycle average peak for burst spikes to cycle average peak for all spikes < 0.1); red: neurons with substantial burst spiking (ratio of cycle average peak for burst spikes to cycle average peak for all spikes ≥ 0.1).

The online version of this article includes the following figure supplement(s) for figure 3:

Figure supplement 1. As for movies (**Figure 1—figure supplement 3**), feedback effects during grating presentation are largely independent of functional cell type classification.

selectivity between CT feedback conditions suggests underlying changes in gain, in accordance with what we observed for naturalistic movies.

Inspecting the spike rasters at different orientations, we realized that dLGN neurons appeared to have a stronger response component at the grating's temporal frequency during V1 suppression than when feedback was intact (**Figure 3, a₁**). To test whether V1 suppression affected the ability of dLGN to respond at the gratings' temporal frequency, for each neuron we computed the amplitude of the response at the stimulus frequency (F_1 component) relative to the mean response (F_0 component) (**Skottun et al., 1991; Carandini et al., 1997**) and found that F_1/F_0 ratios were indeed lower when feedback was intact (1.08 vs 1.22; LMM: $F_{1,43.5} = 15.6$, $p = 0.00028$; **Figure 3g**). To explore the impact of CT feedback on the F_1 response component in more detail, we examined the cycle average responses to the preferred orientation, and asked how CT feedback affected response phase. Similar to the results obtained for the example neurons (**Figure 3, a₃, b₃**), we found that V1 suppression could advance response phase (**Figure 3h**). This phase advance occurred more often for neurons whose responses during V1 suppression included a substantial proportion of burst spikes (**Figure 3i, red**; 25 of 29 neurons showed phase advance, $p = 0.0001$, binomial test) than for neurons which during V1 suppression burst little or not at all (**Figure 3i, dark blue**; 11 of 21 neurons advanced, $p = 1$, binomial test). In agreement with earlier findings from intracellular recordings in anesthetized cats (**Lu et al., 1992**), these analyses demonstrate that the phase advance is driven by the dynamics of burst spiking. Finally, as for our re-assessment of CT feedback effect on responses to naturalistic movies, our conclusions regarding the effects of CT feedback on grating responses did not change when we repeated our experiments using a selective suppression of Ntsr1 + neurons with stGtACR2 (**Mahn et al., 2018, Figure 1—figure supplement 4i-o**). Also, during grating experiments, the Ntsr1- mouse controlling for effects of photostimulation per se showed no effects on neural responses to gratings (**Figure 1—figure supplement 5e-i**).

Effects of CT feedback on dLGN firing rates are more consistent and stronger overall for full-screen movies than full-screen gratings

Our analyses suggest that the impact of CT feedback on firing rates might be stronger overall for naturalistic movie stimuli than for gratings. To test this hypothesis, we focused on the subset of neurons recorded with both types of stimuli. Indeed, when we compared feedback modulation indices (FMIs, i.e. the difference between feedback conditions over their sum of firing rates), we found that FMI was

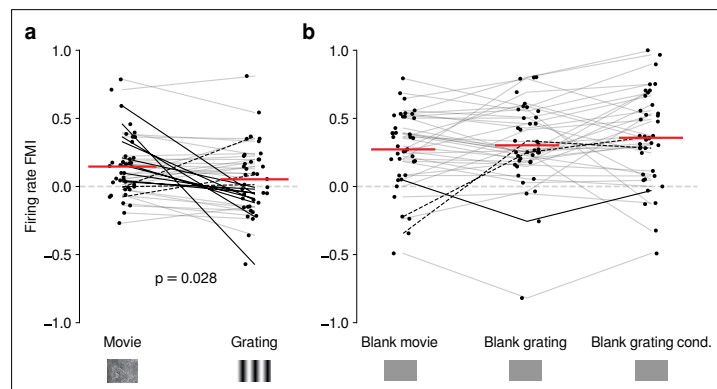


Figure 4. Effects of CT feedback on dLGN firing rate depend on stimulus type. **(a)** Comparison of the strength of CT feedback effects on firing rate (feedback modulation index, FMI) during presentation of full-screen movie clips and gratings. **(b)** Comparison of the strength of CT feedback effect on firing rate for blank stimuli interleaved with movies or gratings. Red: mean (LMM), dark lines: changes in sign of feedback modulation effect with stimulus type from positive for movies to negative for gratings (solid) and vice versa (dashed). For **(a)** and **(b)**, we randomly jittered the horizontal position of the points to avoid overlap; lines connecting the paired samples still end at the central position to represent change. See also **Figure 4—figure supplement 1**.

The online version of this article includes the following figure supplement(s) for figure 4:

Figure supplement 1. Control analyses assessing the difference in CT feedback effects for gratings and movies.

on average more positive for movies than for gratings (0.15 vs 0.053; LMM: $F_{1,38} = 5.21$, $p = 0.028$; **Figure 4a**). Remarkably, in 10/39 neurons (**Figure 4a**, dark lines) V1 suppression decreased firing rates for movies (positive movie FMI), but increased firing rates for gratings (negative grating FMI). The opposite effect only occurred in 3/39 neurons (dark dashed lines). These findings were not a consequence of differences in firing rates that might have already been present in control conditions with CT feedback intact (**Figure 4—figure supplement 1b**), and were also not a consequence of the longer duration of V1 suppression during movie clips (**Figure 4—figure supplement 1c, d**).

The differences in the effects of CT feedback on firing rates during full-screen gratings vs. movies might be related to feedback-induced changes in bursting, which might be stimulus-dependent (Lu *et al.*, 1992; Grubb and Thompson, 2005) and can drive high-frequency firing. To test this hypothesis, we compared CT feedback modulation of burst ratio for gratings vs. movie clips, and found that V1 suppression indeed induced stronger bursting for gratings than for movies (**Figure 4—figure supplement 1e**). However, for both movies (**Figure 1—figure supplement 2c**) and gratings (**Figure 4—figure supplement 1a**), CT feedback effects on firing rates were unrelated to those on bursting. Thus, while suppression of CT feedback engages bursting overall more strongly for gratings than movies, this differential recruitment does not seem to account for differences in CT feedback-related modulations of firing rates for movies vs. grating stimuli.

Differences in CT feedback effects between firing rates to full-screen gratings and movies might instead be related to differences in longer-lasting, systematic changes in neural activity, which might occur due to differential adaptation or differences in behavioral state induced by the two stimulus types. To address this possibility, we focused on periods of blank screen, which were contained in both stimulus types. These were short (~0.3 s) periods directly preceding each full-screen movie and grating trial (see e.g., **Figures 1d and 3a**), as well as blank trials interleaved as one condition in the grating experiments. Applying our analyses to these various blank stimuli (**Figure 4b**, **Figure 4—figure supplement 1g-i**), we found that CT feedback enhanced mean firing rates regardless of blank type or blank period duration (positive firing rate FMIs, mean FMIs: 0.27 vs. 0.30 vs. 0.36; LMM: $F_{2,76} = 1.69$, $p = 0.19$; **Figure 4b**). This CT feedback-related average enhancement for blank stimuli was even stronger than the enhancement observed during movie presentation (LMM: $F_{1,116} = 15.1$, $p = 0.0002$), and stronger than the mixed effects during grating presentation (LMM: $F_{1,116} = 34.9$, $p = 3.6 \times 10^{-8}$). Since the CT feedback effects on these various blank stimuli did not depend on blank period duration or whether blanks were embedded in grating or movie experiments (see also **Figure 4—figure supplement 1f-l**), we conclude that differences in longer lasting changes in neural activity or behavioral state did not underlie the differential effect of CT feedback for full screen movies vs. gratings. Instead, we interpret these findings to highlight that CT feedback modulates dLGN responses in a stimulus-dependent way. In particular, the strength and sign of CT feedback gain might be sensitive to features of the visual stimulus, such as the contrast, the dynamics, or the statistics of the center and the surround stimulation.

Effects of behavioral state on dLGN responses resemble effects of CT feedback, but are largely independent

Previous studies have reported that responses of mouse dLGN neurons to grating stimuli are modulated by behavioral state as inferred by locomotion (Erisken *et al.*, 2014; Aydın *et al.*, 2018; Williamson *et al.*, 2015). To assess how these findings extend to more complex stimuli, we separated the trials with CT feedback intact according to the animals' locomotion behavior. We considered trials as 'run trials' if the animal's speed exceeded 1 cm/s for at least 50% of the stimulus presentation and as 'sit trials' if the animal's speed fell below 0.25 cm/s for at least 50% of the stimulus presentation. When we examined the spike rasters and PSTHs of example neuron 1 in control conditions with CT feedback intact (**Figure 5a and b**), we found that, despite preserved temporal features of the responses (Pearson correlation $r = 0.72$ between run and sit PSTHs, $p < 10^{-6}$), firing rates were higher overall during locomotion than stationary periods. Additionally, during locomotion, the distribution of firing rates was less skewed ($\gamma = 1.15$ vs 1.45 during stationary trials), with a decrease of low and an increase of medium firing rates (KS test, $p < 10^{-6}$). This pattern was also observed in the population of dLGN neurons, where firing rates were consistently higher for trials with locomotion compared to trials when the animal was stationary (11.9 vs 8.9 spikes/s; LMM: $F_{1,63,9} = 94.1$, $p = 3.5 \times 10^{-14}$; **Figure 5c**). Similar to previous reports using gratings (Niell and Stryker, 2010; Erisken *et al.*, 2014), we found that

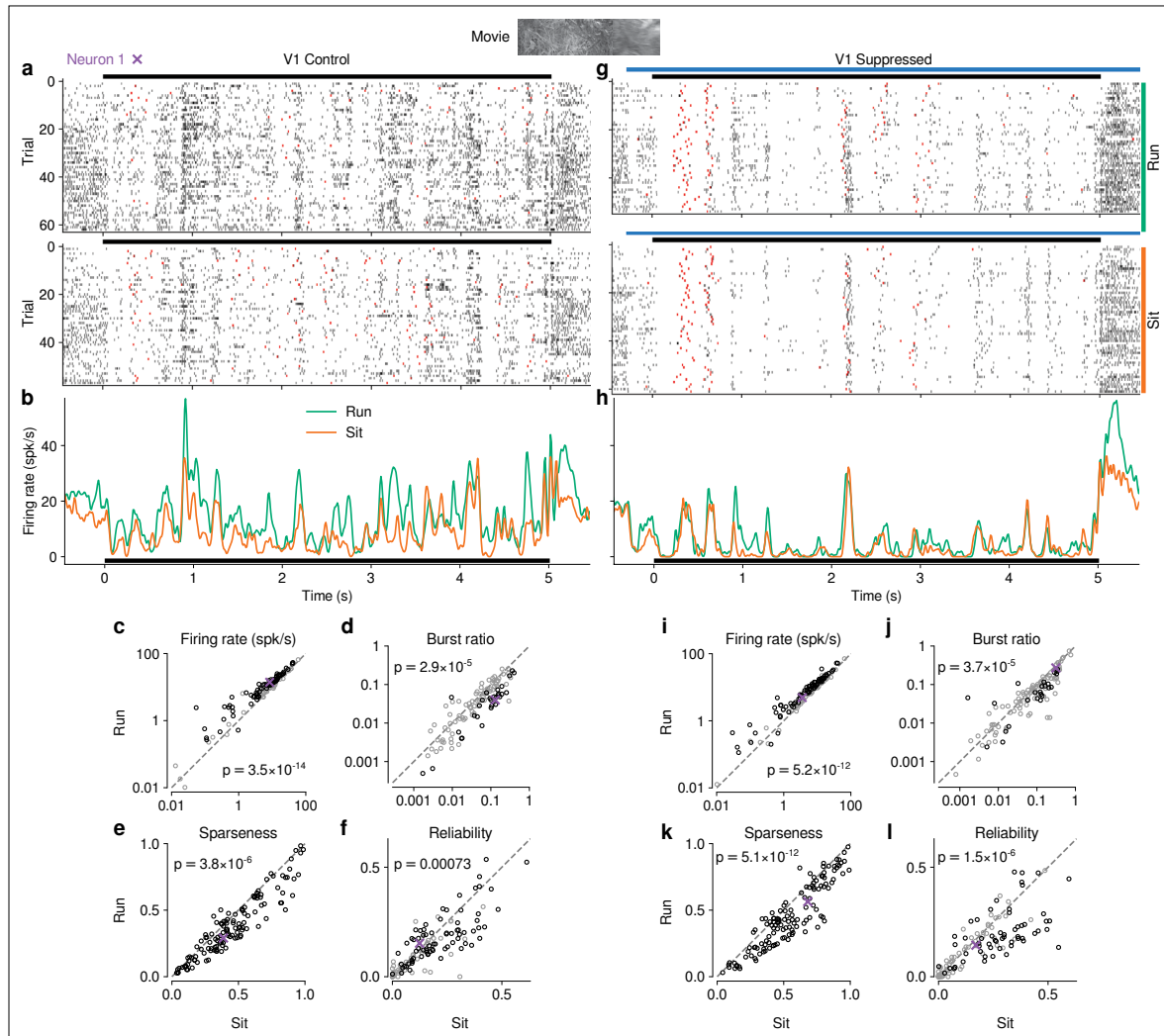


Figure 5. Effects of locomotion on dLGN responses resemble those of CT feedback, but persist even during V1 suppression. (a) Spike raster of example neuron 1 (same as **Figure 1d**) in response to a naturalistic movie clip during locomotion and stationary trials with CT feedback intact. Top: trials with run speed > 1 cm/s; bottom: trials with run speed < 0.25 cm/s, both for at least $> 50\%$ of each trial. Red: burst spikes. (b) Corresponding PSTHs. Green: locomotion, orange: stationary; black bar: duration of movie clip. (c–f) Comparison of firing rates (c), burst ratio (d), sparseness (e), and trial-to-trial reliability (f) during locomotion and stationary trials. Black markers in (c,d,f) correspond to individually significant observations (Welch’s t-test). (g–l) Same as (a–f), for locomotion and stationary trials during V1 suppression. Light blue bar: V1 suppression. See also **Figure 5—figure supplement 1**.

The online version of this article includes the following figure supplement(s) for figure 5:

Figure supplement 1. Effects of locomotion on additional parameters of responses to naturalistic movie clips and relationship with firing rate.

Figure supplement 2. Effects of pupil-indexed arousal on dLGN responses to movies.

bursting was lower during locomotion than stationary periods (0.035 vs 0.063; LMM: $F_{1,66.7} = 20.2$, $p = 2.9 \times 10^{-5}$; **Figure 5d**). Beyond these established measures, using movie clips allowed us to test the effects of locomotion on additional response properties: trials with locomotion were associated with lower sparseness (0.40 vs 0.47; LMM: $F_{1,181.9} = 22.8$, $p = 3.8 \times 10^{-6}$; **Figure 5e**) and lower trial-to-trial reliability (0.13 vs 0.16; LMM: $F_{1,176.1} = 11.8$; **Figure 5f**). This locomotion-related decrease of reliability could be related to, but is likely not fully explained by, the increase in eye movements typically

associated with running (**Figure 5—figure supplement 1h, i**; **Erisken et al., 2014**; **Bennett et al., 2013**). These analyses demonstrate that in dLGN, processing of naturalistic movie clips is robustly modulated by locomotion. Curiously, in all aspects tested, these modulations by locomotion had the same signatures as those of CT feedback: increased firing rates, reduced bursting, and decreased sparseness and trial-to-trial reliability.

Since the effects of CT feedback and locomotion closely resembled each other, and since L6CT neurons themselves are modulated by locomotion (**Augustinaite and Kuhn, 2020**), are the effects of locomotion on dLGN responses inherited via feedback from cortex? To test this hypothesis, we next focused on only those movie trials in which feedback was suppressed by V1 PV+ photostimulation and repeated the separation according to locomotion (**Figure 5g–h**). These analyses revealed that effects of locomotion on the responses to our movies persisted, even if CT feedback was suppressed (**Figure 5i–l**; firing rate: 9.7 vs 7.6 spikes/s; LMM: $F_{1,64.8} = 71.1$, $p = 5.2 \times 10^{-12}$; burst ratio: 0.081 vs 0.11 spikes/s; LMM: $F_{1,68.1} = 19.5$, $p = 3.7 \times 10^{-3}$; sparseness: 0.47 vs 0.56; LMM: $F_{1,179.5} = 54.7$, $p = 5.1 \times 10^{-12}$; reliability: 0.14 vs 0.18; LMM: $F_{1,175.7} = 24.9$, $p = 1.5 \times 10^{-6}$).

Besides running, another often-used indicator for behavioral state is pupil size (**Reimer et al., 2014**; **Vinck et al., 2015**; **Erisken et al., 2014**). Indexing arousal via pupil size, however, is challenging for movie stimuli, whose fluctuations in luminance will themselves drive changes in pupil size (**Figure 5—figure supplement 2a**). To test whether locomotion-independent, pupil-indexed arousal also modulates dLGN responses and whether this modulation depends on CT feedback, we exploited methods initially proposed by **Reimer et al., 2014**, focusing on periods within the movie when the animal was sitting and assuming that the average change in pupil size over multiple movie repetitions was due to luminance changes in the movie, while the variability around this average reflected trial-by-trial differences in behavioral state (**Figure 5—figure supplement 2b–g**). Recapitulating our running-related results, we found that both with CT feedback intact and during V1 suppression, response periods with faster than average pupil dilation (or slower than usual constriction; top quartile pupil change) were associated with higher firing rates, while periods with faster than usual pupil constriction (or slower than usual dilation; bottom quartile pupil change) were associated with lower firing rates (**Figure 5—figure supplement 2b–c**). In contrast, response reliability and SNR were not significantly different during periods of rapid dilation vs. rapid constriction, regardless of photostimulation condition (**Figure 5—figure supplement 2d–g**).

Finally, to further test the relationship between effects of behavioral state and CT feedback, we directly compared CT feedback and running-related modulations on a neuron-by-neuron basis. We focused on experiments with naturalistic movies, because this was the condition in which we observed robust effects of both CT feedback and behavioral state (for a related analysis with gratings and qualitatively similar results, see **Figure 6—figure supplement 1a**). First, we hypothesized that if effects of locomotion on dLGN responses were inherited from primary visual cortex, such effects should vanish during V1 suppression (**Figure 6a₀**). However, consistent with the observations shown in **Figure 5i–l**, even during V1 suppression, running-related modulations were significantly different from 0 (firing rate run modulation index (RMI): 0.18 ± 0.06 ; burst ratio: -0.17 ± 0.1 ; sparseness: -0.12 ± 0.04 ; reliability: -0.11 ± 0.09 ; **Figure 6, a_{1–4,4}**). In fact, the degree of running modulation was correlated between control conditions with feedback intact and V1 suppressed (firing rate: slope of 0.51 ± 0.12 ; burst ratio: slope of 0.38 ± 0.2 ; sparseness: slope of 0.44 ± 0.14 ; reliability: slope of 0.50 ± 0.15 ; **Figure 6, a_{1–4}**). Interestingly, for firing rates and burst ratios, locomotion effects were slightly stronger, on average, with CT feedback intact compared to V1 suppression (firing rate RMI: 0.23 vs 0.20; LMM: $F_{1,168.3} = 4.3$, $p = 0.04$, **Figure 6, a₁**; burst ratio RMI: -0.25 vs. -0.17 ; LMM: $F_{1,154.7} = 6.3$, $p = 0.013$, **Figure 6, a₂**), indicating that these two modulatory influences likely interact.

We next tested the hypothesis that CT feedback might have a stronger impact during active behavioral states than during quiescence. Indeed, it has previously been shown that during brain states associated with anesthesia, the responsiveness of feedback circuits is particularly reduced (**Briggs and Usrey, 2011**; **Makino and Komiyama, 2015**; **Keller et al., 2020**). One might therefore predict that during quiescence, if feedback circuits were already completely disengaged, we should not be able to observe further effects of V1 suppression (**Figure 6, b₀**). This was clearly not the case, because CT feedback effects were correlated across behavioral states (firing rate: slope of 0.72 ± 0.10 ; burst ratio: slope of 0.34 ± 0.15 ; sparseness: slope of 0.85 ± 0.12 ; reliability: slope of 0.43 ± 0.14 ; **Figure 6, b_{1–4}**). In addition, and similar to the slightly stronger run modulation with feedback left intact, we discovered

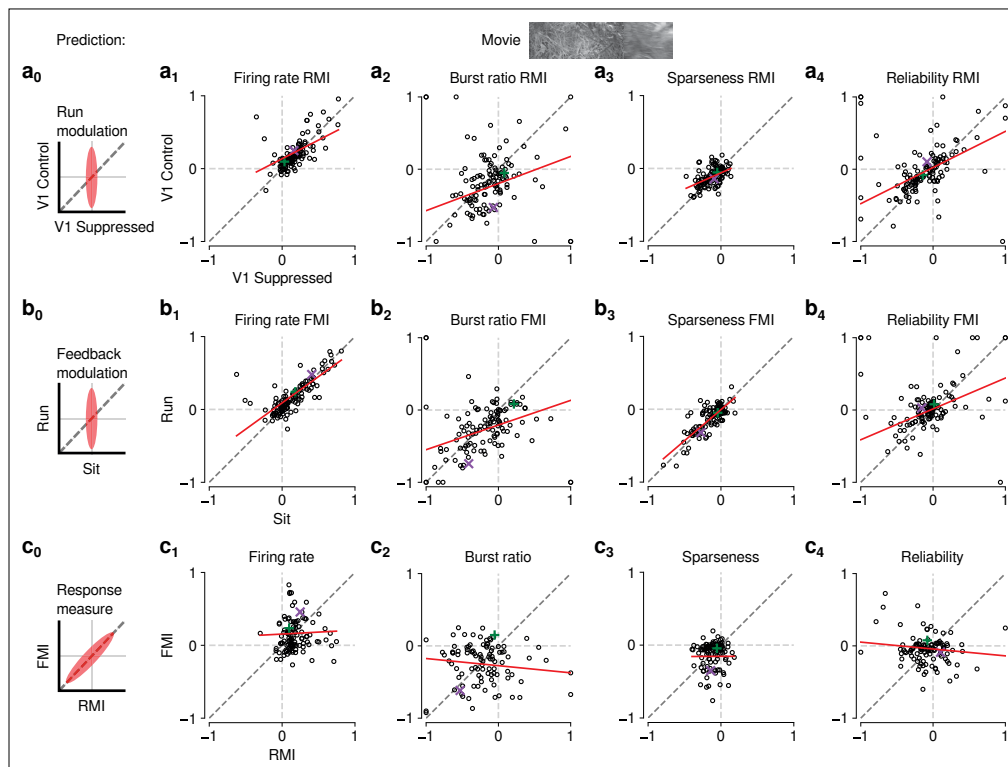


Figure 6. The effects of CT feedback and locomotion on movie responses are largely independent. (**a**₀–**c**₄) Predicted relationships between modulation indices and response measures in different contexts, assuming dependence in the effects of CT feedback and locomotion. (**a**) Comparison of modulation by running (RMI) during CT feedback intact and V1 suppression for firing rates (**a**₁), burst ratio (**a**₂), sparseness (**a**₃), and reliability (**a**₄). Running effects were quantified with a run modulation index (RMI), where $RMI = (\text{running} - \text{sitting}) / (\text{running} + \text{sitting})$. (**b**) Comparison of modulation by CT feedback (FMI) during locomotion and stationary periods for firing rates (**b**₁), burst ratio (**b**₂), sparseness (**b**₃), and reliability (**b**₄). (**c**) Comparison of modulation by feedback (FMI) and modulation by running (RMI) for firing rates (**c**₁), burst ratio (**c**₂), sparseness (**c**₃), and reliability (**c**₄). Red: LMM fit. Green, purple: example neurons from **Figure 2a** and **b**.

The online version of this article includes the following figure supplement(s) for figure 6:

Figure supplement 1. The effects of CT feedback and locomotion on responses to gratings are also largely independent.

a locomotion-dependent CT feedback effect for firing rates and burst ratios: CT feedback effects were slightly stronger, on average, during locomotion than during quiescence (firing rate FMI: 0.18 vs 0.15; LMM: $F_{1,172.8} = 3.5$, $p = 0.065$; **Figure 6**, **b**₁; burst ratio FMI: -0.27 vs. -0.19 ; LMM: $F_{1,166.9} = 6.8$, $p = 0.0097$; **Figure 6**, **b**₂). This subtle interaction between behavioral state and CT feedback effects might relate to a previous finding, where careful dissection of brain states by depth of anesthesia had already suggested that the effects of transient cortical inactivation on dLGN responses were more evident during lighter anesthesia, that is, during desynchronized cortical activity (**Wörgötter et al., 2002**). However, our ability to observe effects of V1 suppression in dLGN while the animal was stationary suggests that CT feedback circuits are engaged even under conditions of behavioral quiescence.

Finally, if modulations by CT feedback and behavioral state exploited the same circuitry, neurons experiencing strong modulation by V1 suppression should also be strongly affected by locomotion (**Figure 6**, **c**₀). Contrary to this prediction, we found that effects of CT feedback (FMI) and behavioral state (RMI) were uncorrelated (firing rate: slope of 0.054 ± 0.13 ; burst ratio: slope of -0.1 ± 0.13 ; sparseness: slope of 0.005 ± 0.23 ; reliability: slope of -0.095 ± 0.12 ; **Figure 6c**_{1–4}). Together, these comparisons demonstrate that effects of behavioral state associated with locomotion and effects of CT feedback are largely independent.

Discussion

In this study, we used naturalistic movies to reveal that corticothalamic feedback and behavioral state can have robust effects on dLGN responses. We found that V1 suppression during movie presentation reduces the gain of time-varying dLGN firing rates, and leads to increases in bursting, sparseness and trial-to-trial reliability. The effects of CT feedback seem to be stimulus-specific, as V1 suppression led to more consistent and therefore stronger overall effects on firing rates for naturalistic movies than for gratings. Interestingly, the signatures of CT feedback closely resembled those of behavioral state. However, we found their effects during movie viewing to be largely independent, demonstrating that behavioral modulations of dLGN activity are not simply inherited from cortex. Overall, our findings highlight that dLGN responses to naturalistic movies can be reliably modulated by two extra-retinal sources – cortical feedback and behavioral state – which likely exert their influences via largely separate neural circuits.

Manipulation of CT feedback

To manipulate CT feedback, we chose a potent, yet global, V1 suppression approach based on optogenetic activation of ChR2 expressed in local PV+ inhibitory interneurons (Lien and Scanziani, 2013; Li et al., 2013; King et al., 2016; Olsen et al., 2012; Wiegert et al., 2017). While silencing by excitation of inhibitory interneurons can exploit the robust effects of GABA-mediated inhibition in cortical circuits, it comes with a limitation in specificity. Hence, in addition to the direct L6 → thalamus circuit, indirect polysynaptic effects might be exerted via alternative routes. One example is L5 corticofugal pyramidal cells projecting to the superior colliculus (SC), where tectogeniculate neurons in the superficial layers provide retinotopically organized, driving inputs to the dorsolateral shell region of the dLGN (Bickford et al., 2015). To address this lack of specificity, in control experiments, we replaced photoactivation of PV +neurons with direct, selective suppression of V1 Ntsr1 +neurons, encompassing the population of L6 CT pyramidal cells (Kim et al., 2014; Bortone et al., 2014). Since photosuppression via the light-gated chloride channel stGtACR2 (Mahn et al., 2018) did not alter any of our conclusions regarding the effects of CT feedback on dLGN responses, we assume that the effects of V1 suppression to a large degree reflect the specific impact of the L6 CT circuit. L6 CT neurons, however, have an intracortical axon collateral making privileged connections with a translaminal PV +interneuron subtype in L6 (Frändolig et al., 2019; Bortone et al., 2014), which in turn strongly regulates the gain of the entire V1 column (Olsen et al., 2012; Bortone et al., 2014; Frändolig et al., 2019), so that even with such specific suppression, polysynaptic effects cannot be excluded. However, since suppression of L6 CT neurons increases the gain in V1 (Olsen et al., 2012), and since this is the opposite of the global effects of V1 suppression via PV +activation, L6 CT gain modulation of V1 seems unlikely to drive our effects. Nevertheless, decisively ruling out alternative circuits would require the selective suppression of L6 CT axon terminals at the thalamic target.

Cortical layer 6 is well known for its particularly high diversity of neuronal cell types (Briggs, 2010). Even within the population of L6 CT pyramidal cells there is heterogeneity, with at least two subtypes defined by morphology (Frändolig et al., 2019; Tasic et al., 2016; Gouwens et al., 2019; Augustinaite and Kuhn, 2020), three subtypes defined by electrophysiology and morphology (Gouwens et al., 2019), and four major subtypes defined by transcriptomics (Tasic et al., 2016; Gouwens et al., 2019). Whether these subtypes mediate different aspects of feedback modulations is currently unknown. In the visual system of primates and carnivores, CT feedback circuits seem to be organized into distinct streams (Briggs et al., 2016; Hasse et al., 2019; Briggs and Usrey, 2009) whose functional organization mimics that of the feedforward streams. Whether the known subtypes in mice can convey independent, stream-specific information is currently unknown, partly because already at the level of feedforward processing, the notion of streams in mouse dLGN is a matter of ongoing debate (Chen et al., 2016; Denman and Contreras, 2016; Morgan et al., 2016; Chen et al., 2016; Zhuang et al., 2019), and dLGN response properties are diverse (Piscopo et al., 2013; Román Rosón et al., 2019; Liang et al., 2018). Our own assessment of CT feedback effects revealed few systematic differences for various dLGN cell-type classifications. Such an absence of differences, however, is not surprising, because our optogenetic circuit manipulations non-specifically suppressed all L6 CT neuron subtypes. Once genetic targeting of L6 CT subtypes will become possible, it will be important to test the stream-specificity of CT feedback in the mouse.

CT feedback effects on gain, reliability, and bursting

Our analyses of the time-varying firing rates in response to naturalistic movies revealed that V1 suppression results in a robust decrease of geniculate response gain. Divisive effects of CT feedback suppression have also been previously reported for contrast response functions of parvocellular dLGN neurons in anesthetized macaques (Przybylski *et al.*, 2000). A crucial element to produce gain modulations seems to be changes in the level of synaptically driven V_m fluctuations, often called ‘synaptic noise’ (Hö and Destexhe, 2000; Shu *et al.*, 2003; Chance *et al.*, 2002). Indeed, in vivo V1 recordings suggest that the combined impact of changes in V_m fluctuations, input resistance, and depolarization is needed to produce gain changes (Cardin *et al.*, 2008). These cellular properties are altered by both feedback (Chance *et al.*, 2002) and neuromodulation (Disney *et al.*, 2007), not only in cortex (Ferguson and Cardin, 2020) but also in the corticothalamic system (Béhuret *et al.*, 2015; Augustinaite *et al.*, 2014). Here, ‘synaptic noise’ together with varying degrees of T-type channel recruitment has been shown to change the slope of the input-output function and alter the temporal filtering characteristics of thalamic relay cells (Wolfart *et al.*, 2005; Béhuret *et al.*, 2015). Thus, by providing variable synaptic input and affecting membrane depolarization, for example, through NMDA plateau potentials (Augustinaite *et al.*, 2014), CT feedback might be in a prime position to dynamically tune the gain of the thalamic relay.

In addition to potentially contributing to the observed gain modulations, ‘synaptic noise’ from CT feedback may also help explain the less precise and less reliable dLGN responses we observed when feedback was left intact. Specifically, V1 neurons are known to exhibit about double the trial-to-trial variability of simultaneously recorded dLGN neurons (Kara *et al.*, 2000), and eliminating variable cortical input might unmask the even greater reliability of feed-forward retinal inputs (Kara *et al.*, 2000).

Our analyses of movie and grating response characteristics showed that V1 suppression robustly and consistently biased geniculate activity toward burst firing mode. Burst firing mode occurs when dLGN neurons undergo sustained (≥ 100 ms) hyperpolarization (Sherman, 2001), which allows for the de-inactivation of low-threshold T-type calcium channels abundant in thalamus (Jahnsen and Llinás, 1984). Such ‘calcium bursts’ can only be unequivocally separated from high-frequency firing in intracellular recordings or calcium imaging, but can be inferred in extracellular recordings, such as ours, by imposing a minimum duration of 100 ms of silence preceding a high-frequency (< 4 ms ISI) firing event (Lu *et al.*, 1992). Previous in vivo intracellular recordings in cat dLGN have revealed that cortical ablation can hyperpolarize the resting membrane potential of dLGN relay cells by ~ 9 mV, enough to push them into burst-firing mode (Dossi *et al.*, 1992). Conversely, direct optogenetic activation of L6 CT neurons in primary somatosensory cortex has been shown to decrease burst mode firing (Mease *et al.*, 2014), potentially mediated by NMDA plateau potentials as observed in slice recordings (Augustinaite *et al.*, 2014). In burst firing mode, reminiscent of the effects we observed during V1 suppression, dLGN spontaneous activity is low (Sherman, 2001), stimulus-evoked responses show phase-advance (Lu *et al.*, 1992; Alitto *et al.*, 2005) and high trial-to-trial reliability (Alitto *et al.*, 2005). The increase in trial-to-trial response reliability we observed during V1 suppression might therefore be explained not only by the removal of a more variable input as mentioned above (Kara *et al.*, 2000), but also by a shift towards burst mode, where retinogeniculate communication efficacy is elevated (Alitto *et al.*, 2019).

Theories about the function of thalamic firing modes can provide a useful framework for interpreting the effects of CT feedback we observed here, in particular since the greater precision and trial-to-trial reliability of responses during V1 suppression might be unexpected at first glance. Thalamic burst mode is often linked with ‘inattentive states’, where the sudden appearance or change of a visual stimulus from non-preferred to preferred RF contents (Lesica and Stanley, 2004; Lesica *et al.*, 2006; Wang *et al.*, 2007) can reliably trigger a thalamic burst. Bursting is associated with high signal-to-noise, well-suited for stimulus detection (Sherman, 2001; Whitmire *et al.*, 2016). In addition, thalamic burst mode is known to augment the efficacy of retinal input to drive spiking in dLGN (Alitto *et al.*, 2019), and increases the probability of relay between thalamus and cortex (Svadlow and Gusev, 2001). This in turn might lead to depolarizing CT feedback, switching the thalamus to tonic mode and allowing more faithful, linear relay of information with a higher dynamic range, better suited for encoding of more finely graded details (Sherman, 2001; Béhuret *et al.*, 2015). Such a ‘wake-up-call’ for cortex (Sherman, 2001; Lesica and Stanley, 2004) could represent a neural implementation

of bottom-up attention in dLGN (*Hochstein and Ahissar, 2002*). To understand if CT feedback is indeed recruited for detailed perceptual analyses, an essential next step would be to measure the activity of L6 CT neurons under behaviorally relevant conditions. Interestingly, in the auditory system, activation of L6 CT feedback has been shown to influence sound perception, with enhancements of sound detection or discrimination behavior, depending on the relative timing between CT spiking and stimulus onset (*Guo et al., 2017*). Beyond having a broad impact on coding regimes and transmission, bursting in thalamus is also known to have specific computational properties, such as efficiently encoding high- and low-frequency information in parallel (*Mease et al., 2017*).

Stimulus-dependence of CT feedback effects

So far, most studies using naturalistic stimuli to probe dLGN responses have been performed in anesthetized animals and have not considered CT feedback (*Dan et al., 1996; Lesica and Stanley, 2004; Lesica et al., 2006; Lesica et al., 2007; Wang et al., 2007; Mante et al., 2005*). Similarly, most studies investigating the impact of CT feedback have relied on artificial stimuli (*Olsen et al., 2012; Denman and Contreras, 2015; Wang et al., 2006; Murphy and Sillito, 1987*). Comparing the effects of CT feedback during naturalistic movies and gratings, we found evidence that CT feedback modulates firing rates at the geniculate level in a stimulus-dependent fashion. What could be the relevant difference? For artificial stimuli, such as gratings and bars, it has long been known that CT feedback can enhance dLGN surround suppression by increasing responses to small stimuli and reducing responses to large stimuli (*Born et al., 2021; McClurkin and Marrocco, 1984; Murphy and Sillito, 1987; Jones et al., 2012; Wang et al., 2018; Cudeiro and Sillito, 1996; Andolina et al., 2013; Hasse and Briggs, 2017; Webb et al., 2002*). Such CT feedback-mediated enhancement of surround suppression might result from recruitment of a more narrow direct excitatory and a wider indirect inhibitory CT feedback component according to grating size (*Born et al., 2021*), with the balance shifting more towards direct excitation for small gratings and more towards indirect inhibition for large gratings. Size, however, is likely not the only determinant of relative recruitment of CT feedback circuits: for instance, V1 ablation or pharmacological suppression in anesthetized cats leads to more prominent reductions of dLGN surround suppression for iso- vs. cross-oriented gratings (*Cudeiro and Sillito, 1996; Sillito et al., 1993*), suggesting an additional role of stimulus context. For naturalistic stimuli with complex context, measurements in area V1 have already demonstrated that surround suppression is generally lower than for iso-oriented gratings, and is flexibly invoked depending on the specific statistics in the RF center and surround (*Coen-Cagli et al., 2015*). The differential effect of CT feedback on dLGN firing rates for full-screen naturalistic movies and iso-oriented gratings observed in our study might therefore be parsimoniously explained by differences in the relative strength of direct excitatory and indirect inhibitory CT feedback. It would be of prime interest to measure, in future experiments, size tuning curves with and without CT feedback using different stimuli, such as naturalistic movies, iso- and cross-oriented gratings. Given our results, we predict that CT feedback would affect firing rate responses to full-screen cross-oriented gratings more similarly to full-screen naturalistic movies than would iso-oriented gratings. Alternatively, CT feedback might change firing rates more consistently for lower contrast stimuli, such as our movies, where additional top-down inputs might be helpful for detection or discrimination.

Relationship between CT feedback and behavioral state

By measuring the effects of V1 suppression on movie responses during different behavioral states, and by measuring effects of behavioral state with and without CT feedback, we found that behavioral state and CT feedback had similar effects on dLGN responses, but seemed to operate via largely separate circuits. The lack of substantial dependence between effects of CT feedback and behavioral state on responses to our naturalistic movies is remarkable: neuromodulation accompanying changes in behavioral state will affect cortical layer 6, which receives dense cholinergic afferents from basal forebrain (*Radnikow and Feldmeyer, 2018*). Accordingly, in slice recordings, upon bath application of ACh, mouse V1 L6 CT neurons increase action potential firing (*Sundberg et al., 2018*). Potentially related, many V1 L6 CT neurons themselves increase activity during locomotion or arousal (*Augustinaite and Kuhn, 2020; Swadlow and Weyand, 1987*). Together, these studies would predict that effects of behavioral state should be augmented during CT feedback. Indeed, two recent studies investigating the interactions between CT feedback and arousal reported, during suppression of CT feedback,

less correlation between dLGN firing and pupil size (Molnár et al., 2021), and a loss of effects of behavioral state on dLGN tuning curves for temporal and spatial frequency, but not for spontaneous activity (Reinhold et al., 2021). Together with other findings more consistent with our results (Murata and Colonnese, 2018; Nestvogel and McCormick, 2022; Schröder et al., 2020), this discrepancy suggests that the degree to which effects of behavioral state in dLGN might be dependent on cortex is not fully understood.

If not inherited from CT feedback, which alternative circuits could mediate the effects of behavioral state in dLGN (Erisken et al., 2014; Aydın et al., 2018; Williamson et al., 2015)? Locomotion is accompanied by arousal (Vinck et al., 2015), which in turn involves various neuromodulatory influences [reviewed in Zaghera and McCormick, 2014]. For instance, norepinephrine from the locus coeruleus (LC) and acetylcholine (ACh) from the midbrain are known to act directly on the thalamus [reviewed in McCormick, 1992; Lee and Dan, 2012] and could drive some of the arousal-related depolarizing effects on firing rate independent of cortical feedback, for instance by blocking a long-lasting Ca^{2+} -dependent K^+ current (Sherman and Koch, 1986). In addition, electrical stimulation of the LC (Holdefer and Jacobs, 1994) and the parabrachial region (PBR) (Lu et al., 1993) within the mesencephalic locomotor region (MLR), and direct application of noradrenergic (Funke et al., 1993) and cholinergic (McCormick, 1992; Sillito et al., 1983) agonists within dLGN, are sufficient to reduce thalamic burst mode firing. Finally, at least part of the locomotion effects in dLGN might also be related to modulations of retinal output (Schröder et al., 2020; Liang et al., 2020). Indeed, two-photon calcium imaging of retinal ganglion cell boutons in dLGN (Liang et al., 2020) and SC (Schröder et al., 2020) revealed that their activity can be modulated by locomotion, albeit with an overall suppressive effect. In future studies, it will be key to further dissect the contributions of retinal, cortical and potentially collicular modulations, and the different neuromodulatory sources of behavioral state-related modulations in thalamic targets.

Materials and methods

Key resources table

Reagent type (species) or resource	Designation	Source or reference	Identifiers	Additional information
Recombinant DNA reagent	pAAV EF1a.DIO.hChR2(H134R)-eYFP.WPRE.hGH	Addgene	#20298-AAV9	
Recombinant DNA reagent	pAAV hSyn1-SIO-stGtACR2- FusionRed	Addgene	#105,677	
Strain, strain background (<i>Mus musculus</i>)	B6;129P2-Pvalb ^{tm1(cre)Arbr} /J	Jackson Laboratory	#008069	PV-Cre, Pvalb-Cre
Strain, strain background (<i>Mus musculus</i>)	B6.FVB(Cg)-Tg(Ntsr1-cre)GN220Gsat/Mmcd	MMRRC	#030648-UCD	Ntsr1-Cre
Chemical compound, drug	Metamizole	MSD Animal Health	Vetalgin	200 mg/kg
Chemical compound, drug	Buprenorphine	Bayer	Buprenovet	0.1 mg/kg
Chemical compound, drug	Lidocaine hydrochloride	bela-pharm		2 %
Chemical compound, drug	Meloxicam	Böhringer Ingelheim	Metacam	2 mg/kg
Chemical compound, drug	Isoflurane	CP Pharma		in oxygen
Chemical compound, drug	Bepanthen	Bayer		eye ointment
Chemical compound, drug	DAPI-containing mounting medium	Vector Laboratories Ltd		
Chemical compound, drug	Vectashield DAPI H-1000	Vector Laboratories Ltd		
Chemical compound, drug	Dil	Invitrogen		electrode stain
Software, algorithm	Python 3.6	http://python.org	RRID:SCR_008394	
Software, algorithm	R	R Core Team, 2017	RRID:SCR_001905	
Software, algorithm	MATLAB R2019b	Mathworks	RRID:SCR_001622	
Software, algorithm	EXPO	https://sites.google.com/a/nyu.edu/expo/home		visual stimulus display

Continued on next page

Continued

Reagent type (species) or resource	Designation	Source or reference	Identifiers	Additional information
Software, algorithm	Kilosort	<i>Pachitariu et al., 2016</i>	RRID:SCR_016422	
Software, algorithm	Spyke	<i>Spacek et al., 2009</i>		
Software, algorithm	Fiji/ImageJ	NIH	RRID:SCR_003070	
Software, algorithm	DataJoint	<i>Yatsenko et al., 2018</i>	RRID:SCR_014543	

Surgical procedures

Experiments were carried out in 6 adult PV-Cre mice (median age at first recording session: 23.5 weeks; B6;129P2-Pvalb^{tm1(cre)Arbr/J}; #008069, Jackson Laboratory) and 3 adult Ntsr1-Cre mice (median age: 29.4 weeks; B6.FVB(Cg)-Tg(Ntsr1-cre)GN220Gsat/Mmcd; #030648-UCD, MMRRCC) of either sex. Thirty minutes prior to the surgical procedure, mice were injected with an analgesic (Metamizole, 200 mg/kg, sc, MSD Animal Health, Brussels, Belgium). To induce anesthesia, animals were placed in an induction chamber and exposed to isoflurane (5% in oxygen, CP-Pharma, Burgdorf, Germany). After induction of anesthesia, mice were fixated in a stereotaxic frame (Drill & Microinjection Robot, Neurostar, Tuebingen, Germany) and the isoflurane level was lowered (0.5–2% in oxygen), such that a stable level of anesthesia could be achieved as judged by the absence of a pedal reflex. Throughout the procedure, the eyes were covered with an eye ointment (Bepanthen, Bayer, Leverkusen, Germany) and a closed loop temperature control system (ATC 1000, WPI Germany, Berlin, Germany) ensured that the animal's body temperature was maintained at 37 °C. At the beginning of the surgical procedure, an additional analgesic was administered (Buprenorphine, 0.1 mg/kg, sc, Bayer, Leverkusen, Germany) and the animal's head was shaved and thoroughly disinfected using iodine solution (Braun, Melsungen, Germany). Before performing a scalp incision along the midline, a local analgesic was delivered (Lidocaine hydrochloride, sc, bela-pharm, Vechta, Germany). The skin covering the skull was partially removed and cleaned from tissue residues with a drop of H₂O₂ (3%, AppliChem, Darmstadt, Germany). Using four reference points (bregma, lambda, and two points 2 mm to the left and to the right of the midline respectively), the animal's head was positioned into a skull-flat configuration. The exposed skull was covered with OptiBond FL primer and adhesive (Kerr dental, Rastatt, Germany) omitting three locations: V1 (AP: -2.8 mm, ML: -2.5 mm), dLGN (AP: -2.3 mm, ML: -2 mm), and a position roughly 1.5 mm anterior and 1 mm to the right of bregma, designated for a miniature reference screw (00–96 X 1/16 stainless steel screws, Bilaney) soldered to a custom-made connector pin. Two µL of the adeno-associated viral vector rAAV9/1. EF1a.DIO.hChR2(H134R)-eYFP.WPRE.hGH (Addgene, #20298-AAV9) was dyed with 0.3 µL fast green (Sigma-Aldrich, St. Louis, USA). After performing a small craniotomy over V1, in PV-Cre mice a total of ~ 0.5 µL of this mixture was injected across the entire depth of cortex (0.05 µL injected every 100 µm, starting at 1000 µm and ending at 100 µm below the brain surface), using a glass pipette mounted on a Hamilton syringe (SYR 10 µL 1701 RN no ND, Hamilton, Bonaduz, Switzerland). In V1 of Ntsr1-Cre mice, we injected 0.35 µL of stGtACR2 (pAAV_hSyn1-SIO-stGtACR2-FusionRed, Addgene, #105677; 0.05 µL injected every 100 µm, starting at 1000 µm and ending at 500 µm below the brain surface). A custom-made lightweight stainless steel head bar was positioned over the posterior part of the skull such that the round opening in the bar was centered on V1/dLGN. The head bar was attached with dental cement (Ivoclar Vivadent, Ellwangen, Germany) to the primer/adhesive. The opening was later filled with the silicone elastomer sealant Kwik-Cast (WPI Germany, Berlin, Germany). At the end of the procedure, an antibiotic ointment (Imex, Merz Pharmaceuticals, Frankfurt, Germany) or iodine-based ointment (Braunodivon, 10%, B. Braun, Melsungen, Germany) was applied to the edges of the wound and a long-term analgesic (Meloxicam, 2 mg/kg, sc, Böhringer Ingelheim, Ingelheim, Germany) was administered and for 3 consecutive days. For at least 5 days post-surgery, the animal's health status was assessed via a score sheet. After at least 1 week of recovery, animals were gradually habituated to the experimental setup by first handling them and then simulating the experimental procedure. To allow for virus expression, neural recordings started no sooner than 3 weeks after injection. On the day prior to the first day of recording, mice were fully anesthetized using the same procedures as described for the initial surgery, and

a craniotomy (ca. 1.5 mm²) was performed over dLGN and V1 and re-sealed with Kwik-Cast (WPI Germany, Berlin, Germany). As long as the animals did not show signs of discomfort, the long-term analgesic Metacam was administered only once at the end of surgery, to avoid any confounding effect on experimental results. Recordings were performed daily and continued for as long as the quality of the electrophysiological signals remained high.

Electrophysiological recordings, optogenetic suppression of V1, perfusion

Head-fixed mice were placed on an air-cushioned Styrofoam ball, which allowed the animal to freely move. Two optical computer mice interfaced with a microcontroller (Arduino Duemilanove) sampled ball movements at 90 Hz. To record eye position and pupil size, the animal's eye was illuminated with infrared light and monitored using a zoom lens (Navitar Zoom 6000) coupled with a camera (Guppy AVT camera; frame rate 50 Hz, Allied Vision, Exton, USA). Extracellular signals were recorded at 30 kHz (Blackrock microsystems). For each recording session, the silicon plug sealing the craniotomy was removed. For V1 recordings, a 32- or 64 channel silicon probe (Neuronexus, A1 × 32-5 mm-25-177, A1 × 32Edge-5mm-20-177 A32 or A1 × 64-Poly2-6mm-23s-160) was lowered into the brain to a median depth of 1025 μm. For dLGN recordings, a 32-channel linear silicon probe (Neuronexus A1 × 32Edge-5mm-20-177 A32) was lowered to a depth of ~2300–3611 μm below the brain surface. We judged recording sites to be located in dLGN based on the characteristic progression of RFs from upper to lower visual field along the electrode shank (Piscopo et al., 2013, Figure 1—figure supplement 1b), the presence of responses strongly modulated at the temporal frequency of the drifting gratings (F1 response), and the preference of responses to high temporal frequencies (Grubb and Thompson, 2003; Piscopo et al., 2013). For post hoc histological reconstruction of the recording site, the electrode was stained with Dil (Invitrogen, Carlsbad, USA) for one of the final recording sessions.

For photostimulation of V1 PV +inhibitory interneurons or photosuppression of V1 L6CT neurons, an optic fiber (910 μm diameter, Thorlabs, Newton, USA) was coupled to a light-emitting diode (LED, center wavelength 470 nm, M470F1, Thorlabs, Newton, USA; or center wavelength 465 nm, LEDC2_465/635_SMA, Doric Lenses, Quebec, Canada) and positioned with a micromanipulator less than 1 mm above the exposed surface of V1. A black metal foil surrounding the tip of the head bar holder prevented most of the photostimulation light from reaching the animal's eyes. To ensure that the photostimulation was effective, the first recording session for each mouse was carried out in V1. Only if the exposure to light reliably induced suppression of V1 activity was the animal used for subsequent dLGN recordings. For gratings, photostimulation started either 0.1 s before stimulus onset and ended 0.1 s after stimulus offset (2 experiments), or photostimulation started 0.3 s before stimulus onset and ended 0.2 s after stimulus offset (11 experiments), or photostimulation started 0.3 s before stimulus onset and ended 0.45 s after stimulus offset (12 experiments). For movie clips, photostimulation started either 0.1 s before stimulus onset and ended 0.1 s after stimulus offset (2 experiments), or photostimulation started 0.3 s before stimulus onset and ended 0.45 s after stimulus offset (45 experiments). LED light intensity was adjusted on a daily basis to evoke reliable effects (median intensity: 13.66 mW/mm² for activating ChR2 in PV-Cre mice, and 10.84 mW/mm² for activating stGtACR2 in Ntsr1-Cre mice, as measured at the tip of the optic fiber). Since the tip of the fiber never directly touched the surface of the brain, and since the clarity of the surface of the brain varied (generally decreasing every day following the craniotomy), the light intensity delivered even to superficial layers of V1 was inevitably lower. Importantly, changes in dLGN firing rates induced by V1 suppression (FMI, see below) did not differ, on average, from those induced by behavioral state (RMI, see below) (firing rate: FMI 0.20 vs. RMI 0.15, LMM: $F_{1,145.7} = 3.02$, $p = 0.08$; burst ratio: FMI -0.27 vs. RMI -0.28, $F_{1,124.0} = 0.002$, $p = 0.97$; sparseness: FMI -0.12 vs. RMI -0.14, $F_{1,144.9} = 1.03$, $p = 0.31$; reliability: FMI -0.084 vs. -0.037, $F_{1,183.0} = 1.96$, $p = 0.16$; Figure 6c), indicating that optogenetic stimulation effects were not outside the physiological range.

After the final recording session, mice were first administered an analgesic (Metamizole, 200 mg/kg, sc, MSD Animal Health, Brussels, Belgium) and following a 30 min latency period were transcardially perfused under deep anesthesia using a cocktail of Medetomidin (Domitor, 0.5 mg/kg, Vetoquinol, Ismaning, Germany), Midazolam (Climasol, 5 mg/kg, Ratiopharm, Ulm, Germany) and Fentanyl (Fentadon, 0.05 mg/kg, Dechra Veterinary Products Deutschland, Aulendorf, Germany) (ip). A few animals, which were treated according to a different license, were anesthetized with sodium

pentobarbital (Narcoren, 400 mg/kg, ip, Böhringer Ingelheim, Ingelheim, Germany). Perfusion was first done with Ringer's lactate solution followed by 4% paraformaldehyde (PFA) in 0.2 M sodium phosphate buffer (PBS).

Histology

To verify recording site and virus expression, we performed histological analyses. Brains were removed, postfixed in PFA for 24 hr, and then rinsed with and stored in PBS at 4 °C. Slices (40 μm) were cut using a vibratome (Leica VT1200 S, Leica, Wetzlar, Germany), stained with DAPI solution before (DAPI, Thermo Fisher Scientific; Vectashield H-1000, Vector Laboratories) or after mounting on glass slides (Vectashield DAPI), and coverslipped. A fluorescent microscope (BX61, Olympus, Tokyo, Japan) was used to inspect slices for the presence of yellow fluorescent protein (eYFP) and Dil. Recorded images were processed using FIJI (Rueden et al., 2017; Schindelin et al., 2012).

Visual stimulation

Visual stimuli were presented on a liquid crystal display (LCD) monitor (Samsung SyncMaster 2233RZ, 47 × 29 cm, 1680 × 1050 resolution at 60 Hz, mean luminance 50 cd/m²) positioned at a distance of 25 cm from the animal's right eye (spanning ~ 108 × 66°, small angle approximation) using custom written software (EXPO, <https://sites.google.com/a/nyu.edu/expo/home>). The display was gamma-corrected for the presentation of artificial stimuli, but not for movies (see below).

To measure receptive fields (RFs), we mapped the ON and OFF subfields with a sparse noise stimulus. The stimulus consisted of nonoverlapping white and black squares on a square grid, each flashed for 200ms. For dLGN recordings, the square grid spanned 60° on a side, while individual squares spanned 5° on a side. For a single experiment, the vertical extent was reduced to 50°. For subsequent choices of stimuli, RF positions and other tuning preferences were determined online after each experiment based on multiunit activity, that is high-pass filtered signals crossing a threshold of 4.5–6.5 SD.

We measured single unit orientation preference by presenting full-screen, full-contrast drifting sinusoidal gratings of either 12 (23 experiments) or 8 (2 experiments) different, pseudo-randomly interleaved orientations (30° or 45° steps). For dLGN recordings, spatial frequency was either 0.02 cyc/° (17 experiments) or 0.04 cyc/° (8 experiments) and temporal frequency was either 2 Hz (2 experiments) or 4 Hz (23 experiments). One blank condition (i.e. mean luminance gray screen) was included to allow measurements of spontaneous activity. The stimulus duration was either 2 s (23 experiments) or 5 s (2 experiments), with an interstimulus interval (ISI) of 2.4 s (21 experiments) or 1.25 s (2 experiments). For two Ntsr1-Cre experiments, ISIs varied and were either 0.58 s or 1.09 s.

For laminar localization of neurons recorded in V1, we presented a full-screen, contrast-reversing checkerboard at 100% contrast, with a spatial frequency of either 0.01 cyc/° (2 experiments) or 0.02 cyc/° (5 experiments) and a temporal frequency of 0.5 cyc/s.

Movies were acquired using a hand-held consumer-grade digital camera (Canon PowerShot SD200) at a resolution of 320 × 240 pixels and 60 frames/s. Movies were filmed close to the ground in a variety of wooded or grassy locations in Vancouver, BC, and contained little to no forward/backward optic flow, but did contain simulated gaze shifts (up to 275°/s), generated by manual camera movements (for example movies, see *Figure 1—video 1* and *Figure 1—video 2*). Focus was kept within 2 m and exposure settings were set to automatic. The horizontal angle subtended by the camera lens was 51.6°. No display gamma correction was used while presenting movies, since consumer-grade digital cameras are already gamma corrected for consumer displays (Poynton, 1998). For presentation, movies were cut into 5 s clips and converted from color to grayscale. Movie clips were presented full-screen with an ISI of 1.25 s (43 experiments). For two Ntsr1-Cre experiments, ISIs varied and were either 0.58 s or 1.08 s.

Spike sorting

To obtain single unit activity from extracellular recordings, we used the open source, Matlab-based, automated spike sorting toolbox Kilosort (Pachitariu et al., 2016). Resulting clusters were manually refined using Spyke (Spacek et al., 2009), a Python application that allows the selection of channels and time ranges around clustered spikes for realignment, as well as representation in 3D space using dimension reduction (multichannel PCA, ICA, and/or spike time). In 3D, clusters were then further split

via a gradient-ascent based clustering algorithm (GAC) (Swindale and Spacek, 2014). Exhaustive pairwise comparisons of similar clusters allowed the merger of potentially over-clustered units. For subsequent analyses, we inspected autocorrelograms and mean voltage traces, and only considered units that displayed a clear refractory period and a distinct spike waveshape. All further analyses were carried out using the DataJoint framework (Yatsenko et al., 2018) with custom-written code in Python.

Response characterization

We used current source density (CSD) analysis for recordings in area V1 to determine the laminar position of electrode contacts. To obtain the LFP data we first down-sampled the signal to 1 kHz before applying a bandpass filter (4–90 Hz, 2nd-order Butterworth filter). We computed the CSD from the second spatial derivative of the local field potentials (Mitzdorf, 1985), and assigned the base of layer 4 to the contact that was closest to the earliest CSD polarity inversion. The remaining contacts were assigned to supragranular, granular and infragranular layers, assuming a thickness of ~1 mm for mouse visual cortex (Heumann et al., 1977).

In recordings targeting dLGN, we used the envelope of multi-unit spiking activity (MUAe) (van der Togt et al., 2005) to determine RF progression (Figure 1—figure supplement 1b). Briefly, we full-wave rectified the high-pass filtered signals (cutoff frequency: 300 Hz, 4th-order non-causal Butterworth filter) before performing common average referencing by subtracting the median voltage across all channels in order to eliminate potential artifacts (e.g. movement artifacts). We then applied a low-pass filter (cutoff frequency: 500 Hz, Butterworth filter) and down-sampled the signal to 2 kHz. Recording sessions for which RFs did not show the retinotopic progression typical of dLGN (Figure 1—figure supplement 1b; Piscopo et al., 2013) were excluded from further analysis.

Each unit's peristimulus time histogram (PSTH, i.e. the response averaged over trials) was calculated by convolving a Gaussian of width $2\sigma = 20$ ms with the spike train collapsed across all trials, separately for each condition.

We defined bursts according to Lu et al., 1992, which required a silent period of at least 100ms before the first spike in a burst, followed by a second spike with an interspike interval < 4 ms. Imposing the silent period was found to be crucial for separating dLGN 'low threshold calcium bursts' from high-frequency firing in extracellular recordings (Lu et al., 1992); note however, that 'low-threshold calcium bursts' can only be unequivocally detected in intracellular recordings or calcium imaging. Any subsequent spikes with preceding interspike intervals < 4 ms were also considered to be part of the burst. All other spikes were regarded as tonic. We computed a burst ratio (the number of burst spikes divided by the total number of spikes) and compared this ratio in conditions with CT feedback intact vs. V1 suppression or during locomotion vs. stationary conditions. PSTHs for burst spikes were calculated by only considering spikes that were part of bursts before collapsing across trials and convolving with the Gaussian kernel (see above). PSTHs for non-burst spikes were calculated in an analogous way.

To quantify the effect of V1 suppression on various response properties, we defined the feedback modulation index (FMI) as

$$\text{FMI} = \frac{\text{feedback} - \text{suppression}}{\text{feedback} + \text{suppression}} \quad (1)$$

Characterization of responses to naturalistic movie clips

Signal to noise ratio (SNR) was calculated according to Baden et al., 2016 by

$$\text{SNR} = \frac{\text{Var}\langle C_r \rangle_t}{\text{Var}[C]_r} \quad (2)$$

where C is the T by R response matrix (time samples by stimulus repetitions) and $\langle \rangle_x$ and $\text{Var}[\]_x$ denote the mean and variance across the indicated dimension, respectively. If all trials were identical such that the mean response was a perfect representative of the response, SNR would equal 1.

The sparseness S of a PSTH was calculated according to Vinje and Gallant, 2000 by

$$S = \left(1 - \frac{\left(\sum_{i=1}^n r_i/n \right)^2}{\sum_{i=1}^n r_i^2/n} \right) \left(\frac{1}{1-1/n} \right) \quad (3)$$

where $r_i \geq 0$ is the signal value in the i^{th} time bin, and n is the number of time bins. Sparseness ranges from 0 to 1, with 0 corresponding to a uniform signal, and 1 corresponding to a signal with all of its energy in a single time bin.

Response reliability was quantified according to **Goard and Dan, 2009** as the mean pairwise correlation of all trial pairs of a unit's single-trial responses. Single-trial responses were computed by counting spikes in 20ms, overlapping time bins at 1ms resolution. Pearson's correlation was calculated between all possible pairs of trials, and then averaged across trials per condition.

To detect response peaks in trial raster plots and measure their widths, clustering of spike times collapsed across trials was performed using the gradient ascent clustering (GAC) algorithm (**Swindale and Spacek, 2014**), with a characteristic neighborhood size of 20ms. Spike time clusters containing less than 5 spikes were discarded. The center of each detected cluster of spike times was matched to the nearest peak in the PSTH. A threshold of $\theta = b + 3$ Hz was applied to the matching PSTH peak, where $b = 2 \text{ median}(x)$ is the baseline of each PSTH x . Peaks in the PSTH that fell below θ were discarded, and all others were kept as valid peaks. Peak widths were measured as the temporal separation of the middle 68% (16th to 84th percentile) of spike times within each cluster.

To determine whether V1 suppression changes dLGN responses in a divisive or subtractive manner, we fit a threshold-linear model using repeated random subsampling cross-validation. To this end, we first selected a random set of 50% of the trials for each condition for fitting to the timepoint-by-

timepoint responses a threshold linear model given by $R_{\text{supp}} = s R_b + b$, where $R_{\text{supp}} > 0$, with s repre-

senting the slope and b the offset. Fitting was done using non-linear least squares (`scipy.optimize.curve_fit`). Throughout **Figure 2**, we report the resulting x -intercept as the threshold. We evaluated goodness of fit (R^2) for the other 50% of trials not used for fitting. We repeated this procedure 1000 times and considered threshold and slope as significant if the central 95% of their distribution did not include 0 and 1, respectively.

Characterization of responses to drifting gratings

For display of spike rasters (**Figure 3**), trials were sorted by condition. We computed orientation tuning curves by fitting a sum of two Gaussians of the same width with peaks 180° apart:

$$R(\theta) = R_0 + R_p e^{-\frac{(\theta - \theta_p)^2}{2\sigma^2}} + R_n e^{-\frac{(\theta - \theta_p + 180)^2}{2\sigma^2}} \quad (4)$$

In this expression, θ is stimulus orientation (0–360°). The function has five parameters: preferred orientation θ_p , tuning width σ , baseline response (offset independent of orientation) R_0 , response at the preferred orientation R_p , and response at the null orientation R_n .

Orientation selectivity was quantified according to **Bonhoeffer et al., 1995; Olsen et al., 2012** as

$$\text{OSI} = \frac{\sqrt{(\sum R_k \sin(2\theta_k))^2 + (\sum R_k \cos(2\theta_k))^2}}{\sum R_k} \quad (5)$$

where R_k is the response to the k th direction given by θ_k . We determined OSI for each unit during both feedback and suppression conditions.

We computed the first harmonic of the response R from the spike trains according to **Carandini et al., 1997** to obtain the amplitude and phase of the best-fitting sinusoid, which has the same temporal frequency as the stimulus. For each trial, we calculated

$$R = (1/D) \sum_k \cos(2\pi f t_k) + i \sin(2\pi f t_k) \quad (6)$$

where D is the stimulus duration, f is the temporal frequency of the stimulus, and the t_k are the times of the individual spikes. We excluded the first cycle to avoid contamination by the onset

response. For (Figure 3g), we calculated average amplitude F_1 by obtaining the absolute value of the complex number R on each trial, before averaging across trials, to avoid potential confounds due to differences in response phase across conditions. For the comparison of response phase, we focused on the orientation which elicited the maximal cycle average response across both feedback and suppression conditions.

Cell typing

Units were classified as suppressed by contrast (SbC) or not suppressed by contrast (non-SbC) by comparing their mean firing rates during full-screen drifting grating presentation to their mean firing rates during blank-screen presentation. Units were classified as SbC if they were visually responsive to gratings (see below) and had a median z-scored response across orientation conditions of ≤ -3 during at least one grating experiment. Otherwise, units were classified as non-SbC. SbC units seem to constitute a sizeable fraction in our dataset, which is similar to our previous results (Román Rosón et al., 2019), where SbC was also found to be among the overrepresented retinal ganglion cell (RGC) types providing input to dLGN.

To identify electrode channels within the dLGN, and their relative depth, which could be useful to distinguish between shell and core, we concentrated on the RF progression as assessed with MUAe maps that were constructed using sparse noise experiments. Because RF progression is mainly along elevation, amplitudes of MUAe for each channel were collapsed across azimuth and then range normalized. Channels with normalized amplitudes higher than an empirically set threshold (0.4) were considered part of dLGN. Non-detected channels located between detected channels were also included.

Direction selectivity index (DSI, Niell and Stryker, 2008) was calculated for each unit as

$$DSI = \frac{R_p - R_n}{R_p + R_n + 2R_0} \quad (7)$$

where R_p and R_n are the firing rates in the preferred and null directions, respectively, extracted from tuning curves fit to drifting grating responses (see above), and R_0 is baseline firing rate independent of orientation.

The RF distance from the center of the screen was calculated for each unit by finding the position of the MUAe RF for the channel on which the unit's mean spike waveform had the largest amplitude.

Exclusion criteria

Neurons with mean evoked firing rates < 0.01 spikes/s were excluded from further analysis. For movie clips, only neurons with $SNR \geq 0.015$ in at least one of the conditions in an experiment were considered. Of this population, 2 neurons were excluded from the analysis of the parameters returned by the threshold linear model, because their R^2 was lt_0 . For gratings, we converted firing rates in response to each orientation to z-scores relative to responses to the mean luminance gray screen. We only considered visually responsive neurons, with an absolute z-scored response ≥ 2.5 to at least 1 orientation. For the analysis of response phase, we only considered neurons with a peak of the cycle average response of at least 10 Hz in both feedback and suppression conditions, and an F_1/F_0 ratio of at least 0.25.

Locomotion

We used the Euclidean norm of three perpendicular components of ball velocity (roll, pitch, and yaw) to compute animal running speed. For the analysis of neural responses as a function of behavioral state, locomotion trials were defined as those for which speed exceeded 1 cm/s for at least 50% of the stimulus presentation, and stationary trials as those for which speed fell below 0.25 cm/s for at least 50% of the stimulus presentation. To quantify the effect of running vs. sitting on various response properties, the run modulation index (RMI) was defined as

$$RMI = \frac{\text{running} - \text{sitting}}{\text{running} + \text{sitting}} \quad (8)$$

Eye tracking

The stimulus viewing eye was filmed using an infrared camera under infrared LED illumination. Pupil position was extracted from the videos using a custom, semi-automated algorithm. Briefly, each video

frame was equalized using an adaptive bi-histogram equalization procedure, and then smoothed using median and bilateral filters. The center of the pupil was detected by taking the darkest point in a convolution of the filtered image with a black square. Next, the peaks of the image gradient along lines extending radially from the center point were used to define the pupil contour. Lastly, an ellipse was fit to the contour, and the center of this ellipse was taken as the position of the pupil. A similar procedure was used to extract the position of the corneal reflection (CR) of the LED illumination. Eye blinks were automatically detected and the immediately adjacent data points were excluded. Adjustable algorithm parameters were set manually for each experiment. Output pupil position time-courses were lightly smoothed, and unreliable segments were automatically removed according to a priori criteria. Finally, the CR position was subtracted from the pupil position to eliminate translational eye movements, and pupil displacement in degrees relative to the baseline (median) position was determined by

$$\theta = 2 \frac{\arcsin(d/2)}{r} \tag{9}$$

where d is the distance between the pupil and the baseline position, and $r = 1.25$ mm is the radius of the eye (Remtulla and Hallett, 1985). Angular displacement was computed separately for x and y directions.

Eye position standard deviation was computed by first taking the standard deviation of the horizontal eye position at each time point across trials, and then averaging over the 5 s during which the visual stimulus was presented. We focused on horizontal eye position because horizontal and vertical eye movements tend to occur in tandem under head-fixed conditions, and the horizontal position variance is larger (Sakatani and Isa, 2007), thus serving as a better proxy for variance in 2D. For each experiment, trials were sorted either by the presence of optogenetic suppression of CT feedback (Figure 1—figure supplement 2h), or by the behavioral state of the animal as described above (Figure 5—figure supplement 1h). The eye position standard deviation FMI and RMI (Figure 1—figure supplement 2i and Figure 5—figure supplement 1i) were calculated in the same manner as for the neural response properties.

Table 1. Breakdown of sample sizes (N) for the analyses of neural data. See text for details.

	Neurons	Mice
Figure 1f–i	65	6
Figure 2e–i	63	6
Figure 3c–e and g	44	4
Figure 3f	28	4
Figure 3h–i	35	3
Figure 4a–b	39	4
Figure 5c–f,i–l	66	6
Figure 6, a _{1,3}	64	6
Figure 6, a ₂	58	6
Figure 6, a ₄	63	6
Figure 6, b ₁ and b ₃	63	6
Figure 6, b ₂	58	6
Figure 6, b ₄	62	6
Figure 6, C _{1,3} and 4	59	6
Figure 6, c ₂	56	6
Figure 1—figure supplement 2a	65	6
Figure 1—figure supplement 2b,g	57	6
Figure 1—figure supplement 2c	63	6
Figure 1—figure supplement 2d–f, i	64	6
Figure 1—figure supplement 2h		6
Figure 1—figure supplement 3a,c	39	4
Figure 1—figure supplement 3b,j	63	6
Figure 1—figure supplement 3d	54	6
Figure 1—figure supplement 3e	64	6
Figure 1—figure supplement 3f, h	38	4
Figure 1—figure supplement 3g	62	6
Figure 1—figure supplement 3i	53	6
Figure 1—figure supplement 4e–h	62	3
Figure 1—figure supplement 4l–n	73	3
Figure 1—figure supplement 5c,d,h,i	19	1
Figure 1—figure supplement 6c–f	35	5
Figure 1—figure supplement 6g	65	6
Figure 1—figure supplement 6h	56	3
Figure 1—figure supplement 6i	64	6
Figure 1—figure supplement 6j	54	3
Figure 3—figure supplement 1a,c,e	44	4
Figure 3—figure supplement 1b,f,h,i	42	4
Figure 3—figure supplement 1d	36	4
Figure 3—figure supplement 1g	40	4

Table 1 continued on next page

Table 1 continued

	Neurons	Mice
Figure 3—figure supplement 1i	35	4
Figure 4—figure supplement 1a	42	4
Figure 4—figure supplement 1b,k,i	43	4
Figure 4—figure supplement 1c-d,g,i	65	6
Figure 4—figure supplement 1e	36	3
Figure 4—figure supplement 1f	29	3
Figure 4—figure supplement 1h, i	44	4
Figure 5—figure supplement 1a	66	6
Figure 5—figure supplement 1g	56	6
Figure 5—figure supplement 1c	57	6
Figure 5—figure supplement 1d-f, i	65	6
Figure 5—figure supplement 1h		6
Figure 5—figure supplement 2d-g	57	6
Figure 6—figure supplement 1, a ₁ , b ₁ , c ₁	37	4
Figure 6—figure supplement 1, a ₂ , c ₂	34	3
Figure 6—figure supplement 1, b ₂	33	3

Analysis of pupil dilation during movies

Following (Reimer et al., 2014), changes in pupil area collected during movie clip presentation (e.g. Figure 5—figure supplement 2a) were measured at 20ms resolution. Spiking responses were binned to match the temporal resolution of the pupil change signal, masked to exclude periods of locomotion (> 0.25 cm/s), and then further masked to only include bins corresponding to the top or bottom quartiles (dilation or constriction) of the pupil area dynamics. Neural responses (firing rate, reliability, and SNR) were then calculated separately for the remaining unmasked top or bottom pupil quartile bins. To make our analyses comparable to those obtained for V1 by Reimer et al., 2014, we considered pupil-related response modulations as a function of instantaneous firing rate. For Figure 5—figure supplement 2c, we therefore separated each time point of the PSTH, determined without taking pupil size into account, into firing rate quartiles. We then computed, for each neuron, the % change in median firing rates between top and bottom pupil quartiles in each of the four firing rate quartiles. While Reimer et al., 2014 observed a multi-

plicative effect of pupil size change on V1 responses to movies, our results for dLGN rather resemble an inverted U-shape pattern.

Statistical methods

To assess statistical significance, we fitted and examined multilevel linear models (Gelman and Hill, 2007). Such models take into account the hierarchical structure present in our data (i.e. neurons nested in experiments, experiments nested in recording sessions, recordings sessions nested in animals), and eliminate the detrimental effect of structural dependencies on the likelihood of Type I errors (false positive reports) (Aarts et al., 2014). By considering the nested structure of the data, multilevel models also eliminate the need for ‘pre-selecting’ data sets, such as one out of several experiments repeatedly performed on the same neurons. Whenever we have several experiments per neuron, we include all of them, and also show them in the scatter plots (‘observations’). We provide the sample size for each analysis in Table 1. To account for repeated measurements, we fitted by-neuron random intercepts and random slopes over measurement conditions (V1 control vs V1 suppressed). By-neuron random intercepts model, the difference between neurons in overall firing rates, while by-neuron random slopes model between-neuron differences in how they responded to V1 suppression. Where possible, we included random intercepts for experiments nested in recording sessions, nested in mice, and random intercepts and slopes for neurons partially crossed in experiments. In cases where the model structure was too complex for a given data set (i.e. did not converge, or gave singular fits), we simplified the random effects structure by removing one or more terms. We fit these models in R (R Core Team, 2017), using the lme4 package (Bates et al., 2015). We estimated F-values, their degrees of freedom, and the corresponding p-values using the Satterthwaite approximation (Luke, 2017) implemented by the lmerTest package (Kuznetsova et al., 2017). For each analysis, we provide the exact model specification and the complete output of the model (see Data and code availability).

Throughout the manuscript, uncertainty in estimated regression slopes is represented as $slope \pm x$, where x is $2 \times$ the estimated standard error of the slope.

Acknowledgements

This research was supported by the German Research Foundation (DFG) SFB 870 TP 19, project number 118803580 (LB), DFG BU 1808/5-1 (LB), DFG SFB 1233, Robust Vision: Inference Principles and Neural Mechanisms, TP 13, project number: 276693517 (LB), and by an add-on fellowship of the Joachim Herz Stiftung (GB). We thank D Metzler for discussions regarding the multi-level modeling, M Sotgia for lab management and support with animal handling and histology, S Schörnich for IT support, and B Grothe for providing excellent research infrastructure.

Additional information

Funding

Funder	Grant reference number	Author
Deutsche Forschungsgemeinschaft	SFB 1233, Robust Vision: Inference Principles and Neural Mechanisms, TP 13, project number: 276693517	Laura Busse
Deutsche Forschungsgemeinschaft	SFB 870, TP 19, project number: 118803580	Laura Busse
Deutsche Forschungsgemeinschaft	DFG BU 1808/5-1	Laura Busse
Joachim Herz Stiftung	add-on fellowship	Gregory Born

The funders had no role in study design, data collection and interpretation, or the decision to submit the work for publication.

Author contributions

Martin A Spacek, Conceptualization, Data curation, Investigation, Methodology, Software, Visualization, Writing – review and editing; Davide Crombie, Data curation, Methodology, Software, Writing – review and editing; Yannik Bauer, Investigation, Software, Visualization; Gregory Born, Data curation, Software, Visualization, Writing - original draft, Writing – review and editing; Xinyu Liu, Investigation, Software; Steffen Katzner, Data curation, Formal analysis, Software, Visualization, Writing – review and editing; Laura Busse, Conceptualization, Data curation, Funding acquisition, Project administration, Supervision, Writing - original draft, Writing – review and editing

Author ORCIDs

Martin A Spacek <http://orcid.org/0000-0002-9519-3284>

Yannik Bauer <http://orcid.org/0000-0003-2613-6443>

Gregory Born <http://orcid.org/0000-0003-0430-3052>

Steffen Katzner <http://orcid.org/0000-0002-4424-2197>

Laura Busse <http://orcid.org/0000-0002-6127-7754>

Ethics

All procedures complied with the European Communities Council Directive 2010/63/EU and the German Law for Protection of Animals, and were approved by local authorities, following appropriate ethics review.

Decision letter and Author response

Decision letter <https://doi.org/10.7554/eLife.70469.sa1>

Author response <https://doi.org/10.7554/eLife.70469.sa2>

Additional files

Supplementary files

- Transparent reporting form

Data availability

Data and source code used to generate the figures in the manuscript has been made available on G-Node (<https://doi.org/10.12751/g-node.58bc8k>).

The following dataset was generated:

References

- Aarts E, Verhage M, Veenvliet JV, Dolan CV, van der Sluis S. 2014. A solution to dependency: using multilevel analysis to accommodate nested data. *Nature Neuroscience* **17**:491–496. DOI: <https://doi.org/10.1038/nn.3648>
- Alitto HJ, Weyand TG, Usrey WM. 2005. Distinct properties of stimulus-evoked bursts in the lateral geniculate nucleus. *The Journal of Neuroscience* **25**:514–523. DOI: <https://doi.org/10.1523/JNEUROSCI.3369-04.2005>
- Alitto H, Rathbun DL, Vandeleest JJ, Alexander PC, Usrey WM. 2019. The Augmentation of Retinogeniculate Communication during Thalamic Burst Mode. *The Journal of Neuroscience* **39**:5697–5710. DOI: <https://doi.org/10.1523/JNEUROSCI.2320-18.2019>
- Andolina IM, Jones HE, Sillito AM. 2013. Effects of cortical feedback on the spatial properties of relay cells in the lateral geniculate nucleus. *Journal of Neurophysiology* **109**:889–899. DOI: <https://doi.org/10.1152/jn.00194.2012>
- Augustinaite S, Kuhn B, Helm PJ, Heggelund P. 2014. NMDA spike/plateau potentials in dendrites of thalamocortical neurons. *The Journal of Neuroscience* **34**:10892–10905. DOI: <https://doi.org/10.1523/JNEUROSCI.1205-13.2014>
- Augustinaite S, Kuhn B. 2020. Complementary Ca²⁺ Activity of Sensory Activated and Suppressed Layer 6 Corticothalamic Neurons Reflects Behavioral State. *Current Biology* **30**:3945–3960. DOI: <https://doi.org/10.1016/j.cub.2020.07.069>
- Aydın Ç, Couto J, Giugliano M, Farrow K, Bonin V. 2018. Locomotion modulates specific functional cell types in the mouse visual thalamus. *Nature Communications* **9**:4882. DOI: <https://doi.org/10.1038/s41467-018-06780-3>
- Baden T, Berens P, Franke K, Román Rosón M, Bethge M, Euler T. 2016. The functional diversity of retinal ganglion cells in the mouse. *Nature* **529**:345–350. DOI: <https://doi.org/10.1038/nature16468>
- Bastos AM, Usrey WM, Adams RA, Mangun GR, Fries P, Friston KJ. 2012. Canonical microcircuits for predictive coding. *Neuron* **76**:695–711. DOI: <https://doi.org/10.1016/j.neuron.2012.10.038>
- Bates D, Mächler M, Bolker B, Walker S. 2015. Fitting Linear Mixed-Effects Models Using lme4. *Journal of Statistical Software* **67**:1. DOI: <https://doi.org/10.18637/jss.v067.i01>
- Béhuret S, Deleuze C, Bal T. 2015. Corticothalamic Synaptic Noise as a Mechanism for Selective Attention in Thalamic Neurons. *Frontiers in Neural Circuits* **9**:80. DOI: <https://doi.org/10.3389/fncir.2015.00080>
- Bennett C, Arroyo S, Hestrin S. 2013. Subthreshold mechanisms underlying state-dependent modulation of visual responses. *Neuron* **80**:350–357. DOI: <https://doi.org/10.1016/j.neuron.2013.08.007>
- Berkes P, Orbán G, Lengyel M, Fiser J. 2011. Spontaneous cortical activity reveals hallmarks of an optimal internal model of the environment. *Science (New York, N.Y.)* **331**:83–87. DOI: <https://doi.org/10.1126/science.1195870>
- Bickford ME, Zhou N, Krahe TE, Govindaiah G, Guido W. 2015. Retinal and Tectal “Driver-Like” Inputs Converge in the Shell of the Mouse Dorsal Lateral Geniculate Nucleus. *The Journal of Neuroscience* **35**:10523–10534. DOI: <https://doi.org/10.1523/JNEUROSCI.3375-14.2015>
- Bonhoeffer T, Kim DS, Maloney D, Shoham D, Grinvald A. 1995. Optical imaging of the layout of functional domains in area 17 and across the area 17/18 border in cat visual cortex. *The European Journal of Neuroscience* **7**:1973–1988. DOI: <https://doi.org/10.1111/j.1460-9568.1995.tb00720.x>
- Born G, Schneider-Soupiadis FA, Erisken S, Vaiceliunaite A, Lao CL, Mobarhan MH, Spacek MA, Einevoll GT, Busse L. 2021. Corticothalamic feedback sculpts visual spatial integration in mouse thalamus. *Nature Neuroscience* **24**:1711–1720. DOI: <https://doi.org/10.1038/s41593-021-00943-0>
- Bortone DS, Olsen SR, Scanziani M. 2014. Translaminar inhibitory cells recruited by layer 6 corticothalamic neurons suppress visual cortex. *Neuron* **82**:474–485. DOI: <https://doi.org/10.1016/j.neuron.2014.02.021>
- Briggs F, Usrey WM. 2009. Parallel processing in the corticogeniculate pathway of the macaque monkey. *Neuron* **62**:135–146. DOI: <https://doi.org/10.1016/j.neuron.2009.02.024>
- Briggs F. 2010. Organizing principles of cortical layer 6. *Frontiers in Neural Circuits* **4**:3. DOI: <https://doi.org/10.3389/fncir.2010.0003.2010>
- Briggs F, Usrey WM. 2011. Corticogeniculate feedback and visual processing in the primate. *The Journal of Physiology* **589**:33–40. DOI: <https://doi.org/10.1113/jphysiol.2010.193599>
- Briggs F, Kiley CW, Callaway EM, Usrey WM. 2016. Morphological Substrates for Parallel Streams of Corticogeniculate Feedback Originating in Both V1 and V2 of the Macaque Monkey. *Neuron* **90**:388–399. DOI: <https://doi.org/10.1016/j.neuron.2016.02.038>
- Carandini M, Heeger DJ, Movshon JA. 1997. Linearity and normalization in simple cells of the macaque primary visual cortex. *The Journal of Neuroscience* **17**:8621–8644. DOI: <https://doi.org/10.1523/JNEUROSCI.17-21-08621.1997>
- Cardin JA, Palmer LA, Contreras D. 2008. Cellular mechanisms underlying stimulus-dependent gain modulation in primary visual cortex neurons in vivo. *Neuron* **59**:150–160. DOI: <https://doi.org/10.1016/j.neuron.2008.05.002>

- Chance FS, Nelson SB, Abbott LF. 1999. Complex cells as cortically amplified simple cells. *Nature Neuroscience* **2**:277–282. DOI: <https://doi.org/10.1038/6381>
- Chance FS, Abbott LF, Reyes AD. 2002. Gain modulation from background synaptic input. *Neuron* **35**:773–782. DOI: [https://doi.org/10.1016/s0896-6273\(02\)00820-6](https://doi.org/10.1016/s0896-6273(02)00820-6)
- Chen C, Bickford ME, Hirsch JA. 2016. Untangling the Web between Eye and Brain. *Cell* **165**:20–21. DOI: <https://doi.org/10.1016/j.cell.2016.03.010>
- Clark A. 2013. Whatever next? Predictive brains, situated agents, and the future of cognitive science. *The Behavioral and Brain Sciences* **36**:181–204. DOI: <https://doi.org/10.1017/S0140525X12000477>
- Coen-Cagli R, Kohn A, Schwartz O. 2015. Flexible gating of contextual influences in natural vision. *Nature Neuroscience* **18**:1648–1655. DOI: <https://doi.org/10.1038/nn.4128>
- Crandall SR, Cruikshank SJ, Connors BW. 2015. A corticothalamic switch: controlling the thalamus with dynamic synapses. *Neuron* **86**:768–782. DOI: <https://doi.org/10.1016/j.neuron.2015.03.040>
- Crandall SR, Patrick SL, Cruikshank SJ, Connors BW. 2017. Infrabarrels Are Layer 6 Circuit Modules in the Barrel Cortex that Link Long-Range Inputs and Outputs. *Cell Reports* **21**:3065–3078. DOI: <https://doi.org/10.1016/j.celrep.2017.11.049>
- Cruz-Martín A, El-Danaf RN, Osakada F, Sriram B, Dhande OS, Nguyen PL, Callaway EM, Ghosh A, Huberman AD. 2014. A dedicated circuit links direction-selective retinal ganglion cells to the primary visual cortex. *Nature* **507**:358–361. DOI: <https://doi.org/10.1038/nature12989>
- Cudeiro J, Sillito AM. 1996. Spatial frequency tuning of orientation-discontinuity-sensitive corticofugal feedback to the cat lateral geniculate nucleus. *The Journal of Physiology* **490** (Pt 2):481–492. DOI: <https://doi.org/10.1113/jphysiol.1996.sp021159>
- Dan Y, Atick JJ, Reid RC. 1996. Efficient coding of natural scenes in the lateral geniculate nucleus: experimental test of a computational theory. *The Journal of Neuroscience* **16**:3351–3362.
- de Labra C, Rivadulla C, Grieve K, Mariño J, Espinosa N, Cudeiro J. 2007. Changes in visual responses in the feline dLGN: selective thalamic suppression induced by transcranial magnetic stimulation of V1. *Cerebral Cortex* (New York, N.Y.) **17**:1376–1385. DOI: <https://doi.org/10.1093/cercor/bhl048>
- Denman DJ, Contreras D. 2015. Complex Effects on In Vivo Visual Responses by Specific Projections from Mouse Cortical Layer 6 to Dorsal Lateral Geniculate Nucleus. *The Journal of Neuroscience* **35**:9265–9280. DOI: <https://doi.org/10.1523/JNEUROSCI.0027-15.2015>
- Denman DJ, Contreras D. 2016. On Parallel Streams through the Mouse Dorsal Lateral Geniculate Nucleus. *Frontiers in Neural Circuits* **10**:20. DOI: <https://doi.org/10.3389/fncir.2016.00020>
- DiCarlo JJ, Zoccolan D, Rust NC. 2012. How does the brain solve visual object recognition? *Neuron* **73**:415–434. DOI: <https://doi.org/10.1016/j.neuron.2012.01.010>
- Disney AA, Aoki C, Hawken MJ. 2007. Gain modulation by nicotine in macaque V1. *Neuron* **56**:701–713. DOI: <https://doi.org/10.1016/j.neuron.2007.09.034>
- Dossi RC, Nuñez A, Steriade M. 1992. Electrophysiology of a slow (0.5–4 Hz) intrinsic oscillation of cat thalamocortical neurones in vivo. *The Journal of Physiology* **447**:215–234. DOI: <https://doi.org/10.1113/jphysiol.1992.sp018999>
- Erisken S, Vaiceliunaite A, Jurjut O, Fiorini M, Katzner S, Busse L. 2014. Effects of locomotion extend throughout the mouse early visual system. *Current Biology* **24**:2899–2907. DOI: <https://doi.org/10.1016/j.cub.2014.10.045>
- Ferguson KA, Cardin JA. 2020. Mechanisms underlying gain modulation in the cortex. *Nature Reviews Neuroscience* **21**:80–92. DOI: <https://doi.org/10.1038/s41583-019-0253-y>
- Frandolig JE, Matney CJ, Lee K, Kim J, Chevée M, Kim S-J, Bickert AA, Brown SP. 2019. The Synaptic Organization of Layer 6 Circuits Reveals Inhibition as a Major Output of a Neocortical Sublamina. *Cell Reports* **28**:3131–3143. DOI: <https://doi.org/10.1016/j.celrep.2019.08.048>, PMID: 31533036
- Funke K, Pape HC, Eysel UT. 1993. Noradrenergic modulation of retinogeniculate transmission in the cat. *The Journal of Physiology* **463**:169–191. DOI: <https://doi.org/10.1113/jphysiol.1993.sp019590>
- Gelman A, Hill J. 2007. *Data Analysis Using Regression and Multilevel/Hierarchical Models*, Ser. Analytical Methods for Social Research. Cambridge: Cambridge University Press.
- Gilbert CD, Li W. 2013. Top-down influences on visual processing. *Nature Reviews Neuroscience* **14**:350–363. DOI: <https://doi.org/10.1038/nrn3476>
- Goard M, Dan Y. 2009. Basal forebrain activation enhances cortical coding of natural scenes. *Nature Neuroscience* **12**:1444–1449. DOI: <https://doi.org/10.1038/nn.2402>
- Godwin DW, Van Horn SC, Eriir A, Sesma M, Romano C, Sherman SM. 1996. Ultrastructural localization suggests that retinal and cortical inputs access different metabotropic glutamate receptors in the lateral geniculate nucleus. *The Journal of Neuroscience* **16**:8181–8192. DOI: <https://doi.org/10.1523/JNEUROSCI.16-24-08181.1996>
- Gouwens NW, Sorensen SA, Berg J, Lee C, Jarsky T, Ting J, Sunkin SM, Feng D, Anastassiou CA, Barkan E, Bickley K, Blesie N, Braun T, Brouner K, Budzillo A, Caldejon S, Casper T, Castelli D, Chong P, Crichton K, et al. 2019. Classification of electrophysiological and morphological neuron types in the mouse visual cortex. *Nature Neuroscience* **22**:1182–1195. DOI: <https://doi.org/10.1038/s41593-019-0417-0>
- Grubb MS, Thompson ID. 2003. Quantitative characterization of visual response properties in the mouse dorsal lateral geniculate nucleus. *Journal of Neurophysiology* **90**:3594–3607. DOI: <https://doi.org/10.1152/jn.00699.2003>
- Grubb MS, Thompson ID. 2005. Visual response properties of burst and tonic firing in the mouse dorsal lateral geniculate nucleus. *Journal of Neurophysiology* **93**:3224–3247. DOI: <https://doi.org/10.1152/jn.00445.2004>

- Gulyás B, Lagae L, Eysel U, Orban GA. 1990. Corticofugal feedback influences the responses of geniculate neurons to moving stimuli. *Experimental Brain Research* **79**:441–446. DOI: <https://doi.org/10.1007/BF00608257>
- Guo W, Clause AR, Barth-Marion A, Polley DB. 2017. A Corticothalamic Circuit for Dynamic Switching between Feature Detection and Discrimination. *Neuron* **95**:180–194. DOI: <https://doi.org/10.1016/j.neuron.2017.05.019>
- Hasse JM, Briggs F. 2017. Corticogeniculate feedback sharpens the temporal precision and spatial resolution of visual signals in the ferret. *PNAS* **114**:E6222–E6230. DOI: <https://doi.org/10.1073/pnas.1704524114>
- Hasse JM, Bragg EM, Murphy AJ, Briggs F. 2019. Morphological heterogeneity among corticogeniculate neurons in ferrets: quantification and comparison with a previous report in macaque monkeys. *The Journal of Comparative Neurology* **527**:546–557. DOI: <https://doi.org/10.1002/cne.24451>
- Heeger DJ. 2017. Theory of cortical function. *PNAS* **114**:1773–1782. DOI: <https://doi.org/10.1073/pnas.1619788114>
- Heumann D, Leuba G, Rabinowicz T. 1977. Postnatal development of the mouse cerebral neocortex. II. Quantitative cytoarchitectonics of visual and auditory areas. *Journal Fur Hirnforschung* **18**:483–500.
- Hô N, Destexhe A. 2000. Synaptic background activity enhances the responsiveness of neocortical pyramidal neurons. *Journal of Neurophysiology* **84**:1488–1496. DOI: <https://doi.org/10.1152/jn.2000.84.3.1488>
- Hochstein S, Ahissar M. 2002. View from the top: hierarchies and reverse hierarchies in the visual system. *Neuron* **36**:791–804. DOI: [https://doi.org/10.1016/s0896-6273\(02\)01091-7](https://doi.org/10.1016/s0896-6273(02)01091-7)
- Holdefer RN, Jacobs BL. 1994. Phasic stimulation of the locus coeruleus: effects on activity in the lateral geniculate nucleus. *Experimental Brain Research* **100**:444–452. DOI: <https://doi.org/10.1007/BF02738404>
- Hubel DH, Wiesel TN. 1962. Receptive fields, binocular interaction and functional architecture in the cat's visual cortex. *The Journal of Physiology* **160**:106–154. DOI: <https://doi.org/10.1113/jphysiol.1962.sp006837>, PMID: [14449617](https://pubmed.ncbi.nlm.nih.gov/14449617/)
- Jahnsen H, Llinás R. 1984. Voltage-dependent burst-to-tonic switching of thalamic cell activity: an in vitro study. *Archives Italiennes de Biologie* **122**:73–82.
- Jones HE, Andolina IM, Ahmed B, Shipp SD, Clements JTC, Grieve KL, Cudeiro J, Salt TE, Sillito AM. 2012. Differential feedback modulation of center and surround mechanisms in parvocellular cells in the visual thalamus. *The Journal of Neuroscience* **32**:15946–15951. DOI: <https://doi.org/10.1523/JNEUROSCI.0831-12.2012>
- Kara P, Reinagel P, Reid RC. 2000. Low response variability in simultaneously recorded retinal, thalamic, and cortical neurons. *Neuron* **27**:635–646. DOI: [https://doi.org/10.1016/s0896-6273\(00\)00072-6](https://doi.org/10.1016/s0896-6273(00)00072-6)
- Keller AJ, Roth MM, Scanziani M. 2020. Feedback generates a second receptive field in neurons of the visual cortex. *Nature* **582**:545–549. DOI: <https://doi.org/10.1038/s41586-020-2319-4>
- Kim J, Matney CJ, Blankenship A, Hestrin S, Brown SP. 2014. Layer 6 corticothalamic neurons activate a cortical output layer, layer 5a. *The Journal of Neuroscience* **34**:9656–9664. DOI: <https://doi.org/10.1523/JNEUROSCI.1325-14.2014>
- King JL, Lowe MP, Stover KR, Wong AA, Crowder NA. 2016. Adaptive Processes in Thalamus and Cortex Revealed by Silencing of Primary Visual Cortex during Contrast Adaptation. *Current Biology* **26**:1295–1300. DOI: <https://doi.org/10.1016/j.cub.2016.03.018>
- Kuznetsova A, Brockhoff PB, Christensen RHB. 2017. lmerTest Package: Tests in Linear Mixed Effects Models. *Journal of Statistical Software* **82**:13. DOI: <https://doi.org/10.18637/jss.v082.i13>
- Lamme VAF, Roelfsema PR. 2000. The distinct modes of vision offered by feedforward and recurrent processing. *Trends in Neurosciences* **23**:571–579. DOI: [https://doi.org/10.1016/s0166-2236\(00\)01657-x](https://doi.org/10.1016/s0166-2236(00)01657-x)
- Larkum M. 2013. A cellular mechanism for cortical associations: an organizing principle for the cerebral cortex. *Trends in Neurosciences* **36**:141–151. DOI: <https://doi.org/10.1016/j.tins.2012.11.006>
- Lee TS, Mumford D. 2003. Hierarchical Bayesian inference in the visual cortex. *Journal of the Optical Society of America. A, Optics, Image Science, and Vision* **20**:1434–1448. DOI: <https://doi.org/10.1364/josaa.20.001434>
- Lee SH, Dan Y. 2012. Neuromodulation of brain states. *Neuron* **76**:209–222. DOI: <https://doi.org/10.1016/j.neuron.2012.09.012>, PMID: [23040816](https://pubmed.ncbi.nlm.nih.gov/23040816/)
- Lesica NA, Stanley GB. 2004. Encoding of natural scene movies by tonic and burst spikes in the lateral geniculate nucleus. *The Journal of Neuroscience* **24**:10731–10740. DOI: <https://doi.org/10.1523/JNEUROSCI.3059-04.2004>
- Lesica NA, Weng C, Jin J, Yeh CI, Alonso JM, Stanley GB. 2006. Dynamic encoding of natural luminance sequences by LGN bursts. *PLOS Biology* **4**:7. DOI: <https://doi.org/10.1371/journal.pbio.0040209>
- Lesica NA, Jin J, Weng C, Yeh CI, Butts DA, Stanley GB, Alonso JM. 2007. Adaptation to stimulus contrast and correlations during natural visual stimulation. *Neuron* **55**:479–491. DOI: <https://doi.org/10.1016/j.neuron.2007.07.013>
- Li Y, Ibrahim LA, Liu B, Zhang LI, Tao HW. 2013. Linear transformation of thalamocortical input by intracortical excitation. *Nature Neuroscience* **16**:1324–1330. DOI: <https://doi.org/10.1038/nn.3494>
- Liang L, Fratzl A, Goldey G, Ramesh RN, Sugden AU, Morgan JL, Chen C, Andermann ML. 2018. A Fine-Scale Functional Logic to Convergence from Retina to Thalamus. *Cell* **173**:1343–1355. DOI: <https://doi.org/10.1016/j.cell.2018.04.041>
- Liang L, Fratzl A, Reggiani JDS, El Mansour O, Chen C, Andermann ML. 2020. Retinal Inputs to the Thalamus Are Selectively Gated by Arousal. *Current Biology* **30**:3923–3934. DOI: <https://doi.org/10.1016/j.cub.2020.07.065>

- Liang Y, Fan JL, Sun W, Lu R, Chen M, Ji N. 2021. A Distinct Population of L6 Neurons in Mouse V1 Mediate Cross-Collosal Communication. *Cerebral Cortex (New York, N.Y)* **31**:4259–4273. DOI: <https://doi.org/10.1093/cercor/bhab084>
- Lien AD, Scanziani M. 2013. Tuned thalamic excitation is amplified by visual cortical circuits. *Nature Neuroscience* **16**:1315–1323. DOI: <https://doi.org/10.1038/nn.3488>
- Lien AD, Scanziani M. 2018. Cortical direction selectivity emerges at convergence of thalamic synapses. *Nature* **558**:80–86. DOI: <https://doi.org/10.1038/s41586-018-0148-5>
- Lu SM, Guido W, Sherman SM. 1992. Effects of membrane voltage on receptive field properties of lateral geniculate neurons in the cat: contributions of the low-threshold Ca²⁺ conductance. *Journal of Neurophysiology* **68**:2185–2198. DOI: <https://doi.org/10.1152/jn.1992.68.6.2185>
- Lu SM, Guido W, Sherman SM. 1993. The brain-stem parabrachial region controls mode of response to visual stimulation of neurons in the cat's lateral geniculate nucleus. *Visual Neuroscience* **10**:631–642. DOI: <https://doi.org/10.1017/s0952523800005332>
- Luke SG. 2017. Evaluating significance in linear mixed-effects models in R. *Behavior Research Methods* **49**:1494–1502. DOI: <https://doi.org/10.3758/s13428-016-0809-y>
- Mahn M, Gibor L, Patil P, Cohen-Kashi Malina K, Oring S, Printz Y, Levy R, Lampl I, Yizhar O. 2018. High-efficiency optogenetic silencing with soma-targeted anion-conducting channelrhodopsins. *Nature Communications* **9**:4125. DOI: <https://doi.org/10.1038/s41467-018-06511-8>
- Makino H, Komiyama T. 2015. Learning enhances the relative impact of top-down processing in the visual cortex. *Nature Neuroscience* **18**:1116–1122. DOI: <https://doi.org/10.1038/nn.4061>
- Mante V, Frazor RA, Bonin V, Geisler WS, Carandini M. 2005. Independence of luminance and contrast in natural scenes and in the early visual system. *Nature Neuroscience* **8**:1690–1697. DOI: <https://doi.org/10.1038/nn1556>
- Marshel JH, Kaye AP, Nauhaus I, Callaway EM. 2012. Anterior-posterior direction opponency in the superficial mouse lateral geniculate nucleus. *Neuron* **76**:713–720. DOI: <https://doi.org/10.1016/j.neuron.2012.09.021>
- McClurkin JW, Marrocco RT. 1984. Visual cortical input alters spatial tuning in monkey lateral geniculate nucleus cells. *The Journal of Physiology* **348**:135–152. DOI: <https://doi.org/10.1113/jphysiol.1984.sp015103>
- McCormick DA. 1992. Neurotransmitter actions in the thalamus and cerebral cortex and their role in neuromodulation of thalamocortical activity. *Progress in Neurobiology* **39**:337–388. DOI: [https://doi.org/10.1016/0301-0082\(92\)90012-4](https://doi.org/10.1016/0301-0082(92)90012-4)
- Mease RA, Krieger P, Groh A. 2014. Cortical control of adaptation and sensory relay mode in the thalamus. *PNAS* **111**:6798–6803. DOI: <https://doi.org/10.1073/pnas.1318665111>
- Mease RA, Kuner T, Fairhall AL, Groh A. 2017. Multiplexed Spike Coding and Adaptation in the Thalamus. *Cell Reports* **19**:1130–1140. DOI: <https://doi.org/10.1016/j.celrep.2017.04.050>
- Mitzdorf U. 1985. Current source-density method and application in cat cerebral cortex: investigation of evoked potentials and EEG phenomena. *Physiological Reviews* **65**:37–100. DOI: <https://doi.org/10.1152/physrev.1985.65.1.37>
- Molnár B, Sere P, Bordé S, Koós K, Zsigri N, Horváth P, Lőrincz ML. 2021. Cell Type-Specific Arousal-Dependent Modulation of Thalamic Activity in the Lateral Geniculate Nucleus. *Cerebral Cortex Communications* **2**:tgab020. DOI: <https://doi.org/10.1093/texcom/tgab020>
- Morgan JL, Berger DR, Wetzel AW, Lichtman JW. 2016. The Fuzzy Logic of Network Connectivity in Mouse Visual Thalamus. *Cell* **165**:192–206. DOI: <https://doi.org/10.1016/j.cell.2016.02.033>
- Murata Y, Colonnese MT. 2018. Thalamus Controls Development and Expression of Arousal States in Visual Cortex. *The Journal of Neuroscience* **38**:8772–8786. DOI: <https://doi.org/10.1523/JNEUROSCI.1519-18.2018>
- Murphy PC, Sillito AM. 1987. Corticofugal feedback influences the generation of length tuning in the visual pathway. *Nature* **329**:727–729. DOI: <https://doi.org/10.1038/329727a0>
- Nestvogel DB, McCormick DA. 2022. Visual thalamocortical mechanisms of waking state-dependent activity and alpha oscillations. *Neuron* **110**:120–138. DOI: <https://doi.org/10.1016/j.neuron.2021.10.005>
- Niell CM, Stryker MP. 2008. Highly selective receptive fields in mouse visual cortex. *The Journal of Neuroscience* **28**:7520–7536. DOI: <https://doi.org/10.1523/JNEUROSCI.0623-08.2008>
- Niell CM, Stryker MP. 2010. Modulation of visual responses by behavioral state in mouse visual cortex. *Neuron* **65**:472–479. DOI: <https://doi.org/10.1016/j.neuron.2010.01.033>
- Oberlaender M, de Kock CPJ, Bruno RM, Ramirez A, Meyer HS, Dercksen VJ, Helmstaedter M, Sakmann B. 2012. Cell type-specific three-dimensional structure of thalamocortical circuits in a column of rat vibrissal cortex. *Cerebral Cortex (New York, N.Y)* **22**:2375–2391. DOI: <https://doi.org/10.1093/cercor/bhr317>
- Olsen SR, Bortone DS, Adesnik H, Scanziani M. 2012. Gain control by layer six in cortical circuits of vision. *Nature* **483**:47–52. DOI: <https://doi.org/10.1038/nature10835>
- Pachitariu M, Steinmetz NA, Kadir SN, Carandini M, Harris KD. 2016. Fast and accurate spike sorting of high-channel count probes with KiloSort. Lee DD, Sugiyama M, Luxburg UV, Guyon I, Garnett R (Eds). *In Advances in Neural Information Processing Systems* **29**. Curran Associates, Inc. p. 4448–4456.
- Pauzin FP, Krieger P. 2018. A Corticothalamic Circuit for Refining Tactile Encoding. *Cell Reports* **23**:1314–1325. DOI: <https://doi.org/10.1016/j.celrep.2018.03.128>
- Piscopo DM, El-Danaf RN, Huberman AD, Niell CM. 2013. Diverse visual features encoded in mouse lateral geniculate nucleus. *The Journal of Neuroscience* **33**:4642–4656. DOI: <https://doi.org/10.1523/JNEUROSCI.5187-12.2013>
- Poltoratski S, Maier A, Newton AT, Tong F. 2019. Figure-Ground Modulation in the Human Lateral Geniculate Nucleus Is Distinguishable from Top-Down Attention. *Current Biology* **29**:2051–2057. DOI: <https://doi.org/10.1016/j.cub.2019.04.068>

- Poynton CA. 1998. Human Vision and Electronic Imaging III. San Jose: Charles Poynton.
- Przybylski AW, Gaska JP, Foote W, Pollen DA. 2000. Striate cortex increases contrast gain of macaque LGN neurons. *Visual Neuroscience* 17:485–494. DOI: <https://doi.org/10.1017/s0952523800174012>
- R Core Team. 2017. R: A Language and Environment for Statistical Computing, R Foundation for Statistical Computing. <https://www.R-project.org/>
- Radnikow G, Feldmeyer D. 2018. Layer- and Cell Type-Specific Modulation of Excitatory Neuronal Activity in the Neocortex. *Frontiers in Neuroanatomy* 12:1. DOI: <https://doi.org/10.3389/fnana.2018.00001>
- Rao RPN, Ballard DH. 1999. Predictive coding in the visual cortex: A functional interpretation of some extra-classical receptive-field effects. *Nature Neuroscience* 2:79–87. DOI: <https://doi.org/10.1038/4580>
- Reimer J, Froudarakis E, Cadwell CR, Yatsenko D, Denfield GH, Tolias AS. 2014. Pupil fluctuations track fast switching of cortical states during quiet wakefulness. *Neuron* 84:355–362. DOI: <https://doi.org/10.1016/j.neuron.2014.09.033>
- Reinhold K, Resulaj A, Scanziani M. 2021. Brain State-Dependent Modulation of Thalamic Visual Processing by Cortico-Thalamic Feedback. [bioRxiv]. DOI: <https://doi.org/10.1101/2021.10.04.463017>
- Remtulla S, Hallett PE. 1985. A schematic eye for the mouse, and comparisons with the rat. *Vision Research* 25:21–31. DOI: [https://doi.org/10.1016/0042-6989\(85\)90076-8](https://doi.org/10.1016/0042-6989(85)90076-8)
- Riesenhuber M, Poggio T. 1999. Hierarchical models of object recognition in cortex. *Nature Neuroscience* 2:1019–1025. DOI: <https://doi.org/10.1038/14819>
- Riesenhuber M, Poggio T. 2000. Models of object recognition. *Nature Neuroscience* 3 Suppl:1199–1204. DOI: <https://doi.org/10.1038/81479>
- Roelfsema PR, de Lange FP. 2016. Early Visual Cortex as a Multiscale Cognitive Blackboard. *Annual Review of Vision Science* 2:131–151. DOI: <https://doi.org/10.1146/annurev-vision-111815-114443>, PMID: 28532363
- Román Rosón M, Bauer Y, Kotkat AH, Berens P, Euler T, Busse L. 2019. Mouse dLGN Receives Functional Input from a Diverse Population of Retinal Ganglion Cells with Limited Convergence. *Neuron* 102:462–476. DOI: <https://doi.org/10.1016/j.neuron.2019.01.040>
- Rueden CT, Schindelin J, Hiner MC, DeZonia BE, Walter AE, Arena ET, Eliceiri KW. 2017. ImageJ2: ImageJ for the next generation of scientific image data. *BMC Bioinformatics* 18:1. DOI: <https://doi.org/10.1186/s12859-017-1934-z>
- Sakatani T, Isa T. 2007. Quantitative analysis of spontaneous saccade-like rapid eye movements in C57BL/6 mice. *Neuroscience Research* 58:324–331. DOI: <https://doi.org/10.1016/j.neures.2007.04.003>
- Schindelin J, Arganda-Carreras I, Frise E, Kaynig V, Longair M, Pietzsch T, Preibisch S, Rueden C, Saalfeld S, Schmid B, Tinevez JY, White DJ, Hartenstein V, Eliceiri K, Tomancak P, Cardona A. 2012. Fiji: an open-source platform for biological-image analysis. *Nature Methods* 9:676–682. DOI: <https://doi.org/10.1038/nmeth.2019>
- Scholl B, Tan AYY, Corey J, Priebe NJ. 2013. Emergence of orientation selectivity in the Mammalian visual pathway. *The Journal of Neuroscience* 33:10616–10624. DOI: <https://doi.org/10.1523/JNEUROSCI.0404-13.2013>
- Schröder S, Steinmetz NA, Krumin M, Pachitariu M, Rizzi M, Lagnado L, Harris KD, Carandini M. 2020. Arousal Modulates Retinal Output. *Neuron* 107:487–495. DOI: <https://doi.org/10.1016/j.neuron.2020.04.026>
- Sherman SM, Koch C. 1986. The control of retinogeniculate transmission in the mammalian lateral geniculate nucleus. *Experimental Brain Research* 63:1–20. DOI: <https://doi.org/10.1007/BF00235642>
- Sherman SM, Guillery RW. 1998. On the actions that one nerve cell can have on another: distinguishing “drivers” from “modulators.” *PNAS* 95:7121–7126. DOI: <https://doi.org/10.1073/pnas.95.12.7121>
- Sherman SM. 2001. Tonic and burst firing: dual modes of thalamocortical relay. *Trends in Neurosciences* 24:122–126. DOI: [https://doi.org/10.1016/s0166-2236\(00\)01714-8](https://doi.org/10.1016/s0166-2236(00)01714-8)
- Sherman SM, Guillery RW. 2002. The role of the thalamus in the flow of information to the cortex. *Philosophical Transactions of the Royal Society of London. Series B, Biological Sciences* 357:1695–1708. DOI: <https://doi.org/10.1098/rstb.2002.1161>
- Sherman SM. 2016. Thalamus plays a central role in ongoing cortical functioning. *Nature Neuroscience* 19:533–541. DOI: <https://doi.org/10.1038/nn.4269>
- Shu Y, Hasenstaub A, Badoual M, Bal T, McCormick DA. 2003. Barrages of synaptic activity control the gain and sensitivity of cortical neurons. *The Journal of Neuroscience* 23:10388–10401.
- Sillito AM, Kemp JA, Berardi N. 1983. The cholinergic influence on the function of the cat dorsal lateral geniculate nucleus (dLGN). *Brain Research* 280:299–307. DOI: [https://doi.org/10.1016/0006-8993\(83\)90059-8](https://doi.org/10.1016/0006-8993(83)90059-8)
- Sillito AM, Cudeiro J, Murphy PC. 1993. Orientation sensitive elements in the corticofugal influence on centre-surround interactions in the dorsal lateral geniculate nucleus. *Experimental Brain Research* 93:6–16. DOI: <https://doi.org/10.1007/BF00227775>
- Sillito AM, Jones HE. 2002. Corticothalamic interactions in the transfer of visual information. *PNAS* 357:1739–1752. DOI: <https://doi.org/10.1098/rstb.2002.1170>
- Skottun BC, De Valois RL, Grosof DH, Movshon JA, Albrecht DG, Bonds AB. 1991. Classifying simple and complex cells on the basis of response modulation. *Vision Research* 31:1079–1086. DOI: [https://doi.org/10.1016/0042-6989\(91\)90033-2](https://doi.org/10.1016/0042-6989(91)90033-2)
- Spacek MA, Blanche TJ, Swindale NV. 2009. Python for large-scale electrophysiology. *Frontiers in Neuroinformatics* 2:2008. DOI: <https://doi.org/10.3389/neuro.11.009.2008>
- Squire RF, Noudoost B, Schafer RJ, Moore T. 2013. Prefrontal contributions to visual selective attention. *Annual Review of Neuroscience* 36:451–466. DOI: <https://doi.org/10.1146/annurev-neuro-062111-150439>

- Stoelzel CR, Bereshpolova Y, Alonso JM, Swadlow HA. 2017. Axonal Conduction Delays, Brain State, and Corticogeniculate Communication. *The Journal of Neuroscience* **37**:6342–6358. DOI: <https://doi.org/10.1523/JNEUROSCI.0444-17.2017>
- Sundberg SC, Lindström SH, Sanchez GM, Granseth B. 2018. Cre-expressing neurons in visual cortex of Ntsr1-Cre GN220 mice are corticothalamic and are depolarized by acetylcholine. *The Journal of Comparative Neurology* **526**:120–132. DOI: <https://doi.org/10.1002/cne.24323>
- Swadlow HA, Weyand TG. 1987. Corticogeniculate neurons, corticotectal neurons, and suspected interneurons in visual cortex of awake rabbits: receptive-field properties, axonal properties, and effects of EEG arousal. *Journal of Neurophysiology* **57**:977–1001. DOI: <https://doi.org/10.1152/jn.1987.57.4.977>
- Swadlow HA. 1989. Efferent neurons and suspected interneurons in S-1 vibrissa cortex of the awake rabbit: receptive fields and axonal properties. *Journal of Neurophysiology* **62**:288–308. DOI: <https://doi.org/10.1152/jn.1989.62.1.288>
- Swadlow HA, Gusev AG. 2001. The impact of “bursting” thalamic impulses at a neocortical synapse. *Nature Neuroscience* **4**:402–408. DOI: <https://doi.org/10.1038/86054>
- Swindale NV, Spacek MA. 2014. Spike sorting for polytrodes: a divide and conquer approach. *Frontiers in Systems Neuroscience* **8**:6. DOI: <https://doi.org/10.3389/fnsys.2014.00006>
- Takahashi N, Oertner TG, Hegemann P, Larkum ME. 2016. Active cortical dendrites modulate perception. *Science (New York, N.Y.)* **354**:1587–1590. DOI: <https://doi.org/10.1126/science.aah6066>
- Tasic B, Menon V, Nguyen TN, Kim TK, Jarsky T, Yao Z, Levi B, Gray LT, Sorensen SA, Dolbeare T, Bertagnonli D, Goldy J, Shapovalova N, Parry S, Lee C, Smith K, Bernard A, Madisen L, Sunkin SM, Hawrylycz M, et al. 2016. Adult mouse cortical cell taxonomy revealed by single cell transcriptomics. *Nature Neuroscience* **19**:335–346. DOI: <https://doi.org/10.1038/nn.4216>
- Usrey WM, Sherman SM. 2019. Corticofugal circuits: Communication lines from the cortex to the rest of the brain. *The Journal of Comparative Neurology* **527**:640–650. DOI: <https://doi.org/10.1002/cne.24423>
- van der Togt C, Spekrijse H, Supèr H. 2005. Neural responses in cat visual cortex reflect state changes in correlated activity. *The European Journal of Neuroscience* **22**:465–475. DOI: <https://doi.org/10.1111/j.1460-9568.2005.04237.x>
- Vélez-Fort M, Rousseau CV, Niedworok CJ, Wickersham IR, Rancz EA, Brown APY, Strom M, Margrie TW. 2014. The stimulus selectivity and connectivity of layer six principal cells reveals cortical microcircuits underlying visual processing. *Neuron* **83**:1431–1443. DOI: <https://doi.org/10.1016/j.neuron.2014.08.001>
- Vinck M, Batista-Brito R, Knoblich U, Cardin JA. 2015. Arousal and locomotion make distinct contributions to cortical activity patterns and visual encoding. *Neuron* **86**:740–754. DOI: <https://doi.org/10.1016/j.neuron.2015.03.028>
- Vinje WE, Gallant JL. 2000. Sparse coding and decorrelation in primary visual cortex during natural vision. *Science (New York, N.Y.)* **287**:1273–1276. DOI: <https://doi.org/10.1126/science.287.5456.1273>
- Wang W, Jones HE, Andolina IM, Salt TE, Sillito AM. 2006. Functional alignment of feedback effects from visual cortex to thalamus. *Nature Neuroscience* **9**:1330–1336. DOI: <https://doi.org/10.1038/nn1768>
- Wang X, Wei Y, Vaingankar V, Wang Q, Koepsell K, Sommer FT, Hirsch JA. 2007. Feedforward excitation and inhibition evoke dual modes of firing in the cat’s visual thalamus during naturalistic viewing. *Neuron* **55**:465–478. DOI: <https://doi.org/10.1016/j.neuron.2007.06.039>
- Wang W, Andolina IM, Lu Y, Jones HE, Sillito AM. 2018. Focal Gain Control of Thalamic Visual Receptive Fields by Layer 6 Corticothalamic Feedback. *Cerebral Cortex (New York, N.Y.)* **28**:267–280. DOI: <https://doi.org/10.1093/cercor/bhw376>
- Webb BS, Tinsley CJ, Barraclough NE, Easton A, Parker A, Derrington AM. 2002. Feedback from V1 and inhibition from beyond the classical receptive field modulates the responses of neurons in the primate lateral geniculate nucleus. *Visual Neuroscience* **19**:583–592. DOI: <https://doi.org/10.1017/s0952523802195046>
- Whitmire CJ, Waiblinger C, Schwarz C, Stanley GB. 2016. Information Coding through Adaptive Gating of Synchronized Thalamic Bursting. *Cell Reports* **14**:795–807. DOI: <https://doi.org/10.1016/j.celrep.2015.12.068>
- Wiegert JS, Mahn M, Prigge M, Printz Y, Yizhar O. 2017. Silencing Neurons: Tools, Applications, and Experimental Constraints. *Neuron* **95**:504–529. DOI: <https://doi.org/10.1016/j.neuron.2017.06.050>
- Williamson RS, Hancock KE, Shinn-Cunningham BG, Polley DB. 2015. Locomotion and Task Demands Differentially Modulate Thalamic Audiovisual Processing during Active Search. *Current Biology* **25**:1885–1891. DOI: <https://doi.org/10.1016/j.cub.2015.05.045>
- Wolfart J, Debay D, Le Masson G, Destexhe A, Bal T. 2005. Synaptic background activity controls spike transfer from thalamus to cortex. *Nature Neuroscience* **8**:1760–1767. DOI: <https://doi.org/10.1038/nn1591>
- Wörgötter F, Eyding D, Macklis JD, Funke K. 2002. The influence of the corticothalamic projection on responses in thalamus and cortex. *Philosophical Transactions of the Royal Society of London. Series B, Biological Sciences* **357**:1823–1834. DOI: <https://doi.org/10.1098/rstb.2002.1159>
- Yatsenko D, Walker EY, Tolia AS. 2018. DataJoint: A Simpler Relational Data Model. [arXiv]. DOI: <https://doi.org/10.48550/arXiv.1807.11104>
- Zagha E, McCormick DA. 2014. Neural control of brain state. *Current Opinion in Neurobiology* **29**:178–186. DOI: <https://doi.org/10.1016/j.conb.2014.09.010>, PMID: 25310628
- Zhao X, Chen H, Liu X, Cang J. 2013. Orientation-selective responses in the mouse lateral geniculate nucleus. *The Journal of Neuroscience* **33**:12751–12763. DOI: <https://doi.org/10.1523/JNEUROSCI.0095-13.2013>
- Zhuang J, Larsen RS, Takasaki KT, Ouellette ND, Daigle TL, Tasic BT, Waters J, Zeng H, Reid RC. 2019. The Spatial Structure of Feedforward Information in Mouse Primary Visual Cortex. [BBioRxiv]. DOI: <https://doi.org/10.1101/2019.12.24.888156>

MODELLING DLGN ACTIVITY TO MOVIES, FEEDBACK & BEHAVIOUR

4.1 BAUER & SCHMORS ET AL. (2022) [*in preparation*]

SUMMARY: The dorsolateral geniculate nucleus of the thalamus (dLGN) is an essential processing stage for retinal signals to reach the primary visual cortex (V_1). How these feedforward signals are modulated by cortico-thalamic (CT) feedback and behaviour remains an open question. Here, we recorded extracellular responses in dLGN of awake mice to a rich, dynamic movie stimulus, while selectively and reversibly photo-suppressing V_1 cortical layer 6 (L6) CT pyramidal cells and simultaneously tracking locomotion behaviour and pupil size. We predicted dLGN responses using a linear-nonlinear-Poisson (LNP) model with a spline basis, a type of the generalized linear model (GLM), to estimate STRFs and kernels for CT feedback and behavior. We found that the model filter kernel shapes for these factors were consistent with condition-wise mean firing rate (FR) effects. Moreover, the model successfully captured a diversity of dLGN STRF shapes. Thus, this interpretable model presents an important step towards a quantitative understanding of how dLGN responses to naturalistic movies are modulated by CT feedback and behaviour.

THE MANUSCRIPT IS IN PREPARATION AS:

Bauer, Y., Schmors, L., Huang, Z., Kotkat, A. H., Crombie, D., Meyerolbersleben, L., Renner, S., Sokoloski, S., Busse, L., & Berens, P. (2022). An interpretable spline-LNP model to characterise feedforward and feedback processing in mouse dLGN. *In preparation**

*shared first authorship between Y.B. and L.S.

CONTRIBUTION SUMMARY: Conceptualization, L.B., P.B., S.S.; Methodology, L.B., P.B., Y.B., L.S., Z.H., S.S.; Software, L.S., Y.B., S.R., D.C., Z.H.; Formal Analysis, L.S., Y.B., A.K.; Investigation, Y.B., L.M., A.K.; Resources, L.B., P.B.; Data Curation, Y.B., L.S., A.K., L.M., D.C.; Writing – Original Draft, Y.B., L.S., L.B.; Writing – Review & Editing, all authors; Visualization, Y.B., L.S.; Supervision, L.B., P.B., S.S.; Project Administration, L.B., P.B.; Funding Acquisition, L.B., P.B.

PERSONAL CONTRIBUTIONS: Y.B. initiated the use and design of a complex, dynamic movie stimulus, adapted the stGtACR2-mediated photosuppression of L6CT cells to the Busse Lab, performed the injection and headbar implantation surgeries, handled mice and provided recordings of dLGN electrophysiology, locomotion and eye-tracking to visual stimulation and optogenetic manipulations, perfusion, and histology/microscopy (Fig1a-e). Y.B. further performed pre-processing of electrophysiological data (spike sorting). Y.B. also created and maintained the database tables and code repositories for the analysis pipeline. This included cell-based and population-wide analyses of condition-wise effects of optogenetics, locomotion and pupil size (Fig1f-k), creation of optogenetic/run/eye modulation indices, tests of predictor correlations, spatial RF contour/area estimation and quality indices; visualization of the spline-LNP model (Fig2, Fig3, FigS1), and comparison of the models for responses to the movie stimulus vs. the sparse noise stimulus (Fig4, FigS2). Y.B. wrote and revised the original draft.

An interpretable spline-LNP model to characterise feedforward and feedback processing in mouse dLGN

Yannik Bauer^{1,2,*}, Lisa Schmors^{3,4,*}, Ziwei Huang^{3,4}, Ann H. Kotkat^{1,2}, Davide Crombie^{1,2}, Lukas Meyerolbersleben^{1,2}, Simon Renner^{1,2}, Sacha Sokoloski^{3,4}, Laura Busse^{1,5,+}, and Philipp Berens^{3,4,6,+}

¹Division of Neurobiology, Faculty of Biology, LMU Munich, 82152 Munich, Germany

²Graduate School of Systemic Neurosciences (GSN), LMU Munich, 82152 Munich, Germany

³Institute for Ophthalmic Research, University of Tübingen, 72076 Tübingen, Germany

⁴Centre for Integrative Neuroscience, University of Tübingen, 72076 Tübingen, Germany

⁵Bernstein Centre for Computational Neuroscience, 82152 Munich, Germany

⁶Bernstein Centre for Computational Neuroscience, 72076 Tübingen, Germany

*These authors contributed equally to this work

+Correspondence: busse@bio.lmu.de (L.B.), philipp.berens@uni-tuebingen.de (P.B.)

ABSTRACT

The dorsolateral geniculate nucleus (dLGN) of the thalamus is an essential processing stage for retinal signals to reach the primary visual cortex (V1). How these feedforward signals are modulated by cortico-thalamic (CT) feedback and behaviour remains an open question. Here, we recorded extracellular responses in dLGN of awake mice to a rich movie stimulus, while selectively and reversibly photo-suppressing V1 layer 6 (L6) CT pyramidal cells and simultaneously tracking locomotion behaviour and pupil size. To estimate spatiotemporal receptive fields (RFs) and the impact of CT feedback and behavioral modulations, we predict the recorded dLGN responses using a generalized linear model (GLM) with a spline basis (spline-LNP). We found that the spline-LNP model successfully captured diverse spatial and temporal RF shapes, such as different RF polarities and uni- vs. bimodal temporal responses. The shapes of the modulatory kernels allowed to independently quantify their contributions: we found, on average, positive model kernels for running and pupil size, consistent with the overall enhancement of dLGN responses with behavioral state; we also found, on average, negative model kernels for optogenetic feedback suppression, capturing the removal of top-down excitation. Finally, training models on either movies or artificial noise stimuli revealed RFs with similar characteristics, although the noise stimulus elicited overall lower firing rates. By integrating feedforward drive, feedback modulation, and behavior into an interpretable spline-LNP model for dLGN responses, this work presents an important step towards a quantitative understanding of how dLGN responses to complex, naturalistic stimuli are modulated by CT feedback and behaviour.

Introduction

The dorsolateral geniculate nucleus (dLGN) of the thalamus occupies a central position in the processing of visual information from retina to primary visual cortex (V1)^{1,2}, being one of the first visual processing stages that combines signals from multiple visual and extra-visual brain areas³. Thus, rather than only relaying retinal information to V1, the local and long-range circuits in dLGN transform the feedforward retinal inputs: these transformations include the recombination of retinal inputs for novel feature selectivity⁴⁻⁸, the sharpening of spatial and temporal responses through inhibition⁹, the contextual modulations by L6 cortico-thalamic (CT) feedback¹⁰⁻¹⁵, as well as the gating of responses according to signals reflecting the animal's behavioural state transmitted by brain stem nuclei¹⁶⁻²⁰. While these factors have often been studied in isolation, it is still poorly understood how feedforward retinal input and the modulations by CT feedback and behavioural state act *in combination* to shape dLGN responses, in particular during wakefulness and in the context of a rich naturalistic visual stimulus^{2,3}.

Past studies have established how CT feedback and behavioural state act separately on dLGN activity. Concerning the effects of CT feedback, in face of a huge diversity of findings it seems agreed that CT feedback can sharpen spatial and temporal properties of dLGN RFs and change dLGN firing mode^{10,14,21-24}. In addition, effects of CT feedback on dLGN firing rates seem to be particularly robust during viewing of naturalistic movies, where they can be well captured by an increase in response

31 gain¹⁸. Concerning state-dependent modulations, the dLGN has long been known as one of the earliest stages in the visual
32 hierarchy where activity is shaped by the animal's behavioural state²⁵⁻²⁷. For instance, in the mouse, arousal, as inferred by
33 locomotion^{28,29} or pupil dilation^{18-20,30}, can enhance the responses of dLGN neurons. A quantitative understanding of the
34 relative strengths of these extraretinal effects on dLGN responses during wakefulness and how they might depend on the visual
35 stimulus is currently lacking.

36 In order to disentangle the combined impact of different extra-visual influences and investigate neuronal response properties
37 to arbitrary visual stimuli, a useful framework is offered by generalized linear models (GLMs)³¹⁻³³. In the early visual
38 system^{34,35}, including the dLGN³⁶, GLMs are generalizations of linear-nonlinear-Poisson (LNP) models. Here, the stimulus
39 is firstly filtered linearly in space and time; the output of this filter is then passed through a non-linear function which
40 translates input to a firing rate; this rate is then used to generate spikes according to Poisson process. GLMs can, in addition,
41 contain predictors accounting for any additional sensory, behavioral, or inter-neuronal influences. While GLMs are purely
42 phenomenological models, they offer the advantage of being interpretable: for instance, GLM filters applied to the stimulus
43 approximate the integration by the spatio-temporal receptive field (RF), and filters applied to any additional inputs represent
44 spike-induced gain adjustments^{33,37}. Pioneered in the retina³⁴, GLMs have since then been used in numerous studies to separate
45 influences of the visual stimulus and other variables, like spike history, interneuronal interaction effects, task-engagement,
46 learning, reward prediction, task-related motor action, locomotion, and arousal³⁸⁻⁴². In dLGN, GLMs have previously been
47 employed to separate retinal from extra-retinal³⁶ and spike-history influences^{36,43}.

48 Here, we investigated how feedforward, feedback and behavioural state signals influence dLGN activity in awake, head-fixed
49 mice viewing a complex, dynamic movie stimulus. To this end, we simultaneously recorded extracellular dLGN activity, mouse
50 run speed and pupil size, while photosuppressing CT feedback during stimulus presentation. We then fitted a spline-based
51 LNP model containing predictors for the spatio-temporal RF, CT feedback and behavioral variables to predict dLGN responses.
52 The model was able to capture dLGN responses to the movie in a held-out test set, and yielded biologically plausible filters.
53 Compared to a null model containing only the visual stimulus as predictor, all additional predictors, representing CT feedback
54 and behavioural state, contributed to successful performance. On average, we found that both CT feedback and behavioural
55 state enhanced dLGN responses. Finally, a comparison of filters obtained from models fitted to responses under different visual
56 stimulation conditions revealed that spatio-temporal RFs predicted from the responses to the dynamic movie stimulus were
57 similar to those based on responses to artificial noise stimuli. Together, our interpretable model of dLGN activity promises to
58 present an important step towards a quantitative understanding of how dLGN responses to complex, naturalistic stimuli are
59 modulated by CT feedback and behavioural state.

60 Results

61 *In vivo* dLGN activity, locomotion and eye-tracking during movie presentation and optogenetic L6CT feed- 62 back suppression

63 To investigate how CT feedback, locomotion and arousal modulate thalamic responses, we recorded *in vivo* extracellular
64 dLGN activity in head-fixed mice together with run speed and pupil size, while randomly photo-suppressing L6CT feedback
65 (Figure 1a-c). We presented a complex, dynamic movie stimulus that consisted of a diverse sequence of black-and-white scenes
66 from various feature films ('movies', Figure 1c). To assess the effect of V1 L6CT feedback suppression, we accompanied the
67 movie stimulus with a random train of 1 s optogenetic pulses occurring each second with 50 % chance. In order to later model
68 dLGN responses to the movies, we designated 80 % of the movie scenes as training sets and 20 % as test set. Training sets were
69 composed of 8 blocks of 36 unique 5 s movie clips (scenes). The test set consisted of 8 scenes repeated 9 times throughout the
70 stimulus.

71 In order to suppress L6CT feedback directly and reversibly, we conditionally expressed the soma-targeting, chloride-
72 conducting channelrhodopsin stGtACR2-RFP⁴⁴ in L6CT pyramidal cells by injecting a small volume of Cre-dependent AAV
73 into V1 of Ntsr1-Cre mice⁴⁵ (Figure 1d,e). The high light sensitivity of stGtACR2, its strong photocurrents, and its targeting
74 to the soma and axon-initial segment (AIS) are ideal to avoid unintended side-effects during photosuppression, which can
75 include accidental axonal depolarization at high light intensities⁴⁶⁻⁴⁸. We used post-mortem histological analyses to confirm
76 both the localisation of stGtACR2 to L6CT somata and the AIS (Figure 1e, left), and the correct electrode position in dLGN
77 (Figure 1e, right).

78 We found rich neural responses while mice viewed our dynamic movie stimulus (Figure 1f). As illustrated for an example
79 neuron during a small segment of our recording, firing rates varied across time, likely reflecting a combination of different input
80 sources. These presumably included aspects related to the visual stimulus, such as the time-varying drive by specific features
81 that occurred in and around the receptive field of the example neuron, and slower modulations of global luminance changes
82 in the different movie scenes ("stimulus intensity"). Responses also encompassed modulations arising from the randomly
83 occurring optogenetic suppression of CT feedback. In addition, other sources of inputs affecting the time-varying firing rates
84 were expected to be modulations of behavioural state, which we inferred from the animal's pupil size and running speed. For

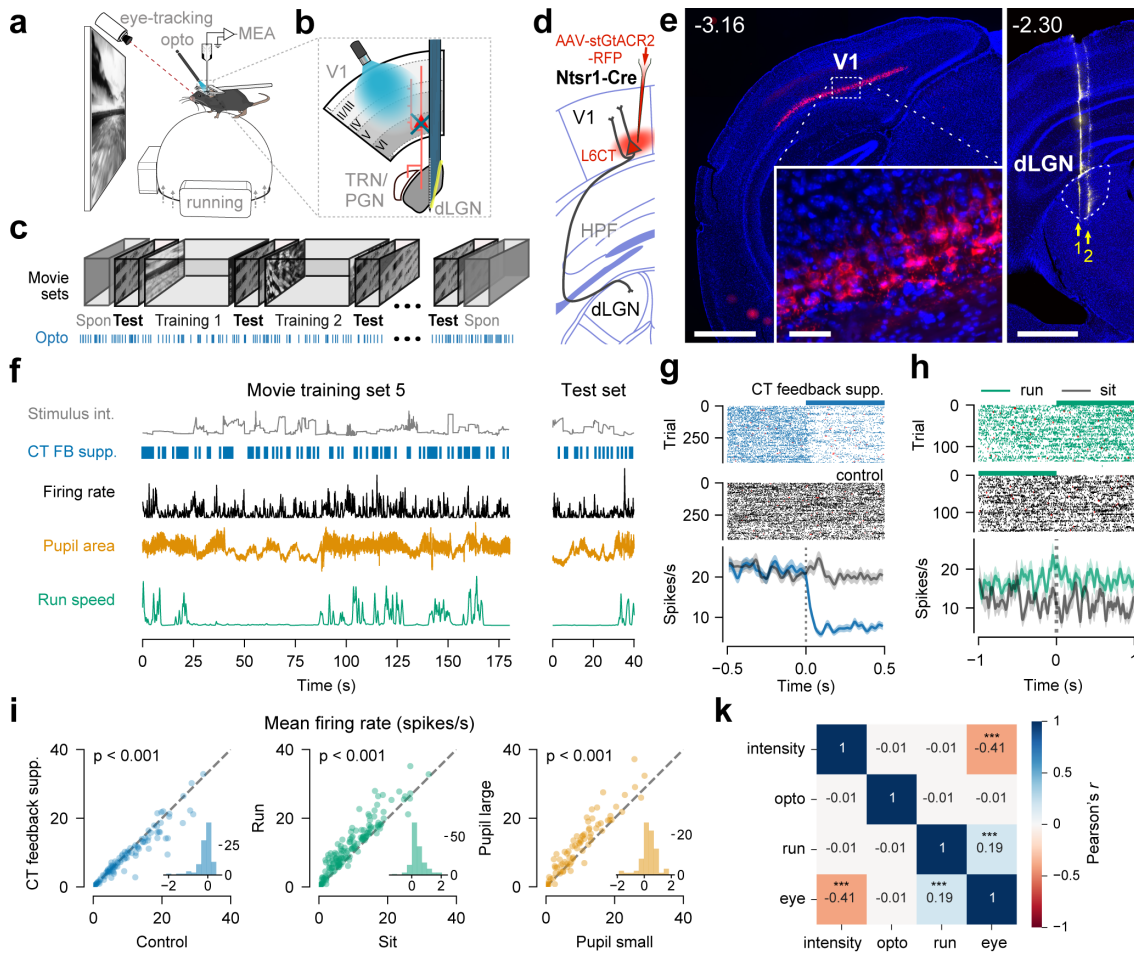


Figure 1 | Experimental design and dLGN responses to the movie stimulus. **(a)** Schematic of the recording setup. **(b)** Schematics of CT feedback suppression. **(c)** Movie stimulus consisting of 8 sets of unique, randomized training scenes (*Training 1, 2, etc.*; 36 unique scenes per training block; 5 s per scene), interleaved with 9 sets of the same repeated test scenes (*Test*; 8 scenes repeated across blocks; 5 s per scene), and flanked by a period of blank grey screen presentation at the beginning and at the end (*Spon*). To assess the effect of L6CT FB suppression, the stimulus presentation was accompanied by a random train of optogenetic pulses (*Opto*, 1 s duration, 50 % probability every second). **(d)** Schematic of viral transduction of V1 L6CT pyramidal neurons in *Ntsr1-Cre* mice with Cre-dependent AAV-stGtACR2-RFP virus expressing RFP-tagged chloride-conducting channelrhodopsin used for optogenetic suppression of V1 L6 CT feedback. **(e)** Histology. *Left*: Coronal section near V1 injection site, with stGtACR2-RFP expression (*red*) in somata and axon-initial segments of *Ntsr1+* cells. *Blue*: DAPI; scale bar: 1 mm. *Inset*: Magnification of area marked by dotted rectangle. Scale bar: 50 μ m; top-left number: slice position relative to Bregma. *Right*: Coronal section of dLGN recording sites, with highlighted dLGN contours (*dotted line*), and electrode tracks for two consecutive recording sessions (arrows 1 and 2) being marked by DiI-stain (*yellow*). Scale bar: 1 mm. **(f)** Example dLGN recording with stimulus intensity averaged per movie frame across the entire screen, opto pulse train, peri-stimulus time histogram (PSTH, spikes/s) of one example neuron, pupil area, and run speed for one example training sequence and one repeat of the test sequence. **(g)** Responses of the example dLGN neuron (same as in **f**) for periods of L6CT feedback photosuppression onsets (*blue*) and for control periods without photosuppression (*black*). *Top*: Raster plots, *red*: Spikes fired in bursts; *bottom*: Corresponding PSTHs. *Blue horizontal bar*: Photosuppression period. **(h)** Responses of the example dLGN neuron (same as in **f**) triggered on transitions in locomotion. *Top*: Raster plots for transition from sit→run (*green*) and from run→sit (*black*), with running periods marked by green bars. *Bottom*: Corresponding PSTHs. (Continued on next page)

Figure 1 (Continued) (i) Effects of L6CT FB photosuppression (*left*), locomotion (*middle*), and pupil size (*right*) on dLGN mean firing rates ($N = 159, 152, 62$ neurons, respectively). *Inset*: Histogram of firing rate fold-change (\log_2 -ratio) relative to control. (k) Correlation matrix of average stimulus intensity, optogenetic light pulses, mouse run speed and pupil area traces, showing average correlation values across experiments ($N = 6$). *** = $p < 0.001$.

85 instance, in the time between 90–130 s, larger pupil size and faster run speed seemed to coincide with increases in firing
86 rates. How these various inputs interact to specifically affect the neural responses on short and longer timescales, however, is
87 impossible to deduce from visual inspection alone.

88 To explore whether a simple approach based on condition-wise averaging could reveal the effects of CT feedback and
89 run-indexed behavioural state, we first split the continuous neuronal responses to the onsets of optogenetic light pulses or
90 transitions between sitting and running, respectively. For the example neuron shown in **Figure 1f**, the concatenation of all
91 onsets of L6CT photosuppression revealed that photosuppression of CT feedback suppression reduced its activity by almost
92 50% (**Figure 1g**). As regards the effect of locomotion, consistent with previous investigations^{28,29}, the activity of this example
93 neuron also slowly changed around transitions from sitting to running and vice versa (**Figure 1h**).

94 We observed similar effects in the population of recorded neurons. First, the net effect of V1 L6CT FB suppression on
95 dLGN mean firing rates (FR) was on average suppressive (**Figure 1i, left**). By contrast, running periods were associated, on
96 average, with increased FRs (**Figure 1i, middle**). Similarly, periods of large pupil sizes coincided with an average increase
97 in FRs (**Figure 1i, right**). For all variables, however, we observed substantial neuron-by-neuron diversity, indicating that
98 average effects will likely be limited in capturing to which degree responses of dLGN neurons are shaped by one or multiple
99 extra-retinal influences.

100 Having found effects of feedforward stimulus drive, CT feedback, run speed, and pupil size on dLGN firing rates separately,
101 we went on to investigate to what extent they might be related. For instance, aside from indicating arousal, pupil size is
102 also influenced by light intensity (pupil light reflex; e.g., **Figure 1f, right**), where increases in average stimulus intensity
103 coincide with decreases in pupil size, and vice versa (**Figure S1a**). Indeed, across experiments, we found a negative correlation
104 between pupil size and stimulus intensity ($r = -0.41 \pm 0.14$ (mean \pm SD); $p < 0.001$ for 6/6 experiments, permutation test;
105 **Figure 1k**). Consistent with previous results^{28,49,50}, we also found a positive correlation between pupil diameter and run speed
106 ($r = 0.19 \pm 0.18$; $p < 0.001$ for 5/6 experiments; **Figure 1k**), indicating that these indicators likely reflecting partially different,
107 but also overlapping set of arousal states^{49,50}. Taken together, we found rich neural responses evoked by our dynamic movie
108 stimulus, which were modulated in complex and neuron-specific ways by several non-retinal inputs, including behavioural
109 variables and L6CT FB suppression.

110 **Modelling dLGN spatio-temporal RFs and their modulation by L6CT feedback, running and pupil size**

111 The need to quantify the complex relations of feedforward input, L6CT feedback, and behaviour, motivated us to next turn
112 to a computational model that allowed us to quantitatively estimate the relative influences of each dLGN neuron's sensory
113 response properties and the various extraretinal modulations. To this end, we employed a spline-based linear-nonlinear-Poisson
114 (spline-LNP) model⁵¹ (**Figure 2a**), a variant of the generalized linear model (GLM)^{33,35,52}. Similar to other forms of GLMs,
115 the spline-LNP offers interpretability, by predicting neural firing rates as a function of a linear filtering step, approximating
116 the spatio-temporal RF, followed by a non-linearity and an inhomogeneous (time-varying) Poisson process to reflect the
117 stochastic nature of neural spiking. Furthermore, the feedback and behavioural components of the model are added to the
118 filtered spatio-temporal RF (**Figure 2a**), and thereby incorporate gain modulations³³ by CT feedback, running, and pupil
119 size. By exploiting a spline basis instead of operating on the pixels of the visual stimulus or the discrete time bins of the
120 additional inputs, our model is efficient in producing smooth and local filters⁵¹. Moreover, in the context of our complex visual
121 stimulus with substantial spatio-temporal redundancies typical of natural environments⁵³, GLM-like models, in comparison to a
122 simple spike-triggered average, are better suited for estimating spatio-temporal RFs, as illustrated for one example neuron in
123 **Figure S2**.

124 Given the known diversity of mouse dLGN response properties^{4,54}, we reasoned that the relative influence of the stimulus,
125 CT feedback and behavioural factors in shaping dLGN responses will differ from neuron to neuron. Hence, for each neuron, we
126 performed a grid search over potential model hyperparameters, to find the most suitable model configuration. Hyperparameters
127 included, for instance, the number of spline bases for spatio-temporal RF fitting, the strength of regularisation, as well as the
128 filter length for optogenetic, locomotion and pupil filter kernels (see Methods). We then chose, for each neuron, the model with
129 the best performance in predicting the responses to the validation set (variance explained R^2).

130 We found a rich diversity of predicted GLM model filters, both for the dLGN neurons' spatio-temporal RFs and the effects
131 of CT feedback and the behavioural variables. As can be seen from the three example neurons shown in **Figure 2b-d**, our GLM
132 model allowed us to describe a neuron's polarity in terms of its spatial RF weights (ON/OFF) and its response dynamics in

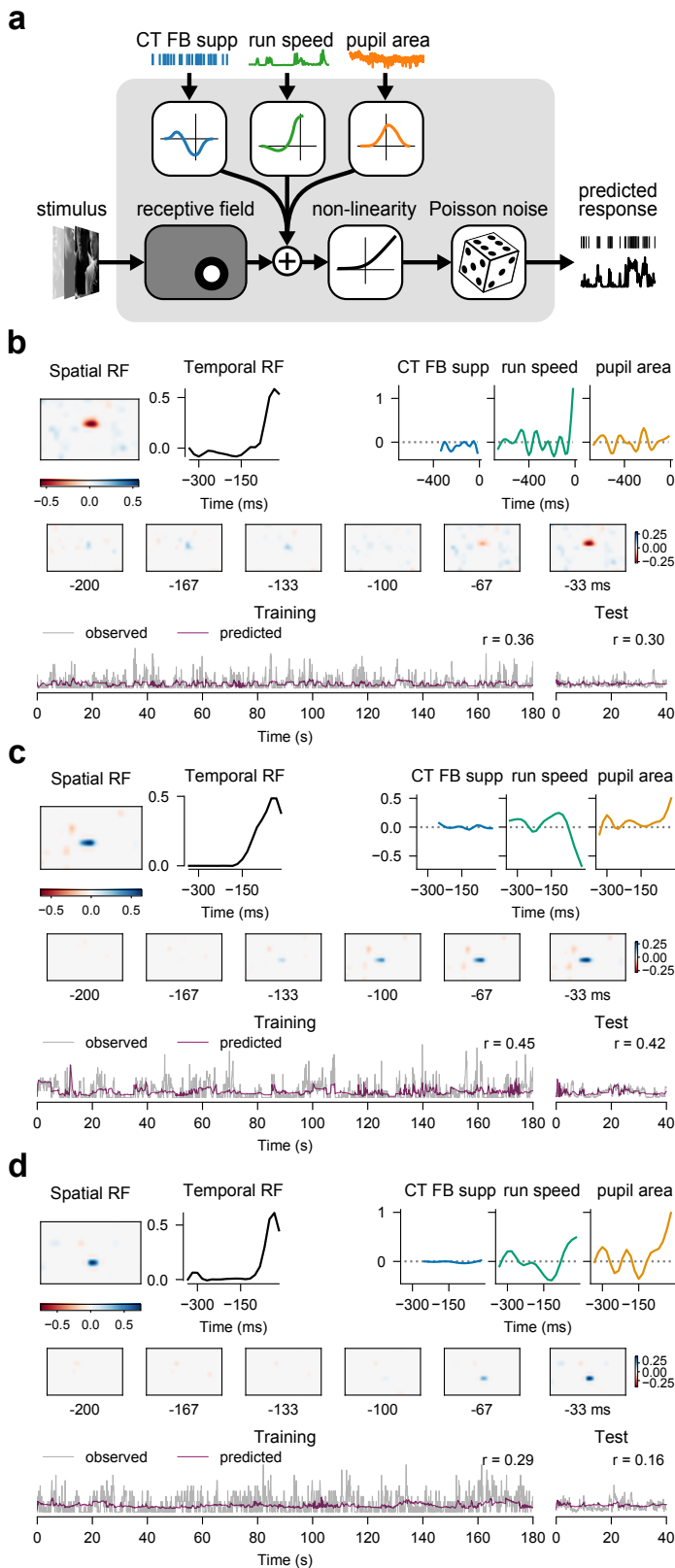


Figure 2 | Spline-based linear-nonlinear-Poisson (spline-LNP) model of dLGN responses to our dynamic movie stimulus and their modulation by non-retinal influences. (a) Schematics of the spline-LNP model. The linear stage filters the stimulus input and corresponds to the spatio-temporal RF. The outputs of filters for CT feedback suppression and the behavioural variables run speed and pupil area are added to the output of the linear-stage, which conceptually corresponds to a gain modulation of the firing rates³³. Finally, the total output is passed through a point non-linearity (here, the *softplus*), resulting in a time-varying rate parameter, which serves as input to a Poisson process to generate stochastic spiking. Spikes are time-binned to create firing rates. During model fitting, the GLM filters are optimized to maximize the correlation between observed and predicted firing rates. **(b)** Fitted model for an example dLGN neuron (same example neuron as in **Figure 1f-h**) with learned filters and firing rate predictions. *Top (left to right)*: Spatial and temporal RF components of the spatio-temporal RF extracted via singular value decomposition (SVD). The negative spatial RF weight values are indicative of an OFF-cell, and the peak of the temporal RF at -33 ms corresponds to a maximal response to a matching dark stimulus 33 ms after its appearance. The non-zero CT feedback suppression and run-filters suggest an influence by those predictors, whereas the flat eye-filter indicates independence of this neuron's activity from pupil size. *Middle*: Spatio-temporal RF at individual time points prior to spiking. *Bottom*: Observed (gray) versus predicted (purple) firing rates to one training block (*left*) and test block (*right*) of the movie stimulus, along with the correlation coefficient (Pearson's r). **(c)** and **(d)**: Same as **(b)** for two more example neurons.

133 terms of its temporal RF kernel. As expected^{54,55}, the predicted spatio-temporal RFs were mostly circular, sometimes with an
134 opposite-polarity surround, and varied across neurons in terms of location, polarity, RF size and temporal response dynamics.
135 Considering the extra-retinal predictors, for the example neuron in **Figure 2b** (same example neuron as in **Figure 1f-h**),
136 the model predicted an enhancing filter for run speed and a slightly suppressive filter for CT feedback suppression. These
137 filter signs were consistent with our previous observations for this neuron, which showed suppression of firing rates during
138 photosuppression of L6CT FB and an enhancement of rates triggered on transitions between sitting and running. Consistent
139 with the diverse effects of the extra-retinal influences on firing rates across the population **Figure 1i**, we found a variety of
140 GLM model filter shapes for the extra-retinal predictors. For instance, for the neuron in **Figure 2c**, the predicted filter shape
141 for CT feedback suppression suggested that CT feedback did not modulate its activity. Yet, this neuron did not only process
142 feedforward information, as the modelled filter for running speed indicated a substantial suppressive effect, whereas the filter
143 for pupil size indicated a response enhancement. The third example neuron (**Figure 2d**) is interesting in that its contribution of
144 the pupil size filter to firing rates seemed even larger than that of the spatio-temporal RF, despite the fact that the RF was well
145 defined both in space and time.

146 Having observed considerable variability in the magnitude and shape of the modelled filters across our example dLGN
147 neurons, we next asked to which degree each predictor contributed to improving model performance. To investigate to which
148 degree the integration of behavioural influences and L6CT FB suppression was relevant for predicting firing rates in our model,
149 we compared the performance of our full model with that of model variants with different sets of predictor variables (**Figure 3a**).
150 Indeed, comparing the correlation coefficient between observed and predicted responses across the population of recorded
151 neurons, we found that a model with only a single filter related to the stimulus ('Stimulus only' model), on average, performed
152 worse than the full model including all predictors ($r = 0.140$ vs. $r = 0.153$; (**Figure 3a, top**)). However, when examining in
153 more detail the contribution of the individual predictors in the current implementation of our GLM model, we realised that the
154 performance gain by the full model was most strongly influenced by the inclusion of L6CT FB ($r = 0.153$, 'Stim + FB' model,
155 (**Figure 3a, 2nd row, left**)), since a model adding only this predictor performed better than the "stimulus only" model and in
156 fact had equal performance compared to the full model. In contrast, models with filters for run speed or pupil size (**Figure 3a,**
157 **3rd and 4th row**)) actually performed worse than the baseline 'Stimulus only' model (all $r < 0.134$).

158 To understand better, on a neuron-by-neuron basis, the various ways in which the non-retinal predictors contributed to
159 the performance of our spline LNP model, and to relate the predicted filters to firing rate modulations by L6CT feedback,
160 locomotion and pupil size, we next examined the GLM filter shapes. To this end, we split the recorded dLGN population
161 into neurons that were modulated or non-modulated by those factors, as judged respectively by the FR opto-modulation index
162 (OMI), the run-modulation index (RMI), and the eye-modulation index (EMI) (see Methods), and examined the averaged filter
163 shapes (**Figure 3b**). As judged by visual inspection, we found that modulated neurons, as expected, had stronger absolute
164 weights compared to non-modulated neurons, whose filter weights fluctuated around zero. In addition, the sign of the filters
165 matched the sign of the average effects, with the filters for CT feedback suppression having overall negative weights, while
166 filters for run speed and pupil size had positive weights. In summary, the absolute magnitude and sign of the filter weights
167 suggest that our GLM model successfully recovered the influence of those factors in modulated vs. non-modulated units. In
168 future analyses, it will be important to quantitatively related the weights and time course of the filters, and investigate whether,
169 on a neuron-by-neuron basis, the modulation by extra-retinal predictors relates to the strength of feedforward processing.

170 **Comparing spatio-temporal receptive fields across stimuli**

171 Since RFs of visual neurons are not fixed, but can vary in size, complexity, and temporal dynamics when measured under
172 different visual stimulation conditions⁵⁶⁻⁶⁰, we next asked whether the spatio-temporal RFs of our dLGN neurons differed when
173 estimated from the movie compared to a sparse noise stimulus, classically used to measure RFs. To allow for a fair comparison,
174 we equated the input image resolution and the models' spatial degrees of freedom (number of spline bases; see Methods).
175 Moreover, for both stimuli, we concentrated on the reduced model containing only a stimulus filter, since our previous analysis
176 had revealed that the run speed and pupil size-related predictors conferred little benefit in terms of predictive performance in
177 the current version of the model. In the future, when results for the improved versions of the model will be available, we will
178 obviously include these predictors, since – in addition to investigating the stimulus dependence of spatio-temporal RFs – it will
179 be equally interesting and relevant to investigate to which degree the modulation by the extra-retinal influences will depend on
180 the stimulus type.

181 As illustrated for an example dLGN neuron, our spline-LNP model was successful in recovering the spatio-temporal RF,
182 also when fitted to responses recorded during the sparse noise stimulus (**Figure 4a, top**). More specifically, the extracted
183 spatio-temporal RF of the example neuron was circular and had an ON-polarity, responding best to bright stimuli at around
184 $t = -40$ ms. However, note that model performance was poor, with only occasional increases in firing rate predicted when the
185 optimal stimulus was presented in the RF, which occurred rarely given the sparse nature of the visual stimulus. We expect
186 that future versions of the model including the behavioural predictors will substantially improve response predictions. With

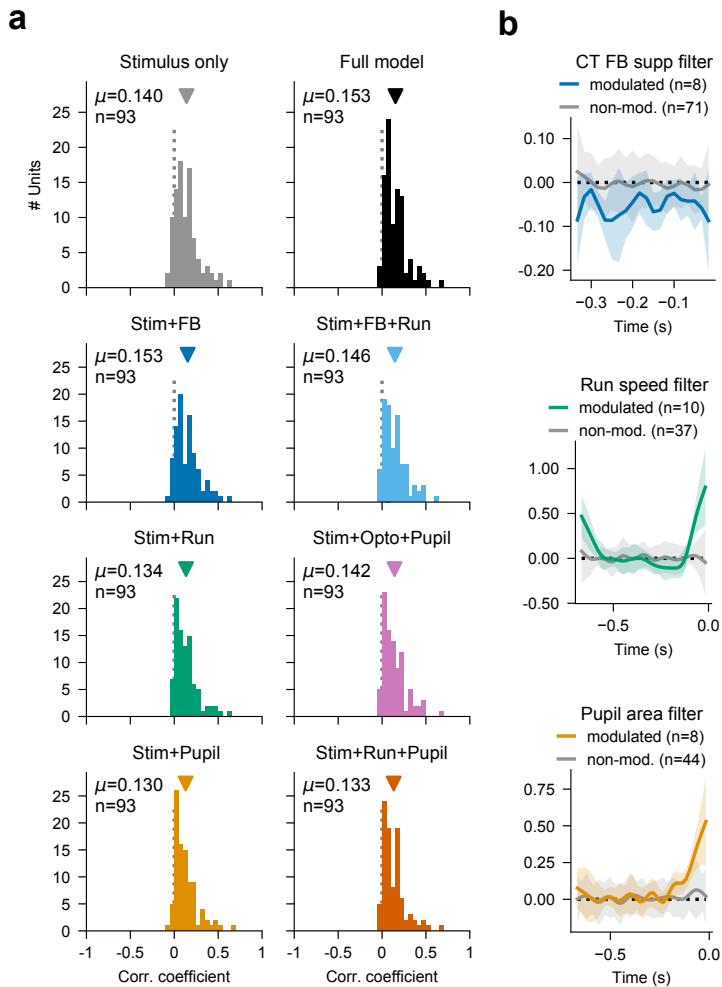


Figure 3 | Spline-LNP model analysis for dLGN population. (a) Comparison of model performance (Pearson's r) for model types with different sets of predictors. *Top left*: 'Stimulus only': Models whose only predictor variable is the spatio-temporal RF for the stimulus. *Top right*: 'Full model': Models which include all tested predictor variables, including the stimulus, L6 CT FB suppression, run speed (cm/s), and pupil dilation (mm^2). *Below*: Model type variations with models that include, in addition to the stimulus filter, either only optogenetics, running or eye-tracking, or combinations thereof. (b) Average model population filters for the other predictors besides the stimulus. *Top*: Average model filters related to L6 CT FB suppression for the dLGN population, split by the opto-modulation index (OMI) into units whose mean FRs were modulated by optogenetics (blue line) versus units that were not modulated (grey line). Shaded areas: Standard deviation. *Middle*: Same for model filters related to run speed. Here, the population was split into modulated vs not modulated via the run-modulation index (RMI). *Bottom*: Same for model filters related to pupil size. Here, the population was split into modulated vs not modulated via the eye-modulation index (EMI).

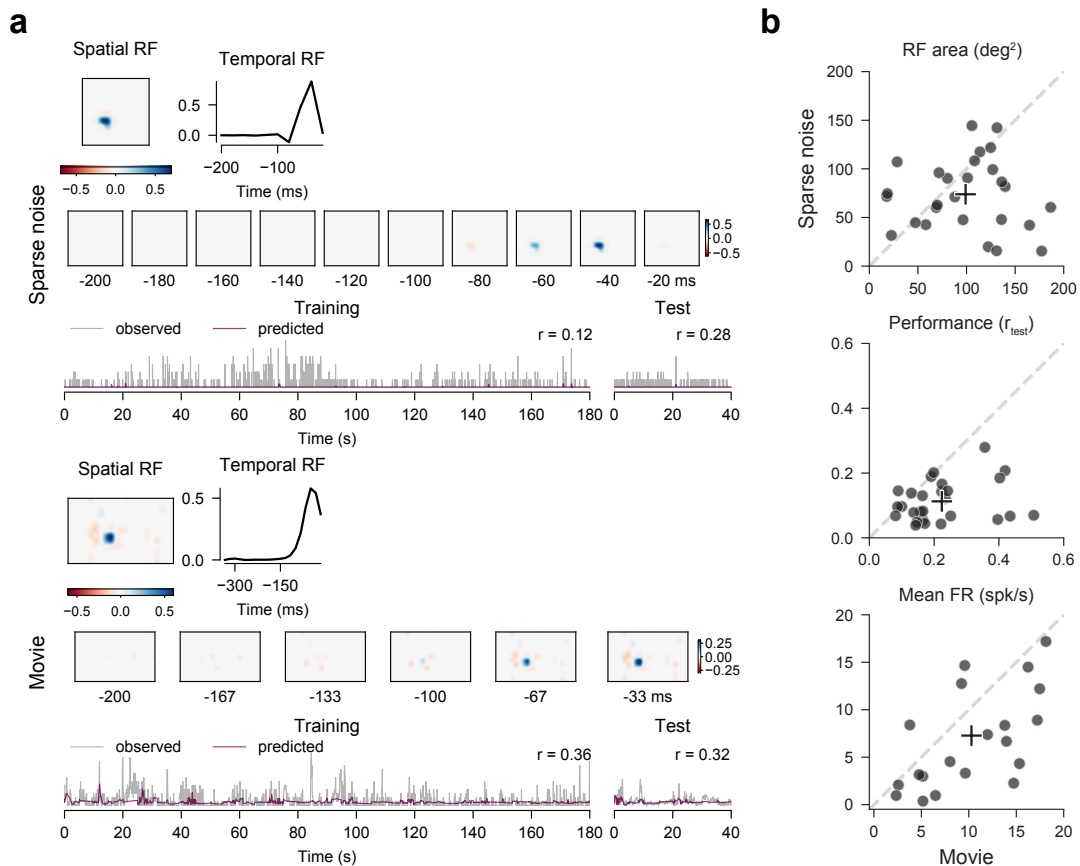


Figure 4 | Comparing spatio-temporal RFs predicted from responses to a sparse noise vs. movie stimulus. (a) *Top*: Predicted spatio-temporal RF for the sparse noise stimulus for one example dLGN neuron. *Bottom*: Same, for the movie stimulus (same example neuron). Both models were fitted with the stimulus filter as the sole predictor (Stimulus-only model configuration). (b) Comparison of spatial RF size (*top*), model prediction performance to the held-out test set (*middle*) and mean firing rates (*bottom*) for the sparse noise vs. movie stimulus across the population of dLGN neurons recorded for both stimulus types ($n = 27$). *Cross*: Population means.

187 these caveats in mind, the spatio-temporal RF predicted for the sparse noise stimulus qualitatively resembled that predicted for
 188 the movie stimulus (Figure 4a, bottom), in terms of general polarity, location, and temporal dynamics. Interestingly, visual
 189 inspection suggested that the opposite polarity surround in the spatial RF might be stronger during movies compared to sparse
 190 noise stimuli.

191 We observed similar results for the population of dLGN neurons recorded in both stimulus conditions ($n = 27$, Figure 4b).
 192 Spatial RFs tended to be larger for the movie compared to the sparse noise stimulus ($99.0 \pm 47.3 \text{ deg}^2$ vs. $73.9 \pm 36.3 \text{ deg}^2$;
 193 Wilcoxon test: $p = 0.08$), which might potentially be related to the spatial correlations in natural movies or the larger variation
 194 in eye position during viewing natural movies. As observed for the example neuron, model prediction performance was worse
 195 for the sparse noise stimulus (r_{test} sparse noise vs. movie: 0.11 ± 0.06 vs. 0.22 ± 0.12 ; Wilcoxon test: $p = 0.00004$). This
 196 might be related to the overall sparser activity during the sparse noise compared to the movie stimulus (mean FR sparse noise
 197 vs. movie: $10.3 \pm 5.3 \text{ sp/s}$ vs. $7.3 \pm 5.1 \text{ sp/s}$; Wilcoxon test: $p = 0.0001$). In future work, the relationship between performance
 198 and firing rate should be explicitly tested by correlating the two variables or mean-matching the firing rates across stimuli⁶¹.
 199 To conclude, the spline-LNP model might be able to successfully generalize its ability to extract spatio-temporal RFs across
 200 stimuli, including a sparse noise stimulus, in spite of the drastically different stimulus nature.

201 Discussion

202 Here, we asked how dLGN responses are influenced by the combined impact of retinal feedforward inputs, CT feedback and
203 behavioural state. To this end, we predicted dLGN single unit responses using a spline-based LNP model, which received as
204 inputs the visual stimulus, periods of optogenetic suppression of CT feedback, and as behavioral variables the animal's run
205 speed and pupil size. Our LNP model was able to recover spatio-temporal RFs of individual dLGN neurons and modulatory
206 influences of CT feedback and behavioral markers for arousal, which were consistent with the previous literature. For the
207 current version of the model, we found that for the population of recorded neurons, at least some of the non-visual model inputs
208 improved response predictions. Finally, comparing the extracted RFs to a movie stimulus and to an artificial noise stimulus,
209 we found overall similar spatio-temporal RFs, with spatial RF sizes tending to be larger for the movie compared to the noise
210 stimulus, potentially related to the lower contrast or the larger variability in eye position for the movie stimulus. Together,
211 our study provides a modelling framework that promises a quantitative understanding of how dLGN responses to complex,
212 naturalistic stimuli are modulated by CT feedback and behaviour.

213 One key advance of our study is to extend previous LNP models of dLGN responses to naturalistic movies, by incorporating
214 additional predictors for CT feedback and behavioural state. Indeed, we directly build on work performed in anaesthetised
215 cats, which explored LNP model architectures and their GLM extensions to predict dLGN responses to artificial stimuli and
216 naturalistic movies^{43,56}. Importantly, as pioneered by Babadi and colleagues for spots of different sizes and luminances in
217 dLGN of the anesthetized cat³⁶, the specific aim of the GLM presented in this study was to provide a quantitative statistical
218 model probing how dLGN responses are shaped by non-retinal factors. While Babadi and colleagues³⁶ exploited simultaneous
219 recordings of retinal S-potentials with dLGN spiking output and could thus separate the impact of the retinal input from
220 the combined role of intra-dLGN computations and influences mediated by the visTRN and CT feedback, the optogenetic
221 suppression of L6 CT pyramidal cells allowed us to tease apart the influence of V1 L6 CT feedback. In line with Babadi's
222 study³⁶, who reported that the incorporation of the non-retinal predictor in their GLM improved prediction quality, in particular
223 for stimulus sizes that exceeded the classical RF size³⁶, we found in our model that including the predictor for CT feedback
224 suppression improved prediction quality. As noted before³⁶, the amount of improvement varied across neurons, in line with
225 experimental observations of diverse effects of CT feedback⁶². Note that for the model version reported here, adding predictors
226 for pupil size and locomotion did not improve the quality of the model predictions. Preliminary results obtained with a modified
227 model, and improved pre-processing and quality control of the pupil size signal, indicate that this conclusion will likely change
228 in future iterations of our methods.

229 In the current model version, we chose to use a softplus nonlinearity over an exponential nonlinearity as we encountered
230 issues with model convergence with the latter. However, there are good theoretical and empirical reasons to prefer an exponential:
231 mathematically, exponentiating the summed filter responses for all three extra-retinal predictors is equivalent to modelling them
232 as multiplicative influences on neural activity³³, i.e. gain modulations. In the context of locomotion, such gain modulations have
233 been known to operate on several stimulus dimensions, such as orientation, contrast, temporal and spatial frequency^{28,29,50,63}
234 (but see^{28,64} for stimulus size). Similarly, in case of pupil size change, multiplicative influences on responses to natural movies
235 have been reported for V1⁵⁰. Finally, a multiplicative model generally captured well the effects of CT feedback on dLGN
236 responses to movies¹⁸. Together, these previous findings would clearly justify such a design for the next iteration of our GLM.
237 The multiplicative behaviour of the predictors, however, will obviously not be able to cover any sharpening of orientation
238 selectivity, as reported for effects of pupil dilation on V1 orientation tuning curves⁵⁰, and the well-known changes in spatial
239 integration of dLGN neurons driven by CT feedback^{13,65}. Nevertheless, some of these shortcomings could be addressed in
240 further extensions of the model (see below).

241 The predicted influences of CT feedback, locomotion, and pupil size matched previous results that considered these
242 extra-retinal factors mainly independently. Consistent with previous findings^{18–20,28,29}, increases in running speed and pupil
243 size were related to overall higher dLGN responses, and were also captured by mostly positive filter shapes in our GLM.
244 Our findings of decreased dLGN responses and negative GLM model filters for optogenetic suppression of CT feedback
245 also matched previous results obtained for naturalistic movies¹⁸. It should be noted, however, that CT feedback effects vary
246 dramatically across studies^{12,62,66–70}, for reasons that are still incompletely understood and that might be related to the type of
247 visual stimulus, the feedback manipulation method, or the state of the animal. Beyond these average effects of the extra-retinal
248 influences reported in our study, one striking observation we made concerns their variability across neurons. Further analyses
249 will be required to explain this variability, by testing, for instance, differential effects for functional cell types, such as ON- vs.
250 OFF-cells, transient vs. sustained cells, suppressed-by-contrast cells, obtained from other stimuli recorded but not yet analysed
251 here.

252 Consistent with previous studies quantifying RFs in the mouse dLGN^{54,55,71,72}, our spline-LNP model predicted circular
253 spatial RFs, which often consisted of a single domain responding to either light increases or decreases. As has been noted
254 before^{54,55}, fewer dLGN neurons also had an opposing surround. Given previous reports of similar proportions of ON- and
255 OFF-center⁷¹, or even a higher proportion of OFF-center dLGN neurons⁵⁴, we were surprised to find a tendency for more

256 ON-center compared to OFF-center cells. For the final version of this study, a statistical quantification of the relative frequencies
257 of ON- and OFF-cells will be imperative. Similarly, dLGN receptive fields differed in their temporal profile, with some
258 neurons having a biphasic profile indicative of transient responses, while others had a monophasic profile indicative of sustained
259 responses (see also⁵⁴).

260 We found a trend for larger spatial RFs obtained from movie vs. sparse noise stimulation. RF size is known to be inherently
261 variable, given its sensitivity to both low level stimulus attributes, such as contrast, stimulus context, and behavioural variables,
262 such as locomotion and eye movements^{28,58-60,64}. To which degree some or all of these factors contribute to the difference in RF
263 size between the two stimuli remains a matter of future quantification. Interestingly, a previous study comparing spatio-temporal
264 RFs fitted by a LNP model to movies vs. white noise stimuli in anesthetized cats⁵⁶ also reported larger RFs for movies
265 compared to white noise, even when the stimuli were equalized in terms of contrast. Strikingly, movies also led to a stronger
266 surround and a shorter temporal width of the RF⁵⁶, potentially to reduce the spatio-temporal redundancy in natural stimuli.

267 In the future, there are a number of possible extensions of our spline-LNP model. First, CT feedback could be modelled as
268 a spatio-temporal filter instead of a single gain factor, accounting for the well-known differential effects of CT feedback on
269 spatial integration^{13,65}. Second, instead of considering the spatio-temporal RF fixed, the model could contain mechanisms
270 for fast adaptation of gain and integration time according to luminance and contrast^{56,73}, accounting for the constant changes
271 in spatial and temporal integration elicited by dynamic natural stimuli. Finally, an important non-linear feature of thalamic
272 responses are bursts, which are thought to be related not only to the behavioral state of the animal^{26,28,63}, but can also be
273 triggered by features of natural stimuli⁷⁴. Different model architectures will be needed to include this non-linear response
274 feature of thalamic neurons.

275 In conclusion, our results add to the growing body of evidence that dLGN activity is influenced not only by retinal visual
276 inputs but also extra-retinal influences from CT feedback and behavioural state. While our model is purely phenomenological³³,
277 this work presents an important step towards a quantitative understanding of how dLGN responses to complex, naturalistic
278 stimuli are shaped by the simultaneous influences of retinal feedforward inputs, CT feedback and behaviour. Future iterations
279 of our model and further quantification of the results will be needed to finalise the conclusions.

References

- 280 **1.** Berson, D. Retinal ganglion cell types and their central projections. In Masland, R. H. (ed.) *The Senses: a Comprehensive*
281 *Reference*, 491–520 (Elsevier Inc., 2008).
- 282 **2.** Usrey, W. M. & Alitto, H. J. Visual Functions of the Thalamus. *Annu. Rev. Vis. Sci.* **1**, 351–371, DOI: [10.1146/annurev-vision-082114-035920](https://doi.org/10.1146/annurev-vision-082114-035920) (2015). [15334406](https://doi.org/10.1146/annurev-vision-082114-035920).
- 283 **3.** Weyand, T. G. The multifunctional lateral geniculate nucleus. *Rev. Neurosci.* **27**, 135–157, DOI: [10.1515/revneuro-2015-0018](https://doi.org/10.1515/revneuro-2015-0018) (2016).
- 284 **4.** Román Rosón, M. *et al.* Mouse dLGN Receives Functional Input from a Diverse Population of Retinal Ganglion Cells
285 with Limited Convergence. *Neuron* **102**, 462–476, DOI: [10.2139/ssrn.3205414](https://doi.org/10.2139/ssrn.3205414) (2019).
- 286 **5.** Morgan, J. L., Berger, D. R., Wetzell, A. W. & Lichtman, J. W. The Fuzzy Logic of Network Connectivity in Mouse
287 Visual Thalamus. *Cell* **165**, 192–206, DOI: [10.1016/j.cell.2016.02.033](https://doi.org/10.1016/j.cell.2016.02.033) (2016).
- 288 **6.** Hammer, S., Monavarfeshani, A., Lemon, T., Su, J. & Fox, M. A. Multiple Retinal Axons Converge onto Relay Cells in
289 the Adult Mouse Thalamus. *Cell Reports* **12**, 1575–1583, DOI: [10.1016/j.celrep.2015.08.003](https://doi.org/10.1016/j.celrep.2015.08.003) (2015).
- 290 **7.** Ellis, E. M., Gauvain, G., Sivyer, B. & Murphy, G. J. Shared and distinct retinal input to the mouse superior colliculus
291 and dorsal lateral geniculate nucleus. *J. Neurophysiol.* **116**, 602–610, DOI: [10.1152/jn.00227.2016](https://doi.org/10.1152/jn.00227.2016) (2016).
- 292 **8.** Liang, L. *et al.* A fine-scale functional logic to convergence from retina to thalamus. *Cell* **173**, 1343–1355.e24, DOI:
293 [10.1016/j.cell.2018.04.041](https://doi.org/10.1016/j.cell.2018.04.041) (2018).
- 294 **9.** Hirsch, J. A., Wang, X., Sommer, F. T. & Martinez, L. M. How inhibitory circuits in the thalamus serve vision. *Annu.*
295 *Rev. Neurosci.* **38**, 309–329, DOI: [10.1146/annurev-neuro-071013-014229](https://doi.org/10.1146/annurev-neuro-071013-014229) (2015).
- 296 **10.** Sillito, A. M., Cudeiro, J. & Jones, H. E. Always returning: feedback and sensory processing in visual cortex and
297 thalamus. *Trends Neurosci.* **29**, 307–316, DOI: [10.1016/j.tins.2006.05.001](https://doi.org/10.1016/j.tins.2006.05.001) (2006).
- 298 **11.** Briggs, F. & Usrey, W. M. Corticogeniculate feedback and parallel processing in the primate visual system. *J. Physiol.*
299 **589**, 33–40, DOI: [10.1113/jphysiol.2010.193599](https://doi.org/10.1113/jphysiol.2010.193599) (2011).
- 300 **12.** Olsen, S. R., Bortone, D. S., Adesnik, H. & Scanziani, M. Gain control by layer six in cortical circuits of vision. *Nature*
301 **483**, 47–52, DOI: [10.1038/nature10835](https://doi.org/10.1038/nature10835) (2012).
- 302 **13.** Born, G. *et al.* Corticothalamic feedback sculpts visual spatial integration in mouse thalamus. *Nat. Neurosci.* **24**,
303 1711–1720, DOI: [10.1038/s41593-021-00943-0](https://doi.org/10.1038/s41593-021-00943-0) (2021).
- 304 **14.** Andolina, I. M., Jones, H. E. & Sillito, A. M. Effects of cortical feedback on the spatial properties of relay cells in the
305 lateral geniculate nucleus. *J. Neurophysiol.* **109**, 889–899, DOI: [10.1152/jn.00194.2012](https://doi.org/10.1152/jn.00194.2012) (2013).
- 306 **15.** Shepherd, G. M. G. & Yamawaki, N. Untangling the cortico-thalamo-cortical loop: cellular pieces of a knotty circuit
307 puzzle. *Nat. Rev. Neurosci.* **22**, 389–406, DOI: [10.1038/s41583-021-00459-3](https://doi.org/10.1038/s41583-021-00459-3) (2021).
- 308 **16.** McCormick, D. A. Neurotransmitter actions in the thalamus and cerebral cortex and their role in neuromodulation of
309 thalamocortical activity. *Prog. Neurobiol.* **39**, 337–388, DOI: [10.1016/0301-0082\(92\)90012-4](https://doi.org/10.1016/0301-0082(92)90012-4) (1992).
- 310 **17.** Sherman, S. M. & Guillery, R. W. Functional organization of thalamocortical relays. *J. Neurophysiol.* **76**, 1367–1395,
311 DOI: [10.1152/jn.1996.76.3.1367](https://doi.org/10.1152/jn.1996.76.3.1367) (1996).
- 312 **18.** Spacek, M. A. *et al.* Robust effects of corticothalamic feedback and behavioral state on movie responses in mouse dlgn.
313 *bioRxiv* DOI: [10.1101/776237](https://doi.org/10.1101/776237) (2022). <https://www.biorxiv.org/content/early/2022/02/09/776237.full.pdf>.
- 314 **19.** Nestvogel, D. B. & McCormick, D. A. Visual thalamocortical mechanisms of waking state-dependent activity and alpha
315 oscillations. *Neuron* **0**, DOI: [10.1016/j.neuron.2021.10.005](https://doi.org/10.1016/j.neuron.2021.10.005) (2021).
- 316 **20.** Molnár, B. *et al.* Cell-Type Specific Arousal-Dependent Modulation of Thalamic Activity in the Lateral Geniculate
317 Nucleus. *bioRxiv* DOI: [10.1093/textcom/tgab020](https://doi.org/10.1093/textcom/tgab020) (2021).
- 318 **21.** Cudeiro, J. & Sillito, A. M. Spatial frequency tuning of orientation-discontinuity-sensitive corticofugal feedback to the
319 cat lateral geniculate nucleus. *The J. Physiol.* **490**, 481–492, DOI: [10.1113/jphysiol.1996.sp021159](https://doi.org/10.1113/jphysiol.1996.sp021159) (1996).
- 320 **22.** Hasse, J. M. & Briggs, F. Corticogeniculate feedback sharpens the temporal precision and spatial resolution of visual
321 signals in the ferret. *Proc. Natl. Acad. Sci. United States Am.* **114**, E6222–E6230, DOI: [10.1073/pnas.1704524114](https://doi.org/10.1073/pnas.1704524114)
322 (2017).
- 323 **23.** Sherman, S. M. Tonic and burst firing: Dual modes of thalamocortical relay. *Trends Neurosci.* **24**, 122–126, DOI:
324 [10.1016/S0166-2236\(00\)01714-8](https://doi.org/10.1016/S0166-2236(00)01714-8) (2001).
- 325
- 326
- 327

- 328 24. Wang, W., Jones, H. E., Andolina, I. M., Salt, T. E. & Sillito, A. M. Functional alignment of feedback effects from
329 visual cortex to thalamus. *Nat. Neurosci.* **9**, 1330–1336, DOI: [10.1038/nm1768](https://doi.org/10.1038/nm1768) (2006).
- 330 25. Swadlow, H. A. & Weyand, T. G. Corticogeniculate neurons, corticotectal neurons, and suspected interneurons in visual
331 cortex of awake rabbits: receptive-field properties, axonal properties, and effects of EEG arousal. *J. Neurophysiol.* **57**,
332 977–1001, DOI: [10.1152/jn.1987.57.4.977](https://doi.org/10.1152/jn.1987.57.4.977) (1987).
- 333 26. Bezdudnaya, T. *et al.* Thalamic burst mode and inattention in the awake LGNd. *Neuron* **49**, 421–432, DOI: [10.1016/j.
334 neuron.2006.01.010](https://doi.org/10.1016/j.neuron.2006.01.010) (2006).
- 335 27. Cano, M., Bezdudnaya, T., Swadlow, H. A. & Alonso, J.-M. Brain state and contrast sensitivity in the awake visual
336 thalamus. *Nat. Neurosci.* **9**, 1240–1242, DOI: [10.1038/nm1760](https://doi.org/10.1038/nm1760) (2006).
- 337 28. Erisken, S. *et al.* Effects of locomotion extend throughout the mouse early visual system. *Curr. Biol.* **24**, 2899–2907,
338 DOI: [10.1016/j.cub.2014.10.045](https://doi.org/10.1016/j.cub.2014.10.045) (2014).
- 339 29. Aydın, Ç., Couto, J., Giugliano, M., Farrow, K. & Bonin, V. Locomotion modulates specific functional cell types in the
340 mouse visual thalamus. *Nat. communications* **9**, 4882, DOI: [10.1038/s41467-018-06780-3](https://doi.org/10.1038/s41467-018-06780-3) (2018).
- 341 30. Liang, L. *et al.* Retinal inputs to the thalamus are selectively gated by arousal. *Curr. Biol.* **30**, 3923–3934.e9, DOI:
342 [10.1016/j.cub.2020.07.065](https://doi.org/10.1016/j.cub.2020.07.065) (2020).
- 343 31. McCullagh, P. *Generalized linear models* (Chapman and Hall, Boca Raton London New York, 1989).
- 344 32. Paninski, L. Maximum likelihood estimation of cascade point-process neural encoding models. *Network: Comput.
345 Neural Syst.* **15**, 243–262, DOI: [10.1088/0954-898x_15_4_002](https://doi.org/10.1088/0954-898x_15_4_002) (2004).
- 346 33. Pillow, J. W. *et al.* Spatio-temporal correlations and visual signalling in a complete neuronal population. *Nature* **454**,
347 995–999, DOI: [10.1038/nature07140](https://doi.org/10.1038/nature07140) (2008).
- 348 34. Pillow, J. W., Paninski, L., Uzzell, V. J., Simoncelli, E. P. & Chichilnisky, E. J. Prediction and decoding of retinal
349 ganglion cell responses with a probabilistic spiking model. *J. Neurosci.* **25**, 11003–11013, DOI: [10.1523/JNEUROSCI.
350 3305-05.2005](https://doi.org/10.1523/JNEUROSCI.3305-05.2005) (2005).
- 351 35. Schwartz, O., Pillow, J. W., Rust, N. C. & Simoncelli, E. P. Spike-triggered neural characterization. *J. Vis.* **6**, 13, DOI:
352 [10.1167/6.4.13](https://doi.org/10.1167/6.4.13) (2006).
- 353 36. Babadi, B., Casti, A., Xiao, Y., Kaplan, E. & Paninski, L. A generalized linear model of the impact of direct and indirect
354 inputs to the lateral geniculate nucleus. *J. Vis.* **10**, 22–22, DOI: [10.1167/10.10.22](https://doi.org/10.1167/10.10.22) (2010).
- 355 37. Paninski, L., Pillow, J. & Lewi, J. Statistical models for neural encoding, decoding, and optimal stimulus design. In
356 *Progress in Brain Research*, 493–507, DOI: [10.1016/s0079-6123\(06\)65031-0](https://doi.org/10.1016/s0079-6123(06)65031-0) (Elsevier, 2007).
- 357 38. Steinmetz, N. A., Zatka-Haas, P., Carandini, M. & Harris, K. D. Distributed coding of choice, action and engagement
358 across the mouse brain. *Nature* **576**, 266–273, DOI: [10.1038/s41586-019-1787-x](https://doi.org/10.1038/s41586-019-1787-x) (2019).
- 359 39. Runyan, C. A., Piasini, E., Panzeri, S. & Harvey, C. D. Distinct timescales of population coding across cortex. *Nature*
360 **548**, 92–96, DOI: [10.1038/nature23020](https://doi.org/10.1038/nature23020) (2017).
- 361 40. Park, I. M., Meister, M. L. R., Huk, A. C. & Pillow, J. W. Encoding and decoding in parietal cortex during sensorimotor
362 decision-making. *Nat. Neurosci.* **17**, 1395–1403, DOI: [10.1038/nn.3800](https://doi.org/10.1038/nn.3800) (2014).
- 363 41. Musall, S., Kaufman, M. T., Juavinett, A. L., Gluf, S. & Churchland, A. K. Single-trial neural dynamics are dominated
364 by richly varied movements. *Nat. Neurosci.* **22**, 1677–1686, DOI: [10.1038/s41593-019-0502-4](https://doi.org/10.1038/s41593-019-0502-4) (2019).
- 365 42. Goltstein, P. M., Reinert, S., Bonhoeffer, T. & Hübener, M. Mouse visual cortex areas represent perceptual and semantic
366 features of learned visual categories. *Nat. Neurosci.* **24**, 1441–1451, DOI: [10.1038/s41593-021-00914-5](https://doi.org/10.1038/s41593-021-00914-5) (2021).
- 367 43. Butts, D. A., Weng, C., Jin, J., Alonso, J.-M. & Paninski, L. Temporal precision in the visual pathway through the
368 interplay of excitation and stimulus-driven suppression. *J. Neurosci.* **31**, 11313–11327, DOI: [10.1523/jneurosci.0434-11.
369 2011](https://doi.org/10.1523/jneurosci.0434-11.2011) (2011).
- 370 44. Mahn, M. *et al.* High-efficiency optogenetic silencing with soma-targeted anion-conducting channelrhodopsins. *Nat.
371 communications* **9**, 4125, DOI: [10.1038/s41467-018-06511-8](https://doi.org/10.1038/s41467-018-06511-8) (2018).
- 372 45. Gong, S. *et al.* Targeting Cre Recombinase to Specific Neuron Populations with Bacterial Artificial Chromosome
373 Constructs. *J. Neurosci.* **27**, 9817–9823, DOI: [10.1523/JNEUROSCI.2707-07.2007](https://doi.org/10.1523/JNEUROSCI.2707-07.2007) (2007).
- 374 46. Mahn, M., Prigge, M., Ron, S., Levy, R. & Yizhar, O. Biophysical constraints of optogenetic inhibition at presynaptic
375 terminals. *Nat. Neurosci.* DOI: [10.1038/nm.4266](https://doi.org/10.1038/nm.4266) (2016).

- 376 47. Wiegert, J. S. & Oertner, T. G. How (not) to silence long-range projections with light. *Nat. Neurosci.* **19**, 527–528, DOI:
377 [10.1038/nn.4270](https://doi.org/10.1038/nn.4270) (2016).
- 378 48. Wiegert, J. S., Mahn, M., Prigge, M., Printz, Y. & Yizhar, O. Silencing Neurons: Tools, Applications, and Experimental
379 Constraints. *Neuron* **95**, 504–529, DOI: [10.1016/j.neuron.2017.06.050](https://doi.org/10.1016/j.neuron.2017.06.050) (2017).
- 380 49. Vinck, M., Batista-Brito, R., Knoblich, U. & Cardin, J. A. Arousal and Locomotion Make Distinct Contributions to
381 Cortical Activity Patterns and Visual Encoding. *Neuron* **86**, 740–754, DOI: [10.1016/j.neuron.2015.03.028](https://doi.org/10.1016/j.neuron.2015.03.028) (2015).
- 382 50. Reimer, J. *et al.* Pupil Fluctuations Track Fast Switching of Cortical States during Quiet Wakefulness. *Neuron* **84**,
383 355–362, DOI: [10.1016/j.neuron.2014.09.033](https://doi.org/10.1016/j.neuron.2014.09.033) (2014).
- 384 51. Huang, Z., Ran, Y., Euler, T. & Berens, P. Estimating smooth and sparse neural receptive fields with a flexible spline
385 basis. *Neurons, Behav. Data analysis, Theory* **8**, 1–14 (2021).
- 386 52. Weber, A. I. & Pillow, J. W. Capturing the dynamical repertoire of single neurons with generalized linear models. *Neural*
387 *Comput.* **29**, 3260–3289, DOI: [10.1162/NECO_a_01021](https://doi.org/10.1162/NECO_a_01021) (2017). [1602.07389](https://doi.org/10.1162/NECO_a_01021).
- 388 53. Felsen, G. & Dan, Y. A natural approach to studying vision. *Nat. Neurosci.* **8**, 1643–1646, DOI: [10.1038/nn1608](https://doi.org/10.1038/nn1608) (2005).
- 389 54. Piscopo, D. M., El-Danaf, R. N., Huberman, a. D. & Niell, C. M. Diverse Visual Features Encoded in Mouse Lateral
390 Geniculate Nucleus. *J. Neurosci.* **33**, 4642–4656, DOI: [10.1523/JNEUROSCI.5187-12.2013](https://doi.org/10.1523/JNEUROSCI.5187-12.2013) (2013).
- 391 55. Grubb, M. S. & Thompson, I. D. Quantitative characterization of visual response properties in the mouse dorsal lateral
392 geniculate nucleus. *J. neurophysiology* **90**, 3594–3607, DOI: [10.1152/jn.00699.2003](https://doi.org/10.1152/jn.00699.2003) (2003).
- 393 56. Lesica, N. A. *et al.* Adaptation to stimulus contrast and correlations during natural visual stimulation. *Neuron* **55**,
394 479–491 (2007).
- 395 57. Walker, E. Y. *et al.* Inception loops discover what excites neurons most using deep predictive models. *Nat. Neurosci.* **22**,
396 2060–2065, DOI: [10.1038/s41593-019-0517-x](https://doi.org/10.1038/s41593-019-0517-x) (2019).
- 397 58. Levitt, J. B. & Lund, J. S. The spatial extent over which neurons in macaque striate cortex pool visual signals. *Vis.*
398 *Neurosci.* **19**, 439–452, DOI: [10.1017/s0952523802194065](https://doi.org/10.1017/s0952523802194065) (2002).
- 399 59. Sceniak, M. P., Ringach, D. L., Hawken, M. J. & Shapley, R. Contrast's effect on spatial summation by macaque v1
400 neurons. *Nat. Neurosci.* **2**, 733–739, DOI: [10.1038/11197](https://doi.org/10.1038/11197) (1999).
- 401 60. Kapadia, M. K., Westheimer, G. & Gilbert, C. D. Dynamics of spatial summation in primary visual cortex of alert
402 monkeys. *Proc. Natl. Acad. Sci.* **96**, 12073–12078, DOI: [10.1073/pnas.96.21.12073](https://doi.org/10.1073/pnas.96.21.12073) (1999).
- 403 61. Churchland, M. M. *et al.* Stimulus onset quenches neural variability: a widespread cortical phenomenon. *Nat. Neurosci.*
404 **13**, 369–378, DOI: [10.1038/nn.2501](https://doi.org/10.1038/nn.2501) (2010).
- 405 62. Denman, D. J. & Contreras, D. Complex effects on in vivo visual responses by specific projections from mouse cortical
406 layer 6 to dorsal lateral geniculate nucleus. *The J. Neurosci.* **35**, 9265–80, DOI: [10.1523/JNEUROSCI.0027-15.2015](https://doi.org/10.1523/JNEUROSCI.0027-15.2015)
407 (2015).
- 408 63. Niell, C. M. & Stryker, M. P. Modulation of Visual Responses by Behavioral State in Mouse Visual Cortex. *Neuron* **65**,
409 472–479, DOI: [10.1016/j.neuron.2010.01.033](https://doi.org/10.1016/j.neuron.2010.01.033) (2010).
- 410 64. Ayaz, A., Saleem, A. B., Schölvinck, M. L. & Carandini, M. Locomotion controls spatial integration in mouse visual
411 cortex. *Curr. Biol.* **23**, 890–894, DOI: [10.1016/j.cub.2013.04.012](https://doi.org/10.1016/j.cub.2013.04.012) (2013).
- 412 65. Murphy, P. C. & Sillito, A. M. Corticofugal feedback influences the generation of length tuning in the visual pathway.
413 *Nature* **329**, 727–729, DOI: [10.1038/329727a0](https://doi.org/10.1038/329727a0) (1987).
- 414 66. Wörgötter, F., Eyding, D., Macklis, J. D. & Funke, K. The influence of the corticothalamic projection on responses in
415 thalamus and cortex. *Philos. Transactions Royal Soc. London. Ser. B: Biol. Sci.* **357**, 1823–1834, DOI: [10.1098/rstb.
416 2002.1159](https://doi.org/10.1098/rstb.2002.1159) (2002).
- 417 67. de Labra, C. *et al.* Changes in visual responses in the feline dLGN: Selective thalamic suppression induced by transcranial
418 magnetic stimulation of v1. *Cereb. Cortex* **17**, 1376–1385, DOI: [10.1093/cercor/bhl048](https://doi.org/10.1093/cercor/bhl048) (2006).
- 419 68. Marrocco, R., McClurkin, J. & Young, R. Modulation of lateral geniculate nucleus cell responsiveness by visual
420 activation of the corticogeniculate pathway. *The J. Neurosci.* **2**, 256–263, DOI: [10.1523/JNEUROSCI.02-02-00256.1982](https://doi.org/10.1523/JNEUROSCI.02-02-00256.1982)
421 (1982).
- 422 69. McClurkin, J. W. & Marrocco, R. T. Visual cortical input alters spatial tuning in monkey lateral geniculate nucleus cells.
423 *The J. Physiol.* **348**, 135–152, DOI: [10.1113/jphysiol.1984.sp015103](https://doi.org/10.1113/jphysiol.1984.sp015103) (1984).

- 424 70. King, J. L., Lowe, M. P., Stover, K. R., Wong, A. A. & Crowder, N. A. Adaptive Processes in Thalamus and
425 Cortex Revealed by Silencing of Primary Visual Cortex during Contrast Adaptation. *Curr. Biol.* **26**, 1295–1300, DOI:
426 [10.1016/j.cub.2016.03.018](https://doi.org/10.1016/j.cub.2016.03.018) (2016).
- 427 71. Tang, J., Jimenez, S. C. A., Chakraborty, S. & Schultz, S. R. Visual receptive field properties of neurons in the mouse
428 lateral geniculate nucleus. *PLoS ONE* **11**, e0146017, DOI: [10.1371/journal.pone.0146017](https://doi.org/10.1371/journal.pone.0146017) (2016).
- 429 72. Durand, S. *et al.* A comparison of visual response properties in the lateral geniculate nucleus and primary visual cortex
430 of awake and anesthetized mice. *J. Neurosci.* **36**, 12144–12156, DOI: [10.1523/JNEUROSCI.1741-16.2016](https://doi.org/10.1523/JNEUROSCI.1741-16.2016) (2016).
- 431 73. Mante, V., Bonin, V. & Carandini, M. Functional Mechanisms Shaping Lateral Geniculate Responses to Artificial and
432 Natural Stimuli. *Neuron* **58**, 625–638, DOI: [10.1016/j.neuron.2008.03.011](https://doi.org/10.1016/j.neuron.2008.03.011) (2008).
- 433 74. Lesica, N. A. & Stanley, G. B. Encoding of natural scene movies by tonic and burst spikes in the lateral geniculate
434 nucleus. *J. Neurosci.* **24**, 10731–10740, DOI: [10.1523/JNEUROSCI.3059-04.2004](https://doi.org/10.1523/JNEUROSCI.3059-04.2004) (2004).
- 435 75. Wietek, J. *et al.* Anion-conducting channelrhodopsins with tuned spectra and modified kinetics engineered for optogenetic
436 manipulation of behavior. *Sci. Reports* **7**, 1–18, DOI: [10.1038/s41598-017-14330-y](https://doi.org/10.1038/s41598-017-14330-y) (2017). [156422](https://doi.org/10.1038/s41598-017-14330-y).
- 437 76. Govorunova, E. G., Sineshchekov, O. A., Janz, R., Liu, X. & Spudich, J. L. Natural light-gated anion channels: A
438 family of microbial rhodopsins for advanced optogenetics. *Science* **349**, 647–650, DOI: [10.1126/science.aaa7484](https://doi.org/10.1126/science.aaa7484) (2015).
439 [15334406](https://doi.org/10.1126/science.aaa7484).
- 440 77. Sherman, S. M. & Guillery, R. W. The role of the thalamus in the flow of information to the cortex. *Philos. transactions*
441 *Royal Soc. Lond.* **357**, 1695–708, DOI: [10.1098/rstb.2002.1161](https://doi.org/10.1098/rstb.2002.1161) (2002).
- 442 78. Sillito, A. M. & Jones, H. E. Corticothalamic interactions in the transfer of visual information. *Philos. Transactions*
443 *Royal Soc. London. Ser. B: Biol. Sci.* **357**, 1739–1752, DOI: [10.1098/rstb.2002.1170](https://doi.org/10.1098/rstb.2002.1170) (2002).
- 444 79. Briggs, F. & Usrey, W. M. Corticogeniculate feedback and visual processing in the primate. *J. Physiol.* **589**, 33–40,
445 DOI: [10.1113/jphysiol.2010.193599](https://doi.org/10.1113/jphysiol.2010.193599) (2010).
- 446 80. Madisen, L. *et al.* A robust and high-throughput Cre reporting and characterization system for the whole mouse brain.
447 *Nat. neuroscience* **13**, 133–140, DOI: [10.1038/nn.2467.A](https://doi.org/10.1038/nn.2467.A) (2010).
- 448 81. Josh Huang, Z., Zeng, H., Huang, Z. J. & Zeng, H. Genetic Approaches to Neural Circuits in the Mouse. *Annu. review*
449 *neuroscience* **36**, 183–215, DOI: [10.1146/annurev-neuro-062012-170307](https://doi.org/10.1146/annurev-neuro-062012-170307) (2013).
- 450 82. Bortone, D. S., Olsen, S. R. & Scanziani, M. Translaminar inhibitory cells recruited by layer 6 corticothalamic neurons
451 suppress visual cortex. *Neuron* **82**, 474–485, DOI: [10.1016/j.neuron.2014.02.021](https://doi.org/10.1016/j.neuron.2014.02.021) (2014).
- 452 83. Frandolig, J. E. *et al.* The Synaptic Organization of Layer 6 Circuits Reveals Inhibition as a Major Output of a Neocortical
453 Sublamina. *Cell Reports* **28**, 3131–3143, DOI: [10.1016/j.celrep.2019.08.048](https://doi.org/10.1016/j.celrep.2019.08.048) (2019).
- 454 84. Poynton, C. A. Rehabilitation of gamma. In Rogowitz, B. E. & Pappas, T. N. (eds.) *Human Vision and Electronic*
455 *Imaging III*, vol. 3299, 232–249, DOI: [10.1117/12.320126](https://doi.org/10.1117/12.320126) (International Society for Optical Engineering, San Jose, CA,
456 1998).
- 457 85. Rueden, C. T. *et al.* ImageJ2: ImageJ for the next generation of scientific image data. *BMC Bioinf.* **18**, DOI:
458 [10.1186/s12859-017-1934-z](https://doi.org/10.1186/s12859-017-1934-z) (2017).
- 459 86. Schindelin, J. *et al.* Fiji: An open-source platform for biological-image analysis. *Nat. Methods* **9**, 676–682, DOI:
460 [10.1038/nmeth.2019](https://doi.org/10.1038/nmeth.2019) (2012).
- 461 87. Pachitariu, M., Steinmetz, N., Kadir, S., Carandini, M. & Harris, K. D. Kilosort: realtime spike-sorting for extracellular
462 electrophysiology with hundreds of channels. *bioRxiv* 061481, DOI: [10.1101/061481](https://doi.org/10.1101/061481) (2016).
- 463 88. Spacek, M. A., Blanche, T. J. & Swindale, N. V. Python for large-scale electrophysiology. *Front. Neuroinform.* **2**, 9,
464 DOI: [10.3389/neuro.11.009.2008](https://doi.org/10.3389/neuro.11.009.2008) (2009).
- 465 89. Swindale, N. V. & Spacek, M. A. Spike sorting for polytrodes: A divide and conquer approach. *Front. Syst. Neurosci.*
466 DOI: [10.3389/fnsys.2014.00006](https://doi.org/10.3389/fnsys.2014.00006) (2014).
- 467 90. Yatsenko, D., Walker, E. Y. & Toliás, A. S. DataJoint: A simpler relational data model (2018). [1807.11104](https://doi.org/10.26434/chemrxiv-2018-1104).
- 468 91. Harris, K. D. Nonsense correlations in neuroscience. *bioRxiv* 1–13, DOI: [10.1101/2020.11.29.402719](https://doi.org/10.1101/2020.11.29.402719) (2020).
- 469 92. Harris, K. D. A shift test for independence in generic time series. *arXiv* 1–6 (2020). [2012.06862](https://doi.org/10.26434/chemrxiv-2020-06862).
- 470 93. Sahani, M. & Linden, J. F. Evidence optimization techniques for estimating stimulus-response functions. *Adv. neural*
471 *information processing systems* 317–324 (2003).

472 **94.** Park, M. & Pillow, J. W. Receptive field inference with localized priors. *PLoS computational biology* **7**, e1002219
473 (2011).

474 **Acknowledgements**

475 This research was supported by the Deutsche Forschungsgesellschaft (DFG) Sonderforschungsbereich (SFB) 1233, *Robust*
476 *Vision: Inference Principles and Neural Mechanisms*, Teilprojekt (TP) 13, project number: 276693517 (L.B., P.B.), by SPP2041
477 (BU 1808/6-1 and BU 1808/6-2) and the RTG2175 “Perception in context and its neural basis”. Lisa Schmors was supported by
478 the International Max Planck Research School for Intelligent Systems (IMPRS-IS). We thank E. Froudarakis (A. Tolias Lab,
479 Baylor College of Medicine, Houston, TX) for provision of the movie stimulus files, and A. Ecker and T. Euler for discussion
480 of the stimulus design. We also thank O. Yizhar, R. Beltramo, C. L. Lao, H. Wohlfrom and C. Kopp-Scheinflug for discussion
481 regarding the AAV vector and stGtACR2 opsin. Thanks also go to M. Sotgia for lab management and support with animal
482 handling and histology, S. Schörnich for IT support, and B. Grothe for providing excellent research infrastructure.

483 **Author contributions**

484 Conceptualization, L.B., P.B., S.S.; Methodology, L.B., P.B., Y.B., L.S., Z.H., S.S.; Software, L.S., Y.B., S.R., D.C., Z.H.;
485 Formal Analysis, L.S., Y.B., A.K.; Investigation, Y.B., L.M., A.K.; Resources, L.B., P.B.; Data Curation, Y.B., L.S., A.K., L.M.,
486 D.C.; Writing – Original Draft, Y.B., L.S., L.B.; Writing – Review & Editing, all authors; Visualization, Y.B., L.S.; Supervision,
487 L.B., P.B., S.S.; Project Administration, L.B., P.B.; Funding Acquisition, L.B., P.B.

488 **Declaration of Interests**

489 The authors declare no competing interests.

490 **Methods**

491 All procedures complied with the European Communities Council Directive 2010/63/EU and the German Law for Protection of
492 Animals, and were approved by local authorities, following appropriate ethics review.

493 **Surgical procedures**

494 Experiments were carried out under under Licence ROB-55.2-2532.Vet_02-17-40 (part 2a) in 6 adult Ntsr1-Cre mice (median
495 age: 16.4 weeks; B6.FVB(Cg)-Tg(Ntsr1-cre)GN220Gsat/Mmcd; MMRRC) of either sex.

496 Stereotactic surgeries were performed to implant a head-post for head-fixation, implant a ground/reference screw for
497 electrophysiology, inject a virus for optogenetic feedback manipulation, and drill a craniotomy for acute electrode insertions.

498 **Stereotactic surgery preparation and initiation**

499 Thirty minutes prior to the surgical procedure, mice were injected with an analgesic (Metamizole, 200 mg/kg, sc, MSD Animal
500 Health, Brussels, Belgium). To induce anesthesia, animals were placed in an induction chamber and exposed to isoflurane (5%
501 in oxygen, CP-Pharma, Burgdorf, Germany). After induction of anesthesia, mice were fixated in a stereotaxic frame (Drill &
502 Microinjection Robot, Neurostar, Tuebingen, Germany) and the isoflurane level was lowered (0.5%–2% in oxygen), such
503 that a stable level of anesthesia could be achieved as judged by the absence of an interstitial reflex. Throughout the procedure,
504 the eyes were covered with an eye ointment (Bepanthen, Bayer, Leverkusen, Germany) and a closed loop temperature control
505 system (ATC 1000, WPI Germany, Berlin, Germany) ensured that the animal’s body temperature was maintained at 37° C.
506 At the beginning of the surgical procedure, an additional analgesic was administered (Buprenorphine, 0.1 mg/kg, sc, Bayer,
507 Leverkusen, Germany) and the animal’s head was shaved and thoroughly disinfected using iodine solution (Braun, Melsungen,
508 Germany). Before performing a scalp incision along the midline, a local analgesic was delivered (Lidocaine hydrochloride, sc,
509 bela-pharm, Vechta, Germany). The skin covering the skull was partially removed and cleaned from tissue residues with a drop
510 of H₂O₂ (3%, AppliChem, Darmstadt, Germany). Using four reference points (bregma, lambda, and two points 2 mm to the
511 left and to the right of the midline respectively), the animal’s head was positioned into a skull-flat configuration for the further
512 steps.

513 **Virus injection**

514 In order to suppress V1 L6 CT FB selectively and reversibly, we conditionally expressed the chloride-conducting channel-
515 rhodopsin stGtACR2^{44,75,76} in L6a CT pyramidal cells^{77–79} by injecting AAV-stGtACR2-RFP into the left hemisphere V1
516 of Ntsr1-Cre mice^{45,80,81} (**Figure 1a**). Ntsr1+ neurons are known to correspond with > 90% specificity to L6CT pyramidal

517 cells^{12,82,83}. Furthermore, the opsin *stGtACR2* restricts expression to somata and the axon-initial segment which prevents possi-
518 ble accidental axonal depolarization due to a differential Cl⁻ ion reversal potential across different neuronal compartments⁴⁶⁻⁴⁸.
519 It also offers improved photocurrents and higher sensitivity, which are of particular relevance to manipulating deeply located
520 L6 CT neurons, while avoiding light artifacts and tissue damage arising from excessive light intensities⁴⁸.

521 Before surgery, the Cre-dependent, *stGtACR2*-expressing *adeno-associated virus* (AAV) vector (pAAV_hSyn1-SIO-
522 *stGtACR2*-FusionRed, Addgene, #105677) stock solution was diluted to 5×10^{11} gc/ml titers, and aliquotted to 4 μ L.

523 During surgery, aliquots were front-loaded into a glass pipette mounted on a Hamilton syringe (SYR 10 μ L 1701 RN no
524 NDL, Hamilton, Bonaduz, Switzerland), controlled by the Injection Robot of the Neurostar Stereotax. After performing a small
525 craniotomy for injection (100 μ m diameter), we injected 300 nl of virus solution into V1 (2 \times 50 nl shots injected at a rate of
526 50 nl / 30 s at a respective depth of 900 μ m, 800 μ m and 700 μ m below the brain surface.

527 **Head-post and ground and reference screw implantation**

528 For implant fixation, the exposed skull was covered with OptiBond FL primer and adhesive (Kerr Dental, Rastatt, Germany)
529 omitting three locations: V1 (AP: -3.28 mm, ML: -2.4 mm), dLGN (AP: -2.3 mm, ML: -2 mm), and a position roughly
530 1.5 mm anterior and 1 mm to the right of bregma, designated for a miniature ground and reference screw.

531 A custom-made lightweight stainless steel head bar was positioned over the posterior part of the skull such that the round
532 opening in the bar was centered on V1/dLGN. The head bar was attached with dental cement (Ivoclar Vivadent, Ellwangen,
533 Germany) to the primer/adhesive. The opening was later filled with the silicone elastomer sealant Kwik-Cast (WPI Germany,
534 Berlin, Germany). Then the miniature screw (00-96 X 1/16 stainless steel screws, Bilaney), which served both as ground and
535 reference that was soldered to a custom-made connector pin, was implanted.

536 **Post-surgical treatment and animal setup habituation**

537 At the end of the procedure, an iodine-based ointment (Braunodivon, 10%, B. Braun, Melsungen, Germany) was applied to
538 the edges of the wound and a long-term analgesic (Meloxicam, 2 mg/kg, sc, Böhringer Ingelheim, Ingelheim, Germany) was
539 administered and for 3 consecutive days. For at least 5 days post-surgery, the animal's health status was assessed via a score
540 sheet.

541 After at least 1 week of recovery, animals were gradually habituated to the experimental setup by first handling them and
542 then simulating the experimental procedure. To allow for virus expression, neural recordings started after an incubation time of
543 2-4 weeks after injection.

544 **Craniotomy**

545 On the day prior to the first day of recording, mice were fully anesthetized using the same procedures as described for the initial
546 surgery, and a craniotomy (ca. 2 \times 1 mm on the AP \times BL axes) was performed over dLGN (ca. 2.5 mm posterior from bregma
547 and 2.3 mm lateral from midline) and V1 and re-sealed with Kwik-Cast (WPI Germany, Berlin, Germany). As long as the
548 animals did not show signs of discomfort, the long-term analgesic Metacam was administered only once at the end of surgery,
549 to avoid any confounding effect on experimental results. Recordings were performed daily and continued for as long as the
550 quality of the electrophysiological signals remained high.

551 **Recordings**

552 After 2-4 weeks of incubation time, we performed *in vivo* extracellular multi-electrode array (MEA) recordings of dLGN
553 neurons in awake, head-fixed mice that were passively viewing visual stimuli on an LCD monitor screen in their right visual
554 field while being free to run on an air-floating Styrofoam ball. Additionally, we optogenetically suppressed L6CT FB, recorded
555 run speed via locomotion sensors, as well as pupil size via an infrared (IR) eye-tracking camera directed at the eye viewing the
556 stimulus (Figure 1a, b).

557 **Extracellular multi-electrode array (MEA) electrophysiology**

558 Extracellular signals were recorded at 30 kHz (Blackrock microsystems, Blackrock Microsystems Europe GmbH, Hanover,
559 Germany). For each recording session, the silicon plug sealing the craniotomy was removed. For dLGN recordings, a 32
560 channel linear silicon probe (Neuronexus A1x32Edge-5mm-20-177-A32) was lowered to a depth of \sim 2700-3500 μ m below
561 the brain surface. We judged recording sites to be located in dLGN based on the characteristic progression of RFs from upper
562 to lower visual field along the electrode shank⁵⁴, the presence of responses strongly modulated at the temporal frequency of the
563 drifting gratings (F1 response), and the preference of responses to high temporal frequencies^{54,55}. For *post hoc* histological
564 reconstruction of the recording site, the electrode was stained with DiI (Invitrogen, Carlsbad, USA) for some (typically the last)
565 recording sessions.

566 **Locomotion-capturing**

567 Two optical computer mice interfaced with a microcontroller (Arduino Duemilanove) sampled ball movements at 90 Hz.

568 **Eye-tracking**

569 To record eye position and pupil size, the animal's eye was illuminated with infrared LED light and monitored using a zoom
570 lens (Navitar Zoom 6000) coupled with a camera (Guppy AVT camera; frame rate 50 Hz, Allied Vision, Exton, USA).

571 **Optogenetic feedback suppression**

572 To photosuppress V1 Ntsr1+ L6CT pyramidal cells, an optic fiber (480 μm core diameter, MFP_480/500/1000-0.63_m_SMA,
573 Doric Lenses, Quebec, Canada) was coupled to a light-emitting diode (blue LED, center wavelength 465 nm, LEDC2_465/635_SMA,
574 Doric Lenses, Quebec, Canada) and positioned with a micromanipulator less than 1 mm above the exposed surface of V1. A
575 black metal foil surrounding the tip of the head bar holder prevented the photostimulation light from reaching the animal's eyes.
576 To ensure that the photostimulation was effective, the first recording session for each mouse was carried out in V1. Only if
577 the exposure to light reliably induced suppression of V1 activity was the animal used for subsequent dLGN recordings. LED
578 light intensity was adjusted on a daily basis to evoke reliable effects and account for variations in exact virus titer, volume,
579 incubation time, virus expression levels, and fiber position (0.85-9.5 mW at the fiber tip). Since the tip of the fiber never
580 directly touched the surface of the brain, and since the clarity of the surface of the brain varied (generally decreasing every day
581 following the craniotomy), the light intensity delivered even to superficial layers of V1 was inevitably lower. For the movie
582 stimulus, optogenetic pulses of 1 s duration were sent randomly each second with a 50 % chance.

583 **Visual stimulation**

584 Visual stimuli were presented on a gamma-calibrated liquid crystal display (LCD) monitor (Samsung SyncMaster 2233RZ,
585 47 \times 29 cm, 1680 \times 1050 resolution at 60 Hz, mean luminance 50 cd/m²) positioned at a distance of 25 cm from the animal's
586 right eye (spanning \sim 108 \times 66 $^\circ$ visual angle by small angle approximation) using custom written software (EXPO, <https://sites.google.com/a/nyu.edu/expo/home>). The display was gamma-corrected for the presentation of artificial
587 stimuli, but not for movies (see below).
588

589 **Movie stimulus**

590 For movie stimulus generation, we adopted a set of randomly picked scenes from various movies. Briefly, source movie scenes
591 were converted to grey scale, temporally downsampled to 30 frames per s, spatially resampled and cropped to 424 \times 264 pixels,
592 to be presented on our 47 \times 29 cm monitor screen at 25 cm distance at 106 \times 66 $^\circ$ (4 pixels/ $^\circ$) visual angle (by small angle
593 approximation, which preserves the desired pixel resolution at the screen center better than the arctangent). Movie frames
594 were not histogram-equalized and presented at 60 Hz (repeating each frame twice) without monitor gamma correction, since
595 cameras are already gamma corrected for consumer displays⁸⁴. To generate the movie sequence, we used a random set of 296
596 unique movie scenes (5 s each), split into a set of 188 training scenes and 8 test scenes. The training scenes were blocked into
597 8 parts of 36 unique scenes (5 s \times 36 = 180 s per part), which were interleaved with the test block of 8 scenes (5 s \times 8 = 40 s)
598 which was repeated 9 times. Test scene repetition served to give an estimate of response variability to the same scenes. The
599 movie sequence was flanked by a period of blank grey screen presentation (1 min) at the beginning and at the end, to record
600 spontaneous activity. This resulted in a total stimulus duration of \sim 32 mins, with a train-test split of 80 % vs. 20 %. To rule
601 out sequence effects, we randomized the scene order for different stimulus presentations. To investigate the effects of L6 CT
602 FB suppression, we simultaneously presented a random optogenetic pulse train of 1 s pulses, occurring each second with a
603 probability of 50 %, throughout the entire stimulus duration, including blank grey screen periods.

604 **Sparse noise stimulus**

605 To measure receptive fields (RFs) in a more standard manner, we also presented an (artificial) sparse noise stimulus. The
606 stimulus consisted of a rapid sequence of non-overlapping white and black squares appearing in succession within a 12 \times 12
607 square grid presented on a grey background of mean luminance (50 cd/m²). The square grid spanned 60 $^\circ$ per side, while
608 individual squares spanned 5 $^\circ$ per side. Each square flashed for 200 ms.

609 **Histology**

610 To verify virus expression and recording sites, we performed post-mortem histological analyses. After the final recording
611 session, mice were first administered an analgesic (Metamizole, 200 mg/kg, sc, MSD Animal Health, Brussels, Belgium)
612 and following a 30 min latency period were transcardially perfused under deep anesthesia using a cocktail of Medetomidin
613 (Domitor, 0.5 mg/kg, Vetoquinol, Ismaning, Germany), Midazolam (Climasol, 5 mg/kg, Ratiopharm, Ulm, Germany) and
614 Fentanyl (Fentadon, 0.05 mg/kg, Dechra Veterinary Products Deutschland, Aulendorf, Germany) (ip). Perfusion was first
615 done with Ringer's lactate solution followed by 4% paraformaldehyde (PFA) in 0.2 M sodium phosphate buffer (PBS). Brains
616 were removed, postfixed in PFA for 24 h, and then rinsed with and stored in PBS at 4 $^\circ$ C. Slices (50 μm) were cut using a
617 vibrotome (Leica VT1200 S, Leica, Wetzlar, Germany), stained with DAPI-solution (DAPI, Thermo Fisher Scientific, Waltham,
618 Massachusetts, USA), mounted on glass slides with Vectashield mounting medium (Vectashield H-1000, Vector Laboratories,

619 Burlingame, USA), and coverslipped. A scanning fluorescent microscope (BX61, Olympus, Tokyo, Japan) was used to inspect
620 slices for the presence of red fluorescent protein (RFP/FusionRed) marking stGtACR2-channels, and DiI, marking electrode
621 tracks. Recorded images were processed off-line using FIJI^{85,86}.

622 Spike sorting and unit extraction

623 Spike sorting was performed to obtain single unit activity from extracellular recordings. Electrophysiological signal recordings
624 were filtered using a 4th-order Butterworth high-pass non-causal filter with a low frequency cutoff of 300 Hz. We then
625 used the open source, MATLAB-based (The Mathworks, Natick, Massachusetts, USA), automated spike sorting toolbox
626 Kilosort and Kilosort2⁸⁷. Resulting clusters were manually refined using Spyke⁸⁸, a Python application that allows for the
627 selection of channels and time ranges around clustered spikes for realignment, as well as representation in 3D space using
628 dimension reduction (multichannel PCA, ICA, and/or spike time). In 3D, clusters were then further split via a gradient-ascent
629 based clustering algorithm (GAC)⁸⁹. Exhaustive pairwise comparisons of similar clusters allowed the merger of potentially
630 over-clustered units. For subsequent analyses, we inspected autocorrelograms and mean voltage traces, and only considered
631 units that displayed a clear refractory period and a distinct spike waveshape.

632 Data analysis framework

633 All further data analyses were carried out in a MySQL-based database using the DataJoint framework⁹⁰ with custom-written
634 code in Python.

635 Firing rate calculations

636 To obtain units firing rates in spikes/s, each unit's spike density function (SDF) was calculated by binning spikes into a firing
637 rate histogram (bin width = 20 ms) and convolving this with a Gaussian of width $2\sigma = 10$ ms. Mean firing rates (FRs) over a
638 given condition were calculated as the mean of the time-varying firing rates for the defined periods.

639 Exclusion criteria

640 Neurons with mean evoked firing rates < 0.1 spikes/s were excluded from all further analysis. Further analysis-specific selection
641 criteria are stated in the appropriate subsections.

642 Optogenetic feedback modulation

To quantify the effect of V1 L6CT suppression on various response properties, we defined the optogenetic modulation index (OMI) based on the mean FRs during L6CT FB suppression ('opto') versus the control condition as

$$\text{OMI} = \frac{\text{opto} - \text{control}}{\text{opto} + \text{control}} \quad (1)$$

643 To test for a significant difference in mean FRs between the photosuppression vs. control conditions matched for each
644 neuron, we used the Wilcoxon signed-rank test (Figure 1i).

645 Locomotion data processing

To compute animal run speed, we used the Euclidean norm of three perpendicular components of ball velocity (roll, pitch and yaw) and smoothed traces with a Gaussian filter ($\sigma = 0.2$ s). To quantify the effect of running vs. sitting on various response properties, the run modulation index (RMI) was defined based on the mean firing rates during running vs. sitting periods as

$$\text{RMI} = \frac{\text{running} - \text{sitting}}{\text{running} + \text{sitting}}, \quad (2)$$

646 where running periods were defined as those for which speed exceeded 1 cm/s, and sit periods as those for which speed fell
647 below 0.25 cm/s.

648 To test for a significant difference in mean FRs between the run vs. sit conditions matched for each neuron, we used the
649 Wilcoxon signed-rank test (Figure 1i).

650 Eye tracking data processing

651 Pupil position was extracted from the eye-tracking videos using a custom, semi-automated algorithm. Briefly, each video
652 frame was equalized using an adaptive bi-histogram equalization procedure, and then smoothed using median and bilateral
653 filters. The center of the pupil was detected by taking the darkest point in a convolution of the filtered image with a black
654 square. Next, the peaks of the image gradient along lines extending radially from the center point were used to define the pupil
655 contour. Lastly, an ellipse was fit to the contour, and the center and area of this ellipse was taken as the position and size of the

656 pupil, respectively. A similar procedure was used to extract the position of the corneal reflection (CR) of the LED illumination.
 657 Eye-closure, grooming, or implausible ellipse fitting was automatically detected and the adjacent data points 0.15 s before and
 658 after were excluded. Linear interpolation and a subsequent Gaussian smoothing ($\sigma = 0.06$ s) was applied to fill the removed
 659 segments. Adjustable algorithm parameters, such as the threshold of the mean pixel-wise difference between each frame and a
 660 reference frame to detect blinks, were set manually for each experiment.

To quantify the effect of large vs. small pupil sizes on various response properties, the eye modulation index (EMI) was defined based on the mean firing rates during periods of large vs. small pupils as

$$\text{EMI} = \frac{\text{pupil large} - \text{pupil small}}{\text{pupil large} + \text{pupil small}}, \quad (3)$$

661 where periods of large pupils were defined as those for which pupil size was above the 50th percentile of the median normalized
 662 pupil trace, and periods of small pupils as those for which pupil size fell below the 25th percentile.

663 To test for a significant difference in mean FRs between the large vs. small pupil conditions matched for each neuron, we
 664 used the Wilcoxon signed-rank test (Figure 1i).

665 Predictor correlations

666 To test for the correlations between the predictors *stimulus*, *opto*, *run*, and *eye*, we temporally aligned these traces, including
 667 only time points for which we had data points in all traces (e.g. removing periods of eye blinks). We then explored their
 668 cross-correlations in order to detect potential delays in their effects on each other. Such is the case, for instance in the pupil
 669 light reflex, where increases in stimulus intensity are followed by a delayed decrease in pupil size (Figure S1a). We then used
 670 the delay time to shift the traces appropriately before computing their correlation value (Pearson's r ; Figure 1k).

671 In order to test for statistical significance of the obtained correlation values (Figure S1b), we first needed to account for the
 672 fact that our time-series inherently contain autocorrelations which would lead to an overestimation of correlations between
 673 them (except for the random opto pulses)⁹¹. We therefore used a permutation test in which we randomly permuted the stimulus
 674 traces for $k = 1000$ iterations, and then computed the p-value of the observed correlation value as its percentile within the null
 675 distribution of p-values for the permuted traces⁹².

676 Spline-based linear-nonlinear-Poisson (spline-LNP) model

To estimate the spatio-temporal receptive fields (STRFs), the RFest Python toolbox for spline-based spatio-temporal RF estimation was used⁵¹. Here, the receptive field is parameterized with a set of basis functions. This reduces the number of hyperparameters compared to alternative approaches of receptive field estimation (such as automatic smoothness determination⁹³ or automatic locality determination⁹⁴). RFest is also less data demanding and reduces the computation time significantly⁵¹. The number of parameters is given by the number of basis functions, also referred to the degrees of freedom. By using natural cubic splines as the basis the estimates are automatically smooth, which is a desirable property for single STRFs. To impose sparsity on the weights (also a desirable property of STRFs) we added L1 regularization, which pushed the weights for less relevant bases to zero. To compute the spline-based STRFs, w_{SPL} , the coefficients, b_{SPL} , were obtained as

$$b_{SPL} = (S^T X^T X S)^{-1} S^T X^T y \quad (4)$$

with X as the stimulus design matrix, y as the neural response vector, and S as the spline matrix. The spatio-temporal RF was computed as

$$w_{SPL} = S b_{SPL} = S (S^T X^T X S)^{-1} S^T X^T y \quad (5)$$

677 To generate the natural cubic spline matrices (S) the package Patsy (0.5.1) is integrated into RFest. The code for RFest is
 678 available from <https://github.com/berenslab/RFest>.

The spline-based spatio-temporal RF was incorporated into a linear-nonlinear-Poisson (LNP) model, where the neural activity is estimated by (1) multiplying the spatio-temporal RF with a weight vector (w), (2) adding an offset, (3) passing the result through a non-linearity ($g(\cdot)$, here a softplus function) and (4) applying a Poisson process to estimate spike times. Hyperparameter tuning was achieved in an ordered grid search: First, evenly spaced numbers of basis were fitted starting from many to few and stopping when a smaller number of basis would decrease the performance. Then, the L1 regularization weights were fitted, starting with the smallest value and interrupting the grid search when the performance stopped increasing. The STRFs were initialized with maximum likelihood estimates (MLE) and optimized using gradient decent and 1500 iterations. The MLE was computed as

$$w_{MLE} = (X^T X)^{-1} X^T y \quad (6)$$

The fitting was interrupted when the training cost changed less than 1e-5 for the last 10 iterations as an early stopping criterion. The set of hyperparameters was selected based on the performance for a held-out validation set. The final performance of the model was reported as the mean correlation coefficient for the repeated nine test data trials (see section 'Movie stimulus'). In addition to the "stimulus only" model, where the prediction of neural activity was solely based on the visual stimulus, other behavioral components, such as running speed and pupil size could be integrated into the model. To estimate the effect of cortico-thalamic (CT) feedback, an additional input comprising the optogenetic light stimulation could be given to the model. All additional inputs were also parameterized with a set of spline basis and multiplied with an extra weight vector (also referred to as filter):

$$f(s, o, r, e) = g(w_s^T s[t : t - \Delta t] + w_o^T o[t : t - \Delta t] + w_r^T r[t : t - \Delta t] + w_e^T e[t : t - \Delta t]) \quad (7)$$

679 with s , o , r , and e denoting the additional model inputs of stimulus, optogenetics, running and eye, respectively, and $[t : t - \Delta t]$
680 defining the temporal integration window for each filter.

681 Spatio-temporal RF component extraction

682 To separate spatial and temporal components of the 3D STRFs, we performed singular value decomposition (SVD) on the norm
683 of the stimulus weight vector w . The temporal RF is extracted as the first left-singular vector of U , i.e. temporal dimension with
684 the highest variance, and the spatial RF as the first right-singular vector of V , reshaped into the height- and width-dimensions of
685 the input vector w . The extremes of the reshaped spatial RF vector are then used to quantify RF position and RF area.

686 Spatial RF contour estimation

687 Model spatial RFs were estimated by extracting the 2D spatial RF component from the model weights (see subsection 'Spatio-
688 temporal RF component extraction'), and then drawing a contour line around the largest absolute peak (assumed to be the
689 center of the spatial RF). The contour threshold gets gradually lowered until any further decrease would result in a second
690 contour around the second largest extremum (background irregularities considered as noise). To avoid overly large RFs in very
691 clean spatial components (without any major second extremum), the contour threshold had to be 2 standard deviations above or
692 below the mean. To improve estimate accuracy, the spatial RF component was upsampled 16-fold via cubic spline interpolation.

693 Spatial RF area estimation

694 The spatial RF area was estimated by using the spatial RF component and contour (see subsection 'Spatial RF contour
695 estimation') and calculating the number of pixels of the spatial RF contour mask in relation to the total number of pixels in the
696 image frame, which was then scaled by the stimulus extent to obtain the value in squared degrees of visual angle. To improve
697 estimate accuracy, the spatial RF component was upsampled 16-fold via cubic spline interpolation.

698 Spatial RF quality index (RF QI)

The spatial RF quality index (RF QI) was calculated by taking the ratio of the smallest possible absolute spatial RF contour
threshold value $SRF_{threshold}$ that still results in a single contour area (see subsection 'Spatial RF contour estimation'), and
 $SRF_{extreme}$, the highest absolute spatial RF component value (i.e. the spatial RF center extremum), and subtracting this from
one:

$$RF_{QI} = 1 - |SRF_{threshold}| / SRF_{extreme}, \quad (8)$$

699 where $RF_{QI} = 1$ indicates one clear spatial RF without any spatial background noise and $RF_{QI} = 0$ indicates no clear spatial RF
700 within background noise.

701 Model comparison for movie versus sparse noise stimulus

702 In order to reduce the effect of different model parameters on the interpretation of our results, we made models as comparable
703 as possible: First, given that the sparse noise stimulus was presented in a 12x12 grid spanning 60°, we reduced the model image
704 input resolution of the movie from the original 424x264 spanning 106x66° to a 21x13 grid, resulting in approximately 5° per
705 pixel in each stimulus. Secondly, we matched the spatial degrees of freedom (sDFs, number of splines), allowing 12x12 sDFs
706 for the sparse noise, and 21x13 sDFs for the movie stimulus, resulting in 1 sDF per pixel for each stimulus. Thirdly, we matched
707 the model predictor configurations by comparing only 'stimulus-only' configurations. For the population comparison of model
708 paired by neuron, we then searched for cells that had both stimuli presented, and further restricted our selection via minimum
709 model quality criteria of the explained variance of model predictions $R^2 > 0.001$ and RF quality index (RF QI) of $RF_{QI} > 0.2$.
710 With these restriction, the best-performing model for each stimulus per neuron was used for the paired comparison.

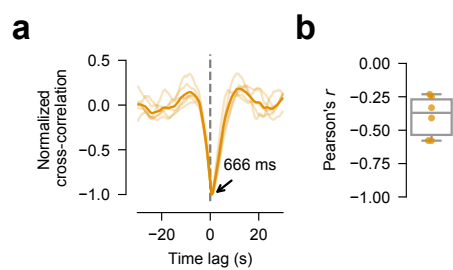


Figure S1 | Pupil light reflex. (a) Normalized cross-correlogram of pupil area and average stimulus light intensity time traces, showing delayed dip in pupil size in response to light increases, indicative of the pupil light reflex (delay-time indicated by arrow annotation). (b) Box plot of correlation values between average stimulus intensity traces and pupil size traces, after time-shifting by pupil response delay found in (a) ($n = 6$ experiments).

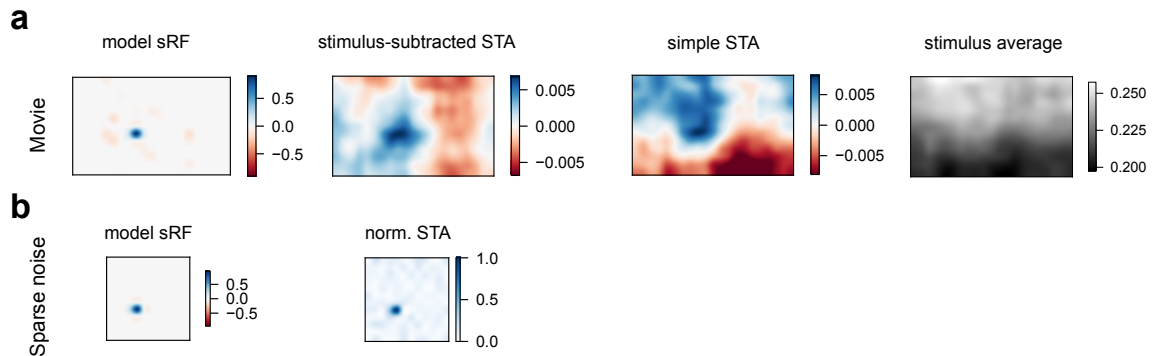


Figure S2 | RF estimation via our spline-LNP model versus spike-triggered average (STA). (a) Spatial RF estimates for the movie stimulus, illustrated for one example dLGN neuron. *Left:* spatial RF for spline-LNP model. *Second from left:* STA corrected for stimulus average intensity gradient (*right*). Agrees with model spatial RF in terms of spatial RF polarity and location but has larger, fuzzy spatial RF area. *Third from left:* Simple STA uncorrected for stimulus average and therefore shows the stimulus intensity gradient in the RF estimate, resulting in an even noisier estimate than the stimulus-subtracted STA. *Right:* Stimulus average intensity showing gradient from top to bottom, reflecting decreasing light intensity gradient from sky to ground in natural scenes. (b) Sparse noise stimulus RF estimates for same example dLGN neuron. *Left:* Model spatial RF estimate. Corresponds to movie spatial RF estimate in terms of polarity and location. *Right:* Normalized spike-triggered average (STA). In contrast to the movie stimulus STA, the sparse noise stimulus STA already yields a sparse, localized spatial RF estimate which corresponds well to the model spatial RF estimate. Thus, the model proves useful for estimating RFs from movie stimuli, whereas it may not be so necessary for sparse noise stimuli (unless one is also interested in other predictors such as feedback and behavioural state). This effect is likely due to the spatio-temporal pixel correlations as well as the global luminance patterns in movies, that are difficult to handle with an STA-based approach, whereas in the sparse noise stimulus, pixels are made statistically independent.

*"Nature is like a genie
that answers exactly the question we pose,
not necessarily the one we intend to ask."*

— Judea Pearl, *The Book of Why*

Robust visual perception starts in the retina, and the dorsolateral geniculate nucleus of the thalamus (dLGN) presents the most direct route to the primary visual cortex (V₁). Yet, our understanding of the underlying neural signal computations in the dLGN is incomplete.

In this thesis, I investigated if and how converging retinal feedforward (FF) signals, cortico-thalamic (CT) feedback (FB) signals and behaviour shape the responses in the mouse dLGN. A guiding framework was that the dLGN is an active signal transformer rather than a mere passive relay. The role of CT FB in the dLGN is particularly controversial, in part due to heterogeneity of approaches as well as the subtlety of functional FB effects. To address these questions, I adopted a mainly functional approach in the mouse as a model organism, using ex vitro retinal two-photon (2P) Ca²⁺ imaging as well as in vivo extracellular multi-electrode array (MEA) recordings and optogenetic perturbation techniques, and exploring the effects of naturalistic movie stimuli in the dLGN of awake, head-fixed mice.

In the first part, I looked at retino-thalamic feedforward convergence (Introduction Section 1.2.2), which resulted in our publication as Román Rosón et al., 2019 (Chapter 2). In the second part, I turned the focus to the influences of cortico-thalamic feedback connections and behavioural state (Introduction Section 1.3 and Section 1.4.1). The results are presented in the study published as Spacek et al., 2022 (Chapter 3), and the manuscript by Bauer et al., 2022 (Chapter 4).

In the following, I will review the key results of each of these parts in turn and discuss their implications, methodological considerations and open questions. After turning to some future directions for this project, I will conclude this thesis with a synthesis of our findings and their implications.

5.1 FEEDFORWARD SIGNALS TO THE DLGN

At the beginning of this project, the role of the dLGN in visual signal transformations had already been subject to much controversy, and it continues to be a topic of debate (Chen et al., 2016) (Introduction Section 1.2.2). On the one hand, the longstanding view of the dLGN as a passive relay of retinal information has been supported by a series of functional studies that found that feature selectivity in dLGN closely resembles that of (a few dominant) retinal afferents (Hubel & Wiesel, 1961; Kaplan et al., 1987; Sincich et al., 2007). On the other, more recent

anatomical data showing massive divergence of RGC projections and retinogeniculate convergence (Morgan et al., 2016; Rompani et al., 2017) suggest the opposing view that the dLGN could recombine signals and thus be an active signal transformer. However, it was unclear which of the ca. 40+ RGC types (Baden et al., 2016; Goetz et al., 2021; Laboissonniere et al., 2019; Peng et al., 2019; Sanes & Masland, 2015; Sümbül et al., 2014) project to the dLGN and what their functional impact on individual dLGN neurons would be.

ROMÁN ROSÓN & BAUER ET AL. (2019)

In the first part of this project, we investigated these questions in our study that was published as Román Rosón et al., 2019. Our results were as follows: First, many of the previously identified functional RGC types innervate the dLGN, with a few exceptions. Second, the dLGN population response revealed a high degree of functional diversity. Third, dLGN responses could be predicted as a linear combination of on average five RGC types, and mostly by two strong inputs. We concluded that dLGN neurons have a higher degree of functional diversity than previously appreciated (Piscopo et al., 2013), and that this diversity is based on the limited convergence of multiple distinct RGCs, two of which exert the strongest influence.

Given that the recent years have brought in ever-increasing estimates for the degree of functional diversity within the RGC population, which seem to be converging towards 40+ RGC types (Baden et al., 2016; Goetz et al., 2021), it might not come as a surprise to find a comparable degree of diversity in the dLGN. On the contrary, it might have been more surprising to see feature selectivity reduced at this later processing stage. On top of that, retino-thalamic convergence and divergence could result in a recombination of features that increases the diversity of functional feature selectivity within the dLGN (Liang et al., 2018). Such recombination would be one process by which the dLGN actively transforms retinal signals.

On the other hand, our finding and that of several other studies (e.g. Bauer et al., 2021; Liang et al., 2018; Litvina & Chen, 2017), that only a few RGC types exert a strong functional impact on dLGN activity, also implies that convergence does not lead to an explosion of the number of dLGN features. Taken together, this offers a reconciliation of the apparently conflicting physiological and anatomical views via considerations of connection strength: dLGN relay cells might indeed receive diverse inputs from many different RGCs but under normal conditions, only a few of those will be functionally relevant.

One open question then is what purpose the non-dominant RGC inputs might serve. To date, we can only speculate that they might have been most relevant during development (Thompson et al., 2016), support adult plasticity through changes in synaptic weight, or that they might be un-silenced via depolarization to improve the signal-to-noise ratio, to create novel RFs, or to synchronize dLGN (see Litvina & Chen, 2017; Román Rosón et al., 2019).

Of course, we should not forget that our results also depend on the design of our non-negative linear regression model. This choice certainly oversimplified retino-thalamic signal processing by approximating dLGN activity as a purely feedforward process. Firstly, it failed to capture non-linear neural amplification properties resulting, for instance, from luminance and contrast adaptations and bursting activity (Bonin et al., 2006; Lesica et al., 2007; Lesica & Stanley, 2004; Mante et al., 2005). Secondly, the model ignored the effects of inhibitory interneurons, cortico-thalamic feedback and behaviour in shaping dLGN responses. Lastly, it was based on the responses to the highly artificial and simplistic full-field flicker ‘chirp’ stimulus, which is unlikely to capture the full dLGN response diversity simply because many neurons will respond to other features not sampled by this stimulus.

We addressed these points in the following studies presented in the next part.

5.2 FEEDBACK AND BEHAVIOURAL STATE SIGNALS TO THE DLGN

If the role of retinogeniculate feedforward (FF) signal processing is considered controversial, then there was even less consensus on the functional role of cortico-thalamic (CT) feedback (FB) signals in shaping dLGN responses (Introduction Section 1.3.2).

One reason why robust findings have been so elusive is that CT FB synapses are only modulatory and that, consequently, their impact on dLGN cells is subtle compared to the impact of strong retinal driving synapses, despite the fact that, from a purely anatomical perspective, CT FB synapses vastly outnumber retinal inputs in all studied species (Erişir et al., 1997; Macknik & Martinez-Conde, 2009; Sherman & Guillery, 2002; Weyand, 2016).

Moreover, given the complexity of the CT FB circuitry (see Figure 1), the functional effects are expected to be complex and highly dependent on the specific experimental design, including choice of species, animal state, perturbation technique, recording technique and stimulus type (Briggs & Usrey, 2011; Usrey & Sherman, 2019). In particular, CT feedback effects might be drastically reduced if the animal is anaesthetized (Durand et al., 2016).

Therefore, it had become increasingly clear that insights into the role of CT FB would likely depend on studies in awake animals performed with sensitive and effective tools for specific and reversible inactivation of cortical layer 6 (L6) CT pyramidal cells, the sole direct route for CT FB (Briggs, 2010). In addition, CT FB effects might be most relevant and thus most apparent for naturalistic stimuli rather than the commonly used artificial stimuli (Cudeiro & Sillito, 1996; Gulyás et al., 1990; Rao & Ballard, 1999; Sillito & Jones, 2002).

Turning to the influence of behaviour on dLGN activity, it had long been known as one of the earliest stages in the visual hierarchy where activity is shaped by the animal’s behavioural state (Bezudnaya et al., 2006; Cano et al., 2006; Swadlow & Weyand, 1987) through signals transmitted by brain stem nuclei (McCormick, 1992; Molnár et al., 2021; Nestvogel & McCormick, 2021; Sherman & Guillery, 1996). For instance, in-

creased arousal states, as indexed by increased run speed or pupil dilation, can increase the response gain in dLGN neurons (Liang et al., 2020; Molnár et al., 2021; Nestvogel & McCormick, 2021).

Yet, how the combination retinal feedforward signals and the modulations by CT feedback and behavioural state shape the dLGN response has been incompletely understood (Usrey and Alitto, 2015), in part due to the challenges of recording them simultaneously and disentangling their separate influences and potential interactions.

SPACEK ET AL. (2022)

In our Spacek et al., 2022 study, we found that CT feedback suppression reduced dLGN firing rates, and increased bursting, sparseness and trial-to-trial reliability. Secondly, we showed that these effects were more consistent and stronger for naturalistic movies than for artificial grating stimuli. Third, we showed that CT FB effects resembled those of behavioural state effects, as assessed by locomotion, but that CT FB effects and behavioural effects were independent. We thus concluded that CT FB can induce reliable effects on dLGN firing rates, and that these are stronger for naturalistic than artificial stimuli, as well as being independent from effects of behavioural state.

Nevertheless, one issue regarding the optogenetic approach in this study was that the indirect CT FB suppression via global V1 PV interneuron photoactivation may have been accompanied by complex side effects mediated by alternative circuits, including the route via the superior colliculus (SC) to the dLGN shell region (see Figure 1). As mentioned earlier, a more specific, direct suppression of L6 CT pyramidal cells would have been preferable. However, the reason for this approach was that, at the time, inhibitory optogenetics has long been much more challenging due to more limited sensitivity, efficacy and the risk of potential excitatory side-effects (see Introduction Section 1.4.2; Wiegert et al., 2017) whereas optogenetic ChR2-activation was well-established to produce reliable, strong effects. We addressed this point with a direct L6 CT neuron suppression approach used in the ongoing Bauer et al., 2022 study and found that the effect on dLGN FRs was qualitatively the same.

A second issue in this study concerned the type of naturalistic movie stimulus employed, which consisted of a single 5 s scene that was repeated multiple times. While this choice still captured the essential image statistics and dynamics of a naturalistic movie (Felsen & Dan, 2005) and was particularly useful for investigating dLGN reliability and precision, which required a large number of trial repeats, the lack of stimulus diversity did not probe a large enough feature space that would have allowed us to identify other dLGN properties, most importantly spatio-temporal RFs. This point, too, was addressed in Bauer et al., 2022, for which we designed a more diverse movie stimulus.

BAUER & SCHMORS ET AL. (2022) [*in prep.*]

In our current Bauer et al., 2022 study, we have been able to address several issues that arose in Román Rosón et al., 2019 and Spacek et al.,

2022. First, instead of suppressing CT feedback via global V_1 suppression (Spacek et al., 2022), we have established an optogenetic approach in the lab to suppress L6 CT cells directly. Second, to probe a larger stimulus space that would allow us to model dLGN STRFs, we have designed a complex, dynamic movie stimulus based on a diverse set of scenes randomly chosen from various feature films. Third, overcoming the inherent limitations of the simple non-negative linear regression model used in our Román Rosón et al., 2019 study, we adapted a spline-based linear-nonlinear Poisson model (spline-LNP) that allowed us to quantify the influence of the stimulus, CT feedback, locomotion and pupil size on dLGN activity.

We found that the net effect of CT feedback suppression on dLGN mean firing rates was suppressive, implying an excitatory effect for intact feedback, consistent with Spacek et al., 2022 and previous studies (Kim et al., 2014; Olsen et al., 2012). Conversely, a behavioural arousal state, as indicated by increased locomotion and pupil size, was associated with higher dLGN mean FRs, in agreement with previously found effects of those variables in Spacek et al., 2022 and other studies (McCormick, 1992; Molnár et al., 2021; Nestvogel & McCormick, 2021). Consistent with previous results Erisken et al., 2014; Reimer et al., 2014; Vinck et al., 2015, we also found a positive correlation between pupil diameter and run speed, confirming that both variables might track overall arousal states.

Our spline-LNP model enabled us to extract interpretable dLGN neuron properties. By feeding in the predictor traces for the stimulus, CT feedback photosuppression, locomotion and pupil size, we were able to disentangle their independent contributions to dLGN firing. The model filter shapes for CT feedback, locomotion and pupil size agreed with our expectations based on their cell-specific effects on mean FRs. Nevertheless, we were surprised to find that the model performance did not improve with added information about run speed and pupil size, which we attribute to potential problems with current model implementation (see Discussion in Bauer et al., 2022).

Beyond the issues discussed in the Bauer et al., 2022 and Spacek et al., 2022 studies, there are remaining questions about the relations between CT feedback and behavioural influences seen in the dLGN. We have seen how CT feedback and behaviour can exert their independent influences at multiple stages of visual processing (Andolina et al., 2013; Cudeiro & Sillito, 1996; Niell & Stryker, 2010; Reimer et al., 2014), including the dLGN (Erisken et al., 2014; Molnár et al., 2021; Spacek et al., 2022), and that we can use modelling techniques to extract them in the form of filter kernels (Bauer et al., 2022). However, although our model design separated the terms for CT feedback, locomotion and running, this separation is likely artificial and should not be taken at face value. Interestingly, Andermann et al., 2013 identified locomotion-suppressed neurons in V_1 L6 and Augustinaite and Kuhn, 2020 could pinpoint locomotion- and pupil-effects more precisely to L6 CT neurons. Relatedly, Molnár et al., 2021 found that the correlation between pupil size and dLGN relay cell membrane potential was abolished when they suppressed CT feedback. In this sense, CT feedback might also serve to send behaviour-related

signals to the dLGN. Since it is unlikely that behavioural information is computed *de novo* in L6 CT cells, but instead is probably inherited from brain stem inputs to V1 (Lee et al., 2014; McCormick, 1992; Nestvogel & McCormick, 2021; Reimer et al., 2016; Sherman & Guillery, 1996), we are likely dealing with overlaps in the circuitry underlying CT feedback and behavioural signals to the dLGN – or put differently: this calls into question the separability of visual and extra-visual input types to dLGN into distinct circuits, both in practice and in principle.

Instead, in modelling dLGN activity as a function of stimulus, CT feedback and behaviour, we should consider potential relations and interactions between these terms. Besides the independent effects of locomotion and pupil size on visual pathway activity (Molnár et al., 2021; Reimer et al., 2014; Vinck et al., 2015), we have already seen in Bauer et al., 2022 and Erisken et al., 2014 that they are also correlated, likely both indicating an arousal state (Busse, 2018). In our model, we could capture their combined effects on dLGN activity by incorporating interaction terms.

In general, we can of course model dLGN activity with arbitrary complexity by adding such terms on top of terms for luminance adaptation and burst activity (see Discussion in Bauer et al., 2022). However, with increased complexity, we are at risk of sacrificing simplicity and interpretability. And in the end, our GLM will still be only a descriptive model that merely provides the first generative description of phenomena to guide further research on the physiological interpretations and mechanisms (Pillow et al., 2008).

In summary, by integrating feedforward drive, CT feedback, and behavior into an interpretable spline-LNP model for dLGN activity, this work presents an important step towards a quantitative understanding of how responses to complex, naturalistic stimuli are modulated by CT feedback and behavior. Nevertheless, some unexpected results also highlight the sensitivity of this process on model design. On top of that, the relations between these predictors and the overlap of their underlying circuitry calls for further research. Lastly, there are potential improvements on our CT feedback manipulation, modelling and visual stimulation that I will address in the next section.

5.3 FUTURE DIRECTIONS

In the following, I will lay out some concrete plans and open avenues with regards to selective CT feedback manipulation, neural systems identification and ecological validity.

SELECTIVE INHIBITION OF THE L6 CT FEEDBACK PATHWAY: Naturally, in spite of the improvements on the optogenetic CT FB manipulation, our current approach in Bauer et al., 2022 can still be optimized even further. In particular, manipulating L6 CT cells in V1 may still elicit confounding effects through the circuit from V1 via the TRN to the dLGN (see Figure 1). In this sense, an optimal manipulation would target L6 CT synapses selectively in the dLGN, a technique that we are in the process of establishing in the Busse Lab.

Furthermore, some newly developed bistable anion-conducting channel-rhodopsins may reduce the need for constant illumination (Govorunova et al., 2015; Mahn et al., 2021) and consequently decrease the risk of artefacts (Wiegert et al., 2017) while being sensitive and effective enough to operate within the spatio-temporal constraints of optogenetic activation (Li et al., 2019).

NEURAL SYSTEMS IDENTIFICATION: In order to reach our goal of neural systems identification in the dLGN, we have moved from a simple feedforward linear regression model (Román Rosón et al., 2019) towards a LNP-GLM that is capable of accounting for non-linear response properties and also integrates optogenetic and behavioural predictors (Bauer et al., 2022). Both models capture a substantial fraction of variance in the dLGN responses. In future, we are planning to benefit from the advantages conferred by more complex deep neural network (DNN) models (Yamins et al., 2014). These have already successfully predicted neural responses in the salamander retina (Maheswaranathan et al., 2018) and macaque V1 (Bashivan et al., 2019; Cadena et al., 2019; Ecker et al., 2018; Walker et al., 2019). Not only do they promise to improve prediction quality with fewer data points, they would also allow us to fit the entire population of recorded cell responses simultaneously and separate general and cell-specific neural features ('what') and their cell-specific RF location ('where') (Klindt et al., 2017). Specifically, based on our existing experiment design, we are planning to develop a multilayer DNN of mouse dLGN responses to naturalistic movies that also includes additional predictor terms for feedback and behavioural state as modulator and shifter networks (Sinz et al., 2018) in order to elucidate how feedforward and feedback computations, as well as behavioural states, contribute to the neural processing of visual stimuli in the dLGN.

ECOLOGICAL VALIDITY: Thanks to the advances of one of our parallel projects on a naturalistic movie stimulus design, we will also be able to improve on the stimulus design towards a more naturalistic, ecologically valid direction (Qiu et al., 2020). Specifically, these movies are recorded in natural environments from the typical vantage point of mice, which will greatly improve on the somewhat unnatural nature of our current feature film stimulus. Moreover, since the movies are recorded at the peak UV and green wavelengths of mouse cones, and will be projected at these wavelengths onto a dome covering most of the mouse visual field, this will improve on the current experimental setup of presenting BW-scenes on an RGB-LCD (human) consumer display. Nevertheless, rather than dismissing less naturalistic stimuli per se, it is an interesting scientific question to what extent degrees of naturalness matter for visual responses, and if they do, what the relevant features are.

Moreover, in future, since the sensory systems are designed to guide action, it would be very interesting to overcome the discrepancy between mouse behaviour and visual stimulus that is present in our open-loop setup, and replace it with a closed-loop design through the use of a virtual reality setup.

5.4 CONCLUSION

What difference does dLGN make? What role do thalamic feedforward, feedback, and behavioural signals play?

It depends on what we look at and how we look at it. One recurrent theme that has become apparent especially throughout the discussion of the role of cortico-thalamic feedback, is the impact of the diverse methods that have led to conflicting results and interpretations. In the series of studies presented here, we have tried to iteratively address the issues raised in the previous steps, e.g. improving our optogenetic stimulation, our models, or our visual stimuli, in an attempt to allay doubts about their validity. However, this is a continuous, endless process. Every experiment is an imperfect approximation of the natural phenomenon that we are trying to uncover. In line with the quote introducing this section, one can say that this is fine so long as we do not confuse the answer given by nature to our experimental ‘question’ with the answer to our original question.

Turning back to the dLGN, first, we have seen that, much like the recent proliferation of cell types being reported in the retina (Baden et al., 2016; Goetz et al., 2021), there is more functional diversity than previously thought (Piscopo et al., 2013; Román Rosón et al., 2019). One potential source of this diversity is the recombination of retinal feedforward input signals from various RGC types that allows novel dLGN response feature creation. Retino-thalamic feedforward signal computations continue to be an active area of investigation and has more recently been advanced by *in vivo* two-photon calcium studies on the role of neuromodulation on retinal terminals in the dLGN (Liang et al., 2018; Schröder et al., 2019).

How cortico-thalamic feedback and behaviour act in concert to shape thalamic processing is still a classic question and a major unknown (Trenholm & Krishnaswamy, 2020). What seems clear is that feedback does shape thalamic signals, albeit subtly. In order to elicit these subtle effects, *in vivo* approaches in awake animals stimulated with naturalistic movies combined with specific and reversible cortico-thalamic feedback manipulations seem to be necessary to evoke a clearer picture. At this stage, it probably does not make sense to speak of a single role, and instead be open to the possibility of multiple roles being served.

In summary, both feedforward, feedback and behavioural signals seem to shape dLGN signals. This is in support of the view of the dLGN as an active signal transformer, not a passive relay. One question is to what extent this is surprising or makes the dLGN stand out from other parts of the brain which arguably are all about transforming signals.

BIBLIOGRAPHY

- Ahmed, B., Anderson, J. C., Douglas, R. J., Martin, K. A., & Nelson, J. C. (1994). Polynuclear innervation of spiny stellate neurons in cat visual cortex. *J Comp Neurol*, 341(1), 39–49. <https://doi.org/10.1002/cne.903410105> (cit. on p. 8)
- Alitto, H. J., & Usrey, W. M. (2008). Origin and Dynamics of Extraclassical Suppression in the Lateral Geniculate Nucleus of the Macaque Monkey. *Neuron*, 57(1), 135–146. <https://doi.org/10.1016/j.neuron.2007.11.019> (cit. on pp. 2, 10)
- Andermann, M. L., Gilfooy, N. B., Goldey, G. J., Sachdev, R. N., Wölfel, M., McCormick, D. A., Reid, R. C., & Levene, M. J. (2013). Chronic Cellular Imaging of Entire Cortical Columns in Awake Mice Using Microprisms. *Neuron*, 80(4), 900–913. <https://doi.org/10.1016/j.neuron.2013.07.052> (cit. on pp. 9, 121)
- Andermann, M. L., Kerlin, A. M., Roumis, D. K., Glickfeld, L. L., & Reid, R. C. (2011). Functional specialization of mouse higher visual cortical areas. *Neuron*. <https://doi.org/10.1016/j.neuron.2011.11.013> (cit. on p. 11)
- Andolina, I. M., Jones, H. E., Wang, W., & Sillito, A. M. (2007). Corticothalamic feedback enhances stimulus response precision in the visual system. *Proceedings of the National Academy of Sciences*, 104(5), 1685–1690. <https://doi.org/10.1073/pnas.0609318104> (cit. on p. 10)
- Andolina, I. M., Jones, H. E., & Sillito, A. M. (2013). Effects of cortical feedback on the spatial properties of relay cells in the lateral geniculate nucleus. *Journal of Neurophysiology*, 109(3), 889–899. <https://doi.org/10.1152/jn.00194.2012> (cit. on pp. 2, 9, 121)
- Angelucci, A., & Sainsbury, K. (2006). Contribution of feedforward thalamic afferents and corticogeniculate feedback to the spatial summation area of macaque V1 and LGN. *Journal of Comparative Neurology*. <https://doi.org/10.1002/cne.21060> (cit. on p. 7)
- Atallah, B. V., Bruns, W., Carandini, M., & Scanziani, M. (2012). Parvalbumin-Expressing Interneurons Linearly Transform Cortical Responses to Visual Stimuli. *Neuron*, 73(1), 159–170. <https://doi.org/10.1016/j.neuron.2011.12.013> (cit. on p. 12)
- Augustinaite, S., & Kuhn, B. (2020). Complementary Ca²⁺ Activity of Sensory Activated and Suppressed Layer 6 Corticothalamic Neurons Reflects Behavioral State. *Current Biology*, 30(20), 3945–3960.e5. <https://doi.org/10.1016/j.cub.2020.07.069> (cit. on pp. 8, 9, 121)
- Aydın, Ç., Couto, J., Giugliano, M., Farrow, K., & Bonin, V. (2018). Locomotion modulates specific functional cell types in the mouse visual thalamus. *Nature communications*, 9(1), 4882. <https://doi.org/10.1038/s41467-018-06780-3> (cit. on p. 11)
- Babadi, B., Casti, A., Xiao, Y., Kaplan, E., & Paninski, L. (2010). A generalized linear model of the impact of direct and indirect inputs to the lateral geniculate nucleus. *Journal of vision*, 10(10), 22. <https://doi.org/10.1167/10.10.22> (cit. on pp. 2, 15)

- Baden, T., Berens, P., Franke, K., Román Rosón, M., Bethge, M., & Euler, T. (2016). The functional diversity of mouse retinal ganglion cells. *Nature*, 529(7586), 1–21. <https://doi.org/10.1038/nature16468> (cit. on pp. 2–6, 118, 124)
- Baker, C. A., Elyada, Y. M., Parra, A., & Bolton, M. M. L. (2016). Cellular resolution circuit mapping with temporal-focused excitation of soma-targeted channelrhodopsin. *eLife*, 5(8), 1–15. <https://doi.org/10.7554/eLife.14193> (cit. on p. 13)
- Bar, M. (2004). Visual objects in context. *Nature Reviews Neuroscience*, 5(8), 617–629. <https://doi.org/10.1038/nrn1476> (cit. on p. 7)
- Barlow, H. B. (1953). Summation and inhibition in the frog's retina. *The Journal of Physiology*, 119(1), 69–88. <https://doi.org/10.1113/jphysiol.1953.sp004829> (cit. on p. 3)
- Barlow, H. B. (1961). Possible principles underlying the Transformations of sensory messages. In W. A. Rosenblith (Ed.), *Sensory communication* (pp. 217–234). <https://doi.org/10.7551/mitpress/9780262518420.001.0001>. (Cit. on p. 2)
- Bashivan, P., Kar, K., & DiCarlo, J. J. (2019). Neural population control via deep image synthesis. *Science*, 364(6439). <https://doi.org/10.1126/science.aav9436> (cit. on p. 123)
- Bastos, A. M., Usrey, W. M., Adams, R. A., Mangun, G. R., Fries, P., & Friston, K. J. (2012). Canonical Microcircuits for Predictive Coding. *Neuron*, 76(4), 695–711. <https://doi.org/10.1016/j.neuron.2012.10.038> (cit. on p. 7)
- Bauer, J., Weiler, S., Fernholz, M. H., Laubender, D., Scheuss, V., Hübener, M., Bonhoeffer, T., & Rose, T. (2021). Limited functional convergence of eye-specific inputs in the retinogeniculate pathway of the mouse. *Neuron*, 109(15), 2457–2468.e12. <https://doi.org/10.1016/J.NEURON.2021.05.036> (cit. on pp. 6, 118)
- Bauer, Y., Schmors, L., Huang, Z., Kotkat, A. H., Crombie, D., Meyerolbersleben, L., Renner, S., Sokoloski, S., Busse, L., & Berens, P. (2022). An interpretable spline-LNP model to characterise feedforward and feedback processing in mouse dLGN. *In preparation* (cit. on pp. 3, 93, 117, 120–123, 154).
- Baylor, D. A., Lamb, T. D., & Yau, K. W. (1979). Responses of retinal rods to single photons. *The Journal of Physiology*, 288(3), 613–634. <https://doi.org/10.1113/jphysiol.1979.sp012716> (cit. on p. 3)
- Berndt, A., Lee, S. Y., Ramakrishnan, C., & Deisseroth, K. (2014). Structure-guided transformation of channelrhodopsin into a light-activated chloride channel. *Science*, 344(6182), 420–4. <https://doi.org/10.1126/science.1252367> (cit. on p. 12)
- Berndt, A., Lee, S. Y., Wietek, J., Ramakrishnan, C., Steinberg, E. E., Rashid, A. J., Kim, H., Park, S., Santoro, A., Frankland, P. W., Iyer, S. M., Pak, S., Ährlund-Richter, S., Delp, S. L., Malenka, R. C., Josselyn, S. A., Carlén, M., Hegemann, P., & Deisseroth, K. (2015). Structural foundations of optogenetics: Determinants of channelrhodopsin ion selectivity. *Proceedings of the National Academy of Sciences*, 113(4), 822–829. <https://doi.org/10.1073/pnas.1523341113> (cit. on p. 12)

- Berson, D. (2008). Retinal ganglion cell types and their central projections. In R. H. Masland (Ed.), *The senses: A comprehensive reference* (pp. 491–520). Elsevier Inc. (Cit. on p. 2).
- Bezdudnaya, T., Cano, M., Bereshpolova, Y., Stoelzel, C. R., Alonso, J. M., & Swadlow, H. A. (2006). Thalamic burst mode and inattention in the awake LGNd. *Neuron*, 49(3), 421–432. <https://doi.org/10.1016/j.neuron.2006.01.010> (cit. on p. 119)
- Bickford, M. E., Zhou, N., Krahe, T. E., Govindaiah, G., & Guido, W. (2015). Retinal and Tectal ‘Driver-Like’ Inputs Converge in the Shell of the Mouse Dorsal Lateral Geniculate Nucleus. *Journal of Neuroscience*, 35(29), 10523–10534. <https://doi.org/10.1523/JNEUROSCI.3375-14.2015> (cit. on p. 16)
- Bonin, V., Mante, V., & Carandini, M. (2006). The statistical computation underlying contrast gain control. *The Journal of Neuroscience*, 26(23), 6346–6353. <https://doi.org/10.1523/JNEUROSCI.0284-06.2006> (cit. on pp. 14, 119)
- Bortone, D. S., Olsen, S. R., & Scanziani, M. (2014). Translaminar inhibitory cells recruited by layer 6 corticothalamic neurons suppress visual cortex. *Neuron*, 82(2), 474–485. <https://doi.org/10.1016/j.neuron.2014.02.021> (cit. on pp. 7, 9, 16)
- Boyden, E. S., Zhang, F., Bamberg, E., Nagel, G., & Deisseroth, K. (2005). Millisecond-timescale, genetically targeted optical control of neural activity. *Nature neuroscience*, 8(9), 1263–8. <https://doi.org/10.1038/nn1525> (cit. on p. 12)
- Briggs, F., & Usrey, W. M. (2011). Corticogeniculate feedback and visual processing in the primate. *Journal of Physiology*, 589(1), 33–40. <https://doi.org/10.1113/jphysiol.2010.193599> (cit. on pp. 2, 9, 10, 15, 119)
- Briggs, F. (2010). Organizing principles of cortical layer 6. *Frontiers in Neural Circuits*. <https://doi.org/10.3389/neuro.04.003.2010> (cit. on pp. 7–9, 119)
- Busse, L. (2018). The influence of locomotion on sensory processing and its underlying neuronal circuits. *Neuroforum*, 24(1), A41–A51. <https://doi.org/10.1515/nf-2017-A046> (cit. on pp. 10, 122)
- Butts, D. A., Weng, C., Jin, J., Alonso, J. M., & Paninski, L. (2011). Temporal precision in the visual pathway through the interplay of excitation and stimulus-driven suppression. *Journal of Neuroscience*. <https://doi.org/10.1523/JNEUROSCI.0434-11.2011> (cit. on p. 15)
- Cadena, S. A., Denfield, G. H., Walker, E. Y., Gatys, L. A., Tolias, A. S., Bethge, M., & Ecker, A. S. (2019). Deep convolutional models improve predictions of macaque V1 responses to natural images. *PLoS computational biology*, 15.4, e1006897. <https://doi.org/10.1101/201764> (cit. on p. 123)
- Cano, M., Bezdudnaya, T., Swadlow, H. A., & Alonso, J. M. (2006). Brain state and contrast sensitivity in the awake visual thalamus. *Nature neuroscience*, 9(10), 1240–1242. <https://doi.org/10.1038/NN1760> (cit. on p. 119)
- Carandini, M., Demb, J. B., Mante, V., Tolhurst, D. J., Dan, Y., Olshausen, B. A., Gallant, J. L., & Rust, N. C. (2005). Do we know what the early visual system does? *Journal of Neuroscience*, 25(46), 10577–10597. <https://doi.org/10.1523/JNEUROSCI.3726-05.2005> (cit. on p. 1)

- Chen, C., Bickford, M. E., & Hirsch, J. A. (2016). Untangling the Web between Eye and Brain. *Cell*, 165(1), 20–21. <https://doi.org/10.1016/j.cell.2016.03.010> (cit. on pp. 5, 117)
- Chen, C., & Regehr, W. G. (2000). Developmental remodeling of the retinogeniculate synapse. *Neuron*, 28(3), 955–966. [https://doi.org/10.1016/S0896-6273\(00\)00166-5](https://doi.org/10.1016/S0896-6273(00)00166-5) (cit. on p. 5)
- Chow, B. Y., Han, X., Dobry, A. S., Qian, X., Chuong, A. S., Li, M., Henninger, M. A., Belfort, G. M., Lin, Y., Monahan, P. E., & Boyden, E. S. (2010). High-performance genetically targetable optical neural silencing by light-driven proton pumps. *Nature*, 463(7277), 98–102. <https://doi.org/10.1038/nature08652> (cit. on p. 10)
- Cruz-Martín, A., El-Danaf, R. N., Osakada, F., Sriram, B., Dhande, O. S., Nguyen, P. L., Callaway, E. M., Ghosh, A., & Huberman, A. D. (2014). A dedicated circuit links direction-selective retinal ganglion cells to the primary visual cortex. *Nature*, 507(7492), 358–61. <https://doi.org/10.1038/nature12989> (cit. on pp. 2, 6)
- Cudeiro, J., & Sillito, A. M. (1996). Spatial frequency tuning of orientation-discontinuity-sensitive corticofugal feedback to the cat lateral geniculate nucleus. *The Journal of Physiology*, 490(2), 481–492. <https://doi.org/10.1113/jphysiol.1996.sp021159> (cit. on pp. 2, 9, 10, 15, 119, 121)
- Dacey, D. M., Peterson, B. B., Robinson, F. R., & Gamlin, P. D. (2003). Fireworks in the Primate Retina. *Neuron*, 37(1), 15–27. [https://doi.org/10.1016/S0896-6273\(02\)01143-1](https://doi.org/10.1016/S0896-6273(02)01143-1) (cit. on p. 5)
- Dana Ballard. (2015). Brain Computation as Hierarchical Abstraction. *Mit press* (pp. 3–40). Cambridge University Press. <https://doi.org/10.7551/mitpress/9780262028615.003.0001>. (Cit. on p. 8)
- De Labra, C., Rivadulla, C., Grieve, K., Marino, J., Espinosa, N., Cudeiro, J., Mariño, J., Espinosa, N., & Cudeiro, J. (2007). Changes in visual responses in the feline dLGN: Selective thalamic suppression induced by transcranial magnetic stimulation of V1. *Cerebral Cortex*, 17(6), 1376–1385. <https://doi.org/10.1093/cercor/bhl048> (cit. on p. 10)
- Deisseroth, K. (2011). Optogenetics. *Nature methods*, 8(1), 26–9. <https://doi.org/10.1038/nmeth.f.324> (cit. on p. 12)
- Denman, D. J., & Contreras, D. (2015). Complex effects on in vivo visual responses by specific projections from mouse cortical layer 6 to dorsal lateral geniculate nucleus. *The Journal of Neuroscience*, 35(25), 9265–80. <https://doi.org/10.1523/JNEUROSCI.0027-15.2015> (cit. on pp. 9, 10)
- Dhande, O. S., Estevez, M. E., Quattrochi, L. E., El-Danaf, R. N., Nguyen, P. L., Berson, D. M., & Huberman, A. D. (2013). Genetic dissection of retinal inputs to brainstem nuclei controlling image stabilization. *Journal of Neuroscience*, 33(45), 17797–813. <https://doi.org/10.1523/JNEUROSCI.2778-13.2013> (cit. on pp. 4, 6)
- Dhande, O. S., & Huberman, A. D. (2014). Retinal ganglion cell maps in the brain: Implications for visual processing. *Current Opinion in Neurobiology*, 24(1), 133–142. <https://doi.org/10.1016/j.conb.2013.08.006> (cit. on p. 3)
- Dhande, O. S., Stafford, B. K., Lim, J.-H. A., & Huberman, A. D. (2015). Contributions of Retinal Ganglion Cells to Subcortical Visual Processing

- and Behaviors. *Annual Review of Vision Science*, 1(1), 291–328. <https://doi.org/10.1146/annurev-vision-082114-035502> (cit. on p. 3)
- Dodge, S., & Karam, L. (2016). Understanding how image quality affects deep neural networks. *2016 8th International Conference on Quality of Multimedia Experience, QoMEX 2016*. <https://doi.org/10.1109/QoMEX.2016.7498955> (cit. on p. 1)
- Dong, D. W., & Atick, J. J. (1995). Temporal decorrelation: A theory of lagged and nonlagged responses in the lateral geniculate nucleus. *Network: Computation in Neural Systems*, 6(2), 159–178. https://doi.org/10.1088/0954-898X_6_2_003 (cit. on pp. 2, 14)
- Drinnenberg, A., Franke, F., Morikawa, R. K., Jüttner, J., Hillier, D., Hantz, P., Hierlemann, A., Azeredo da Silveira, R., & Roska, B. (2018). How Diverse Retinal Functions Arise from Feedback at the First Visual Synapse. *Neuron*, 99(1), 117–134.e11. <https://doi.org/10.1016/j.neuron.2018.06.001> (cit. on p. 7)
- Dugué, G. P., Akemann, W., & Knöpfel, T. (2012). A comprehensive concept of optogenetics. *Progress in Brain Research*, 196, 1–28. <https://doi.org/10.1016/B978-0-444-59426-6.00001-X> (cit. on p. 12)
- Durand, S., Iyer, R., Mizuseki, K., De Vries, S., Mihalas, S., & Reid, R. C. (2016). A comparison of visual response properties in the lateral geniculate nucleus and primary visual cortex of awake and anesthetized mice. *Journal of Neuroscience*, 36(48), 12144–12156. <https://doi.org/10.1523/JNEUROSCI.1741-16.2016> (cit. on pp. 2, 10, 119)
- Ecker, A. S., Sinz, F. H., Froudarakis, E., Fahey, P. G., Cadena, S. A., Walker, E. Y., Cobos, E., Reimer, J., Tolias, A. S., & Bethge, M. (2018). A rotation-equivariant convolutional neural network model of primary visual cortex. *arXiv*, 1809.10504 (cit. on p. 123).
- Ecker, J. L., Dumitrescu, O. N., Wong, K. Y., Alam, N. M., Chen, S. K., LeGates, T., Renna, J. M., Prusky, G. T., Berson, D. M., & Hattar, S. (2010). Melanopsin-expressing retinal ganglion-cell photoreceptors: Cellular diversity and role in pattern vision. *Neuron*, 67(1), 49–60. <https://doi.org/10.1016/j.neuron.2010.05.023> (cit. on p. 6)
- Einevoll, G. T., & Plesser, H. E. (2012). Extended difference-of-Gaussians model incorporating cortical feedback for relay cells in the lateral geniculate nucleus of cat. *Cognitive Neurodynamics*, 6(4), 307–324. <https://doi.org/10.1007/s11571-011-9183-8> (cit. on p. 15)
- Ellis, E. M., Gauvain, G., Sivyer, B., & Murphy, G. J. (2016). Shared and distinct retinal input to the mouse superior colliculus and dorsal lateral geniculate nucleus. *Journal of Neurophysiology*, 116(2), 602–610. <https://doi.org/10.1152/jn.00227.2016> (cit. on pp. 2, 4, 6, 16)
- Erişir, A., Van Horn, S. C., & Sherman, S. M. (1997). Relative numbers of cortical and brainstem inputs to the lateral geniculate nucleus. *Proceedings of the National Academy of Sciences of the United States of America*, 94(4), 1517–20. <https://doi.org/10.1073/pnas.94.4.1517> (cit. on pp. 8, 119)
- Erisken, S., Vaiceliunaite, A., Jurjut, O., Fiorini, M., Katzner, S., & Busse, L. (2014). Effects of locomotion extend throughout the mouse early visual system. *Current Biology*, 24(24), 2899–2907. <https://doi.org/10.1016/j.cub.2014.10.045> (cit. on pp. 11, 15, 121, 122)

- Fairhall, A. L., Lewen, G. D., Bialek, W., & de Ruyter Van Steveninck, R. R. (2001). Efficiency and ambiguity in an adaptive neural code. *Nature*, *412*(6849), 787–92. <https://doi.org/10.1038/35090500> (cit. on p. 3)
- Felleman, D. J., & Van Essen, D. C. (1991). Distributed hierarchical processing in the primate cerebral cortex. *Cerebral cortex*, *1*(1), 1–47. <https://doi.org/10.1093/cercor/1.1.1> (cit. on p. 1)
- Felsen, G., & Dan, Y. (2005). A natural approach to studying vision. *Nature Neuroscience*, *8*(12), 1643–1646. <https://doi.org/10.1038/nn1608> (cit. on pp. 13, 14, 120)
- Fenko, L., Yizhar, O., & Deisseroth, K. (2011). The development and application of optogenetics. *Annual review of neuroscience*, *34*, 389–412. <https://doi.org/10.1146/annurev-neuro-061010-113817> (cit. on p. 12)
- Frandonig, J. E., Matney, C. J., Lee, K., Kim, J., Chev e, M., Kim, S.-J., Bickert, A. A., & Brown, S. P. (2019). The Synaptic Organization of Layer 6 Circuits Reveals Inhibition as a Major Output of a Neocortical Sublamina. *Cell Reports*, *28*(12), 3131–3143. <https://doi.org/10.1016/j.celrep.2019.08.048> (cit. on p. 8)
- Franke, K., Berens, P., Schubert, T., Bethge, M., Euler, T., & Baden, T. (2017). Inhibition decorrelates visual feature representations in the inner retina. *Nature*, *542*(7642), 439–444. <https://doi.org/10.1038/nature21394> (cit. on p. 3)
- Gazzaley, A., & Nobre, A. (2012). Top-down modulation: bridging selective attention and working memory. *Trends in cognitive sciences*, *16*(2), 129–135. <https://doi.org/10.1016/j.tics.2011.11.014>. Top-down (cit. on pp. 1, 7)
- Ghodrati, M., Khaligh-Razavi, S. M., & Lehky, S. R. (2017). Towards building a more complex view of the lateral geniculate nucleus: Recent advances in understanding its role. *Progress in Neurobiology*, *156*, 214–255. <https://doi.org/10.1016/j.pneurobio.2017.06.002> (cit. on pp. 2, 14, 15)
- Gibson, J. J. (1972). A theory of direct visual perception (J. Royce & W. Rozeboom, Eds.). (Cit. on p. 1).
- Gilbert, C. D., & Li, W. (2013). Top-down influences on visual processing. *Nature Reviews Neuroscience*, *14*(5), 350–363. <https://doi.org/10.1038/nrn3476> (cit. on p. 7)
- Gilbert, C. D., & Sigman, M. (2007). Brain States: Top-Down Influences in Sensory Processing. *Neuron*, *54*(5), 677–696. <https://doi.org/10.1016/j.neuron.2007.05.019> (cit. on p. 1)
- Godwin, D. W., Van Horn, S. C., Eriřir, A., Sesma, M., Romano, C., & Sherman, S. M. (1996). Ultrastructural localization suggests that retinal and cortical inputs access different metabotropic glutamate receptors in the lateral geniculate nucleus. *Journal of Neuroscience*, *16*(24), 8181–8192. <https://doi.org/10.1523/jneurosci.16-24-08181.1996> (cit. on p. 8)
- Goetz, J., Jessen, Z. F., Jacobi, A., Mani, A., Cooler, S., Greer, D., Kadri, S., Segal, J., Sanes, J., & Schwartz, G. W. (2021). Unified classification of mouse retinal ganglion cells using function, morphology, and gene expression. *bioRxiv*, 1–27 (cit. on pp. 4, 118, 124).
- Gollisch, T., & Meister, M. (2010). Eye Smarter than Scientists Believed: Neural Computations in Circuits of the Retina. *Neuron*, *65*(2), 150–164. <https://doi.org/10.1016/j.neuron.2009.12.009> (cit. on p. 3)

- Gong, S., Doughty, M., Harbaugh, C. R., Cummins, A., Hatten, M. E., Heintz, N., & Gerfen, C. R. (2007). Targeting Cre Recombinase to Specific Neuron Populations with Bacterial Artificial Chromosome Constructs. *Journal of Neuroscience*, 27(37), 9817–9823. <https://doi.org/10.1523/JNEUROSCI.2707-07.2007> (cit. on p. 7)
- Gouwens, N. W., Sorensen, S. A., Berg, J., Lee, C., Jarsky, T., Ting, J., Sunkin, S. M., Feng, D., Anastassiou, C. A., Barkan, E., Bickley, K., Blesie, N., Braun, T., Brouner, K., Budzillo, A., Caldejon, S., Casper, T., Castelli, D., Chong, P., . . . Koch, C. (2019). Classification of electrophysiological and morphological neuron types in the mouse visual cortex. *Nature Neuroscience*, 22(7), 1182–1195. <https://doi.org/10.1038/s41593-019-0417-0> (cit. on p. 8)
- Govorunova, E. G., Sineshchekov, O. A., Janz, R., Liu, X., & Spudich, J. L. (2015). Natural light-gated anion channels: A family of microbial rhodopsins for advanced optogenetics. *Science*, 349(6248), 647–650. <https://doi.org/10.1126/science.aaa7484> (cit. on pp. 12, 123)
- Graybuck, L., Daigle, T., Sedeño-Cortés, A., Walker, M., Kalmbach, B., Lenz, G., Nguyen, T. N., Garren, E., Kim, T. K., Siverts, L. A., Bendrick, J., Zhou, T., Mortrud, M., Yao, S., Cetin, A., Larsen, R., Esposito, L., Gore, B., Szelenyi, E., . . . Tasic, B. (2020). Enhancer viruses and a transgenic platform for combinatorial cell subclass-specific labeling. *BioRxiv*. <https://doi.org/10.1101/525014> (cit. on p. 8)
- Grubb, M. S., & Thompson, I. D. (2003). Quantitative characterization of visual response properties in the mouse dorsal lateral geniculate nucleus. *Journal of neurophysiology*, 90(6), 3594–3607. <https://doi.org/10.1152/jn.00699.2003> (cit. on p. 5)
- Gulyás, B., Lagae, L., Eysel, U., & Orban, G. A. (1990). Corticofugal feedback influences the responses of geniculate neurons to moving stimuli. *Experimental Brain Research*, 79(2), 441–446. <https://doi.org/10.1007/BF00608257> (cit. on pp. 10, 119)
- Hammer, S., Monavarfeshani, A., Lemon, T., Su, J., & Fox, M. A. (2015). Multiple Retinal Axons Converge onto Relay Cells in the Adult Mouse Thalamus. *Cell Reports*, 12(10), 1575–1583. <https://doi.org/10.1016/j.celrep.2015.08.003> (cit. on pp. 2, 6)
- Hasse, J. M., & Briggs, F. (2017). Corticogeniculate feedback sharpens the temporal precision and spatial resolution of visual signals in the ferret. *Proceedings of the National Academy of Sciences of the United States of America*, 114(30), E6222–E6230. <https://doi.org/10.1073/pnas.1704524114> (cit. on pp. 9, 10)
- Hasson, U., Avidan, G., Gelbard, H., Vallines, I., Harel, M., Minshew, N., & Behrmann, M. (2009). Shared and idiosyncratic cortical activation patterns in autism revealed under continuous real-life viewing conditions. *Autism Research*, 2(4), 220–231. <https://doi.org/10.1002/aur.89> (cit. on p. 14)
- Heeger, D. J. (2017). Theory of cortical function. *Proceedings of the National Academy of Sciences of the United States of America*, 114(8), 1773–1782. <https://doi.org/10.1073/pnas.1619788114> (cit. on p. 7)
- Hubel, D. H., & Wiesel, T. N. (1962). Receptive fields, binocular interaction and functional architecture in the cat's visual cortex. *The Journal of Physiol-*

- ogy, 160(1), 106–154. <https://doi.org/10.1113/jphysiol.1962.sp006837> (cit. on p. 1)
- Hubel, D. H., & Wiesel, T. N. (1961). Integrative Action in the Cat's Lateral Geniculate Body. *The Journal of Physiology*, 155, 385–398. <https://doi.org/10.1113/jphysiol.1961.sp006635> (cit. on pp. 5, 117)
- Huberman, A. D., Manu, M., Koch, S. M., Susman, M. W., Lutz, A. B., Ullian, E. M., Baccus, S. A., & Barres, B. A. (2008). Architecture and Activity-Mediated Refinement of Axonal Projections from a Mosaic of Genetically Identified Retinal Ganglion Cells. *Neuron*, 59(3), 425–438. <https://doi.org/10.1016/j.neuron.2008.07.018> (cit. on pp. 4, 6)
- Huberman, A. D., & Niell, C. M. (2011). What can mice tell us about how vision works? *Trends in Neurosciences*, 34(9), 464–473. <https://doi.org/10.1016/j.tins.2011.07.002> (cit. on p. 5)
- Huberman, A. D., Wei, W., Elstrott, J., Stafford, B. K., Feller, M. B., & Barres, B. A. (2009). Genetic Identification of an On-Off Direction- Selective Retinal Ganglion Cell Subtype Reveals a Layer-Specific Subcortical Map of Posterior Motion. *Neuron*, 62(3), 327–334. <https://doi.org/10.1016/j.neuron.2009.04.014> (cit. on p. 6)
- Irvin, G. E., Casagrande, V. A., & Norton, T. T. (1993). Center/surround relationships of magnocellular, parvocellular, and koniocellular relay cells in primate lateral geniculate nucleus. *Visual Neuroscience*, 10(2), 363–373. <https://doi.org/10.1017/S0952523800003758> (cit. on p. 14)
- Jehee, J. F. M., & Ballard, D. H. (2009). Predictive Feedback Can Account for Biphasic Responses in the Lateral Geniculate Nucleus. *PLoS Computational Biology*, 5(5), e1000373. <https://doi.org/10.1371/journal.pcbi.1000373> (cit. on p. 14)
- Jones, H. E., Andolina, I. M., Ahmed, B., Shipp, S. D., Clements, J. T. C., Grieve, K. L., Cudeiro, J., Salt, T. E., & Sillito, A. M. (2012). Differential feedback modulation of center and surround mechanisms in parvocellular cells in the visual thalamus. *Journal of Neuroscience*, 32(45), 15946–51. <https://doi.org/10.1523/JNEUROSCI.0831-12.2012> (cit. on p. 9)
- Josh Huang, Z., Zeng, H., Huang, Z. J., & Zeng, H. (2013). Genetic Approaches to Neural Circuits in the Mouse. *Annual review of neuroscience*, 36(1), 183–215. <https://doi.org/10.1146/annurev-neuro-062012-170307> (cit. on p. 7)
- Kaplan, E., Purpura, K., & Shapley, R. M. (1987). Contrast affects the transmission of visual information through the mammalian lateral geniculate nucleus. *The Journal of Physiology*, 391(1), 267–288. <https://doi.org/10.1113/jphysiol.1987.sp016737> (cit. on pp. 5, 117)
- Keat, J., Reinagel, P., Reid, R. C., & Meister, M. (2001). Predicting every spike: A model for the responses of visual neurons. *Neuron*, 30(3), 803–817. [https://doi.org/10.1016/S0896-6273\(01\)00322-1](https://doi.org/10.1016/S0896-6273(01)00322-1) (cit. on p. 14)
- Keller, A. J., Roth, M. M., & Scanziani, M. (2020). Feedback generates a second receptive field in neurons of the visual cortex. *Nature*, 582(7813), 545–549. <https://doi.org/10.1038/s41586-020-2319-4> (cit. on pp. 10, 15)
- Kim, J., Matney, C. J., Blankenship, A., Hestrin, S., & Brown, S. P. (2014). Layer 6 corticothalamic neurons activate a cortical output layer, layer 5a. *J Neurosci*, 34(29), 9656–9664. <https://doi.org/10.1523/JNEUROSCI.1325-14.2014> (cit. on pp. 8, 16, 121)

- King, J. L., Lowe, M. P., Stover, K. R., Wong, A. A., & Crowder, N. A. (2016). Adaptive Processes in Thalamus and Cortex Revealed by Silencing of Primary Visual Cortex during Contrast Adaptation. *Current Biology*, 26(10), 1–6. <https://doi.org/10.1016/j.cub.2016.03.018> (cit. on p. 10)
- Klindt, D. A., Ecker, A. S., Euler, T., & Bethge, M. (2017). Neural system identification for large populations separating 'what' and 'where'. *arXiv*, (NIPS), 4–6 (cit. on p. 123).
- Knill, D. C., & Pouget, A. (2004). The Bayesian brain: The role of uncertainty in neural coding and computation. *Trends in Neurosciences*, 27(12), 712–719. <https://doi.org/10.1016/j.tins.2004.10.007> (cit. on p. 7)
- Kok, P., Jehee, J. F., & de Lange, F. P. (2012). Less Is More: Expectation Sharpens Representations in the Primary Visual Cortex. *Neuron*, 75(2), 265–270. <https://doi.org/10.1016/j.neuron.2012.04.034> (cit. on p. 7)
- Kreiman, G., & Serre, T. (2020). Beyond the feedforward sweep: feedback computations in the visual cortex. *Annals of the New York Academy of Sciences*, 1464(1), 222–241. <https://doi.org/10.1111/nyas.14320> (cit. on p. 7)
- Kremkow, J., & Alonso, J.-M. (2018). Thalamocortical Circuits and Functional Architecture. *Annual Review of Vision Science*, 4(1), 263–285. <https://doi.org/10.1146/annurev-vision-091517-034122> (cit. on p. 4)
- Laboissonniere, L. A., Goetz, J. J., Martin, G. M., Bi, R., Lund, T. J., Ellson, L., Lynch, M. R., Mooney, B., Wickham, H., Liu, P., Schwartz, G. W., & Trimarchi, J. M. (2019). Molecular signatures of retinal ganglion cells revealed through single cell profiling. *Scientific Reports*, 9(1), 1–15. <https://doi.org/10.1038/s41598-019-52215-4> (cit. on pp. 4, 118)
- Lamme, V. A., & Roelfsema, P. R. (2000). The distinct modes of vision offered by feedforward and recurrent processing. *Trends in Neurosciences*, 23(11), 571–579. [https://doi.org/10.1016/S0166-2236\(00\)01657-X](https://doi.org/10.1016/S0166-2236(00)01657-X) (cit. on pp. 1, 7)
- LeCun, Y., Bengio, J., & Hinton, G. (2015). Deep learning. *Nature*, 521(7553), 436–444 (cit. on p. 1).
- Lee, A. M., Hoy, J. L., Bonci, A., Wilbrecht, L., Stryker, M. P., & Niell, C. M. (2014). Identification of a brainstem circuit regulating visual cortical state in parallel with locomotion. *Neuron*, 83(2), 455–466. <https://doi.org/10.1016/j.neuron.2014.06.031> (cit. on pp. 11, 122)
- Lee, T. S., & Mumford, D. (2003). Hierarchical Bayesian inference in the visual cortex. *Journal of the Optical Society of America A*, 20(7), 1434. <https://doi.org/10.1364/josaa.20.001434> (cit. on p. 13)
- Lesica, N. A., Jin, J., Weng, C., Yeh, C.-i., Butts, D. A., Stanley, G. B., & Alonso, J.-m. (2007). Adaptation to stimulus contrast and correlations during natural visual stimulation. *Neuron*, 55(3), 479–491 (cit. on pp. 14, 15, 119).
- Lesica, N. A., & Stanley, G. B. (2004). Encoding of natural scene movies by tonic and burst spikes in the lateral geniculate nucleus. *Journal of Neuroscience*, 24(47), 10731–10740. <https://doi.org/10.1523/JNEUROSCI.3059-04.2004> (cit. on pp. 14, 15, 119)
- Lettvin, J. Y., Maturana, H. R., McCulloch, W. S., & Pitts, W. H. (1959). What the Frog's Eye Tells the Frog's Brain. *Proceedings of the IRE*, 47(11), 1940–1959 (cit. on p. 3).

- Li, N., Chen, S., Guo, Z. V., Chen, H., Huo, Y., Inagaki, H. K., Chen, G., Davis, C., Hansel, D., Guo, C., & Svoboda, K. (2019). Spatiotemporal constraints on optogenetic inactivation in cortical circuits. *eLife*, *8*, 1–31. <https://doi.org/10.7554/eLife.48622> (cit. on p. 123)
- Li, Y. T., Ibrahim, L. A., Liu, B. H., Zhang, L. I., & Tao, H. W. (2013). Linear transformation of thalamocortical input by intracortical excitation. *Nature Neuroscience*. <https://doi.org/10.1038/nn.3494> (cit. on p. 10)
- Liang, L., Fratzl, A., Goldey, G., Ramesh, R. N., Sugden, A. U., Morgan, J. L., Chen, C., & Andermann, M. L. (2018). A Fine-Scale Functional Logic to Convergence from Retina to Thalamus. *Cell*, *173*(6), 1343–1355.e24. <https://doi.org/10.1016/j.cell.2018.04.041> (cit. on pp. 6, 118, 124)
- Liang, L., Fratzl, A., Reggiani, J. D., El Mansour, O., Chen, C., & Andermann, M. L. (2020). Retinal Inputs to the Thalamus Are Selectively Gated by Arousal. *Current biology : CB*, *30*(20), 3923–3934.e9. <https://doi.org/10.1016/J.CUB.2020.07.065> (cit. on p. 120)
- Lien, A. D., & Scanziani, M. (2013). Tuned thalamic excitation is amplified by visual cortical circuits. *Nature Neuroscience*, *16*(9), 1315–1323. <https://doi.org/10.1038/nn.3488> (cit. on p. 10)
- Litvina, E. Y., & Chen, C. (2017). Functional Convergence at the Retinogeniculate Synapse. *Neuron*, *96*(2), 330–338.e5. <https://doi.org/10.1016/j.neuron.2017.09.037> (cit. on pp. 6, 118)
- Macknik, S., & Martinez-Conde, S. (2009). The role of feedback in visual attention and awareness. *Cognitive Neurosciences*, 1165–1180 (cit. on pp. 7, 8, 119).
- Madisen, L., Zwingman, T. A., Sunkin, S. M., Oh, S. W., Hatim, A., Gu, H., Ng, L. L., Palmiter, R. D., Hawrylycz, M. J., Allan, R., Lein, E. S., & Zeng, H. (2010). A robust and high-throughput Cre reporting and characterization system for the whole mouse brain. *Nature neuroscience*, *13*(1), 133–140. <https://doi.org/10.1038/nn.2467.A> (cit. on p. 7)
- Maheswaranathan, N., McIntosh, L. T., Kastner, D. B., Melander, J., Brezovec, L., Nayebi, A., Wang, J., Ganguli, S., & Baccus, S. A. (2018). Deep learning models reveal internal structure and diverse computations in the retina under natural scenes. *bioRxiv*. <https://doi.org/10.1101/340943> (cit. on p. 123)
- Mahn, M., Gibor, L., Patil, P., Cohen-Kashi Malina, K., Oring, S., Printz, Y., Levy, R., Lampl, I., & Yizhar, O. (2018). High-efficiency optogenetic silencing with soma-targeted anion-conducting channelrhodopsins. *Nature communications*, *9*(1), 4125. <https://doi.org/10.1038/s41467-018-06511-8> (cit. on p. 13)
- Mahn, M., Prigge, M., Ron, S., Levy, R., & Yizhar, O. (2016). Biophysical constraints of optogenetic inhibition at presynaptic terminals. *Nature Neuroscience*, *19*(4), 554–556. <https://doi.org/10.1038/nn.4266> (cit. on p. 12)
- Mahn, M., Saraf-Sinik, I., Patil, P., Pulin, M., Bruentgens, F., Palgi, S., Gat, A., Dine, J., Wietek, J., Davidi, I., Levy, R., Sauter, K., Soba, P., Schmitz, D., Rost, B., & Simon Wiegert, J. (2021). Optogenetic silencing of neurotransmitter release with a naturally occurring invertebrate rhodopsin. *bioRxiv* (cit. on p. 123).

- Mante, V., Bonin, V., & Carandini, M. (2008). Functional Mechanisms Shaping Lateral Geniculate Responses to Artificial and Natural Stimuli. *Neuron*, 58(4), 625–638. <https://doi.org/10.1016/j.neuron.2008.03.011> (cit. on pp. 13–15)
- Mante, V., Frazor, R. A., Bonin, V., Geisler, W. S., & Carandini, M. (2005). Independence of luminance and contrast in natural scenes and in the early visual system. *Nature Neuroscience*, 8(12), 1690–1697. <https://doi.org/10.1038/nn1556> (cit. on pp. 14, 119)
- Marr, D., & Poggio, T. (1976). *From Understanding Computation to Understanding Neural Circuitry*. Massachusetts Institute of Technology, Artificial Intelligence Laboratory. (Cit. on p. 1).
- Marshel, J. H., Kaye, A. P., Nauhaus, I., & Callaway, E. M. (2012). Anterior-Posterior Direction Opponency in the Superficial Mouse Lateral Geniculate Nucleus. *Neuron*, 76(4), 713–720. <https://doi.org/10.1016/j.neuron.2012.09.021> (cit. on pp. 2, 6)
- Martersteck, E. M., Hirokawa, K. E., Zeng, H., Sanes, J. R., Harris, J. A., Evarts, M., Bernard, A., Duan, X., Li, Y., Ng, L., Oh, S. W., Ouellette, B., Royall, J. J., Stoecklin, M., & Wang, Q. (2017). Diverse Central Projection Patterns of Retinal Ganglion Cells. *Cell Reports*, 18(21), 2058–2072. <https://doi.org/10.1016/j.celrep.2017.01.075> (cit. on pp. 4, 6, 16)
- Martin, P. R. (1986). The projection of different retinal ganglion cell classes to the dorsal lateral geniculate nucleus in the hooded rat. *Experimental Brain Research*, 62(1), 77–88. <https://doi.org/10.1007/BF00237404> (cit. on p. 4)
- Masland, R. H. (2012). The Neuronal Organization of the Retina. *Neuron*, 76(2), 266–280. <https://doi.org/10.1016/j.neuron.2012.10.002> (cit. on p. 3)
- Matsuno-Yagi, A., & Mukohata, Y. (1980). ATP synthesis linked to light-dependent proton uptake in a red mutant strain of Halobacterium lacking bacteriorhodopsin. *Archives of Biochemistry and Biophysics*, 199(1), 297–303. [https://doi.org/10.1016/0003-9861\(80\)90284-2](https://doi.org/10.1016/0003-9861(80)90284-2) (cit. on p. 12)
- Mattis, J., Tye, K. M., Ferenczi, E. a., Ramakrishnan, C., O’Shea, D. J., Prakash, R., Gunaydin, L. a., Hyun, M., Fenno, L. E., Gradinaru, V., Yizhar, O., & Deisseroth, K. (2011). Principles for applying optogenetic tools derived from direct comparative analysis of microbial opsins. *Nature Methods*, 9(2), 159–172. <https://doi.org/10.1038/nmeth.1808> (cit. on p. 12)
- McCormick, D. A. (1992). Neurotransmitter actions in the thalamus and cerebral cortex and their role in neuromodulation of thalamocortical activity. *Progress in neurobiology*, 39(4), 337–388. [https://doi.org/10.1016/0301-0082\(92\)90012-4](https://doi.org/10.1016/0301-0082(92)90012-4) (cit. on pp. 10, 11, 119, 121, 122)
- Mineault, P. J., Tring, E., Trachtenberg, J. T., & Ringach, D. L. (2016). Enhanced Spatial Resolution During Locomotion and Heightened Attention in Mouse Primary Visual Cortex. *The Journal of Neuroscience*, 36(24), 6382–6392. <https://doi.org/10.1523/JNEUROSCI.0430-16.2016> (cit. on p. 11)
- Molnár, B., Sere, P., Bordé, S., Koós, K., Zsigri, N., Horváth, P., & Lőrincz, M. L. (2021). Cell-Type Specific Arousal-Dependent Modulation of Thalamic Activity in the Lateral Geniculate Nucleus. *bioRxiv*. <https://doi.org/10.1093/texcom/tgab020> (cit. on pp. 11, 15, 119–122)
- Montero, V. M. (1991). A quantitative study of synaptic contacts on interneurons and relay cells of the cat lateral geniculate nucleus. *Experimental Brain*

- Research*, 86(2), 257–270. <https://doi.org/10.1007/BF00228950> (cit. on p. 16)
- Morgan, J. L., & Lichtman, J. W. (2020). An Individual Interneuron Participates in Many Kinds of Inhibition and Innervates Much of the Mouse Visual Thalamus. *Neuron*, 106(3), 468–481.e2. <https://doi.org/10.1016/j.neuron.2020.02.001> (cit. on p. 6)
- Morgan, J. L., Berger, D. R., Wetzel, A. W., & Lichtman, J. W. (2016). The Fuzzy Logic of Network Connectivity in Mouse Visual Thalamus. *Cell*, 165(1), 192–206. <https://doi.org/10.1016/j.cell.2016.02.033> (cit. on pp. 2, 6, 118)
- Murphy, P. C., & Sillito, A. M. (1987). Corticofugal feedback influences the generation of length tuning in the visual pathway. *Nature*, 329(6141), 727–729. <https://doi.org/10.1038/329727a0> (cit. on p. 9)
- Murphy, P. C., & Sillito, A. M. (1996). Functional morphology of the feedback pathway from area 17 of the cat visual cortex to the lateral geniculate nucleus. *The Journal of Neuroscience*, 16(3), 1180–92 (cit. on p. 8).
- Nagel, G., Ollig, D., Fuhrmann, M., Kateriya, S., Musti, A. M., Bamberg, E., & Hegemann, P. (2002). Channelrhodopsin-1: a light-gated proton channel in green algae. *Science*, 296(5577), 2395–8. <https://doi.org/10.1126/science.1072068> (cit. on p. 12)
- Nagy, A. (2000). Cre recombinase: The universal reagent for genome tailoring. *Genesis*, 26(2), 99–109. [https://doi.org/10.1002/\(SICI\)1526-968X\(200002\)26:2<99::AID-GENE1>3.0.CO;2-B](https://doi.org/10.1002/(SICI)1526-968X(200002)26:2<99::AID-GENE1>3.0.CO;2-B) (cit. on p. 7)
- Nestvogel, D. B., & McCormick, D. A. (2021). Visual thalamocortical mechanisms of waking state-dependent activity and alpha oscillations. *Neuron*, 0(0). <https://doi.org/10.1016/j.neuron.2021.10.005> (cit. on pp. 11, 119–122)
- Niell, C. (2015). Cell Types, Circuits, and Receptive Fields in the Mouse Visual Cortex. *Annual review of neuroscience*, 38(4), 413–431. <https://doi.org/10.1146/annurev-neuro-071714-033807> (cit. on p. 8)
- Niell, C. M., & Stryker, M. P. (2010). Modulation of Visual Responses by Behavioral State in Mouse Visual Cortex. *Neuron*, 65(4), 472–479. <https://doi.org/10.1016/j.neuron.2010.01.033> (cit. on pp. 11, 121)
- Nolt, M. J., Kumbhani, R. D., & Palmer, L. a. (2007). Suppression at high spatial frequencies in the lateral geniculate nucleus of the cat. *Journal of neurophysiology*, 98(3), 1167–80. <https://doi.org/10.1152/jn.01019.2006> (cit. on p. 9)
- Olsen, S. R., Bortone, D. S., Adesnik, H., & Scanziani, M. (2012). Gain control by layer six in cortical circuits of vision. *Nature*, 483(7387), 47–52. <https://doi.org/10.1038/nature10835> (cit. on pp. 7, 9, 10, 121)
- Olshausen, B. A., & Field, D. J. (2005). How Close Are We to Understanding V1? *Neural Computation*, 17(8), 1665–1699. <https://doi.org/10.1162/0899766054026639> (cit. on p. 14)
- Osterhout, J. A., El-Danaf, R. N., Nguyen, P. L., & Huberman, A. D. (2014). Birthdate and outgrowth timing predict cellular mechanisms of axon target matching in the developing visual pathway. *Cell Reports*, 8(4), 1006–1017. <https://doi.org/10.1016/j.celrep.2014.06.063> (cit. on p. 6)

- Osterhout, J. A., Stafford, B. K., Nguyen, P. L., Yoshihara, Y., & Huberman, A. D. (2015). Contactin-4 Mediates Axon-Target Specificity and Functional Development of the Accessory Optic System. *Neuron*, 86(4), 985–999. <https://doi.org/10.1016/j.neuron.2015.04.005> (cit. on p. 6)
- Pearl, J., & Mackenzie, D. (2018). *The Book of Why - The New Science of Cause and Effect* (1st). Basic Books. (Cit. on p. 117).
- Peng, Y. R., Shekhar, K., Yan, W., Herrmann, D., Sappington, A., Bryman, G. S., van Zyl, T., Do, M. T. H., Regev, A., & Sanes, J. R. (2019). Molecular Classification and Comparative Taxonomics of Foveal and Peripheral Cells in Primate Retina. *Cell*, 176(5), 1222–1237. <https://doi.org/10.1016/j.cell.2019.01.004> (cit. on pp. 4, 118)
- Perry, V. H., & Cowey, A. (1984). Retinal ganglion cells that project to the superior colliculus and pretectum in the macaque monkey. *Neuroscience*, 12(4), 1125–1137. [https://doi.org/10.1016/0306-4522\(84\)90007-1](https://doi.org/10.1016/0306-4522(84)90007-1) (cit. on p. 4)
- Peters, A., Payne, B. R., & Budd, J. (1994). A numerical analysis of the geniculocortical input to striate cortex in the monkey. *Cerebral Cortex*, 4(3), 215–229. <https://doi.org/10.1093/cercor/4.3.215> (cit. on p. 8)
- Pillow, J. W., Shlens, J., Paninski, L., Sher, A., Litke, A. M., Chichilnisky, E. J., & Simoncelli, E. P. (2008). Spatio-temporal correlations and visual signalling in a complete neuronal population. *Nature*, 454(7207), 995–999. <https://doi.org/10.1038/nature07140> (cit. on pp. 15, 122)
- Pinto, L., Goard, M. J., Estandian, D., Xu, M., Kwan, A. C., Lee, S. H., Harrison, T. C., Feng, G., & Dan, Y. (2013). Fast Modulation of Visual Perception by Basal Forebrain Cholinergic Neurons. *Nature neuroscience*, 16(12), 1857. <https://doi.org/10.1038/NN.3552> (cit. on p. 11)
- Piscopo, D. M., El-Danaf, R. N., Huberman, a. D., & Niell, C. M. (2013). Diverse Visual Features Encoded in Mouse Lateral Geniculate Nucleus. *Journal of Neuroscience*, 33(11), 4642–4656. <https://doi.org/10.1523/JNEUROSCI.5187-12.2013> (cit. on pp. 2, 6, 118, 124)
- Pluta, S., Naka, A., Veit, J., Telian, G., Yao, L., Hakim, R., Taylor, D., & Adesnik, H. (2015). A direct translaminar inhibitory circuit tunes cortical output. *Nature Neuroscience* 2015 18:11, 18(11), 1631–1640. <https://doi.org/10.1038/nn.4123> (cit. on p. 11)
- Przybyczewski, A. W., Gaska, J. P., Foote, W., & Pollen, D. A. (2000). Striate cortex increases contrast gain of macaque LGN neurons. *Visual Neuroscience*, 17(4), 485–494. <https://doi.org/10.1017/S0952523800174012> (cit. on p. 10)
- Qiu, Y., Zhao, Z., Klindt, D., Kautzky, M., Szatko, K. P., Schaeffel, F., Rifai, K., Franke, K., Busse, L., & Euler, T. (2020). Mouse retinal specializations reflect knowledge of natural environment statistics, 1–46 (cit. on p. 123).
- Rao, R. P., & Ballard, D. H. (1999). Predictive coding in the visual cortex: a functional interpretation of some extra-classical receptive-field effects. *Nature neuroscience*, 2(1), 79–87. <https://doi.org/10.1038/4580> (cit. on pp. 1, 7, 10, 13, 119)
- Reimer, J., Froudarakis, E., Cadwell, C. R., Yatsenko, D., Denfield, G. H., & Tolias, A. S. (2014). Pupil Fluctuations Track Fast Switching of Cortical

- States during Quiet Wakefulness. *Neuron*, 84(2), 355–362. <https://doi.org/10.1016/j.neuron.2014.09.033> (cit. on pp. 11, 121, 122)
- Reimer, J., McGinley, M. J., Liu, Y., Rodenkirch, C., Wang, Q., McCormick, D. A., & Tolias, A. S. (2016). Pupil fluctuations track rapid changes in adrenergic and cholinergic activity in cortex. *Nature Communications* 2016 7:1, 7(1), 1–7. <https://doi.org/10.1038/ncomms13289> (cit. on pp. 11, 122)
- Riesenhuber, M., & Poggio, T. (1999). Hierarchical models of object recognition in cortex. *Nature Neuroscience*, 2(11), 1019–1025. <https://doi.org/10.1038/14819> (cit. on p. 1)
- Rivadulla, C., Martínez, L. M., Varela, C., & Cudeiro, J. (2002). Completing the Corticofugal Loop: A Visual Role for the Corticogeniculate Type 1 Metabotropic Glutamate Receptor. *Journal of Neuroscience*, 22(7), 2956–2962. <https://doi.org/10.1523/jneurosci.22-07-02956.2002> (cit. on pp. 9, 10)
- Robinson, P. A. (2006). Patchy propagators, brain dynamics, and the generation of spatially structured gamma oscillations. *Physical Review E - Statistical, Nonlinear, and Soft Matter Physics*, 73(4), 041904. <https://doi.org/10.1103/PhysRevE.73.041904> (cit. on p. 14)
- Roelfsema, P. R., & de Lange, F. P. (2016). Early Visual Cortex as a Multiscale Cognitive Blackboard. *Annual Review of Vision Science*, 2(1), 131–151. <https://doi.org/10.1146/annurev-vision-111815-114443> (cit. on p. 7)
- Román Rosón, M., Bauer, Y., Kotkat, A., Berens, P., Euler, T., & Busse, L. (2019). Mouse dLGN Receives Functional Input from a Diverse Population of Retinal Ganglion Cells with Limited Convergence. *Neuron*, 102(2), 462–476. <https://doi.org/10.2139/ssrn.3205414> (cit. on pp. 3, 17, 117, 118, 120, 121, 123, 124, 153)
- Rompani, S. B., Müllner, F. E., Wanner, A., Zhang, C., Roth, C. N., Yonehara, K., & Roska, B. (2017). Different Modes of Visual Integration in the Lateral Geniculate Nucleus Revealed by Single-Cell-Initiated Transsynaptic Tracing. *Neuron*, 93(4), 767–776.e6. <https://doi.org/10.1016/j.neuron.2017.01.028> (cit. on pp. 6, 118)
- Roska, B., & Meister, M. (2014). The retina dissects the visual scene into distinct features. *The New Visual Neurosciences*, 163–182 (cit. on p. 3).
- Rust, N. C., & Movshon, J. A. (2005). In praise of artifice. *Nature Neuroscience*, 8(12), 1647–1650. <https://doi.org/10.1038/nn1606> (cit. on p. 13)
- Sanes, J. R., & Masland, R. H. (2015). The Types of Retinal Ganglion Cells: Current Status and Implications for Neuronal Classification. *Annual Review of Neuroscience*, 38(1), 221–246. <https://doi.org/10.1146/annurev-neuro-071714-034120> (cit. on pp. 4, 118)
- Schneider, D. M., Nelson, A., & Mooney, R. (2014). A synaptic and circuit basis for corollary discharge in the auditory cortex. *Nature*, 513(7517), 189–194. <https://doi.org/10.1038/NATURE13724> (cit. on p. 11)
- Schröder, S., Steinmetz, N. A., Krumin, M., Pachitariu, M., Rizzi, M., Lagnado, L., Harris, K. D., & Carandini, M. (2019). Retinal outputs depend on behavioural state. *bioRxiv* (cit. on p. 124).
- Schröder, S., Steinmetz, N. A., Krumin, M., Pachitariu, M., Rizzi, M., Lagnado, L., Harris, K. D., & Carandini, M. (2020). Arousal Modulates Reti-

- nal Output. *Neuron*, 107(3), 487–495.e9. https://doi.org/10.1016/J.NEURON.2020.04.026/AROUSAL_MODULATES_RETINAL_OUTPUT.PDF (cit. on p. 11)
- Schwartz, O., Pillow, J. W., Rust, N. C., & Simoncelli, E. P. (2006). Spike-triggered neural characterization. *Journal of Vision*, 6(4), 13. <https://doi.org/10.1167/6.4.13> (cit. on p. 15)
- Seabrook, T. A., Burbridge, T. J., Crair, M. C., & Huberman, A. D. (2017). Architecture, Function, and Assembly of the Mouse Visual System. *Annual Review of Neuroscience*, 40(1), 499–538. <https://doi.org/10.1146/annurev-neuro-071714-033842> (cit. on pp. 1, 4, 16)
- Shepherd, G. M., & Yamawaki, N. (2021). Untangling the cortico-thalamo-cortical loop: cellular pieces of a knotty circuit puzzle. *Nature Reviews Neuroscience*, 0123456789(7), 389–406. <https://doi.org/10.1038/s41583-021-00459-3> (cit. on p. 7)
- Sherman, S. M. (2001). Tonic and burst firing: Dual modes of thalamocortical relay. *Trends in Neurosciences*, 24(2), 122–126. [https://doi.org/10.1016/S0166-2236\(00\)01714-8](https://doi.org/10.1016/S0166-2236(00)01714-8) (cit. on pp. 6, 10)
- Sherman, S. M. (2007). The thalamus is more than just a relay. *Current opinion in neurobiology*, 17(4), 417–22. <https://doi.org/10.1016/j.conb.2007.07.003> (cit. on p. 2)
- Sherman, S. M., & Guillery, R. W. (1996). Functional organization of thalamocortical relays. *Journal of neurophysiology*, 76(3), 1367–1395. <https://doi.org/10.1152/JN.1996.76.3.1367> (cit. on pp. 10, 11, 119, 122)
- Sherman, S. M., & Guillery, R. W. (2002). The role of the thalamus in the flow of information to the cortex. *Philosophical transactions of the Royal Society of London*, 357(1428), 1695–708. <https://doi.org/10.1098/rstb.2002.1161> (cit. on pp. 2–5, 7, 8, 16, 119)
- Siegle, J. H., Jia, X., Durand, S., Gale, S., Bennett, C., Graddis, N., Heller, G., Ramirez, T. K., Choi, H., Luviano, J. A., Groblewski, P. A., Ahmed, R., Arkhipov, A., Bernard, A., Billeh, Y. N., Brown, D., Buice, M. A., Cain, N., Caldejon, S., ... Koch, C. (2021). A survey of spiking in the mouse visual system reveals functional hierarchy. *Nature*, 592(12), 11–16. <https://doi.org/10.1038/s41586-020-03171-x> (cit. on p. 1)
- Sillito, A. M., Cudeiro, J., & Jones, H. E. (2006). Always returning: feedback and sensory processing in visual cortex and thalamus. *Trends in Neurosciences*, 29(6), 307–316. <https://doi.org/10.1016/j.tins.2006.05.001> (cit. on pp. 2, 8, 9, 16)
- Sillito, A. M., & Jones, H. E. (2002). Corticothalamic interactions in the transfer of visual information (P. Adams, R. W. Guillery, S. M. Sherman, & A. M. Sillito, Eds.). *Philosophical Transactions of the Royal Society of London. Series B: Biological Sciences*, 357(1428), 1739–1752. <https://doi.org/10.1098/rstb.2002.1170> (cit. on pp. 7, 9, 10, 15, 119)
- Sincich, L. C., Adams, D. L., Economides, J. R., & Horton, J. C. (2007). Transmission of spike trains at the retinogeniculate synapse. *The Journal of Neuroscience*, 27(10), 2683–92. <https://doi.org/10.1523/JNEUROSCI.5077-06.2007> (cit. on pp. 5, 117)
- Sinz, F. H., Ecker, A. S., Fahey, P. G., Walker, E. Y., Cobos, E., Froudarakis, E., Yatsenko, D., Pitkow, X., Reimer, J., & Tolias, A. S. (2018). Stimulus domain transfer in recurrent models for large scale cortical population

- prediction on video. *Advances in Neural Information Processing Systems*, (32), 7199–7210 (cit. on p. 123).
- Sonkusare, S., Breakspear, M., & Guo, C. (2019). Naturalistic Stimuli in Neuroscience: Critically Acclaimed. *Trends in Cognitive Sciences*, 23(8), 699–714. <https://doi.org/10.1016/j.tics.2019.05.004> (cit. on p. 13)
- Spacek, M. A., Crombie, D., Bauer, Y., Born, G., Liu, X., Katzner, S., & Busse, L. (2022). Robust effects of corticothalamic feedback and behavioral state on movie responses in mouse dLGN. *eLife*, 11, e70469. <https://doi.org/10.7554/eLife.70469> (cit. on pp. 3, 59, 117, 120, 121, 153)
- Stringer, C., Pachitariu, M., Steinmetz, N., Reddy, C. B., Carandini, M., & Harris, K. D. (2019). Spontaneous behaviors drive multidimensional, brain-wide activity. *Science*, 364(6437), 1–26. <https://doi.org/10.1126/science.aav7893> (cit. on p. 11)
- Sümbül, U., Song, S., McCulloch, K., Becker, M., Lin, B., Sanes, J. R., Masland, R. H., & Seung, H. S. (2014). A genetic and computational approach to structurally classify neuronal types. *Nature Communications*, 5(1), 3512. <https://doi.org/10.1038/ncomms4512> (cit. on pp. 4, 118)
- Summerfield, C., & Egner, T. (2009). Expectation (and attention) in visual cognition. *Trends in cognitive sciences*, 13(9), 403–9. <https://doi.org/10.1016/j.tics.2009.06.003> (cit. on p. 7)
- Swadlow, H. A., & Weyand, T. G. (1987). Corticogeniculate neurons, corticotectal neurons, and suspected interneurons in visual cortex of awake rabbits: receptive-field properties, axonal properties, and effects of EEG arousal. *Journal of neurophysiology*, 57(4), 977–1001. <https://doi.org/10.1152/JN.1987.57.4.977> (cit. on pp. 10, 119)
- Szegedy, C., Zaremba, W., Sutskever, I., Bruna, J., Erhan, D., Goodfellow, I., & Fergus, R. (2013). Intriguing properties of neural networks. *arXiv*, 1–10 (cit. on p. 1).
- Tasic, B., Menon, V., Nguyen, T. N., Kim, T. K., Jarsky, T., Yao, Z., Levi, B., Gray, L. T., Sorensen, S. A., Dolbeare, T., Bertagnolli, D., Goldy, J., Shapovalova, N., Parry, S., Lee, C., Smith, K., Bernard, A., Madisen, L., Sunkin, S. M., . . . Zeng, H. (2016). Adult mouse cortical cell taxonomy revealed by single cell transcriptomics. *Nature Neuroscience*, 19(2), 335–346. <https://doi.org/10.1038/nn.4216> (cit. on p. 8)
- Thompson, A. D., Picard, N., Min, L., Fagiolini, M., & Chen, C. (2016). Cortical Feedback Regulates Feedforward Retinogeniculate Refinement. *Neuron*, 91(5), 1021–1033. <https://doi.org/10.1016/j.neuron.2016.07.040> (cit. on pp. 8, 118)
- Trenholm, S., & Krishnaswamy, A. (2020). An Annotated Journey through Modern Visual Neuroscience. *The Journal of Neuroscience*, 40(1), 44–53. <https://doi.org/10.1523/JNEUROSCI.1061-19.2019> (cit. on pp. 3, 124)
- Ullman, S. (1980). Against direct perception. *Behavioral and Brain Sciences*, 3(3), 373–381. <https://doi.org/10.1017/S0140525X0000546X> (cit. on p. 1)
- Usrey, W. M., & Alitto, H. J. (2015). Visual Functions of the Thalamus. *Annual Review of Vision Science*, 1(1), 351–371. <https://doi.org/10.1146/annurev-vision-082114-035920> (cit. on pp. 1, 2, 4, 5, 120)
- Usrey, W. M., & Sherman, S. M. (2019). Corticofugal circuits: Communication lines from the cortex to the rest of the brain. *Journal of Comparative*

- Neurology*, 527(3), 640–650. <https://doi.org/10.1002/cne.24423> (cit. on pp. 9, 119)
- Vaiceliunaite, A., Eriskien, S., Franzen, F., Katzner, S., & Busse, L. (2013). Spatial integration in mouse primary visual cortex. *Journal of neurophysiology*, 110(4), 964–72. <https://doi.org/10.1152/jn.00138.2013> (cit. on p. 12)
- van Bergen, R. S., & Kriegeskorte, N. (2020). Going in circles is the way forward: the role of recurrence in visual inference. *Current Opinion in Neurobiology*, 65, 176–193. <https://doi.org/10.1016/j.conb.2020.11.009> (cit. on p. 7)
- Vanderwal, T., Eilbott, J., & Castellanos, F. X. (2019). Movies in the magnet: Naturalistic paradigms in developmental functional neuroimaging. *Developmental Cognitive Neuroscience*, 36(5), 100600. <https://doi.org/10.1016/j.dcn.2018.10.004> (cit. on p. 13)
- Velez-Fort, M., Rousseau, C. V., Niedworok, C. J., Wickersham, I. R., Rancz, E. A., Brown, A. P. Y., Strom, M., & Margrie, T. W. (2014). The stimulus selectivity and connectivity of layer six principal cells reveals cortical microcircuits underlying visual processing. *Neuron*, 83(6), 1431–1443. <https://doi.org/10.1016/j.neuron.2014.08.001> (cit. on pp. 7–9)
- Vinck, M., Batista-Brito, R., Knoblich, U., & Cardin, J. A. (2015). Arousal and Locomotion Make Distinct Contributions to Cortical Activity Patterns and Visual Encoding. *Neuron*, 86(3), 740–754. <https://doi.org/10.1016/j.neuron.2015.03.028> (cit. on pp. 11, 121, 122)
- von Helmholtz, H. (1867). *Handbuch der physiologischen Optik*. Leopold Voss. (Cit. on p. 1).
- Walker, E. Y., Sinz, F. H., Cobos, E., Muhammad, T., Froudarakis, E., Fahey, P. G., Ecker, A. S., Reimer, J., Pitkow, X., & Tolias, A. S. (2019). Inception loops discover what excites neurons most using deep predictive models. *Nature Neuroscience*, 22(12), 2060–2065. <https://doi.org/10.1038/s41593-019-0517-x> (cit. on p. 123)
- Wang, H. P., Spencer, D., Fellous, J. M., & Sejnowski, T. J. (2010). Synchrony of thalamocortical inputs maximizes cortical reliability. *Science*, 328(5974), 106–109. <https://doi.org/10.1126/science.1183108> (cit. on p. 14)
- Wang, W., Andolina, I. M., Lu, Y., Jones, H. E., & Sillito, A. M. (2018). Focal gain control of thalamic visual receptive fields by layer 6 corticothalamic feedback. *Cerebral Cortex*, 28(1), 267–280. <https://doi.org/10.1093/cercor/bhw376> (cit. on p. 10)
- Wang, W., Jones, H. E., Andolina, I. M., Salt, T. E., & Sillito, A. M. (2006). Functional alignment of feedback effects from visual cortex to thalamus. *Nature Neuroscience*, 9(10), 1330–1336. <https://doi.org/10.1038/nn1768> (cit. on p. 10)
- Wang, X., Wei, Y., Vaingankar, V., Wang, Q., Koepsell, K., Sommer, F. T., & Hirsch, J. A. (2007). Feedforward Excitation and Inhibition Evoke Dual Modes of Firing in the Cat's Visual Thalamus during Naturalistic Viewing. *Neuron*, 55(3), 465–478. <https://doi.org/10.1016/j.neuron.2007.06.039> (cit. on pp. 14, 15)
- Wark, B., Lundstrom, B. N., & Fairhall, A. (2007). Sensory adaptation. *Current Opinion in Neurobiology*, 17(4), 423–429. <https://doi.org/10.1016/j.conb.2007.07.001> (cit. on p. 3)

- Webb, B. S., Tinsley, C. J., Barraclough, N. E., Easton, A., Parker, A., & Derington, A. M. (2002). Feedback from V1 and inhibition from beyond the classical receptive field modulates the responses of neurons in the primate lateral geniculate nucleus. *Visual Neuroscience*, *19*(5), 583–592. <https://doi.org/10.1017/S0952523802195046> (cit. on p. 10)
- Weyand, T. G. (2016). The multifunctional lateral geniculate nucleus. *Reviews in the Neurosciences*, *27*(2), 135–157. <https://doi.org/10.1515/revneuro-2015-0018> (cit. on pp. 9, 119)
- Wiegert, J. S., Mahn, M., Prigge, M., Printz, Y., & Yizhar, O. (2017). Silencing Neurons: Tools, Applications, and Experimental Constraints. *Neuron*, *95*(3), 504–529. <https://doi.org/10.1016/j.neuron.2017.06.050> (cit. on pp. 12, 120, 123)
- Wiegert, J. S., & Oertner, T. G. (2016). How (not) to silence long-range projections with light. *Nature Neuroscience*, *19*(4), 527–528. <https://doi.org/10.1038/nn.4270> (cit. on p. 12)
- Wietek, J., Rodriguez-Rozada, S., Tutas, J., Tenedini, F., Grimm, C., Oertner, T. G., Soba, P., Hegemann, P., & Simon Wiegert, J. (2017). Anion-conducting channelrhodopsins with tuned spectra and modified kinetics engineered for optogenetic manipulation of behavior. *Scientific Reports*, *7*(1), 1–18. <https://doi.org/10.1038/s41598-017-14330-y> (cit. on p. 12)
- Wörgötter, F., Eyding, D., Macklis, J. D., & Funke, K. (2002). The influence of the corticothalamic projection on responses in thalamus and cortex (P. Adams, R. W. Guillery, S. M. Sherman, & A. M. Sillito, Eds.). *Philosophical Transactions of the Royal Society of London. Series B: Biological Sciences*, *357*(1428), 1823–1834. <https://doi.org/10.1098/rstb.2002.1159> (cit. on p. 10)
- Yamins, D. L. K., Hong, H., Cadieu, C. F., Solomon, E. A., Seibert, D., & DiCarlo, J. J. (2014). Performance-optimized hierarchical models predict neural responses in higher visual cortex. *Proceedings of the National Academy of Sciences*, *111*(23), 8619–8624. <https://doi.org/10.1073/pnas.1403112111> (cit. on pp. 1, 123)
- Yizhar, O., Fenno, L. E., Davidson, T. J., Mogri, M., & Deisseroth, K. (2011). Optogenetics in neural systems. *Neuron*, *71*(1), 9–34. <https://doi.org/10.1016/j.neuron.2011.06.004> (cit. on p. 12)
- Zhao, X., Chen, H., Liu, X., & Cang, J. (2013). Orientation-selective responses in the mouse lateral geniculate nucleus. *The Journal of Neuroscience*, *33*(31), 12751–63. <https://doi.org/10.1523/JNEUROSCI.0095-13.2013> (cit. on p. 6)

YANNIK BAUER

PHD CANDIDATE | COMPUTATIONAL VISION NEUROSCIENCE

WORK ADDRESS:

Faculty of Biology, Division of Neurobiology,
LMU Munich, 82151 Munich, GERMANY



ACADEMIC EDUCATION

- 10/2017 – *present* PHD PROGRAM IN SYSTEMIC NEUROSCIENCES
**Graduate School of Systemic Neurosciences (GSN),
Ludwig-Maximilians University (LMU) Munich**
Thesis: ‘Robust processing of visual feedforward and feedback signals in the mouse dLGN’
Advisers: Prof Laura Busse (LMU), Prof Philipp Berens & Prof Thomas Euler (Tübingen)
- 10/2016 – 10/2017 SMARTSTART2 PRE-PHD PROGRAM FOR COMPUTATIONAL NEUROSCIENCE
**Bernstein Network for Computational Neuroscience (BNCN),
University of Tübingen & Ludwig-Maximilians University Munich**
- 10/2014 – 09/2016 MSC NEURAL & BEHAVIOURAL SCIENCES
**International Max-Planck Research School,
Graduate Training Centre of Neuroscience, University of Tübingen**
Grade: 1.2 (very good)
Thesis: ‘In Vivo Optogenetics with the Inhibitory Step-Function Opsin SwiChR⁺⁺ – Cortico-Thalamic Feedback Neurons for Robust Vision’
Adviser: Prof Laura Busse (then Tübingen)
- 10/2011 – 06/2014 BA (HONS) PSYCHOLOGY & PHILOSOPHY
Balliol College, University of Oxford
Grade: Second class, Division one
Thesis: ‘Expectations and Anticipatory Alpha-Modulations in Visual Distractor Inhibition’
Adviser: Prof Mark Stokes (Oxford)

RESEARCH EXPERIENCE

- 10/2016 – *present* PHD RESEARCH IN COMPUTATIONAL VISION NEUROSCIENCE
Advisers:
Prof Laura Busse (LMU), Prof Philipp Berens, Prof Thomas Euler (Tübingen)
DFG-funded collaborative research center '*Robust Vision*' (CRC1233) on experimental and theoretical aspects of visual signal transformations in the dorsolateral geniculate nucleus (dLGN): data analysis: statistics, neural signal processing, modelling, clustering, matrix factorization; experimentation: see section *Master's Thesis*
- 02 – 09/2016 MASTER'S THESIS
Adviser: Prof Busse
In vivo extracellular silicon-probe recordings from mouse early visual system, optogenetic manipulation of V1-activity, animal handling, surgery, microinjection of retrograde tracers/viral vectors, perfusion, histology, data analysis
- 11/2015 – 02/2016 LABORATORY ROTATION
Adviser: Marcel Oberländer, Computational Neuroanatomy, Max-Planck Institute for Biological Cybernetics Tübingen
In vivo patch-clamp electrophysiology in somatosensory cortex of anaesthetized rats, biocytin-filling, perfusion, histology, and computational reconstruction of 3D-morphology
- 09 – 11/2015 LABORATORY ROTATION
Adviser: Prof Thomas Euler
Simultaneous two-photon Ca²⁺-imaging and patch-clamp electrophysiology in *ex vivo* wholemount retinæ of transgenic mice; data analysis for spike inference from a probabilistic model trained via supervised machine learning
- 05 – 11/2015 GRADUATE RESEARCH ASSISTANT
Advisers: Prof Thomas Euler, Prof Philipp Berens & Prof Laura Busse
Clustering of dLGN-neuron types based on extracellular silicon probe recordings
- 2013 – 2014 BACHELOR'S THESIS AND RESEARCH ASSISTANT
Prof Mark Stokes, Attention Group, Oxford Centre of Human Brain Activity, University of Oxford
Visuospatial attention and inhibition in humans, experiment design, coding, human participant recruitment, data recording (behaviour, EEG), EEG time-frequency analysis

PROFESSIONAL TRAINING, WORKSHOPS & SCHOOLS

- 08/2021 SUMMER SCHOOL 'ADVANCED SCIENTIFIC PROGRAMMING IN PYTHON'
- 10/2019 TEACHING ASSISTANT: INTRODUCTION TO SCIENTIFIC PYTHON PROGRAMMING
LMU, Martin Spacek
- 12/2019 COMPUTATIONAL NEUROSCIENCE
Coursera, Prof Adrienne Fairhall & Prof Rajesh Rao
<https://coursera.org/share/adb3ced7550d7eef2b702351de94c21f>
- 02/2019 DEEP LEARNING SPECIALIZATION
Coursera, Andrew Ng
<https://coursera.org/share/315885c7826728cde9b21d2a3231be19>

- 03/2018 MACHINE LEARNING
Coursera, Prof Andrew Ng
<https://coursera.org/share/f7d9ec279014440df35a5febef9d0343>
- 2015 – 2016 ANIMAL RESEARCH TRAINING (‘VERSUCHSTIERKUNDL. PRIVATISSIMUM’)
University Clinics, University of Tübingen
 Theoretical and practical training course (40 h) according to FELASA (Federation of European Laboratory Animal Science Association) level B (animal experimenter)
- 2012 – 2014 LIFE SCIENCES COLLEGE, GROUP ‘RESEARCH IN COGNITIVE NEUROSCIENCES’
Studienstiftung des deutschen Volkes
 4 semesterly 5-day meetings for group work
- 07/2012 SUMMER ACADEMY (NICE, FRANCE); GROUP ‘LANGUAGE & DEMENTIA’
Studienstiftung des deutschen Volkes
- 07/2008 SUMMER COURSE ‘CARROT & STICK - REWARD PROCESSING IN THE BRAIN’
Deutsche Schülerakademie, Collegium Augustianum Gaesdonck, Germany

SCHOLARSHIPS, GRANTS & AWARDS

- 10/2016 – 10/2017 SmartStart2 stipend by the Bernstein Network for Computational Neuroscience in collaboration with the VolkswagenFoundation
 Fully-funded pre-PhD position (30,000 €)
- 06 – 08/2013 Brackenbury Fund, Balliol College, University of Oxford
 Funding summer research project with Prof Mark Stokes
- 2011 – 2016 Scholarship from the Studienstiftung des deutschen Volkes
- 07/2008 Stipend for the Deutsche Schülerakademie

PUBLICATIONS

- 2019 Román Rosón, M.*, **Bauer Y.***, Kotkat, A., Berens, P., Euler, T., & Busse, L. (2019). Mouse dLGN Receives Functional Input from a Diverse Population of Retinal Ganglion Cells with Limited Convergence. *Neuron*, 102(2), 462–476. <https://doi.org/10.1016/j.neuron.2019.01.040>.
**equal contributions*
- 2022 Spacek, M. A., Crombie, D., **Bauer, Y.**, Born, G., Liu, X., Katzner, S., & Busse, L. (2022). Robust effects of corticothalamic feedback and behavioral state on movie responses in mouse dLGN. *ELife*, 11, e70469. <https://doi.org/10.7554/eLife.70469>
- 2022 **Bauer, Y.***, Schmors, L.*, Huang, Z., Kotkat, A.H., Crombie, D., Meyerolbersleben, L., Renner, S., Sokoloski, S., Busse, L., and Berens, P. (2022). An interpretable spline-LNP model to characterise feedforward and feedback processing in mouse dLGN. *In preparation*
**equal contributions*
- 2022 Kraynyukova, N., Renner, S., Born, G., **Bauer, Y.**, Spacek, M., Tushev, G., Busse, L., and Tchumatchenko, T. (2022). In vivo recordings of V1 and thalamic extracellular activity reveal cortical connectivity rules. *In revision*

TALKS

- 03/2019 Mouse dLGN receives functional input from a diverse population of retinal ganglion cells with limited convergence. *13th meeting of the German Neuroscience Society (NWG), Göttingen, Germany*
- 06/2018 Mouse dLGN receives input from a diverse population of retinal ganglion cells with limited functional convergence. *LMU Bernstein Center Retreat, Tutzingen, Germany*

CONFERENCES & POSTERS

- 03/2018 **Y Bauer**, M Román Rosón, P Berens, T Euler, L Busse. Sparse linear recombination using most retinal output channels yields highly diverse visual representations in mouse dLGN. *Computational and Systems Neuroscience (Cosyne) Conference, 2018, Denver, Colorado, USA*
- 09/2017 **Y Bauer**, M Román-Rosón, L Busse, P Berens, T Euler. Functional Characterization of the Signal Processing Chain in the Mouse Early Visual System. *Bernstein Conference for Computational Neuroscience, 2017, Göttingen, Germany*
- 11/2015 **Y Bauer**, H A von Lutz, M P Noonan, M G Stokes. Experience and Anticipatory Alpha-Wave Modulations in Distractor Suppression. *NeNa ('Neurowissenschaftliche Nachwuchskonferenz') Conference for Junior Neuroscientists, 2015, Schramberg, Germany*
- 10/2015 M Román Rosón, P Berens, **Y Bauer**, T Euler, L Busse. Functional Characterization of the Signal Processing Chain in the Mouse Early Visual System. *European Retina Meeting, 2015, Brighton, UK*

ROLES, MEMBERSHIPS & VOLUNTARY WORK

- 2019 – *present* Talking Science, member organizing committee
LMU MUNICH
- 2016 – *present* Bernstein Network Computational Neuroscience, member
- 2015 – *present* Pro-Test Deutschland, organization for public communication of animal research
TÜBINGEN UNIVERSITY
- 2014 – 2016 Student representative *MSc Neural & Behavioural Sciences*
TÜBINGEN UNIVERSITY
- 2013 – 2014 Student representative for the *British Psychological Society*
OXFORD UNIVERSITY
- 2012 – 2013 Peer Supporter, Balliol College Team
OXFORD UNIVERSITY
- 02 – 05/2010 Journalistic internship via *Students Travel & Exposure South Africa*
NEWS AGENCY 'L'INDÉPENDENT EXPRESS', LOMÉ, TOGO
- 10/2008 – 10/2009 Freiwilliges Soziales Auslandsjahr (Voluntary Social Year)
SPECIAL NEEDS CARE COMMUNITY 'BEANNACHAR', ABERDEEN, SCOTLAND

2006 – 2008 Class president German Abitur graduation year
GYMNASIUM WALSRÖDE

PROFESSIONAL SKILLS

PROGRAMMING / IT / DATA SCIENCE	MATLAB / Octave Python (PyCharm, Jupyter) Command line (Bash) Git / GitHub / GitLab Docker LATEX Adobe Photoshop, Illustrator, InDesign, Lightroom FIJI / ImageJ
LANGUAGES	German (native), English (fluent), French (fluent), Spanish (beginner), Estonian (beginner)

PUBLICATIONS

- Bauer, Y., Schmors, L., Huang, Z., Kotkat, A. H., Crombie, D., Meyerolbersleben, L., Renner, S., Sokoloski, S., Busse, L., & Berens, P. (2022). An interpretable spline-LNP model to characterise feed-forward and feedback processing in mouse dLGN. *In preparation*.
- Kraynyukova, N., Renner, S., Born, G., Bauer, Y., Spacek, M., Tushev, G., Busse, L., & Tchumatchenko, T. (2022). In vivo recordings of V1 and thalamic extracellular activity reveal cortical connectivity rules. *In revision*.
- Román Rosón, M., Bauer, Y., Kotkat, A., Berens, P., Euler, T., & Busse, L. (2019). Mouse dLGN Receives Functional Input from a Diverse Population of Retinal Ganglion Cells with Limited Convergence. *Neuron*, 102(2), 462–476. <https://doi.org/10.2139/ssrn.3205414>
- Spacek, M. A., Crombie, D., Bauer, Y., Born, G., Liu, X., Katzner, S., & Busse, L. (2022). Robust effects of corticothalamic feedback and behavioral state on movie responses in mouse dLGN. *eLife*, 11, e70469. <https://doi.org/10.7554/eLife.70469>

EIDESSTATTLICHE VERSICHERUNG / AFFIDAVIT

Hiermit versichere ich an Eides statt, dass ich die vorliegende Dissertation *Robust Visual Feedforward and Feedback Signal Processing in the Mouse Thalamus* selbstständig angefertigt habe, mich außer der angegebenen keiner weiteren Hilfsmittel bedient und alle Erkenntnisse, die aus dem Schrifttum ganz oder annähernd übernommen sind, als solche kenntlich gemacht und nach ihrer Herkunft unter Bezeichnung der Fundstelle einzeln nachgewiesen habe.

I hereby confirm that the dissertation *Robust Visual Feedforward and Feedback Signal Processing in the Mouse Thalamus* is the result of my own work and that I have only used sources or materials listed and specified in the dissertation.

Munich, 28th February 2022

Yannik T. Bauer

AUTHOR CONTRIBUTIONS

ROMÁN ROSÓN & BAUER ET AL. (2019):

The manuscript was published as:

Román Rosón, M., Bauer, Y., Kotkat, A., Berens, P., Euler, T., & Busse, L. (2019). Mouse dLGN Receives Functional Input from a Diverse Population of Retinal Ganglion Cells with Limited Convergence. *Neuron*, 102(2), 462–476. <https://doi.org/10.2139/ssrn.3205414>*

*shared first authorship between M.R.R. and Y.B.

CONTRIBUTION SUMMARY: Conceptualization, T.E., L.B., P.B.; Methodology, T.E., L.B., P.B., M.R.R., Y.B.; Software, Y.B., P.B., L.B., T.E., A.H.K., M.R.R.; Formal Analysis, Y.B., A.H.K., M.R.R.; Investigation, Y.B. M.R.R.; Writing – Initial Draft, P.B., L.B., T.E.; Writing – Reviewing and Editing, Y.B., P.B., L.B., T.E., M.R.R.; Funding Acquisition, Y.B., P.B., L.B., T.E.; Supervision, P.B., L.B., T.E.

PERSONAL CONTRIBUTIONS: Y.B. provided analyses for the functional characterization of dLGN-p RGCs, signal deconvolution and creation of a match index (Mi) to assign dLGN-p RGC to functional RGC types, and calculated cluster proportions in dLGN-p and RGC-all cells (Fig2). Y.B. also provided the analyses of the cross-validated non-negative matrix factorization (CV-NNMF) (Fig4), as well as the linear feedforward model (Fig5). For supplemental materials, Y.B. created the injection histology overview (FigS1), deconvolution of retinal 2P traces (FigS3), match index population histogram (FigS4), cluster assignments (FigS5), assesment of model limitations (FigS9), and comparison of distributions (FigS10). Y.B. also ran additional injection experiments for retrograde labelling of dLGN-p RGCs, and functional two-photon imaging of ex vivo retina visual responses (data not used in publication). Y.B. maintained the code repository. Lastly, Y.B. secured project funding via the Volkswagen-Stiftung-funded *SmartStart* programme for Computational Neuroscience by the *Bernstein Network Computational Neuroscience*.

SPACEK ET AL. (2022):

The manuscript was published as:

Spacek, M. A., Crombie, D., Bauer, Y., Born, G., Liu, X., Katzner, S., & Busse, L. (2022). Robust effects of corticothalamic feedback and behavioral state on movie responses in mouse dLGN. *eLife*, 11, e70469. <https://doi.org/10.7554/eLife.70469>

CONTRIBUTION SUMMARY: Conceptualization, L.B. and M.A.S.; Methodology, M.A.S., D.C.; Software, M.A.S., S.K., D.C., G.B., Y.B., X.L.; Formal Analysis, S.K.; Investigation, M.A.S., Y.B., X.L.; Data Curation, M.A.S., G.B., D.C., S.K., L.B.; Writing – Original Draft, L.B., G.B.; Writing – Review & Editing, L.B., S.K., M.A.S., G.B., D.C.; Visualization, M.A.S., G.B., Y.B., S.K.; Supervision, L.B.; Project Administration, L.B.; Funding Acquisition, L.B.

PERSONAL CONTRIBUTIONS: Y.B. adapted the experimental method for direct L6 CT photosuppression with stGtACR2 in Ntsr1-Cre-mice to the Busse Lab (Fig1S4), and conducted a control experiment on an Ntsr1-Cre-negative mouse (Fig1S5). Y.B. also created Fig1b to illustrate the histological expression volume of ChR2 in V1 of PV-Cre mice.

BAUER & SCHMORS ET AL. (2022) [*in preparation*]:

The manuscript is in preparation as:

Bauer, Y., Schmors, L., Huang, Z., Kotkat, A. H., Crombie, D., Meyerolbersleben, L., Renner, S., Sokoloski, S., Busse, L., & Berens, P. (2022). An interpretable spline-LNP model to characterise feedforward and feedback processing in mouse dLGN. *In preparation**

*shared first authorship between Y.B. and L.S.

CONTRIBUTION SUMMARY: Conceptualization, L.B., P.B., S.S.; Methodology, L.B., P.B., Y.B., L.S., Z.H., S.S.; Software, L.S., Y.B., S.R., D.C., Z.H.; Formal Analysis, L.S., Y.B., A.K.; Investigation, Y.B., L.M., A.K.; Resources, L.B., P.B.; Data Curation, Y.B., L.S., A.K., L.M., D.C.; Writing – Original Draft, Y.B., L.S., L.B.; Writing – Review & Editing, all authors; Visualization, Y.B., L.S.; Supervision, L.B., P.B., S.S.; Project Administration, L.B., P.B.; Funding Acquisition, L.B., P.B.

PERSONAL CONTRIBUTIONS: Y.B. initiated the use and design of a complex, dynamic movie stimulus, adapted the stGtACR2-mediated photosuppression of L6CT cells to the Busse Lab, performed the injection and headbar implantation surgeries, handled mice and provided recordings of dLGN electrophysiology, locomotion and eye-tracking to visual stimulation and optogenetic manipulations, perfusion, and histology/microscopy (Fig1a-e). Y.B. further performed pre-processing of electrophysiological data (spike sorting). Y.B. also created and maintained the database tables and code repositories for the analysis pipeline. This included cell-based and population-wide analyses of condition-wise effects of optogenetics, locomotion and pupil size (Fig1f-k), creation of optogenetic/run/eye modulation indices, tests of predictor correlations, spatial RF contour/area estimation and quality indices; visualization of the spline-LNP model (Fig2, Fig3, FigS1), and comparison of the models for responses to the movie stimulus vs. the sparse noise stimulus (Fig4, FigS2). Y.B. wrote and revised the original draft.

We assert that the aforementioned author contributions are correct and accurate.

Munich, 28th February 2022

Yannik T. Bauer

Prof. Dr. Laura Busse

Miroslav Román Rosón

Lisa Schmors